Effects of Non-Ionizing Electromagnetic Radiation to the Human Body and Environment

Thesis submitted for the partial fulfilment of the requirements for the degree of

Doctor of Philosophy (Engineering)

by

Md. Faruk Ali

Electronics and Telecommunication Engineering
Faculty Council of Engineering & Technology
Jadavpur University, Kolkata-700032
India

2017

JADAVPUR UNIVERSITY

KOLKATA – 700 032, INDIA

INDEX NO. 131/13/E

1. Title of the thesis: Effects of Non-Ionizing Electromagnetic Radiation to the Human Body and Environment

2. Name, Designation & Institution of the Supervisor/s:

Dr. Sudhabindu Ray

Associate Professor, Department of Electronics and Telecommunication Engineering

Jadavpur University, Kolkata – 700 032, West Bengal, India.

3. List of publications:

(Journal Papers)

I. **Md.Faruk Ali** and Sudhabindu Ray, "SAR Analysis in a Spherical Inhomogeneous Human Head Model Exposed to Radiating Dipole Antenna for 500 MHz –3 GHz Using FDTD method", *International Journal of microwave and Optical Technology*, vol. 4. No.1, pp. 35-40, January -2009. ISSN: 1553-0396.

II. **Md. Faruk Ali** and Sudhabindu Ray, "SAR Analysis for Handheld Mobile Phone Using DICOM Based Voxel Model", *Journal of Microwaves, Optoelectronics and Electromagnetic Applications (JMOe)*, Vol. 12, No. 2, pp. 363-375, December-2013.

III. **M. F. Ali** and S. Ray, "Quasi Optical Effects of Non-Ionizing Radiation inside Pregnant Woman Abdomen," *Progress In Electromagnetics Research M*, Vol. 35, pp. 31-38, 2014. doi:10.2528/PIERM14010703.

IV. **M. F. Ali** and S. Ray, "Study of EM Wave Absorption and Shielding Characteristics for a Bonsai Tree for GSM-900 Band," *Progress In Electromagnetics Research C*, Vol. 49, pp. 149-157, 2014.

V. **Md. Faruk Ali** and Sudhabindu Ray, "FDTD based SAR analysis in human head using irregular volume averaging techniques of different resolutions at GSM 900 band," *Indian Journal of Radio & Space Physics*, Vol. 43, pp. 235-242, June 2014.

VI. **M. F. Ali** and S. Ray, "Estimation of Whole-body average SAR in Human Body Exposed to a Base Station Antenna," *Progress In Electromagnetics Research* M, Vol. 39, 2014, pp. 19-26, 2014. doi:10.2528/PIERM14080201.

VII. **Md. Faruk Ali** and Sudhabindu Ray, "Offline RF Thermal Ablation Planning Using CT/MRI Scan Data," *Egyptian Journal of Radiology and Nuclear Medicine*, ELSEVIER, Vol. 46, pp. 141-150, 2015.

VIII. **Md. Faruk Ali**, S.B.Belamgi and Sudhabindu Ray, "A Study of Specific Absorption Rate and Shielding Effectiveness for Money Plant at 2.4 GHz," *Microwave Review*, Vol. 21, No. 2, pp. 2-6, December 2015.

(International/National Conference Papers)

IX. **Md.Faruk Ali** and Sudhabindu Ray, "SAR Analysis on Human Head Exposed to Radiating Dipole Antenna for 500 MHz – 5 GHz Frequency Band Using FDTD Method", *National Conference on Communication (NCC),* IIT Bombay*, India,* pp.481-485, 2008.

X. **Md.Faruk Ali** and Sudhabindu Ray, "SAR Distributions in a Spherical Inhomogeneous Human Head Model Exposed to Electromagnetic Field for 500 MHz – 3 GHz Using FDTD method", *National Conference on Communications,* IIT Guwahati, India, pp.64-67, January - 2009.

XI. **Md.Faruk Ali** and Sudhabindu Ray, "SAR Analysis on Child and Adult Head Models for Radiating Dipole Antenna Using FDTD method", *International Symposium on Microwaves and Millimeterwaves : Basics and Technology,* Bose Institute, Kolkata, India, pp.46-48, January - 2009.

XII. **Md.Faruk Ali**, Sujoy Mukherjee and Sudhabindu Ray, "SAR Analysis in Human Head Model Exposed to Mobile Base-Station Antenna for GSM-900 band", *Loughborough Antennas & Propagation Conference,* Loughborough, UK, pp. 289-292, January - 2009, 10.1109/LAPC.2009.5352413.

XIII. **Md.Faruk Ali** and Sudhabindu Ray, "SAR Evaluation in a Tilted Human Head Model in Near-Field of a Half-Wave Dipole Antenna in GSM-900 Band", *International Conference on Control Communication and Computing,* College of Engineering, Thiruvananathapuram, Kerala, India, pp. 316-319, February - 2010.

XIV. **Md.Faruk Ali**, Santanu Mondal and Sudhabindu Ray, "MLSAR Analysis in a Realistic Grounded Human Head Model for a Dipole antenna using FDTD method at 930 MHz", *IEEE CASCOM Post Graduate Student Paper Conference*, Jadavpur University, Kolkata, India, pp. 34-37, November - 2010**.**

XV. **Md. Faruk Ali** and Sudhabindu Ray, "Study of Induced EM Field Parameters Inside a Realistic Human Head Model", *International Conference on Communications Computers and Devices*, IIT Kharagpur, India, Paper ID-82, December - 2010.

XVI. **Md. Faruk Ali** and Sudhabindu Ray, "SAR Analysis in a Realistic Grounded Human Head for Radiating Dipole Antenna", *National Conference on Communications (NCC)*, IISc. Bangalore, India, pp. 211-125, January- 2011. doi: 10.1109/NCC.2011.5734736.

XVII. **Md. Faruk Ali** and Sudhabindu Ray, "SAR Analysis Using DICOM Based Voxel Model", *National Conference on Communications (NCC)*, IIT Kharagpur, India, Paper ID-621, February- 2012. doi: 10.1109/NCC.2012.6176755.

XVIII. **Md. Faruk Ali** and Sudhabindu Ray, "Detection and Selective Destruction of Bacteria Colony at THz Frequencies", *National Conference on Communications (NCC)*, IIT Kharagpur, India, Paper ID-417, February-2012. doi: 10.1109/NCC.2012.6176808.

XIX. **Md. Faruk Ali** and Sudhabindu Ray, "SAR Analysis Using SFDTD and Hybrid FDTD", *Conference on Computers and Devices for Communication (CODEC)*, Institute of Radio Physics and Electronics, University of Calcutta, India, December-2012.

XX. **Md. Faruk Ali** and Sudhabindu Ray, "Study of Dipole Antenna Characteristic using Different Numerical methods", *International Conference on Communications, Devices and Intelligent Systems (CODIS)*, Department of Electronics and Telecommunication Engineering, Jadavpur University, India, December-2012.

XXI. **Md. Faruk Ali**, Rashmi Ranjan Sahoo and Sudhabindu Ray, "Study of Maximum Local Temperature Rise and Hotspots Distribution in a Human Head for GSM900 Mobile Phone", *International Conference on Eco-friendly Computing and Communication Systems* (*ICECCS*), Advances in Energy Aware Computing and Communication System, Tata McGraw Hill, India, pp. 72-78, October-2013, ISBN-13:978-9-35-13432-5.

4. List of patents: Nil

5. List of Presentations in National / International:

[1] Md.Faruk Ali and Sudhabindu Ray, "SAR Analysis on Human Head Exposed to Radiating Dipole Antenna for 500 MHz – 5 GHz Frequency Band Using FDTD Method", *National Conference on Communication (NCC),* IIT Bombay*, India,* pp.481-485, 2008.

[2] Md.Faruk Ali and Sudhabindu Ray, "SAR Distributions in a Spherical Inhomogeneous Human Head Model Exposed to Electromagnetic Field for 500 MHz – 3 GHz Using FDTD method", *National Conference on Communications,* IIT Guwahati, India, pp.64-67, January - 2009.

[3] Md.Faruk Ali and Sudhabindu Ray, "SAR Analysis on Child and Adult Head Models for Radiating Dipole Antenna Using FDTD method", *International Symposium on Microwaves and Millimeterwaves : Basics and Technology,* Bose Institute, Kolkata, India, pp.46-48, January - 2009.

[4] Md.Faruk Ali, Sujoy Mukherjee and Sudhabindu Ray, "SAR Analysis in Human Head Model Exposed to Mobile Base-Station Antenna for GSM-900 band", *Loughborough Antennas & Propagation Conference,* Loughborough, UK, pp. 289-292, January - 2009, 10.1109/LAPC.2009.5352413.

[5] Md.Faruk Ali and Sudhabindu Ray, "SAR Evaluation in a Tilted Human Head Model in Near-Field of a Half-Wave Dipole Antenna in GSM-900 Band", *International Conference on Control Communication and Computing,* College of Engineering, Thiruvananathapuram, Kerala, India, pp. 316-319, February - 2010.

[6] Md.Faruk Ali, Santanu Mondal and Sudhabindu Ray, "MLSAR Analysis in a Realistic Grounded Human Head Model for a Dipole antenna using FDTD method at 930 MHz", *IEEE CASCOM Post Graduate Student Paper Conference*, Jadavpur University, Kolkata, India, pp. 34-37, November - 2010.

[7] Md. Faruk Ali and Sudhabindu Ray, "Study of Induced EM Field Parameters Inside a Realistic Human Head Model", *International Conference on Communications Computers and Devices*, IIT Kharagpur, India, Paper ID-82, December - 2010.

[8] Md. Faruk Ali and Sudhabindu Ray, "SAR Analysis in a Realistic Grounded Human Head for Radiating Dipole Antenna", *National Conference on Communications (NCC)*, IISc. Bangalore, India, pp. 211-125, January- 2011. doi: 10.1109/NCC.2011.5734736.

[9] Md. Faruk Ali and Sudhabindu Ray, "SAR Analysis Using DICOM Based Voxel Model", *National Conference on Communications (NCC)*, IIT Kharagpur, India, Paper ID-621, February- 2012. doi: 10.1109/NCC.2012.6176755.

[10] Md. Faruk Ali and Sudhabindu Ray, "Detection and Selective Destruction of Bacteria Colony at THz Frequencies", *National Conference on Communications*

(NCC), IIT Kharagpur, India, Paper ID-417, February-2012. doi: 10.1109/NCC.2012.6176808.

[11] Md. Faruk Ali and Sudhabindu Ray, "SAR Analysis Using SFDTD and Hybrid FDTD", *Conference on Computers and Devices for Communication (CODEC)*, Institute of Radio Physics and Electronics, University of Calcutta, India, December-2012.

[12] Md. Faruk Ali and Sudhabindu Ray, "Study of Dipole Antenna Characteristic using Different Numerical methods", *International Conference on Communications, Devices and Intelligent Systems (CODIS)*, Department of Electronics and Telecommunication Engineering, Jadavpur University, India, December-2012.

[13] Md. Faruk Ali, Rashmi Ranjan Sahoo and Sudhabindu Ray, "Study of Maximum Local Temperature Rise and Hotspots Distribution in a Human Head for GSM900 Mobile Phone", *International Conference on Eco-friendly Computing and Communication Systems (ICECCS)*, Advances in Energy Aware Computing and Communication System, Tata McGraw Hill, India, pp. 72-78, October-2013, ISBN-13:978-9-35-13432-5.

CERTIFICATE FROM THE SUPERVISOR

This is to certify that the thesis entitled **"Effects of non-ionizing electromagnetic radiation to the human body and environment**" submitted by **Md. Faruk Ali,** who got his name registered on 7th **February 2013 [D-7/E/113/13]** for the award of Ph.D. (Engg.) degree of Jadavpur University is absolutely based upon his own work under the supervision of **Dr. Sudhabindu Ray**, Department of Electronics and Telecommunication Engineering, Jadavpur University, Kolkata, West Bengal and that neither his thesis nor any part of the thesis has been submitted for any degree/diploma or any other academic award anywhere before.

_____

Signature of the Supervisor and date with Official Seal

DEDICATION

This thesis is dedicated to my respected teachers
for their endless support and encouragement.

ACKNOWLEDGEMENTS

A thesis like this is never possible without the help, encouragement, motivation and influence of a large number of people, above all, my supervisor **Dr. Sudhabindu Ray**, Associate Professor, Department of Electronics and Telecommunication Engineering., Jadavpur University, Jadavpur, India, who taught me many things, but most importantly, how to make dreams come true.

First of all I would like to express my appreciation to **Prof. D. Mukherjee**, Former H.O.D, Department of Electronics & Telecommunication Engineering, Bengal Engineering and Science University, Shibpur, India, for his technical advice and provision of important references. My special thanks are extended to reverent **Prof. George Zubal,** Department of Diagnostic Radiology, Yale School of Medicine, New Haven, for his kind assistance in using the **Zubal phantom** data. I am also grateful to **Prof. Murilo A. Romero**, Editor-in-chief, Journal of Microwaves, Optoelectronics and Electromagnetic Applications (JMOe), Brazil and **Dr. (Mrs) Kamlesh Arora**, Editor, Indian Journal of Radio & Space Physics (IJRSP), New Delhi, India, for their kind assistance, technical advices and provision of important references.

I would like to extend my gratitude to the research scholars and authorities of the Department of Electronics and Telecommunication Engineering, Jadavpur University, Jadavpur, India, for their support in using the microwave laboratories.

Last, but not least, I would like to express the warmest thanks to **my father, family** and **colleague** for always backing me up and encouraging me to keep me struggling for the best execution of my work.

Md. Faruk Ali Jadavpur, 2017.

Table of Contents

LIST OF TABLES

LIST OF FIGURES

LIST OF ABBREVIATIONS AND ACRONYMS

ABC	Absorbing Boundary Conditions
ADI	Alternating Direction Implicit
AR	Auto-regressive
BBB	Blood Brain Barrier
BHE	Bioheat Equation
BSA	Base Station Antenna
CAD	Computer Aided Design
CCD	Colony Collapse Disorder
CST	Computer Simulation Technology
CST MWS	CST Microwave Studio
CT	Computed Tomography
DICOM	Digital Imaging and Communication in Medicine
DNA	Deoxyribonucleic Acid (genetic molecules)
EEG	Electroencephalogram
EIRP	Effective Isotropic Radiated Power
EM	Electromagnetic
ELF	Extremely low frequency
EMF	Electromagnetic Field
FCC	Federal Communication Commission
FD	Finite Difference
FDA	United States' Food and Drug Administration
FDTD	Finite Difference in Time Domain
FEM	Finite Element Method
FET	Field Effect Transistor
FIT	Finite Integral Technique
FT	Fourier Transform
FVTD	Finite Volume Time-Domain
GHP	Generic Head Phantom
GMP	Generic Mobile Phone
GO	Geometrical Optics
GSM	Global System for Mobile communications
HEMT	High Electron Mobility Transistor

HIFU	High Focused Ultrasound
HR-EFH	High-Resolution European Female Head
HU	Hounsfield Unit
IEC	International Electrotechnical Commission
IEEE	Institution of Electrical and Electronic Engineering
ICNIRP	International Commission on Non-Ionising Radiation Protection
ILA	Ionic Liquid Antenna
IOD	Information Object Definition
LAN	Local Area Network
LED	Light Emitting Diode
LPF	Low Pass Filter
MOM	Method of Moments
MLFMM	Multilevel Fast Multipole Method
MLSAR	Maximum Local Specific Absorption Rate
MNM	Multiport Network Model
MRI	Magnetic Resonance Imaging
MSS	Multilevel Subgridding Scheme
NA	Network Analyzer
NCRP	National Council on Radiation Protection and Measurements
NEMA	National Electrical Manufacturers Association
NIT	Nagoya Institute of Technology
NRPB	National Radiological Protection Board
PACS	Picture Archiving and Communication System
PBA	Perfect Boundary Approximation
PDA	Personal Data Assistant
PIFA	Planar Inverted Folded Antenna
PO	Physical Optics
RCS	Radar Cross Section
RFA	Radio Frequency Ablation
SAM	Specific Anthropomorphic Mannequin
SAR	Specific Absorption Rate
SAR_{WB}	Whole-body average SAR

SOP	Service-Object Pair
TIS	Total Isotropic Sensitivity
TLM	Transmission line model
TS	Thermoregulatory System
TST	Thin Sheet Technique
US	Ultrasound
UTD	Uniform Theory of Diffraction
WHO	World Health Organization
WLAN	Wireless LAN

Chapter 1

Introduction

1.1 Introduction

During the last few years, use of different wireless communication devices and the number of users have been increased considerably. Most of these wireless devices work in the microwave and millimetre wave bands and some of these devices radiate significant amount of energy. This electromagnetic (EM) energy can be absorbed by any lossy dielectric media when it comes across the path of propagation. Absorption of non-ionizing EM radiation may cause conversion of EM energy into other different forms. In a lossy dielectric media, EM energy may mainly be converted into electric or heat energy. Newly generated electric and heat energy may initiate thermo-chemical or electro-chemical changes inside the media. When living cells or tissues are exposed to these radiated EM field at radio frequency (RF), some part of it is absorbed resulting in local heating and other thermo-chemical or electro-chemical changes.

The possibility of health hazards or environmental changes from non-ionizing RF radiation is a burning question worldwide and research topics in the related area have been increased enormously. The interest is even accentuated by the fact that the hand-held cellular phone is used keeping very close to the user's head and body parts, as a result the user is being exposed by the EM field directly. Many theoretical and practical research works have been carried out to investigate on the Specific Absorption Rate (SAR), temperature rise or energy coupling from wireless communication sources on human operators. SAR value is an important quantity in this field of research because the human exposure guidelines are set in terms of it and the rise of temperature inside tissue is directly related to SAR.

The studies associated with the assessment of EM field interaction with biological structures, can be classified into two general categories depending on whether the tissue samples are inside the body or isolated from the body called in-vivo and in-vitro, respectively. In the in-vitro studies on tissue scale level, evaluation of fields inside tissue

samples has been performed and the energy absorption rate and temperature rising induced by the RF field exposure are studied by several groups. Below the tissue scale, a number of studies have looked into the underlying interaction mechanisms at the cellular and membrane scales, including a variety of bio EM phenomena, such as the Dielectrophoresis (DEP), Electroporation (EP) and ion-channel performances. However, the small size and thickness of cells and their thin membranes result in great difficulty for undertaking experimental dosimetry. It is difficult to measure different energy levels or observe different biological changes experimentally in laboratory inside living tissues especially inside human being. So, different computational methods play significant roles to calculate various RF characteristics inside living objects including tissues and cells. Among these numerical methods, Finite Element Method (FEM), Finite-Difference in Time-Domain (FDTD) or Method of Moment (MoM) are used extensively in assessing the effects of EM wave radiation on plant or animal tissues.

Microwave radiation can also be used for some good purposes. It has been used extensively in last several years for food processing. Non-ionizing radiation is also used for sterilization process in different laboratories or in medical science for hyperthermia treatment and for RF ablation. Design of suitable RF source is very crucial in these applications. Just like earlier, EM simulators hold significant roles for designing these RF radiating systems.

In this thesis, theoretical studies have been carried out to observe localized SARs, RF power dissipations or EM field intensities inside human body parts and plant tissues for various RF sources at different frequency bands. Apart from the dosimetry calculations, various investigations have been carried out on RF applications like bacteria treatment process and RF ablation techniques. Several new investigation methodologies have also been proposed and obtained results are discussed.

1.2 Motivation and aim of the thesis

Health and environmental hazards due to non-ionizing RF radiation emitted from the different wireless communication devices is a threat to humanity. Controlled exposure of non-ionizing RF radiation is advised by various organizations. Exposure limits are also prescribed by different agencies and research organizations like (Institution of Electrical and Electronic Engineering) IEEE, (Federal Communication Commission) FCC or (International Commission on Non-Ionising Radiation Protection) ICNIRP. However most of these limits

are based on various conditions and assumptions. Day by day, the pattern or technologies of RF radiating systems are changing and more investigation are required to understand all types direct or indirect effects of RF radiation inside living tissues. Thus, the main motive of this research work is to investigate these biological effects from RF radiations on human body and environment. The knowledge base and resources required for study the effects of RF radiation on living cell or tissue are also very useful for studying the possibility of controlled RF exposure for bacteria treatment or RF ablation systems. So, these areas are also included in this thesis.

The scientific research aims that are identified for this thesis along with different considerations are:

1. Every commercially available EM simulators have their own limitation, and have some restriction on intermediate required data. Thus, the first and very essential aim is to develop suitable in-house full-wave 3D EM numerical programs and validate these programs using commercially available 3D EM simulation software like FIDELITY or CST Microwave Studio®.
2. EM full wave methods are not always very suitable for a very large simulation models. Thus, another goal is set to develop efficient numerical codes by hybridizing them with simpler classical methods or by splitting the simulation domain for large simulation models.
3. Investigate the effects of no ionizing radiation from cellular handset and Base Station Antennas (BSA) on different human body parts. Evaluate the SAR and power absorption levels using various types of realistic tissue models considering various types of assumptions using FDTD-based in-house programs. Localized hot-spots and dielectric lens effects are included in the study.
4. Investigate the interaction between the EM wave radiation from a BSA and green plants to find the absorption level inside the plant tissues and their shielding effectiveness.
5. Apart from the hazardous effect of EM waves on the living creature, study some possible applications like:
    a. Detection and selective destruction of bacteria colony at THz frequencies.

b. Investigation of EM energy absorption and image formation by the pollen grains at GHz frequencies.

c. Numerical investigation to determine the usefulness of EM wave for detection and identification of caries in a human tooth model at GHz frequencies.

d. Study the steady state temperature variations in human brain due to different electrical and physical changes considering different thermal ablation treatment requirements using RF probe.

1.3 Commonly available methods for theoretical analysis

Since measurements of different energy levels inside living tissues especially inside human being is very difficult, theoretical investigations can be carried out in most cases. Analyses using full wave EM simulation techniques can be used to observe different energy parameters inside cells or tissue models.

Various available methods of EM analysis can be broadly classified as analytical and numerical methods [1]. The analytical methods provide a physical insight into the parameters affecting the performance of the configuration. Typical analytical models are Transmission line model (TLM), cavity model, Multiport network model (MNM) etc. The main disadvantage of these methods is that they are not generalized methods and are usually restricted to regular shapes. Numerical methods like FEM, MoM, and FDTD or Finite Integration Technique (FIT) methods are widely used for accurate analysis of arbitrary shape configurations. These models provide a rigorous treatment and are able to handle simulation model of arbitrary shapes. Also, they are computationally more intensive compared to the analytical methods. Brief overview of some EM numerical methods are presented in the following subsections with an emphasis on their advantages and drawbacks.

1.3.1 Finite Element Method (FEM)

In 1943, mathematical treatment of the FEM was first proposed by Courant [2]. Initially the FEM method was used for most of the applications of mechanical and civil engineering but not applied to EM problems until 1968. Since then the method has been employed in such diverse areas as waveguide problems, electric machines, semiconductor devices, microstrips, and absorption of EM radiation by biological bodies [3]. The main advantage of this method is that it can be applied to all physical problems in BVP or structural and solid mechanics.

Irregularly shaped boundaries can be approximated using elements with straight sides or matched exactly using elements with curved boundaries. So, this method is not only limited to nice shapes with simple geometry but can also be used for any complex geometry. On the other hand, the main disadvantages of FEM are: (a) FEM needs for computer programs and facilities; (b) it is still an approximate technique and gives solution only at nodal points. Thus FEM obtains only approximate solutions. As FEM has inherent errors so any mistake made by users can be produced fatal error.

1.3.2 Method of Moments (MoM)

The MoM or boundary element method (BEM) is one of the efficient full-wave numerical methods used for EM compatibility (EMC) and antenna applications. It is essentially the method taking moments by multiplying with appropriate weighting functions and integrating, which can be used for solving both differential and integral equations. Use of MoM to solve the EM problems has become popular since the work of Richmond in 1965 and Harrington in 1967 [4],[5]. MoM is fairly efficient for the problems with appropriate properties but during the last few years, where computer performance has increased dramatically, the importance of MoM has decreased while the use of other techniques like FDTD or FEM has increased. Yet, the MoM still provides advantages for certain complex structures, like metal objects and wires. There are significant advantages and disadvantages of this method. One of the advantages of this method is the simplicity. Other benefit of this method is that in evaluating the matrix elements, no integration is required over the range of the testing function, only that of the source function. Primary disadvantage of this method is that the boundary conditions are matched only at discrete locations through out the solution domain, allowing them to assume a different value at points other than those used for testing. Other disadvantage of this method is that they are often not available and do not have the desirable optimality properties of maximum likelihood and least squares estimators.

1.3.3 Finite-Difference Time-Domain Method (FDTD)

FDTD is a widely used numerical computational method in the range of a few MHz to several GHz [6]. The main advantages of the FDTD-based techniques for solving EM problems are simplicity and the ability to handle complex geometries. Compared to the other computational methods FDTD is more efficient in terms of computer time and memory as there is no matrix to fill and solve [7],[8]. Derivation from Maxwell's equations is based on

traditional mathematical methods of approximating derivatives by finite differences and approximating line integrals, surface integrals, and volume integrals by summations [9]. It involves basic arithmetic operations: addition, subtraction, multiplication, and division. FDTD can model material through parameter averaging or, in case of a more sophisticated approach, choosing grids to conform to the geometries of the material boundaries [10].

1.3.4 Finite Integration Technique (FIT)

The FIT is a method that is closely related to the FDTD method, but where the integral form of Maxwell's equations is solved by one-to-one translation from the integral form of Maxwell's Equations to a discrete space formulation. FIT was first introduced in 1977 by T. Weiland [11]. Like FDTD method, formulation of the FIT algorithm is based on enclosing the computational volume with a numerical region representing the outer boundary condition. The next stage involves decomposition the computational volume into a finite number of simplified material-filled homogeneous cell volumes defined as voxel. The resulting matrix equations for the EM integral quantities obtained from the FIT maintain the inherent properties of Maxwell's equations with respect to charge and energy conservation.

1.4 In-house developed tools for theoretical analysis

Direct measurement of EM field components and SAR is difficult inside a living human head or body parts using the experimental techniques. Therefore, the numerical techniques are used to calculate EM field components and SAR inside human head or body parts [12]. Several standard commercial 3D EM simulation tools are available which are suitable for calculation of SAR inside tissues. But various limitations make them unsuitable for carry out research in this field of research. For example, currently 1g SAR or 10g SAR can be calculated by many simulation tools but scope of calculation of SAR with higher resolution is not readily available. In many commercially EM simulators, intermediate data are not available and hybridization with other technique is restricted. So, in-house developed EM simulation tools based on available full wave EM computational techniques hold a crucial role to take care of these problems.

To carry out various researches described in this thesis, an efficient simulator based on Segmented FDTD (SFDTD) is developed using MATLAB. Another tool has been is developed by hybridizing FDTD with Friis transmission equation. This method is much faster than normal FDTD and suitable for very large structures.

1.4.1 Segmented FDTD Method for simulation of large models

Using FDTD method for modelling EM wave propagation was first proposed by Yee in 1966 [10]. Since then FDTD method has been successfully used to design and analyse both the guiding and scattering structures. But as the computer memory limits the number of mathematical cells so it is impractical to achieve desired details in large areas using FDTD method. Sub-gridding and multi-grid FDTD codes have been developed in order to overcome the problem of FDTD [13],[14]. Again the sub-gridding method has two limitations. First, the numerical dispersion varies considerably with the density of the mesh and second, the computational efficiency of the method is compromised by the need to use the time step corresponding to the smallest grid throughout the computational space [15]. On the other hand, when the multigrid FDTD method is used for the simulation containing dielectric materials inside the fine-grid region, the simulation begins to diverge and becomes unstable [16]. It is also observed that multi-grid FDTD method becomes unstable when the fine grid region contains complex geometries. To solve large scale problems using FDTD method, a non uniform FDTD technique has been developed where non uniform cells are used to form the problem space which reduces computational burden but stored only four field components in the whole domain [17]. SFDTD method divides large problem space into different segments to reduce the computational requirements and enhances the practicability of running the simulation on a PC [18].

1.4.2 Transmission equation incubated Hybrid FDTD Method for simulation of very large simulation models

During dosimetry calculation, some hybrid numerical EM techniques have been adopted to reduce the computational resource requirements. A mixed FDTD-integral equation approach is used to evaluate SAR inside a human model for the radiation from BSAs and the SAR values obtained with mixed FDTD-integral equation are found close to that obtained using the full FDTD simulations [19]. FDTD method combined with the Method of Moments in the Time Domain (MoMTD) is used to calculate the SAR induced in a homogeneous phantom model placing at a distance of 10.0 cm from a BSA [20],[21]. Green's integral equation combined with FDTD method has been reported for SAR calculation in human head model due to radiation from BSA [22]. Hybrid FDTD method is newly developed by combining Friis transmission equation with FDTD method. In this method, EM modelling of the simulating elements is prepared using either conventional or non-uniform FDTD method

and power calculation of the source required for the simulation is made by Friis transmission formula [23].

1.5 Simulation using commercially available software

Commercially available simulators are very popular for 3D EM analysis and can be used to observe different energy parameters inside cells or tissue models. Many research investigations have been carried out in recent years which are based on these commercial simulators. CST Microwave Studio, Zeland Fidelity, SEMCAD-X, XFDTD, and FEKO are very popular commercially available EM simulators which have been referred by several research article published in this area of research. Brief descriptions and capabilities of these simulators are included in the following sub-sections. Some of these simulation tools have been used in different studies reported in this thesis.

1.5.1 CST Microwave Studio®

CST Microwave Studio® is a powerful and easy to use FIT based EM field simulation software package [24]. It combines both a user friendly interface and simulation performance in an incomparable manner. This simulator is equipped with the new Multilevel Subgridding Scheme (MSS™) which helps to improve the meshing efficiency and thus can significantly speed up simulations especially for complex devices. The usage of advanced signal processing techniques (AR-filters) provided by CST Microwave Studio® allows the speeding up these simulations by orders of magnitude compared to standard time domain methods. For best fitting with different type of applications CST Microwave Studio® contains seven different solvers: transient solver (T), frequency domain solver (F), eigenmode solver (E), integral equation solver (I), asymptotic solver (A), thermal stationary solver (THs) and thermal transient solver (THt). This package has been used frequently in this research work. The advantage of CST Microwave Studio® is that within on run one can obtain the results on a wide band because it starts in time domain and convert the results to frequency domain via Fourier Transform (FT).

1.5.2 Zeland Fidelity

Zeland Software, Inc. was founded in 1992 to develop powerful and practical EM design tools [25]. After that, Zeland software has been recognized as a leading developer to provide unparalleled high-frequency EM simulation and design tools for microwave,

semiconductor, wireless and telecom industries. Zeeland version 14.0 is powered by the seven products and among them only Fidelity is a FDTD based full wave 3D EM simulator. It is based on combination of specific geometries. It can be used in those areas where the EM field effects are the major concerns, for example microwave engineering, HF electronic component and circuitry design, EMC/EMI, electronic device packaging, bio-electromagnetic signal analysis. Fidelity is mainly suitable for regular shaped simple structures but not suitable for large or complex structures.

1.5.3 SEMCAD-X

The SEMCAD-X is a multipurpose FDTD based 3-D full wave EM modelling and computational simulator. The simulator is designed to address the EM needs of the wireless and medical sectors in terms of antenna design, EMC and dosimetry. SEMCAD-X is one of the most advanced software now being used for RF simulations. It is a very powerful tool for computational EM applications and it has excellent usability. It helps any user from a beginner to an expert to be proficient in a very short time. Compared with other commercial EM tools, SEMCAD-X is capable of providing more perspective and precise information to help designers understand the behaviour, mechanism and the interrelation of any radiators, which greatly shortens the design process in the early development stage. Its unique accelerator can largely reduce the simulation time by two-third compared with other simulators. It gives engineers more flexibility to execute, practice and study the design concept.

1.5.4 FEKO

FEKO is a leading MoM based 3-D full wave EM modelling and computational simulator. Other techniques such as the Multilevel Fast Multipole Method (MLFMM), FEM, Uniform Theory of Diffraction (UTD), Geometrical Optics (GO) and Physical Optics (PO) have been included in FEKO to solve the electrically large problems and inhomogeneous dielectric bodies of arbitrary shape. FEKO supports for parallel processing usage on a range of workstations, servers and clusters. The performance for each platform, operating system and deployment method has been optimised for the delivery of accurate and timely results.

1.5.5 Other commercially available EM tools

Ansoft HFSS is one of the commonly used EM simulators. It is one of the essential tools for engineers involved in project in the field of high-speed electronic and high frequency components. Finite Element based Ansoft HFSS is used for simulating 3-D full-wave EM fields. It has much better interface which enables the user to include very fine details in the geometry of simulated structure. Both techniques are still suitable for small or moderate objects compared with the operating wavelength. Different options are found in HFSS, but it is still frequency domain solution. Its gold-standard accuracy, advanced solver and compute technology have made it an essential tool for engineers designing high-frequency and high-speed electronic components.

HFSS offers multiple state-of the-art solver technologies based on finite element, integral equation or advanced hybrid methods to solve a wide range of applications. Each HFSS solver incorporates a powerful, automated solution process, so you need only to specify geometry, material properties and the desired output. From there, HFSS automatically generates an appropriate, efficient and accurate mesh for solving the problem using the selected solution technology. With HFSS, the physics defines the mesh; the mesh does not define the physics.

MoM based IE3D is an efficient and powerful 3-D full-wave EM analysis tool. This software is optimized for design and simulation of planar structures. This package is used in this research work for cross checking the efficiency of in-house developed simulation tool. It is also been used to design some antennas used in some investigations included in this thesis.

MDSpice is a Mixed-Domain SPICE simulator combing a time-domain simulation engine with a frequency-domain simulation engine. The most significant feature of MDSpice is that it can perform robust, accurate, and efficient time-domain simulation based upon frequency domain S-parameters. It also has a broadband SPICE model extraction capability for coupled transmission lines and interconnects. MDSpice is particularly useful in modelling high-speed digital circuits and high-frequency nonlinear devices. This software has been used to crosscheck the performance of the in-house developed EM simulator in time domain.

The accuracy of FEM is slightly less than the accuracy of MoM. Thus for regular shapes like rectangular patch antenna you may obtain slight difference between HFSS and Zeland IE3D. In this case the result of Zeland IE3D is the more accurate result. However, for complicated geometry, you may find the accuracy of HFSS and CST Microwave Studio® is

much better than IE3D due to the approximations which you have to do in the geometry of the structure.

1.6 Measurement techniques

Direct measurement of EM field components and SAR is difficult inside a living human head or body parts using the experimental techniques. In the experimental methods, equivalent homogeneous head or other body parts are considered for the measurement. These homogeneous models are not a faithful representation of the complex heterogeneous human organs because actual electrical properties of different tissues are not considered. Again, the homogeneous models give a slight overestimate for the gram-averaged spatial peak SAR.

Generally, short length isotropic electric-field sensor is used during measurement to obtain good resolution. Then gram-averaged spatial peak SAR is calculated from measured electric fields. In this study, a far field RF power sensor dipole antenna connected with handheld RF power meter has been to measure power.

1.7 Scope of Present work

Electrical and thermal changes due to the interaction between the non-ionizing EM waves on human beings and environment have been investigated thoroughly considering various tissues models using the numerical methods like FEM, MoM, and FDTD or FIT. To solve the large-scale problems FDTD based SFDTD and hybrid method consisting of Friis transmission equation and FDTD are used. To carry out the theoretical investigations, different types of electrical models are developed for representing human head, body tissues, green plants and microwave sources. Homogeneous box model, three layered spherical type human head model, freely available Computed Tomography (CT) and Magnetic Resonance Imaging (MRI)-based heterogeneous human head model, and Digital Imaging and Communication in Medicine (DICOM) data based voxel type human head and hand models are considered for various investigations and found to play very crucial roles in case of numerical analysis to obtain the induced energy parameters. Interaction of EM waves can also be used for many helpful applications for human being, like for detection and selective destruction of bacteria colony, detection and identification of caries in human tooth and in medical treatment.

1.8 Organization of the Thesis

This thesis presents a comprehensive numerical dosimetry study due to the interaction between the non-ionizing EM waves with human beings and environment. It also demonstrates an accurate methodology for assessing different induced energy parameters inside cells or tissue. Furthermore, apart from the hazardous effects, a few effective and helpful applications of microwave are also studied and proposed.

An introduction to the background of bioelectromagnetics and the basic fundamentals is presented in Chapter 1. A brief literature review on the interaction of non-ionizing EM radiation with human being and environment is presented in Chapter 2. The development of the numerical analysis tools used in this study to assess the different induced energy parameters within biological cells or tissue has been summarised in Chapter 3.

In Chapters 4 and 5, a comprehensive study on the effects of non-ionizing EM radiation on human body is highlighted. In these chapters, the interaction of EM fields radiated from wireless communication devices and BSAs with human brain and other body parts is assessed considering for different exposure scenarios.

Chapters 6 presents the EM wave absorption and shielding characteristics of a Bonsai tree and Money plant. EM energy absorption characteristic and image formation by the pollen grains have also been investigated in this chapter.

In Chapter 7, a comprehensive study on some useful applications based on interaction of microwave with living being is highlighted.

Finally, a conclusion of this research work, scope for practical use of some observations and further investigations are suggested in Chapter 8.

1.9 Conclusions

A brief introduction has been presented on the possible biological hazards due to the EM waves generated by the wireless mobile communication devices. The general objective, scope of present work and organization of this thesis have also been presented in this chapter. A brief overview of the in house analysis tools has been included in this chapter.

References

[1] V. Srinivasan, "Multiport network model for variations in rectangular microstrip antennas," Ph.D. dissertation, Indian Institute of Technology, Bombay, 1999.

[2] R. Courant, "Variational methods for the solution of problems of equilibrium and vibrations," *Bull. Am. Math. Soc.*, vol. 49, pp. 1–23, 1943.

[3] J.M. Osepchuk and R.C. Petersen, "Safety Standards for Exposure to RF Electromagnetic Fields," *IEEE, Microwave Magazine*, vol. 2, pp. 55-69, June 2001.

[4] J.H. Richmond, ''Digital computer solutions of the rigorous equations for scattering problems," *Proc., IEEE*, vol. 53, pp. 796-804, Aug. 1965.

[5] R.F. Harrington, "Matrix methods for field problems," *Proc. IEEE*, vol. 55, No. 2, pp. 136-149, February 1967.

[6] P. Stavroulakis, "Biological effects of electromagnetic fields," *Springer*-V erlag Berlin Heidelberg 2003, ISBN 3-540-429891.

[7] D. Krstic, "The influence of electromagnetic radiation in GHz bend on biological tissue," [PhD thesis], Nis: University of Nis, Faculty of Occupatinal Safety, Serbia, April 2010.

[8] K.S. Kunz, R.J. Luebbers, "The Finite-Difference Time-Domain Method," Boca Raton, FL: CRC., pp. 448, 1993.

[9] K.S. Yee and J.S. Chen, "The Finite-Difference Time-Domain (FDTD) and the Finite-Volume Time-Domain (FVTD) Methods in Solving Maxwell's Equations," *IEEE Trans. Antennas Propagation*, vol. 45, No. 3, pp. 354-363, March 1997.

[10] K.S. Yee, "Numerical solution of initial boundary value problems involving Maxwell's equations," *IEEE Trans. Antenna Propagation*, vol. 14, No. 3, pp. 302-307, May 1966.

[11] T. Weiland, "A discretization method for the solution of Maxwell's equations for six-component fields," *Electronics and Comms.* AEU, vol. 31, No. 3, pp. 116-120, 1977.

[12] M.N.O. Sadiku, Numerical Techniques in Electromagnetics, Second Edition, by, CRC Press LLC, 2001.

[13] S.S. Zivanovic, K.S. Yee and K. Mei, "A subgridding method for the time domain finite difference method to solve Maxwell's equations," *IEEE Trans. Microwave Theory Tech.*, vol. MTT - 39, No. 3, pp. 471-479, March 1991.

[14] M.E. Okoniewski, and M.A. Stuchly, "Three dimensional subgridding algorithm for FDTD," *IEEE Trans. Antenna Propagation*, vol. APT- 45, No. 3, pp.422-429, March 1997.

[15] M.J. White, M.F. Iskander and Z. Huang, "Development of a multigrid FDTD code for three dimensional applications," *IEEE Trans. Antenna Propagation*, vol. APT- 45, No. 10, pp. 1512-1517, October 1997.

[16] J. Svigelji, and R. Mitra, "Grid dispersion error using the nonuniform orthogonal finite difference time domain method," *Microwave Opt. Tech. Letter*, vol. 10, pp. 199-201, September 1995.

[17] D. White, M. Stowell, J. Koning, R. Rieben, A. Fisher, N. Champagne and N. Madsen, "Higher-oredr mixed finite element methods for time domain electromagnetics," February 2004 [Online]. Available: http://www.llnl.gov/tid/lof/documents/pdf/304775.pdf.

[18] Y. Wu, and I. Wassell, "Introduction to the Segmented Finite-Difference Time-Domain Method," *IEEE Trans. on Magnetics*, vol. 45, No. 3, pp. 1364-1367, March 2009.

[19] G. Lazzy and O.P. Gandhi, "A Mixed FDTD-Integral Equation Approach for On-Site Safety Assessment in Complex Electromagnetic Environment," *IEEE Trans. Antenna Propagation*, vol. 48, pp. 1830-1836, December 2000.

[20] D. Lautru, J. Wiart, W. Tabbara and R. Mitra, "A MoMTD/FDTD Hybrid method to Calculate the SAR induced by a Base Station Antenna," *IEEE* Antennas and Propagation Society International Symposium, vol. 2, pp. 757-760, 2000.

[21] A.R. Bretones, R.G. Martin and A. Salinas, "DOGTIGI, a Time Domain Numerical Code for the Study of the Interaction of Electromagnetic Pulse with Thin-Wire Structures," *COMPEL*, vol. 8. No. 1, pp. 39-61, 1989.

[22] L. Nonidez, M. Martinez, A. Martin, M. De.Mier and R. Villar, "Using FDTD and High Frequency Techniques in the Time Domain for SAR Assesment in Human Exposure to Base-Station Antennas," URSI International Union of Radio Science 2002, Proc. GA02, 08-July, 2002.

[23] John. D.Kraus and R.J. Marhefka, "Antennas for All Applications," Tata Mc.Graw-Hill Publishing Company Limited, New Delhi, India, Third Reprint, 2003.

[24] CST-Computer Simulation Technology, Available at: http://www.cst.com.

[25] Zeland Software, Inc., Available at: http://www.zeland.com.

Chapter 2

Literature Survey on Interaction of Non-Ionizing EM Radiation with Human Being and Environment

2.1 Introduction

The complexity of the living creatures is being found to be influenced by the most delicate field of the EM energy. The findings are confirmed from the observations of many researchers made over for the several years of the effects of very small energy sources on the living beings. Almost all news papers and magazines have routine articles to highlight the adverse health effects of the cell phones on living creatures. In this chapter summarizes various studies reported in scientific literatures on the effects of non-ionizing EM radiation on human beings and environment. More importance has been given on the effects of radiation from modern wireless communication devices and their base stations.

2.2 Effects of Non-ionizing EM radiation on human beings

Interaction of EM fields at RF with biological tissue has been investigated by a large number of researchers. It is observed that when an electric (*E*) field or magnetic (*H*) field penetrates into the body, it is attenuated and a part of it is absorbed inside the body [1]. Many types of interaction mechanisms have been considered so far, and guidelines and limits are proposed by various government and non-government organizations [2]-[4]. Most of these guidelines are based on thermal effects and average radiated RF energy over some specific time period. The prescribed levels are different for some of these agencies, and these may create enough confusion to a new researcher and general people [5]. So, further investigations have been initiated only after extensive literature survey. Scientific principles underlying in various reported articles have been well reviewed in the following sub-sections. The aim of

the present section is to give a qualitative discussion on the possible effects of non-ionizing EM radiation on human beings obtained from literature.

2.2.1 Thermal Effects

At Extremely Low Frequency (ELF), heating effect causes due to the magnetic field leads to induction of circulating currents inside the living body. But the microwaves produce thermal effects on biological systems at high power levels by RF energy deposited or absorbed in biological systems through local, partial-body or whole-body exposures. The energy absorption at high power levels probably leads to non-specific stimulation of hypothalamic-hypophysealadrenal axis with liberation of corticosterone that causes sequestration of cells, an effect induced by any known stressor [6]. Some of the reported thermal effects due to non-ionizing radiation include cataract formation in eye, foetal abnormalities, decreased thyroid function, suppression of behavioural responses, gonadal function and natural killer cell activity, increase in the number of complement receptor positive cells and increased phagocytic activity of peritoneal macrophages [7]-[10]. The rise of temperature in tissues due to RF exposure is an important parameter and few studies have carried out this type of analysis [11]-[14]. This rise of temperature is one of the dominant factors to induce adverse health effects into the living tissues. For longer durations and especially at sufficiently high intensities, RF energy can produce temperature rises that can result in thermal effects and adversely impact functioning of the human body. Nature of temperature rise depends on the animal or tissue target and their thermal regulatory behaviour and active compensation process. For local or partial body exposures, if the amount of RF energy absorbed is excessive, rapid temperature rise may damage local tissues. The mechanisms of interaction have been described as thermal effects, with rise in body/tissue temperature of more than $1^{o}C$, non thermal effects, with no obvious increase in body temperature and micro-thermal with thermo-elastic expansion in the brain giving rise to microwave hearing effect [15],[16]. At non thermal levels ($<0.5^{o}C$ rise in rectal temperature) stimulation of thyroid, increased susceptibility of the organism to bacterial infections, decline in neutrophil and complement activity, increased lymphoblastoid transformation of lymphocytes, abnormalities in the erythrocyte/lymphocyte precursors in bone marrow are some of the reported effects [6], [8],[9].

2.2.1.1 Theoretical investigations

Experimentally, it is very difficult to measure the temperature rise for the RF exposure inside the human body directly. Therefore, to overcome this difficulty, computational scheme i.e., thermal modelling for calculating temperature variations has been adopted. Thermal modelling of human tissue is important as a tool to investigate the effect of external heat sources as well as in predicting the abnormalities within the tissue. Most studies of heat transfer analysis in biological tissue have used FDTD method for solving the EM problem and Bio-Heat Equation (BHE) for thermal modelling. The BHE was proposed by Pennes in 1948 [17],[18] The BHE is used to calculate the temperature rise of the human head or other body parts exposed to EM fields only if the subject is at a thermal equilibrium state. It takes into account only the heat exchange mechanisms: heat conduction, blood flow, metabolic process and SAR as the input EM heating. The dose rate at which EM energy at RF imparted into the human head and other body parts is measured in terms of SAR. It is defined as the rate at which a person absorbs EM energy per unit mass and is expressed in watts per kilogram (W/kg) of biological tissue [19]. It has also been internationally accepted that SAR is the most appropriate metric for determining EM energy exposure in the very near field of a RF source [20],[21]. For safety evaluation, SAR is generally quoted as a figure averaged over a tissue volume which is still not harmonized among the different countries and states [4]. SAR averaged over X-g of tissue can be denoted by X-g SAR. In this way, local peak SAR averaged over 1-g of tissue is called peak 1-g SAR. Technical details of SAR have been included in Chapter 4.

The computation of temperature rise is consisted of two steps. The first step is to compute the SAR distribution in the human head model using FDTD method. In the second step, the temperature rise inside bio-tissue is determined by solving the BHE using FDTD method. Some investigations are only based on SAR analysis only and SAR can provide information related to energy absorption. Both SAR and rise of temperature inside human body parts for various RF sources have been investigated by many researchers using the aforesaid methods. A few such pioneering works have been summarized in the next paragraph and some of other technical reports were reviewed in the following paragraphs.

In 1976, single layer and multilayered spherical human head model exposed to EM plane wave was studied theoretically [22]. The human head model is consisting of skin, fat, bone and brain. It has been found that for spheres of radii 10 cm and 5 cm, a relative peak of the normalized heating potential occurs in the vicinity of the centre of the sphere. For the case

of the 5 cm sphere in the range of frequencies 400 MHz to 2.76 GHz, the maximum value of the heating potential occurs at the centre suggesting the possibility of a hot spot. In 1980, thermal response of a human body under varied EM field exposures has been analyzed using modified heat transfer equations considering a series of two-dimensional transient conduction equations with internal heat generation due to metabolism, internal convective heat transfer due to blood flow, external interaction by convection and radiation, and cooling of the skin by sweating and evaporation [23]. In 1982, the local temperature rise at 61 discrete locations as well as the thermoregulatory responses of vasodilatation and sweating has been computed for a number of EM field intensities and two frequencies, one near whole-body resonance. Internal heating patterns and temperature rise have been calculated for two cases inside the human body placing in the near-zone of a quarter-wave monopole and a half-wave dipole operating at 45 MHz and 200 MHz, respectively [24]. The calculated results show that negligible heating occurred for antennas with input power levels of less than 50 W. In 1984, temperature distribution in detailed cross sections of the human body has been studied using Finite Difference (FD) based BHE [25]. Calculated results show that it is related to the utilization of the detailed EM power deposition patterns obtained numerically using the MoM. The obtained results clearly showed a significant dependence of the temperature distribution on the values of the blood flow rates used in the modelling.

In 1988, FDTD method was used to calculate the SAR distributions at 100 MHz and 350 MHz for i) a homogeneous phantom in free space, ii) an inhomogeneous phantom in free space and iii) an inhomogeneous phantom standing on a ground plane [26]. For 100 MHz and 350 MHz, the model used was composed of 23 × 12 × 68 cubical cells and 45 × 24 × 135 cubical cells of cell size 2.62 cm and 1.31 cm respectively. Both the models were represented by a "standard man" of 175 cm height and 70 kg weight. In all SAR's calculations, a mass density of 103 kg/m^3 was assumed for the tissues. The power density of the incident plane wave was taken to be 1 mW/cm^2. The layer-averaged SAR distributions obtained in the three different human models show that the magnitude of SAR value changes for homogeneous, inhomogeneous, ungrounded and grounded models. The effects are more prominent at 100 MHz than 350 MHz. At 100 MHz, for instance the peak that occurs at 50 cm is much higher when the inhomogeneous model is used. And when the model is grounded, the SAR's in the lower part of the body are severely affected. In contrast, at 350 MHz there is no significant difference in the characteristic of SAR distributions. Again for grounded model, effects are

not as prominent as in case of 100 MHz. Finally, the results obtained were compared with those obtained experimentally and with simulated results based on MoM.

In 1991, FDTD method was used to calculate the internal electric fields and the induced current densities in anatomically based models of a human body consisting of 5,628 and 45,024 cubical cells of dimensions equal to 2.62 cm and 1.31 cm, respectively [27]. A layer of dielectric constant ε_r = 4.2 and thickness of 2.62 cm were assumed under the feet to simulate the aforesaid model wearing rubber-soled shoes. The total induced currents for the various sections of the body and the specific absorptions for several organs were calculated. The calculated results for the induced currents are in excellent agreement with the data measured for a human subject.

In 1994, SAR was evaluated based on thermal consideration in a human head model averaged over 1-g and 10-g tissue [28]. The induced current and SAR distributions were computed in an inhomogeneous box type human head model exposed to the EM wave irradiated from a cellular phone [29]. The human head was simulated by a model of 57,263 block cells of cell size equal to 0.5 cm with inhomogeneous dielectric constant and conductivity. The cellular phone was modelled by an equivalent dipole antenna with an equivalent resistor of 120 Ω located at the center gap between the two arms of the dipole antenna. The transmitted power of the cellular phone was assumed to be 0.6 watts at a frequency of 835 MHz. The value of currents and SAR's induced in the head were found in the ranges of 356 mA to 551 mA and 1.23 W/kg to 2.63 W/kg respectively, for the distance between the head and the dipole antenna in the range of 1.0 cm to 2.5 cm. It is found that the maximum SAR induced in the head is below the IEEE's upper safety limit of 1.6 W/kg for the head to keep a distance from the dipole antenna by larger than 2.0 cm [3]. EM coupling effects in terms of antenna input impedance, radiation patterns, radiation power (into free space), power absorbed by the body, radiation efficiency of a human operator on the radiation characteristics of a portable communication dipole antenna were investigated in detail [30]. A 3-D shaped human model and an approximate linear dipole antenna were used to simulate the problem. Coupled integral equations (CIE) and MoM were employed to numerically solve this antenna-body coupling problem. Here the concept of non uniform cubical cell modelling had been used. Numerical results were obtained for the different positions of the antenna at a frequency of 840 MHz. The antenna was first placed in front of the head (distance ranging from 5.0 cm to 1.0 cm) then adjacent to the abdomen (0.6 cm distance). It was found that when coupled with the operator body, the antenna input impedance would have significant

deviation from that in free space. The H-plane antenna gain was obtained about 15 dB and 25 dB for the antenna at the head and abdomen positions respectively. Also, the radiation efficiency is reduced in the range from 0.72 to 0.29 for the head position and 0.15 for the abdomen position of the antenna, respectively.

In 1996, FDTD method along with a new millimeter-resolution anatomically based human model were used to study EM energy coupled to the head due to mobile telephones at 835 MHz and 1900 MHz [31]. Considering the reduced dimensional characteristic of today's mobile telephones, SAR distributions were obtained for two different monopole antennas of length equal to λ/4 and 3λ/8 and a model of the adult male and reduced-scale models of 10 and 5 year-old children. It was found that particularly at 835 MHz both peak 1-voxel and 1-g SAR's are larger for the smaller models of children. Also, a larger in-depth penetration of absorbed energy was observed in the smaller models. The effect of using widely disparate tissue properties as reported in the literature [32],[33] and using of homogeneous models instead of anatomically based realistic heterogeneous models on the SAR distributions were studied. Both the peak 1-voxel and 1-g SAR's were shown to grossly overestimate in case of homogeneous models. It was also found that it is possible to use truncated one-half or one-third models of the human head with negligible errors in the calculation of SAR distributions. This simplification allowed considerable savings in computer memory and computation time. SAR distribution obtained for an MRI based experimental model of the human head exposed to a λ/4 monopole antenna placed above a box, for both the full model as well as for the truncated half and one third models of the head. The peak SAR of 3000 mW/kg is obtained for Z = 0, where Z-axis is taken along the base of the antenna. Nearly identical SAR's are obtained for the electromagnetically coupled region in proximity to the antenna for each of the models. But for the truncation of the models, lower SAR's are obtained due to discarding of tissues. The difference in the peak and averaged SAR's calculated for 1-g tissue using the full and the truncated models is less than 1.5 %. Another study on the interaction of handset antenna with human body had been performed to carry out the investigation on the parameters that influence the antenna-user interaction [34]. Various canonical models predict those in the human head had been used to calculate antenna efficiency (η), the peak SAR, the maximum SAR averaged over 1-g and 10-g of tissue and the effect of distance between the antenna and the head on peak 1-g and 10-g values of SAR. Effect of the presence of hand on the radiation pattern of the handset antenna and SAR had also been obtained. Changes in η, power absorbed (P_{abs}) and SAR's with separation between the antenna and various models of

the head obtained in the study are shown in Table 2.1. From Table 2.1, it is found that peak 1-g and 10-g SARs are lower for an anatomically correct model of the human head (Gent and Yale head) compare to either homogeneous box or spherical head models. The other specific findings are: a) a box model of a human head provides grossly distorted and unreliable results for the antenna radiation pattern, b) a spherical model of the human head provides results that are relatively close to those obtained with a relatively simple, but more realistic, head model, c) the SAR values obtained with spherical or simplified head models, that do not include the ear, are greater than those for a realistic head model that includes the ear and d) a hand holding the handset absorbs significant amount of antenna output power, which can be considerably decreased by modifying the geometry of the handset metal box.

Table 2.1: Effects of the change in the separation between the antenna and the head model: 915 MHz, 1 W

Model	Separation (cm)	η (%)	P_{abs} (W)	SAR in the head (W/kg)		
				Peak	1-g	10-g
Homogeneous box	1.5	16	0.84	18.1	14.1	9.25
	2.0	25	0.75	11.2	8.5	5.6
	2.5	40	0.60	5.7	4.3	3.1
	3.0	51	0.49	3.2	2.6	1.9
Homogeneous sphere	1.5	46	0.54	13.4	10.9	7.0
	2.0	57	0.43	8.5	6.8	4.6
	2.5	66	0.34	5.5	4.4	3.0
	3.0	73	0.27	3.7	3.0	2.1
Gent head	1.5	51	0.49	11.2	8.6	4.8
	2.0	57	0.43	7.1	5.6	3.3
	3.0	72	0.28	3.2	2.4	1.4
Yale head	1.5	60	0.40	3.5	2.65	1.8
	2.0	67	0.33	2.4	1.7	1.4
	2.5	73	0.27	1.9	1.2	0.9
	3.0	77	0.23	1.7	1.1	0.8

In 1997, RF energy absorbed in a simulated human head model was determined at various 450 MHz, 900 MHz and 1800 MHz operating frequencies [35]. The SAR was determined by measuring the temperature rise ΔT during an irradiation time Δt with a non-perturbing type thermistor, using the relation: $SAR=C\times\Delta T/\Delta t$, where C = specific heat of the liquid mixture used to simulate muscle and brain. The thermistor was calibrated from 18ºC to 30ºC against a calibrated mercury thermometer. Two different liquid mixtures composed of water, sugar and salt (NaCl) were used to simulate muscle and brain.

In 1998, at 1800 MHz, the antenna performance and SAR analysis were presented for a half wave-length dipole and monopole antenna in free space using different head phantoms [36]. The phantoms used were a homogeneous sphere, a layered sphere and a realistic head mode1 all consisting of 2.5 mm cubic voxel grid. The primary tool used for the investigation was the commercial FDTD based software XFDTD, available from Remcom Inc. In addition a planar inverted-F antenna (PIFA) (length = 20.0 mm, width = 15.0 mm, height = 12.5 mm, feed probe = 5.0 mm from the shorting post at the upper edge of the handset and feed gap = 2.5 mm) was taken for investigations. A separation of 5 mm was maintained between the handset and the head. A realistic head model obtained from Remcom Inc. was used to compare SAR predictions in the simplified and more realistic head phantoms. It was seen that the directivity of the PIFA results in significantly reduced SARs in the phantom head models compared to either of the other antennas.

In 1999, temperature rises in the human head for portable wireless phones were computed with an anatomically approximated head model at 900 MHz and 1.5 GHz [37]. The portable wireless phone was modelled by a quarter-wavelength monopole antenna mounted on a dielectric covered metal box with output power of 0.6 W at 900 MHz and 0.27 W at 1.5 GHz. The maximum temperature rise in the brain is found to be 0.06^{o}C for restricting the peak 1-g SAR to 1.6 W/kg following ANSI/IEEE safety guidelines and that of 0.11^{o}C obtained for restricting the peak 10-g SAR to 2.0 W/kg following ICNIRP safety guideline, both at 900 MHz and 1.5 GHz [2]-[4].

In 2000, EM power absorption and the corresponding temperature rises induced in an anatomical heterogeneous model of the human head have been evaluated due to exposure of various types of cellular phones equipped with different kinds of antennas: half-wavelength dipole, quarter-wavelength monopole, whip, and PIFA available on the market [13]. Maximum temperature increases obtained in the head, brain, and lens for four types of phone models and their vertical or tilted positions. These steady-state temperature increases are

obtained after about 50 min of exposure, with a time constant of approximately 6 min. The maximum temperature increases obtained in the head, brain and lens lies between 0.22^{o}C to 0.43^{o}C, 0.08^{o}C to 0.19^{o}C and 0.002^{o}C to 0.022^{o}C respectively. These data show that the correlation between local SAR values and temperature rise and between SAR and thermal distributions are not straight forward. Tissue heating is not only influenced by SAR but also by the way in which the RF energy absorption is distributed in the surrounding area, by the thermal characteristics of the considered and neighbouring tissues and by the heat exchange mechanism with external environment. The SAR generated by cellular phones inside an anatomical head model was computed using four different models of commercially available phones working at 900 MHz and 1800 MHz [38]. The phones were modelled by using a Computer-Aided Design (CAD) representation obtained through the reverse engineering technique. The phones were classified according to their antenna length: Phone A - 92 mm, Phone B - 126 mm, Phone C - 85 mm, and Phone D - 143 mm. Both SAR distributions and averaged SAR values had been computed inside the anatomical head model using FDTD method as shown in the Table 2.2. The column SAR_{peak} gives the maximum SAR found in a cell of the discretized space. The column P_{abs} is the ratio between the total radiated power and the power absorbed by the head. From the table, it is seen that the antenna's length play a vital role in SAR distributions. Computations had been experimentally validated through the measurements performed inside anthropomorphic phantoms irradiated by a dipole antenna and a cellular phone.

Digital anatomical models of man and animals were used in numerical calculations to predict EM field induced SAR [39]. To use these models, different permittivity values were assigned to the various tissues at different frequencies. Averaged and localized SAR values were calculated in the RF range of 1 MHz to 1 GHz. It was found that when the dimensions of spherical head are small compared to the wavelength (i.e., wavelength inside the material is greater than ten times the dimensions of the object), the averaged SAR is inversely proportional to the permittivity of the material composing the spherical head. However, the localized SAR values do not have the same relation and vary greatly depending on the location within the sphere. These results indicated that care must be taken in choosing the permittivity values used in calculating SAR values and some estimate of the dependence of the calculated SAR values on variability in permittivity should be determined.

Table 2.2: Computed SAR inside a human head

Phone	Frequency	SAR_{peak} (1 cell)	$SAR_{1\ gm}$	$SAR_{10\ gm}$	P_{abs}
	[MHz]	[W/kg]	[W/kg]	[W/kg]	[%]
Phone A	900	5.03	0.45	0.21	29.3
Phone B	900	4.82	0.30	0.21	29.4
Phone C	900	4.69	0.56	0.40	44.7
Phone C	1785	1.04	0.17	0.08	11.6
Phone D	900	1.00	0.15	0.11	20.2

In 2001, induced *E* field and current density in a child's body exposed to a 60 Hz electric field was calculated and compared with that for an adult's body [40]. Induced electric fields were computed using a hybrid method for the adult model and the quasistatic FDTD method for the child. Both models were consisted of 80 different types of tissues with each voxel assigned conductivity value corresponding to a given tissue. For adults, at an exposure limit of 4.17 kV/m, the induced current limit obtained in the brain and spinal cord was 2 mA/m^2. But in the cerebrospinal fluid (CSF) for the same exposure limit, the value of the induced current obtained for child and adult model were 3.26 mA/m^2 and 4.43 mA/m^2, respectively.

In 2002, a comprehensive EM and thermal analysis of radiation and its impact on human beings due to the use of various types of commonly used mobile phones and communication antennas was reported [41]. To carry out that analysis, a large number of numerical simulations were conducted for the GSM 900 and 1800 band with an input power of 600 mW and 250 mW, respectively using monopole, helical, side-mounted PIFA and patch antennas. Like the previous study both the vertical (V) and tilted (T) positions of the phones have been examined. The WLAN (Wireless-LAN) antenna has an input power of +20 dBm at the frequency of 2.45 GHz. Maximum temperature rises obtained in head and brain for 10 min exposure with the four considered mobile phone antennas along with the WLAN antenna due to two positions: V and T are shown in Table 2.3.

An attempt has been taken to correlate the maximum temperature increase in the head and brain with the peak SAR value due to handset antennas considering total 660 situations [42]. On the basis of statistics, it has been found that these correlations are less affected by

the positions, polarizations and frequencies of a dipole antenna. They are also reasonably valid for different antennas and head models. The maximum temperature rises in the head and brain are found to be 0.31°C and 0.13°C for restricting the peak 1-g SAR to 1.6 W/kg following FCC safety guideline and that of 0.60°C and 0.25°C obtained for restricting the peak 10-g SAR to 2.0 W/kg following ICNIRP safety guideline.

Table 2.3: Maximum temperature rise (°C) in human head and brain

Antenna	Position	ΔT_{MAX_HEAD}			ΔT_{MAX_BRAIN}		
		900 MHz	1800 MHz	2.45 GHz	900 MHz	1800 MHz	2.45 GHz
Monopole	**V**	0.355	0.158	--	0.177	0.0302	--
	T	0.562	0.102	--	0.331	0.0389	--
Helix	**V**	0.381	0.089	--	0.169	0.045	--
	T	0.369	0.061	--	0.178	0.033	--
Side PIFA	**V**	0.551	0.712	--	0.139	0.058	--
	T	0.416	0.571	--	0.139	0.058	--
Patch antenna	**V**	0.541	0.109	--	0.240	0.079	--
	T	0.569	0.072	--	0.380	0.016	--
WLAN	**--**	--	--	5.011e-5	--	--	1.982e-5

In 2004, relationships between SAR and temperature distributions in the human head due to RF energy deposition during MRI have been examined at 64 MHz and 300 MHz following safety limits defined by the United States' Food and Drug Administration (FDA) and the International Electrotechnical Commission (IEC) [43]. An explicit FDTD formulation of the BHE has been employed with a 3-D human head-eye model to evaluate the temperature rise in the eye and surrounding head tissues at 10 MHz for several different operational conditions of an implanted stimulator IC chip of a retinal prosthesis designed to restore partial vision to the blind [44]. In the vitreous cavity, temperature elevation of 0.26°C has been observed after 26 min for a chip dissipating 12.4 mW when positioned in the mid-vitreous cavity while it is 0.16°C when the chip is positioned in the anterior portion between

the eye's ciliary muscles. Corresponding temperature rises observed on chip are 0.82^{o}C for both the positions of the chip.

In 2005, Using FDTD method, a set of SAR calculations were performed for anatomically correct adult and child head models [45]. A half-wave dipole antenna was used as an EM exposure source at 900 MHz, 1800 MHz and 2450 MHz frequencies. MRI based experiment with one female, one adult, two child-head models of aged 3 year and 7 year were used. In order to compare the results all the values of SAR obtained were normalized to the antenna input power of 1 W. The normalized SAR of each model was compared to the largest SAR value in the group of each frequency. BHE has been solved using Alternating Direction Implicit (ADI) technique to analyse temperature rise inside an anatomical model of the human head exposed to a cellular phone with a radiated power of 250 mW operating at 900 MHz [46]. It has been found that the maximum temperature increase in the internal tissues of the human head model due to SAR deposition does not exceed 0.1^{o}C. A temperature difference of 1.6^{o}C in the skin has been recorded due to the presence of a switched off cellular phone, which has been confirmed by the experimental measurements. Using Finite Volume Time-Domain (FVTD) simulator MAXDG0 has been used to obtain accurate numerical modelling of EM wave propagation in a MRI based human head model and its thermal effects [47]. The FVTD solver is quite fast and the maximal time step required in order to achieve stability is directly related to the smallest elements of the mesh, even if the mesh is only locally refined. The maximum value of temperature rise obtained inside the head model is less than 1^{o}C. A broadband PIFA was proposed for International Mobile Telecommunications-2000 (IMT-2000) / WLAN / Digital Multimedia Broadcasting (DMB) terminal for reduction of SAR in human head [48]. FDTD based SEMCAD software was used in order to simulate SAR. The simulated and measured values of peak average SAR on 1-g and 10-g human head tissue caused by the triple band PIFA mounted on the folder type hand-sets were analyzed. A sine wave of 1.9 GHz was taken as the wave source. The 1-g and 10-g peak averaged SAR values obtained for proposed antenna were 1.09 W/kg and 0.61 W/kg and for measured antenna were 1.17 W/kg and 0.62 W/kg.

In 2006, maximum temperature rises inside the head models of a 3-year-old child, 7-year-old child and adult models exposed to a dipole antenna have been calculated for SAR limits in safety guidelines [49],[50]. Each type of head models have been developed separately at the Nagoya Institute of Technology (NIT) and the Osaka the University.

Maximum temperature rises obtained in head and brain for different head models are shown in Table 2.4.

Table 2.4: Maximum temperature rise (^{o}C) in human head and brain

	Head model	Peak SAR	Maximum temperature rise (^{o}C)	
			Head	Brain
3-year-old child	Osaka University	1-g cube	0.23	0.11
		10-g cube	0.53	0.20
	NIT	1-g cube	0.23	0.10
		10-g cube	0.65	0.23
7-year-old child	Osaka University	1-g cube	0.26	0.10
		10-g cube	0.59	0.21
	NIT	1-g cube	0.19	0.10
		10-g cube	0.52	0.21
Adult	Osaka University	1-g cube	0.26	0.10
		10-g cube	0.59	0.21
	NIT	1-g cube	0.19	0.10
		10-g cube	0.52	0.21

The SAR was calculated for human head models exposed to mobile phone radiation at 900 MHz and 1800 MHz [51]. Radiated energy distributions and averaged SAR values in 1-g and 10-g of tissue were computed inside the head models using near-field FDTD method. Two models for mobile phone (half-wavelength dipole and a quarter wavelength monopole) and two simple models for head (homogenous and multi-layer spherical) were considered. Computational results were compared with a realistic MRI based human head model [52], [53]. The distribution of the local SAR in the realistic head model was similar to that of the simplified head models. The values of maximum local SAR averaged over 1-g and 10-g of tissue were equal to 5.34 W/kg and 2.96 W/kg respectively, for 1.0 W output power from the antenna. The results indicated that the area of the maximum local SAR was situated in outer layer of skull which is consisted of muscle and skin. Type of antenna, operating frequency,

current distribution and the distance between head and antenna were found to be as the important parameters related with RF energy absorption. But the type of head models used for simulation had been proved as an insignificant. A modern method for calculating maximum SAR (10-g) was introduced and the results were compared with MRI images. Averaged SARs in adult and child models for frequency range from 30 MHz to 3 GHz were evaluated using FDTD method [54]. A detailed error analysis was performed for the average SAR calculation using the FDTD method in conjunction with the perfectly matched layer (PML) absorbing boundaries. A basic rule was derived for the PML employment based on a dielectric sphere and the Mie theory solution. The results obtained showed that the averaged SAR under the ICNIRP reference level exceeds the basic safety limit nearly 20 % for the child model.

Preliminary study of SAR reduction with inclusion of metamaterials in the space between the antenna and the head was performed using the FDTD method with lossy Drude model [55]. The antenna was arranged parallel to the head axis. The distance between the antenna and head surface was kept constant at 3.0 cm. The peak value of SAR in 1 gm of tissue was calculated for an antenna output power equal to 600 mW. The calculated peak 1-g SAR without metamaterials was 2.43 W/kg. Effects of metamaterials on SAR reduction is shown in Table 2.5 where P_R is the radiated or antenna output power (mW/kg) and P_{abs} is the power absorbed in head (mW/kg). For verification, the simulated results were compared with that available in literature [56].

Table 2.5: Effects of metamaterials on SAR reduction at 900 MHz

Inclusion of material	P_R (mW)	P_{abs} (mW)	Peak 1-g SAR (W/kg)
No material	600	317.98	2.43
$\mu = 1. \varepsilon = 0.3$	547.3	224.3	1.73
$\mu = 1. \varepsilon = 0.5$	560.9	271.7	2.07

In 2007, temperature rise induced by SAR dissipation of cellular phone in a 3- D anatomical human head model composed of 15 types of tissues has been calculated using FDTD method considering the effects of the Thermoregulatory System (TS) [57]. The cellular phone has been modelled as a half-wavelength dipole antenna resonating at 1.8 GHz

with a power of 120 mW. The average steady state temperature for all tissues has been calculated in the head model with and without TS. It has been found that the inclusion of the TS resulted in a maximum temperature rise of 0.029^{o}C in the skin. Considering the TS, it has been suggested that modern cellular phones operating at full power would produce SAR dissipation within the limits of the safety guidelines and temperature rise in the human head in the same order of the basal temperature of these tissues.

In 2008, correlation between locally averaged SAR and temperature rise for plane-wave travelling along horizontal directions, whole-body exposure conditions, at 30 MHz, 75 MHz, 150 MHz, 450 MHz and 800 MHz has been investigated for various SAR averaging masses [58]. For each frequency 4 cases are considered, for both vertical *E* and horizontal *H* polarizations and for 2 types of exposure: front and side (right). The coupled EM-Thermo simulations were performed using the FDTD based EM and thermal solver FDTDLab [59],[60]. From the obtained result it has been suggested that on average 5-g locally averaged SAR is the best SAR related metric to represent temperature response of the human body exposure to RF energy. Also in all cases, not depended on exposure conditions of frequency, the 10-g SAR is better correlated with the global temperature distribution than the 1-g SAR, which appears to strengthen the rationale behind the choice of the former as the basic restriction IEEE C95.1-2005 standard and ICNIRP guidelines. Here it should be mentioned that difference between correlation coefficients for 1, 5 and 10-g averaged SAR distributions and appropriate temperature rise distributions are not more than several percents.

In 2009, a formula has been derived for simply predicting core temperature rise in human for whole-body microwave exposure considering the main factors influencing the core temperature rise such as body surface area-to-weight ratio, sweating rate etc. [61]. It has been found that core temperature rises are in reasonable agreement between the results from the formula and FDTD computation. Simulations of SAR and temperature rise in the human head under plane-wave exposure are performed for the assessment of computational uncertainty of temperature rise and SAR in the human eyes and brain in the frequency range 1 GHz to 10 GHz [62]. From the obtained results it has been suggest that 2 mm resolution should only be used for frequencies smaller than 2.5 GHz, and 1 mm resolution only under 5 GHz.

In 2010, temperature rise in the human head due to use of different mobile phone models has been computed using a conformal FDTD-based EM solver, SEMCAD-X [63]. A heterogeneous High-Resolution European Female Head (HR-EFH) with twenty five different tissues is used to simulate the human head model, whereas four semi-realistic CAD models,

i.e., candy-bar with external antenna, candy-bar with internal antenna, clamshell with external antenna, and clamshell with internal antenna, operating at 900 MHz with antenna output power of 600 mW are used to simulate the commercially available mobile phone models. The simulated results show different temperature rise values in the user's head obtained due to the use of different mobile phone handset models. Distributions of SAR and steady state thermal elevation inside a multi-layered human head model irradiated by an obliquely incident EM plane wave at 900 MHz, 1800MHz and 2.4 GHz for perpendicular and parallel polarizations have been calculated by FDTD method [64]. It is found that the induced temperature elevation in the brain region, in all the examined conditions, never exceeds 0.4^{o}C. This value is well below the threshold value of 3.5^{o}C for the induction of adverse thermal effects to the neurons.

In 2011, a method for estimating SAR-induced temperature increase inside a realistic human head model has been proposed that is many times faster than existing conventional numerical methods for calculating either temperature increase or 10-g average SAR [65]. The method provides a reasonably accurate calculation of the temperature increase in a very short time: about 60 times faster than a finite-difference implementation of the BHE and about 10 times faster than 10-g SAR averaging algorithms, depending on the mesh resolution. FDTD method has been used to calculate peak localized temperature rise in six children and two adult body models exposed to orthogonal plane-wave at frequencies in the range of 10 MHz to 5600 MHz [66]. Considering the uncertainties in the model parameters, it has been found that a peak temperature rise as high as 1^{o}C can occur for worst-case scenarios at the ICNIRP reference levels. The BHE has been solved using FDTD method to estimate temperature rise for an anatomically based human head model with a resolution of 2.5 × 2.5 × 2.5 mm due to portable telephones of 600 mW at 900 MHz [67]. The steady-state temperature increases are obtained after about 50 min of exposure, with a time constant of approximately 6 min. The maximum temperature increases obtained in the ear are found to be in the range of 0.22^{o}C to 0.39^{o}C, while that in the brain lie between 0.07^{o}C to 0.17^{o}C following ANSI/IEEE safety guidelines.

In 2012, numerical analysis of SAR and temperature distributions inside a realistic human head model exposed to mobile phone radiation at 900 MHz and 1800 MHz have been obtained using the FEM based COMSOL^{TM} Multiphysics solver [68]. The temperature increases in the human head are found to be correlated with the *E* field and SAR, and found to be much lower than the thermal damage temperature of 3.5^{o}C. Maximum local temperature

rise observed in each frequency is not much different but the observed temperature distribution pattern in each frequency is significantly different and is dominated by the dielectric properties and thermal properties of the tissues.

The number of cell towers is increasing rapidly for providing the link to and from the mobile phone. In the year of 2013, it was estimated that more than one billion people would be having with cell phone connection in India [69]. The EM waves emitted from the BSAs may have adverse effects on human beings or on other living animals [70]-[72]. Exposure of an anatomical model of the human body to the EM field radiated from a rooftop mounted BSA operating around 900 MHz has been studied by using a hybrid ray-tracing/FDTD technique [73]. Three typical exposure conditions for the rooftop mounted BSA have been considered and analyzed. In all cases, the antenna is positioned with a mechanical tilting of 8^{o} on the top of a 6 m high trestle. The radiated power of the antenna is set to 30 W, corresponding to a typical value for a four-transmitter base station in urban area. In the first case, the subject i.e. the human body stands on the building roof, where the antenna is mounted, at a distance of 8 m from the trestle. In the second case, the subject stands on a balcony in front of the building where the antenna is mounted at a distance of 30 m. In the third case, the subject stands on the street beneath the building of height 30 m and assumed to be presence of another building at his back. In all the examined cases, the obtained results expressed in terms of *E* field and SAR as shown in Table 2.6. Comparison of the results shown in Table 2.6 with reference levels and basic limits proposed in the main international protection standards [3],[72],[74] shows that all the *E* field and SAR values are well below the safety levels reported in the standards.

Table 2.6: Spatial maximum, spatial average of *E* field and SAR averaged over 1-g, 10-g and whole body

Case No.	E_{max} (V/m)	E (V/m)	SAR_{1g} (mW/kg)	SAR_{10g} (mW/kg)	SAR_{WB} (mW/kg)
Case I	4.2	2.8	5.3	3.0	0.12
Case II	8.1	5.5	13.2	8.5	0.46
Case III	1.3	1.1	0.26	0.17	0.01

2.2.1.2 Experimental investigations

As it is very difficult to measure the temperature rise inside the human body experimentally for the RF exposure yet the experimental documentation of the existence of RF effect is of utmost importance in preventing any health risk aimed at the human subject evaluated in microwave frequencies. Among the techniques to document actual EM field distributions, temperature measurements are most accurate. In addition, they are more direct for safety studies as they acquire real temperature changes as the final outcome of the RF deposition and are independent of simulations or numerical model variables.

During 1996-1997, experimental dosimetry related to the thermal effects of EM waves radiated from handheld mobile phones and other wireless communication devices has been mainly focused on the measurement of peak SAR for the evaluation of the compliance within safety guidelines. Measurement of SAR is generally performed in a realistic human-head shaped homogeneous liquid or solid phantom [75]-[77]. Numerical comparison between homogeneous and anatomically based human head models for both peak 1-g and 10-g SAR shows that the homogeneous models give a slight overestimate over the inhomogeneous models.

In 1999, a rudimentary test has been performed by measuring the temperature rise at the skin using a 915 MHz tuned dipole antenna for the validity of the simulation results [78]. The antenna was placed vertically oriented at a distance of 2.0 cm from the head of a volunteer. The skin temperature close to the transmitting antenna was measured using two small 0.5 mm diameter, seven-sensor thermocouple probes. With the input antenna power of 1.0 W, measured values of temperature rise are found to be 0.6^{o}C and 0.8^{o}C for the antenna probe and 0.2^{o}C for the contra lateral probe. There were too many fluctuations in the measurements to allow an analysis in terms of equilibration times. With a solid ceramic phantom, a simple measuring method with an *E* field probe was proposed for portable-telephone compliance evaluation [79]. The *E* field probe is fixed within the head model, close to the auricle, while the portable telephone is moved to find the spatial peak SAR. An advantage of this method is that the spatial peak SAR can be evaluated in a very short time compare to the thermographic method for the evaluation of the SAR of portable telephones. The thermographic method is generally difficult, because the antenna output power is large enough to produce an evident temperature rise in the human head.

In 2001, more detailed investigations have been made on the head-tissue heterogeneity required for peak SAR evaluation in the frequency range from 900 MHz to 2000 MHz [80]. The dependence of the peak SAR on tissue heterogeneity is found to be antenna dependent. The homogeneous modelling may result in an underestimate of about 20% at the maximum for portable telephones with a $\lambda/2$ monopole or dipole antenna, and an overestimate to the same extent for portable telephones with a $\lambda/4$ monopole or helical antenna. A head model with a simple skin-fat-muscle-bone-brain structure gives almost the same gram-averaged spatial peak SAR value as a highly complex head model.

In 2003, a four-channel fluoroptic thermometry system has been used to record temperature rise inside a head phantom made of ground turkey breast at RF power levels ranging from a value of SAR up to 4.0 W/kg for 10-minutes exposure [81]. Continuous temperatures were recorded simultaneously for four different fluoroptic optical fiber positions in the head phantom and it was found that the distribution of temperature changes was not homogeneous, with a maximum temperature increase of $0.7^{o}C$ occurring near one of the struts for the 10-minute exposure.

In 2005, a new human head phantom has been proposed by CENELEC/IEEE, based on a large scale anthropometric survey for compliance testing of mobile telephone equipment with respect to SAR assessment [82]. SAR obtained for this proposed head phantom is compared to a homogeneous Generic Head Phantom (GHP) and three other high resolution anatomical head models. All the head phantoms are exposed to the radiation of a Generic Mobile Phone (GMP) with different antenna types and a commercial mobile phone. The phones are placed in the standardized testing positions and operate at 900 MHz and 1800 MHz. The average peak SAR is evaluated using both experimental (DASY3 near field scanner) and numerical (FDTD simulations) techniques. The numerical and experimental results compare well and confirm that the applied SAR assessment methods constitute a conservative approach. Assessment of RF radiation energy deposited on human head was conducted by far-field measurement and verified with numerical FDTD method at 1900 MHz [83]. The difference between experimental result and numerical analysis is found to be within 5%.

In 2009, parallel-FDTD method has been used to characterize the way of EM waves interact with the human head at 900 MHz [84]. In order to achieve results, average of realistic parameters of bio-materials, such as bones and head liquids, as well as near field radiation parameters of a half-wave dipole antenna are being considered. All averaged SAR values and

E field distributions inside modelled analysed structures have been compared to experimental results obtained in a full setup laboratory with all equipments necessary to perform dosimetric validations of telecommunication devices according to IEEE 1528 specification. Whole-body averaged SAR (SAR_{WB}) in human models due to plane wave exposure has been measured using the cylindrical fields scanning technique [85]. To confirm the validity of the proposed experimental technique, the SAR_{WB} obtained by the proposed method was compared with results obtained using the conventional FDTD method and found an increase of about 29.7% is expected when compared with conventional FDTD method.

In 2010, SAR measurements at 894 MHz, 1710 MHz, 1895 MHz and 1980 MHz frequencies have been done using DASY4 equipment [86]. Measurement setup for DASY4 equipment is consisted of a dipole antenna for pre system accuracy check, a device holder, phantom head and body model with tissue simulating liquid, a robot, a probe with optical surface detection, data acquisition unit and DAYS software. The measured 1-g and 10-g SAR values are compared with that obtained by CST Microwave Studio® software as shown in Table 2.7.

Table 2.7: Comparison of measured and simulated SAR values

Frequency (MHz)	Measured SAR (mW/kg)		Simulated SAR (mW/kg)	
	1-g	10-g	1-g	10-g
894	1.72	1.26	1.29	0.98
1710	0.48	0.29	0.36	0.23
1895	0.93	0.59	0.47	0.32
1980	0.93	0.57	0.62	0.38

In 2013, temperature change of human head due to the use of handheld mobile phone working at frequencies 900 MHz and 1800 MHz were measured by collection of image from thermal imaging camera in an anechoic chamber with average of 45 minutes talking hour [87]. Measured values of temperature rise are found to be in the range of 2.6^{o}C to 3.7^{o}C at the place near the ear skull after 45 minutes of operation.

In 2015, SAR measurements were carried out using the modified SAM head, the SAM twin phantom and DASY4 system at 1.8 GHz due to RF radiation from Personal Data Assistant (PDA) device with hands-free kits [88]. Two different PDAs were involved in this study, one is the LG KE850 while the other is the IPHONE 3GS. The highest SAR value measured from both PDAs showed good agreement with the official data. It is shown from the results that SAR value decreases by using hands free-kit.

2.2.2 Non thermal Effects

The vast majority of the sustained cell phone EM radiation related biological consequences can be explained by "Non thermal effects". These effects include all the interactions of EM wave with biological tissues without production of heat or a measurable rise in temperature. Specifically, the *H* field, rather than the *E* field of EM wave has the most harmful effects on living organism because of its ability to penetrate through human bodies while *E* field has poor human skin penetration ability [89]. In fact, the induced alternating currents in our bodies resulting from cell phone EM wave exposure can explain the biological non thermal effects at tissue, cellular and sub-cellular levels.

2.2.2.1 Theoretical investigations

In 1982, it has been reported that weak EM fields release calcium ions from cell membranes [90]. Leakage of calcium ions into the cytosol acts as a metabolic stimulant, which accelerates growth and healing, but it also promotes the growth of tumors. Loss of calcium ions causes leaks in the membranes of lysosomes releasing DNA's that causes DNA damage.

In 1989, various tests were conducted on the effects of the EM field at the Microwave Institute of Zhejiang Medical University. It was found that the energy field can affect the central nervous and immune systems of human body. The data obtained from the tests indicate that chronic exposure to EM field is associated with significant changes in the physiological parameters [91].

In 1997, based on the case studies obtained from the different countries regarding the effects of EM radiations from mobile tower, it has been reported that the people who are living near mobile tower receive strong signal strength but at the expense of health [92]. So, little bit poor connectivity is better to have better health. It has also been reported that continuous exposure to EM radiations from mobile phone towers, TV and FM towers cause

serious health problems over the years. Apart from these studies, there is large number of studies and reports are available in the literature associated with the health hazards of mobile tower.

In 1998, it has been reported that the mobile telephones carry a health warning ranging from headaches to brain tumors [93]. In the mean time, The National Radiological Protection Board (NRPB) of Britain fixed up the standards for RF exposure. The NRPB recommended a limiting value of SAR which is equal to 10 mW/gm. The biological effect of EM field was reviewed and found that exposure to excessive levels of EM power over prolonged period causes adverse health effects [94]. The work presented occupational and general exposure limits adopted by World Health Organization (WHO). It was made a survey over 25 microwave engineers, research students and technicians working eight hours per day in the microwave laboratories in India and found a variety of reversible asthenia problems that constitute the hypothetic microwave syndrome such as headache, perspiration, emotional instability, irritability, tiredness, lack of concentration and insomnia. The evaluation of these subjective complaints is difficult due to the absence of a control group and well established dosimetric data.

In 1999, the exposure to cell phone radiation causes red blood cells to leak hemoglobin, the build up of which can cause heart disease and kidney stones [95]. Scientists exposed samples of blood to microwave radiation and found that even at lower levels than those emitted by cell phones, the blood cells leaked haemoglobin. Two minutes exposure to radiation emitted from mobile phones can disable a safety barrier in the blood causing proteins and toxins to leak into the brain. This can cause the chances of developing diseases such as Alzheimer's, multiple sclerosis and Parkinson's. Symptoms reported by mobile phone users include fatigue, dizzy spells and memory loss. Cell phone transmits microwave signal from antenna to base stations or towers over a long distance. When the phone is far away from the tower or if it is inside a building or a car, more power is send out by the tower to make or to keep the connection. Depending on how close the cell phone antenna is, as much as 60% of the microwave radiation is absorbed by the head. Actually the microwave radiation penetrates through the area around the head, some reaching to one and a half inch into the brain [96].

In 2004, non-thermal microwave interaction mechanism with biological tissues below frequency of 0.1 MHz was investigated and found that the microwave *E* field excitation

stimulated the excitable biological tissues which have significant implications on human health and safety [97].

In 2005, it has been reported that mobile phones can cause EM interference in the functioning of implanted pacemakers [98]. Due to the EM interference, the pacemaker can be affected either by impedance to delivery of the stimulated pulses which regulate the heart's rhythm or by causing the device to deliver irregular pulses and leading to arrhythmias or by causing it to ignore the heart's rhythm and deliver pulses at a fixed rate. It has also been reported that the RF radiation may stop pacemaker from delivering pulses in a regular way or may generate some kind of external controlling pulse putting the patient to death [99].

In 2009, reviews from various epidemiological and experimental studies show that significant biological effects are found due to the continuous exposure to microwave radiations from Cell phone towers, TV and FM towers far below the current standards [100]. Radiation from cell phone towers has been associated with greater increase in brain tumour [101]. This is due to the damage in the Blood Brain Barrier (BBB) and the cells in the brain which are concerned with learning, memory and movement. Another possibility of DNA damage is via increased free radical formation inside cells, which further causes cellular damage in the mitochondria.

2.2.2.2 Experimental investigations

Non thermal effects of RF exposure inside the human body can not be measured except the effects of EM fields on Electroencephalogram (EEG). Non thermal effects are not well defined [102]. But as they are 3 or 4 times more harmful than the thermal effects so they are required to be considered. The non thermal effects are quantified by means of statistical analysis and case studies.

In 1995, it was found that the EEG data of a man is altered in the range of alpha-activity (8-13 Hz) due to exposure of the EM field radiation for some hours [103]. In 2003, experiments were conducted to find out the effects of EM fields radiated from mobile phone on EEG of the human brain [104],[105]. The results obtained from these studies show that EM fields emitted from mobile phones alter the EEG data. Later a huge number of studies and reports available in the literature have lent support to these findings [106]-[109].

In 2008, a study was made over 500 people with benign and malignant tumours of the salivary gland and 1,300 healthy people, and it has been reported that the people who use cell phones for many hours in a day are 50% more likely to develop mouth cancer than those who

never use cell phones [110]. They also found that cell phone users in rural areas may be at increased risk for cancer because cell phones need to emit higher levels of radiation in order to make contact with fewer available antennas. The parotid glands, the largest salivary gland, located near the jaw and ear, where cell phones are typically held during use, are much more affected. The findings appear in the American Journal of Epidemiology.

In 2010, it has been reported that continuous RF exposure has irreversible infertility effect [102]. It reports that there is 30% sperm decrease in intensive mobile users, in addition to damage of sperms.

In 2012, case studies of different countries have been reviewed to discuss the harmful effects of mobile towers radiations [111]. Most of the case studies show negative impacts of EM radiation on the biological systems and environment. However most of the available scientific literature on the negative environmental effects of EM fields reports the results of experimental and epidemiological studies examining the impact on various aspects of human health. But it has also been reported that individuals differ in their response to similar levels of EM field. For some people, short term effects from cell tower radiation exposure may include headaches, sleep disorders, poor memory, mental excitation, confusion, anxiety, depression, appetite disturbance and listlessness.

A study had been performed by doctors in Germany city of Naila on 1000 residents living within an area around two cell towers for 10 years [112]. During the last 5 years of study, it was found that those living within 400 m of either tower had a newly-diagnosed cancer rate three times higher than those who lived further away.

In 2014, power density of RF radiation have been measured and a questionnaire survey was conducted in close vicinity of a mobile BSA working at GSM 900 band at the selected locality in Aizawl ($23^{o}44'53.5''$N, $92^{o}43'29.4''$E), Mizoram, India [113]. The mobile base station was erected in 2006 and the study was carried in the year of 2012. The survey was conducted to study 12 different types of health hazards and problems on 38 persons (21 female and 17 male) of 15 different houses living within 50 m close to the base station. Health hazards faced by the inhabitants obtained from the survey were analysed and compared based on sex as shown in the Table 2.8. From the Table 2.8, it is found that the females have more complaints than the males and the complaints with more frequencies are fatigue, dizziness and muscle pain. It has been found that the measured power density varies

with distance from the tower and all the measured values are well below the current ICNIRP and Indian Standard.

Table 2.8: Analysis of health symptoms of inhabitants living near the base station (within 50 m)

Symptom	Occurrence (%)							
	Never		Sometimes		Often		Very often	
	Male	Female	Male	Female	Male	Female	Male	Female
Fatigue	41	33	47	29	6	29	6	9
Nausea	67	57	22	19	5	14	6	10
Sleep disruption	65	48	35	19	0	28	0	5
Feeling of discomfort	63	33	16	43	10	14	10	11
Headache	60	28	10	38	15	29	11	5
Difficulty in concentration	35	38	35	43	15	9	15	10
Memory loss	33	34	33	38	17	14	17	14
Skin problem	47	33	29	43	12	14	12	10
Visual disruption	45	52	33	24	11	19	11	5
Hearing problem	63	67	16	14	10	19	11	0
Dizziness	32	29	47	29	10	29	11	13
Muscle pain	38	35	35	14	15	29	12	22

2.3 Effects of Non-ionizing EM radiation on other Animals, Plants and Environment

Like the human body, EM field radiating from mobile BSA or other microwave and wireless communication devices has the adverse effect upon the other lives such as vegetal organisms, crops, plants, butterflies, bees, insects, rats, sparrows etc. But it is embarrassing

fact to state that less literature is dedicated to the impact of high frequency EM waves upon vegetation because, people is interested first of all in the risks of human professional exposure to radiofrequency waves and microwaves as well as in the assessing of the EM pollution health risks [114]. However, there are some experimental investigations on living bodies exposed to non-thermal microwaves and radiofrequency waves that focused on plants during early ontogenetic stages when the sensitivity to external constraints is higher - as in any other young organisms. The non-thermal effect of microwaves on the germination was reported on the basis of experiments with cabbage seeds which exhibited delayed germination in contrast with the expectation of stimulated germination - related to the well known thermal effect of microwaves [115]. EM waves radiating from cell towers can also affect vegetables, crops and plants in its vicinity [116]. Studies show definitive clues that cell phone/tower radiation can choke seeds, inhibit germination and root growth, thereby affecting the overall growth of agricultural crops and plants. Trees located inside the main lobe or beam, have much lower fruit yield, have dried tops, show slow growth and high susceptibility to illnesses and plagues [117],[118]. Also, EM radiation generates heat, which may kill micro-organisms present in the soil near it. This in turn harms those organisms which feed on them and disturbs the ecological cycle. EM radiation emanating from cell towers slows down the growth rate of the green plants.

It has been reported that the farm animals like dairy cows, sheep, dogs, cats, rabbits living near base stations are affected by the RF radiation emitted from the BSAs [102]. EM radiation emitted from cell phone and cell phone tower has adverse effect on birds, animals and bees. Birds having nest near towers were found to leave their nests within one week. The eggs laid in nests near towers failed to hatch.

2.4 Use of Non-ionizing EM radiation for human beings and environment

Apart from the hazardous effect of EM waves at RF range onto the living creature, they can also be utilized in many applications which are helpful for human being. Typical applications of EM waves at microwave frequencies are given below.

2.4.1 Microwave Sterilization

Water, food and air act as carrying agents of bacteria. Almost 99% bacteria are helpful and defined as helpful bacteria. Disease is caused by only a few types of bacteria which are defined as harmful bacteria. There are two main methods of controlling microbes one is to kill them and the other is to inactivate (stop them growing) the microbes. Both methods have their advantages and disadvantages. Killing or inactivating microbes using heat, radiation, chemicals and ultra-sound is effective and well known methods to keep them in control [119]-[121]. Using different killing methods, such as by heat, radiation, poisonous gases, chemicals, or ultra-sound, microbes can be killed. There are two important parameters which should be taken in account for every method in killing the microbes. They are time and intensity. Time is the duration of application or exposure and the intensity is the level of killing agent used (e.g. temperature, concentration of chemical, intensity of radiation etc.). In every case the exposure time is inversely related to the intensity.

Killing bacteria using a temperature less than 100^{o}C is called *Pasteurization*. Whereas, killing bacteria using a temperature over 100^{o}C is called *Sterilization*. Pasteurization is used for killing bacteria in foods and health drinks like egg, milk, fruit juice etc [122]. Sterilization is used for instruments, surgical gloves and other items that come in direct contact with the blood stream or normally sterile tissues [123]. Sterilization can be achieved by using high-pressure steam, dry heat, chemical sterilants or radiation. Three common forms of radiation used in sterilization are UV light, atomic and microwaves radiation. UV light causes mutation and leads to faulty protein synthesis. With sufficient mutation, bacterial metabolism is blocked and the organism dies. UV light shows poor penetrating capability and only micro organisms on the directly exposed surface are susceptible to destruction. UV light is ionizing in nature and can damage the eyes, cause burn and mutation in the cells of the skin. The costlier atomic radiation has much more energy and penetrating power than UV radiation and enables to ionize water and other molecules to form radicals and often used to sterilize pharmaceuticals and disposable medical supplies such as syringes, surgical gloves, catheters, sutures, and Petri plates. On the other hand, sterilization using microwave radiation is less costly and the non-ionizing microwave radiation has less penetrating power than UV radiation. Very common example of sterilization using microwave radiation is the microwave ovens. In a microwave oven using either 900 MHz or 2.4 GHz high power EM energy is very common and they are also used to disinfect medical instruments and accessories using RF heating [124].

Investigation has been carried out to find the specific EM effects of microwave radiation on Escherichia coli bacteria at a frequency of 18 GHz and at a temperature below 40°C to avoid the thermal degradation of bacterial cells during exposure [125]. The absorbed power by Escherichia coli was calculated to be 1,500 kW/m^3, and the *E* field was determined to be 300 V/m. Both values were theoretically confirmed using CST Microwave Studio® software.

2.4.2 Radiofrequency Ablation

Thermal ablation is an invasive medical treatment which is used to destroy or ablate the abnormal malfunctioning organs, tissues or tumors particularly for the cases where surgical resection is too complex or even impossible [126]-[128]. Thermal ablation is also used for pain control at different joints and muscles by heat up a small area of nerve tissue and decreasing pain signals from that specific area [129]. Thermal ablation can be done by using Laser beam, microwave and High Focused Ultrasound (HIFU). Thermal ablation performed by non-ionizing EM waves at RF defined as Radiofrequency Ablation (RFA). Sometimes a balloon filled with saline solution is heated electrically to destroy abnormal body parts, which is also known as thermal balloon ablation. The treated area heals by scarring, which usually reduces or prevents the scope of bleeding [130].

RFA is a minimally invasive treatment option of thermal ablation, which implements localized treatment to kill tumor cells with heat generated from RF alternating current while preserving the healthy surrounding tissue. The main tumoricidal effect of RFA occurs because the absorption of EM energy induces thermal injury to the tissue. But RF energy and the heat it generates does not alter the basic chemical structure of cells. With the use of Ultrasound (US) imaging guidance, interventional radiologists perform RFA for direct local destruction of cancerous tumor cells [131]. Due to the localized nature of this treatment, RFA does not have any systemic side effects. RFA can be performed without affecting the patient's overall health and most patients can resume normal daily activity within a few days. The main advantage of RF low frequency current is that, it does not interfere with bioelectric signals. Documented benefits have led to RFA becoming widely used during the last few years [132]-[134].

To realize RFA, a closed-loop circuit is created by placing a RF generator, a large dispersive electrode (ground pad), a patient and a needle electrode in series [133]. The needle electrode is inserted into the site of the tumor with the help of real-time US image guidance.

Both the dispersive electrode and needle electrode are active, while the patient acts as a resister. An alternating *E* field is created within the patient's body. The pattern of the *E* field is governed essentially by electrostatic equations. Electrical resistance of the tissue is greater than that of the metal electrodes which causes agitation of the ions present in the tumor tissue surrounding the electrode. This ionic agitation creates friction within the body and produces heat, which can be tightly controlled through modulation of the amount of RF energy deposited with in the tumor tissue. The use of multiple large grounding pads oriented to ensure maximal surface area facing the electrode maximizes dispersion of equal amounts of energy and heat at the grounding pad sites and thereby minimizes the risk of grounding pad burns [135].

The nature of the thermal damage caused by RF heating in RFA depends on both the tissue temperature achieved and the duration of heating. To accomplish RF tumor ablation, one or more new commercial and experimental RFA probes made of 14 to 21 gauge needle-like electrodes are used [136]. In a multiple electrode systems, more than one single-shaft RF electrodes are combined together. Five basic electrode designs are plain, cooled, expandable, wet and bipolar electrodes. Combination designs included cooled–wet, expandable–wet, bipolar–wet, bipolar–cooled, bipolar–expandable and bipolar–cooled–wet electrodes [137].

To reduce accidental destruction of healthy tissues, planning of RFA using EM simulation is an indispensable tool [127],[138]. Results obtained from the simulations provide information about a suitable probe position, power setup and ablation time.

2.5 Conclusions

A brief literature survey has been presented in this chapter on the interaction of the non-ionizing EM radiation with human being, other animals and environment. The mechanisms of the EM interaction with biological matter has been characterised in terms of two main categories: thermal effects and non-thermal effects. For analysis purpose, each category is again subdivided into two: theoretical and experimental.

An overview related to the applications of EM waves at microwave frequencies in the field of microwave sterilization and RF ablation has also been presented in this chapter.

References

[1] P.P. Pathak, V. Kumar and R.P. Vats, "Harmful electromagnetic environment near transmission tower," *Indian J Radio Space Physics*, vol. 32, pp. 238-241, 2003.

[2] Federal Communication Commission (FCC), Evaluating compliance with FCC guidelines for human exposure to radiofrequency electromagnetic fields", Bulletin 65, Supplement C, 1997. Home Page. http://www.fcc.gov.

[3] Safety levels with respect to human exposure to radio – frequency electro – magnetic fields, 3 KHz to 300 GHz, ANSI Standard C 95.1 – 1992.

[4] ICNIRP, "Guidelines for limiting exposure to time-varying electric, magnetic, and electromagnetic fields (up to 300 GHz)," *Health Phys*., vol. 74, no. 4, pp. 494–522, 1998.

[5] L.J. Challis, "Mechanisms for interaction between RF fields and biological tissue," *Bioelectromagnetics*, vol. 26, No. S7, pp. S98–S106, 2005.

[6] K.S. Nageswari, "Biological Effects of Microwaves and Mobile Telephony," Proceedings of the International Conference on Non-Ionizing Radiation at UNITEN (*ICNIR 2003*) Electromagnetic Fields and Our Health, 20-22nd October, 2003.

[7] K.S. Nageswari, "A Review on immunological Effects of Microwave Radiation," *IETE Technical Review* (India), vol. 5, pp. 203-210, 1988.

[8] M.A. Stuchly, "Health Effects of Exposure to Electromagnetic Fields," *Aerospace Applications Conference*, IEEE, pp. 351-368, February 4-11, 1995.

[9] K.S. Nageswari, "Biological Effects of Microwaves–A Review," *Ann Natl Acad Med Sci* (India), vol. 26, No. 1&2, pp. 1-16, 1990.

[10] W.R. Hendee and J.C. Boteler, "The Question of Health Effects From Exposure to Electromagnetic Fields," *Health Physics*, vol. 66, pp. 127-136, 1994.

[11] O.P. Gandhi, Q.X. Li and G. Kang, "Temperature rise for the human head for cellular telephones and for peak SARs prescribed in safety guidelines," *IEEE Trans. Microwave Theory Tech.*, vol. 49, No. 9, pp. 1607-1613, 2001.

[12] P. Bernardi, M. Cavagnaro, S. Pisa and E. Piuzzi, "SAR distribution and temperature increase in an anatomical model of the human eye exposed to the field radiated by the user antenna in a wireless LAN," *IEEE Trans. Microwave Theory Tech.*, vol. 46, No. 12, pp 2074 – 2082, 1998.

[13] P. Bernardi, M. Cavagnaro, S. Pisa and E. Piuzzi, "Specific Absorption Rate and Temperature increases in the head of a cellular phone user," *IEEE Trans. Microwave Theory Tech.*, vol. 48, No. 7, pp. 1118-1126, 2000.

[14] A. Hirata, M. Morita and T. Shiozawa, "Temperature increase in the human head due to a dipole antenna at microwave frequencies," *IEEE Trans. EMC*, vol. 45, No. 1, pp. 109-116, 2003.

[15] K.D. Kido, T.W. Morris, J.L. Erickson, D.B. Plewes and J.H. Simon, "Physiologic changes during high field strength MR imaging," *American Journal of Neuroradiology*, vol. 8, pp. 263–266, 1987.

[16] K.S. Yee, "Numerical solution of initial boundary value problems involving Maxwell's equations of isotropic media", *IEEE Trans. Antenna Propagation*, vol. APT- 14, pp.302-307, 1966.

[17] F.G. Shellock, D.J. Schaefer and J.V. Crues, "Alterations in body and skin temperatures caused by magnetic resonance imaging: is the recommended exposure for radiofrequency radiation too conservative?" *Br. J. Radiology*, vol. 62, pp. 904-912, 1989.

[18] H.H. Pennes, "Analysis of tissue and arterial blood temperatures in the resting human forearm," *J. Applied Physiology*, vol. 1, No. 2, pp. 93–122, 1948.

[19] H. Shabani, M.R. Islam, AHM Z. Alam and H.E. Abd EI-Raouf, "EM Radiation from Wi-LAN Base Station and Its' Effects in Human Body," 5th International Conference on Electrical and Computer Engineering, Dhaka, Bangladesh, pp. 86-91, 2008.

[20] S.G. Allen, "Radiofrequency field measurements and hazard assessment," *Journal of Radiological Protection*, vol. 11, pp. 49-62, 1996.

[21] Specific Absorption Rate (SAR) Estimation for Cellular Phone, Association of Radio Industries and businesses, ARIB STD-T56, 2002.

[22] H.N. Kritikos and H.P. Schwan, "Formation of hot spots in multilayer spheres," *IEEE Trans. Biomedical Engineering*, vol. 23, pp. 168–172, 1976.

[23] R.J. Spiegel, D.M. Deffenbaugh and J.E. Mann, "A thermal model of the human body exposed to an electromagnetic field," *Bioelectrormagnetics*, vol. 1, No. 3, pp. 253–270, 1980.

[24] R.J. Spiegel, "The thermal response of a human in the near-zone of a resonant thin-wire antenna," *IEEE Trans. Microwave Theory Tech*., vol. 30, pp. 177-185, 1982.

[25] M.F. Iskander and O. Khoshdel-Milani, "Numerical calculations of the temperature distribution in realistic cross sections of the human body," *International Journal of Rad. Oncol. Biol. Physics*, vol. 10, No. 10, pp. 1907-1912, 1984.

[26] D.M. Sullivan, O.P. Gandhi and A. Taflove, "Use of the finite-difference time-domain method in calculating EM absorption in man models", *IEEE Trans. Biomed. Engg.* vol. BME-35. pp. 179-185, 1988.

[27] J.Y. Chen and O.P. Gandhi, "Currents induced in an anatomically based model of a human for exposure to vertically polarized electromagnetic pulses", *IEEE Trans. Microwave Theory Tech.,* vol. 39, pp. 31-39, January, 1991.

[28] Dimboylow and P.J. Mann, "SAR calculation in an anatomically Realistic human head model at 3 GHz", *Physics.Med.* vol. Biol. 39, pp. 1537-1553, 1994.

[29] H.Y. Chen and H.H. Wang,"Current and SAR induced in a human head model by the electromagnetic fields irradiated from a cellular phone", *IEEE Trans. Microwave Theory Tech.*, vol. MTT – 42, No.12, pp. 2249-2254, December, 1994.

[30] H.R. Chuang, "Human operator coupling effects on radiation characteristics of a portable communication dipole antenna", *IEEE Trans. Antenna Propagation*, vol. APT-42**,** NO. 4, April.1994.

[31] O.P. Gandhi, G. Lazzi, and C.M. Furse, "Electromagnetic absorption in the human head and neck for mobile telephones at 835 and 1900MHz", *IEEE Trans. Microwave Theory Tech.,* vol. MTT-44, pp. 1884-1897, 1996.

[32] C.H. Durney, H. Massoudi and M.F. Iskander, "Radiofrequency Radiation Dosimetry Handbook", 4th ed.,USAF SAM-TR-85-73,USAF School of Aerospace Medicine, Aerospace Med. Div. (AFSC), Brooks Air Force Base, TX, 78235-5301, October 1986.

[33] M.A. Stuchly and S.S. Stuchly, "Dielectric properties of biological substances-Tabulated", *J Microwave Power*, vol. 15, pp. 19-26, 1980.

[34] M. Okoniewski and M.A. Stuchly, "A Study of the Handset Antenna and Human Body Interaction," *IEEE Trans. Microwave Theory Tech.*, vol. 44, no. 10, pp. 1855-1864, October, 1996.

[35] Research Program on "Biological effects of electromagnetics fields", University of Kuopio, Finnish Institute of Occupational Health, VTT Technical Research Centre of Finland, 1997.

[36] J.T. Rowley, R.B. Waterhouse and K.H. Joyner, "FDTD handset antenna modeling at 1800 MHz for electrical performance and SAR results", *2nd International conference on Bio-electromagnetism*, February.1998. Telstra Research Laboratories, PO Box 249, Clayton, VIC 3.168, Australia.

[37] J. Wang and O. Fujiwara, "FDTD computation of temperature rise in the human head for portable telephones," *IEEE Trans. Microwave Theory Tech*., vol. 47, pp. 1528-1534, 1999.

[38] J.A. Schiavoni, P. Bertotto, G. Richiardi and P. Bielli, "SAR generated by commercial cellular phones – phone modeling, head modeling and measurements", *IEEE Trans. Microwave Theory Tech.,* vol.MTT- 48, pp. 2064-2071, November, 2000.

[39] William D. Hurt, John M. Ziriax and Patrick A. Mason, "Variability in EMF Permittivity values implications for SAR calculations", *IEEE Trans. Biomed. Engg.* vol. BME-47. pp. 396-401, 2000.

[40] A. Hirata, T.W. Dawson and M.A. Stuchly, "Dosimetry in models of child and adult for low-frequency electric field", *IEEE Trans. Biomed. Engg.* vol. BME-48. pp. 1007-1012, 2001.

[41] T.V. Yioultsis, T.I. Kosmanis, E.P. Kosmidou, T.T. Zygiridis, N.V.Kantartzis, T.D.Xenos, and T.D.Tsiboukis, "A comparative study of the biological effects of various mobile phone and wireless LAN antennas," *IEEE Trans. on Magnetics*, vol. 38, No. 2, pp. 777-780, 2002.

[42] A. Hirata and T. Shiozawa, "Correlation of Maximum Temperature Increase and Peak SAR in the Human Head Due to Handset Antennas," *IEEE Trans. Microwave Theory Tech*., vol. 51, No. 7, pp. 1834-1841, 2003.

[43] C.M. Collins, W. Liu, J. Wang, R. Gruetter, J.T. Vaughan, K. Ugurbil and M.B. Smith, "Temperature and SAR calculations for a human head within volume and surface coils at 64 and 300 MHz," *Journal of Magnetic Resonance Imaging*, vol. 19, pp. 650-656, 2004.

[44] K. Gosalia, J. Weiland, M. Humayun and G. Lazzi, "Thermal elevation in the human eye and head due to the operation of a retinal prosthesis," *IEEE Trans. on Biomedical Engineering*, vol. 51, No. 8, pp. 1469-1477, 2004.

[45] J. Keshvari and S. Lang, "Comparision of radio frequency energy absorption in ear and eye region of children and adults at 900, 1800 and 2450 MHz", *Physics. Med.*Biol., vol. 50, pp. 4355-4369, 2005.

[46] A. Ibrahiem, C. Dale, W. Tabbara and J. Wiart, "Analysis of the temperature increase linked to the power induced by RF source," *Progress In Electromagnetics Research, PIER*, vol. 52, pp. 23–46, 2005.

[47] S. Piperno, M. Remaki and L. Fezoui, "A non-diffusive finite volume scheme for the 3D Maxwell equations on unstructured meshes," SIAM *J. Numerical Analysis*, vol. 39, No. 6, pp. 2089–2108, 2002.

[48] D.G. Choi, C.S. Shin, N.K. Kim and H.S. Shin, "Design and SAR analysis of broadband PIFA with triple band", *Progress In Electromagnetics Research symposium* 2005, Hangzhur, China, August.22 – 26.

[49] M. Fujimoto, A. Hirata, J. Wang, O. Fujiwara and T. Shiozawa, "FDTD-derived correlation of maximum temperature increase and peak SAR in child and adult head models due to dipole antenna," *IEEE Transactions on Electromagnetic Compatibility*, vol. 48, No. 1, pp. 240-247, 2006.

[50] G. Scarella et al., "Realistic numerical modelling of human head tissue exposure to electromagnetic waves from cellular phones," *C.R.Physique*, *ELSEVIER*, vol. 7, pp. 501–508, 2006.

[51] S. Khalatbari, D. Sardari, A.A. Mirzare and H.A. Sadafi, "Calculating SAR in two models of the human head exposed to mobile phones radiations at 900 and 1800 MHz", *Progress In Electromagnetics Research symposium*, Cambridge, USA, March, 26-29, 2006.

[52] A.D. Tinniswood and O.P. Gandhi, "Computations of SAR distributions for two anatomically based models of human head using CAD files of commercial telephones and parallelized FDTD code", *IEEE Trans. Antenna Propagation*, vol. APT- 46, pp. 829-833, 1998.

[53] J. Wang, O. Fujiwara, S. Kodera and S. Watanabe, "FDTD calculation of whole-body average SAR in adult and child models for frequencies from 30 MHz to 3 GHz", *Phys. Med.Biol*., vol. 51**,** pp. 4119-4127, 2006.

[54] J.N. Hwang and F.C. Chen, "Reduction of the peak SAR in the human head with metamaterials", *IEEE Trans. Antenna Propagation*, vol. APT-42**,** no. 12, pp. 3763-3770, December, 2006.

[55] C.M. Kuo and C. W.Kuo, "SAR distribution and temperature increase in the human head for mobile communication", *APS Int. Symp. Dig.*, IEEE, Columbus, pp. 1025-1028, 2003.

[56] C.M. Kuo and C.W. Kuo, "SAR distribution and temperature increase in the human head for mobile communication", *APS Int. Symp. Dig.*, IEEE, Columbus, pp. 1025-1028, 2003.

[57] A.O. Rodrigues, J.J. Viana, L.O.C. Rodrigues and J.A. Ramirez, "Calculation of temperature rise induced by cellular phones in the human head," *Journal of Microwaves and Optoelectronics*, vol. 6, No. 1, pp. 310-322, 2007.

[58] A. Razmadze, L. Shoshiashvili, D. Kakulia and R. Zaridze, "Influence on averaging masses on correlation between mass-averaged SAR and temperature rise," *Journal of Applied Electromagnetism*, vol. 10, No. 2, pp. 8-21, 2008.

[59] A. Bijamov, A. Razmadze, L. Shoshiashvili, K. Tavzarashvili, R. Zaridze, G. Bit-Babik and A. Faraone, "Advanced electro-thermal analysis for the assessment of human exposure in the near-field of EM sources," ICEAA'03 *International Conference on Electromagnetics in Advanced Applications*, Torino, Italy, September 8-12, 2003.

[60] R.S. Zaridze, N. Gritsenko, G. Kajaia, E. Nikolaeva, A. Razmadze, L. Shoshiashvili, A. Bijamov, G. Bit-Babik and A. Faraone, "Electro-Thermal computational suit for investigation of RF power absorption and associated temperature change in human body," IEEE AP-S *International Symposium* and USNC/URSI *National Radio Science Meeting*, Washington DC, USA. pp. 175, July 3-8, 2005.

[61] A. Hirata, H. Sugiyama and O. Fujiwara, "A formula for simply estimating body core temperature rise in humans due to microwave exposures," *International Symposium on Electromagnetic Compatibility*, Japan, pp. 381-384, July 20-24, 2009.

[62] I. Laakso, "Assessment of the computational uncertainty of temperature rise and SAR in the eyes and brain under far-field exposure from 1 to 10 GHz," *Physics in Medicine and Biology*, vol. 54, pp. 3393–3404, 2009.

[63] Salah I. Al-Mously, "Computation of the temperature-rise in the human head due to different mobile phone models," *Microwave Symposium* (MMS), Guzelyurt, pp. 370-373, August 25-27, 2010.

[64] A.I. Sabbah and N.I. Dib, "SAR and temperature elevation in a multi-layered human head model due to an obliquely incident plane wave," *Progress in Electromagnetics Research M*, vol. 13, pp. 95-108, 2010.

[65] G. Carluccio, S. Oh and C.M. Collins, "Ultra-fast calculation of SAR-induced temperature increase," *Proc. Intl. Soc. Mag. Reson. Med*., vol. 19, pp. 3844, 2011.

[66] J.F. Bakker, M.M. Paulides, E. Neufeld, A. Christ, N. Kuster and G.C. Van Rhoon, "Children and adults exposed to electromagnetic fields at the ICNIRP reference levels: theoretical assessment of the induced peak temperature increase," *Physics in Medicine and Biology*, vol. 56, pp. 4967–4989, 2011.

[67] M.R.I. Faruque, N. Misran, R. Nordin, M.T. Islam and B. Yatim, "Estimation of specific absorption rate and temperature increases in the human head due to portable telephones," *Scientific Research and Essays*, vol. 6, No. 6, pp. 1209-1215, 2011.

[68] T. Wessapan, S. Srisawatdhisukul and P. Rattanadecho, "Specific absorption rate and temperature distributions in human head subjected to mobile phone radiation at different frequencies," *International Journal of Heat and Mass Transfer*, vol. 55, pp. 347–359, 2012.

[69] S.H. Saeid, "Study of the Cell Towers Radiation Levels in Residential Areas," *International Conference on Electronics and Communication Systems*, 2013.

[70] S. Sivani and D. Sudarsanam, "Impacts of radio-frequency electromagnetic field (RF-EMF) from cell phone towers and wireless devices on biosystem and ecosystem – a review", *Biology and Medicine,* vol. 4, no. 4, pp. 202–216, 2012.

[71] O. Genc, M. Bayrak, and E. Yaldiz, "Analysis of the Effects of GSM Bands to the Electromagnetic Pollution in the RF Spectrum," *Progress In Electromagnetics Research*, *PIER*, vol. 101, pp. 17-32, 2010.

[72] P. Bernardi, M. Cavagnaro, S. Pisa and E. Piuzzi, "Human Exposure to Radio Base-Station Antennas in Urban Environment," *IEEE Trans. on Microwave Theory and Techniques*, vol. 48, No. 11, pp. 1996-2002, November, 2000.

[73] G. Lazzy and O.P. Gandhi, "A Mixed FDTD-Integral Equation Approach for On-Site Safety Assessment in Complex Electromagnetic Environment," *IEEE Trans. Antenna Propagation*, vol. 48, pp.1830-1836, December 2000.

[74] *Human Exposure to Electromagnetic Fields*. High Frequency (10 kHz to 300 GHz), European Communities Prestandard ENV 50 166-2, January, 1995.

[75] Hombach, K. Meier, M. Burkhardt, E. Kuhn, and N. Kuster, "The Dependence of EM Energy Absorption upon Human Head Modeling at 900 MHz," *IEEE Trans. Microwave Theory Tech.*, vol. MTT-44, No. 10, pp. 1865-1873, 1996.

[76] S. Watanabe, M. Taki, T. Nojima, and O. Fujiwara, "Characteristics of the SAR Distributions in a Head Exposed to Electromagnetic Fields Radiated By a Hand-Held Portable Radio," *IEEE Trans. Microwave Theory Tech.*, vol. MTT-44, No. 10, pp. 1874-1883, 1996.

[77] K. Meier, V. Hombach, R. Kastle, R.Y.S. Tay, and N. Kuster, "The Dependence of EM Energy Absorption upon Human Head Modeling at 1800 MHz," *IEEE Trans. Microwave Theory Tech.*, vol. MTT-45, No. 11, pp. 2058-2062, 1997.

[78] G.M.J. Van Leeuwen, J.J.W. Lagendijk, B.J.A.M. Van Leersum, A.P.M. Zwamborn, S.N.Hornsleth and A.N.T.J.Kotte, "Calculation of change in brain temperatures due to exposure to a mobile phone," *Physics Medicine and Biology*, vol. 44, pp. 2367–2379, 1999.

[79] T. Nojima, Y. Tarusawa, and Y. Suzuki, "An Easy Handing SAR Meter for Cellular and Personal Portable Radios," *XXVIth General Assembly of the International Union of Radio Science Abstracts*, vol. KA-4, pp. 846, 1999.

[80] J. Wang and O. Fujiwara, "Head Tissue Heterogeneity Required in Computational Dosimetry for Portable Telephones," *IEICE Trans. Commun.*, vol. E84-B, pp. 100-105, 2001.

[81] A. Kangarlu, F.G. Shellock and D.W. Chakeres, "8.0-Tesla human MR System: Temperature changes associated with radiofrequency-induced heating of a head phantom," *Journal of Magnetic Resonance Imaging*, vol. 17, pp. 220–226, 2003.

[82] A. Christ, N. Chavannes, N. Nikoloski, H.U. Gerber, K. Pokovic and N. Kuster, "A numerical and experimental comparison of human head phantoms for compliance testing of mobile telephone equipment," *Bioelectromagnetics*, vol. 26, pp. 125-137, 2005.

[83] S.Y. Huang, S.Y. Chen and J.S. Sun, "Measurement of RF radiation energy deposited on human head," *ISCOM*, 2005.

[84] R.H.T.C. Filho, R.M.S. Oliveira, C.L.S.S. Sobrinho and A.M. Almeida, "Parallel-FDTD and experimental results of SAR for flat and head phantoms @ 900 MHz," *SBMO/IEEE MTT-S International Microwave and Optoelectronics Conference* (*IMOC*-2009), pp. 373-378, 2009.

[85] Y. Kawamura, T. Hikage and T. Nojima, "Experimental whole-body average SAR estimation system using cylindrical field scanning method," *IEICE*, pp. 257-260, 2009.

[86] A. Ikram, "Design and development of a multiband loop antenna for cellular mobile handsets," [Master's thesis], Department of technology and Built Environment, University of Gavel, June 2010.

[87] M.A. Bhat and V. Kumar, "Calculation of SAR and measurement of temperature change of human head due to the mobile phone waves at frequencies 900 MHz and 1800 MHz," *Advances in Physics Theories and Applications*, IISTE, vol. 16, pp. 54-63, 2013.

[88] M.I. Khattak, J. Ma, M. Shafi and M. Saleem, "A Study of SAR in Human Head Due to Radiofrequency Radiation from Personal Data Assistant Device with Hands-Free Kits," *Research Journal of Recent Sciences*, vol. 4, No. 1, pp. 51-54, 2015.

[89] "Evaluating compliance with FCC guidelines for human exposure to radiofrequency electromagnetic fields," Federal Commun. Commission, Washington, DC, OET Bulletin 65, August-1997.

[90] C.F. Blackman et al , "Effects of ELF fields on calcium-ion efflux from brain tissue in vitro," *Radiation Research*, vol. 92, pp. 510-520, 1982.

[91] Chiang et al, "Health effects of environmental electromagnetic fields", *Journal of Bioelectricity*. 8(1), 127-131 (1989). EPI2064.

[92] A. Firstenberg, "Microwaving Our Planet: The Enviromental Impact of the Wireless Revolution: Cellular Phone," *Taskforce Press*, 1997.

[93] Ridley and Kirstin, "British Scientists Demand Cell Phone Warnings", *Reuters,* January. 1, 1998. EPI1788.

[94] Sajal Kr Palit, " Biological Effects of Electromagnetic Waves- an Overview", *2nd International conference on Bio-electromagnetism,* February.1998 Department of Electrical and Computer Systems Engineering Monash University, P.O.Box: 197, Caulfield East, Vic-3.145, Australia.

[95] Harris, Sarah, "Now Mobiles Give You Kidney Damage", *Daily Mail,* December. 13, 1999. EPI1812.

[96] 20/20 ABC TV. "Worried About Your Wireless?" October.20, 1999. *Unedited transcript*. EPI1828.

[97] N.S. Stoykov, J.W. Jerome, L.C. Pierce and A. Taflove, "Computational modeling evidence of a nonthermal electromagnetic interaction mechanism with living cells: microwave nonlinearity in the cellular sodium ion channel", *IEEE Trans. Microwave Theory Tech.,* vol. MTT-52, pp. 2040-2045, August, 2004.

[98] I. Tandogan, A. Temizhan, E. Yetkin, Y. Guray, M. Ileri and E. Duru, "The effects of mobile phones on pacemaker function," *International Journal of Cardiology*, vol. 103, No. 1, pp. 51-58, 2005.

[99] G. Altamura et al, "Influence of digital and analogue cellular telephones on implanted pacemakers," *European Heart Journal*, vol. 18, No. 10, pp. 1632-4161, 1997

[100] N. Kumar and G. Kumar, "Biological Effects of Cell Tower Radiation on Human Body," *International Symposium on Microwave and Optical Technology* (*ISMOT*), pp. 1365-1368, New Delhi, India, December 16-19, 2009.

[101] H. Lennart et al, "Epidemiological evidence for an association between use of wireless phones and tumor diseases", *Pathophysiology*, PATPHY-595, 2009.

[102] G. Kumar, "Report on Possible Impact of Communication Towers on Wildlife including Birds and Bees," December 2010. [Online] Available: http://www.ee.iitb.ac.in/~mwave/Report%20on%20Possible%20Impacts%20of%20Communication%20Towers.pdf.

[103] Klitzing and L. Von, "Low-Frequency pulsed electromagnetic fields influence EEG of man", *Physica medica,* April 28, 1995. EPI1863.

[104] H.F.D' Costa, G. Trueman, L. Tang, U. Abdel-rahman, W. Abdel-rahman, K. Ong and I. Cosic, "Human brain wave activity during exposure to radiofrequency field emissions from mobile phones," *Australas Phys. Eng. Sci. Med.*, vol. 26, No. 4, pp. 162-167, 2003.

[105] A.V. Kramarenko and U. Tan, "Effects of high-frequency electromagnetic fields on human EEG: a brain mapping study," *International Journal of Neuroscience*, vol. 113, pp. 1007–1019, 2003

[106] C.M. Krause, C. Haarala, L. Sillanmaki, M. Koivisto, K. Alanko, A. Revonsuo, M. Laine and H. Hamalainen, "Effects of electromagnetic field emitted by cellular phones on the EEG during an auditory memory task: a double blind replication study," *Bioelectromagnetics*, vol. 25, No. 1, pp. 33-40, 2004.

[107] R.J. Croft, D.L. Hamblin, J. Spong, A.W. Wood, R.J. McKenzie and C. Stough, "The effect of mobile phone electromagnetic fields on the alpha rhythm of human electroencephalogram," *Bioelectromagnetics*, vol. 29, No. 1, pp. 1-10, 2008.

[108] H.F.D' Costa, "Influence of mobile phone electromagnetic field exposures on nervous function in the human brain and heart," [PhD thesis], School of Electrical & Computer Engineering Portfolio RMIT, December 2008.

[109] G. Singh, "The effects of mobile phone usage on human brain using EEG," *International Journal of Computer Applications*, vol. 105, No. 13, pp. 16-20, 2014.

[110] Health24 February 19, 2008 [Online] Available: http://www.health24.com/Lifestyle/Environmental-health/News/Cell-phones-up-mouth-cancer-risk-20120721.

[111] M. Kaushal, T. Singh and A. Kumar, "Effects of Mobile Tower Radiations & Case Studies from different Countries Pertaining the Issue," *International Journal of Applied Engineering Research*, vol. 7, no.11, 2012. [Online] Available: http://www.ripublication.com/ijaer.htm.

[112] EM Watch, [Online] Available: http://www.emwatch.com/Cellmasts.html.

[113] L. Pachuau, L. Sailo, Z. Pachuau and P.C. Langneia, "RF radiation from mobile phone towers and their effects on human body," *Indian Journal of Radio & Space Physics* (*IJRSP*), vol. 43. No. 2, pp. 186-189, April 2014.

[114] V. Russello, C. Tamburello and A. Scialabba, "Microwave effects on germination and growth of Brassica drepanensis seed," Proceedings of 3rd *International Congress of the European BioElectromagnetics Association*, 89, 1996.

[115] S.K. Guha, S. Neogi and G. Kumar, "Report on: Cell phone towers radiation hazards," October 2011. Available: https://www.ee.iitb.ac.in/~mwave/Cell-tower-rad-report-WB-Environ-Oct 2011.pdf.

[116] G. Soja, B. Kunsch and M. Gerzabek, "Growth and yield of winter wheat (Triticum aestivum L.) and corn (Zea mays L.) near a high voltage transmission line," *Bioelectromagnetics*, vol. 24, pp. 91–102, 2003. Available: http://www.ncbi.nlm.nih.gov/pubmed/125246755.

[117] T. Selga and M. Selga, "Response of Pinus sylvestris L. needles to electromagnetic fields, cytological and ultrastructural aspects," *Sci*. *Total Environ*., vol. 180, pp. 65–73, 1996.

[118] M. Tkalec, K. Malarik, M. Pavlica, B. Pevalek-Kozlina and Z. Vidakovic-Cifrek, "Effects of radiofrequency electromagnetic fields on seed germination and root meristematic cells of Alliumcepa L.," *Mut. Res.*, vol. 672, pp. 76–81, 2009. Available: http://www.ncbi.nlm.nih.gov/pubmed/19028599.

[119] E.J. Morris, "The practical use of Ultraviolet radiation for disinfection purposes," *Med. Lab. Technology*, vol. 29, no. 1, pp. 41–47, 1972.

[120] R.L. Riley and E.A.Nardell, "Clearing the air, the theory and application of Ultraviolet air disinfection," *Am. Rev. Respir. Dis*., vol. 139, no. 5, pp. 1286–1294, 1989.

[121] D.K.H. Jeng, K.A. Kaczmarek, A.G. Woodworth and G. Balasky, "Mechanism of Microwave Sterilization in the Dry State," vol. 53, no. 9, pp. 2133-2137, *Applied and Environmental Microbiology*, September, 1987.

[122] B. Brazier, Lecture 13: Control of Microbes. [Online] Available: http://barry-b.tripod.com/micro113.html.

[123] M. Fishman, "Handling of surgical instruments in a presymptomatic familial carrier of Creutzfeldt-Jakob disease," *Am. J. Infect. Control*., vol. 30, no. 5, pp. 303-306, 2002.

[124] D. Arndt, "Microwave radiation: therapeutic application for cure of subcutaneous bacterial infections. Space Life Sciences," *NASA Biennial Research and Technology Report*, National Aeronautics and Space Administration, Houston, TX, 2005.

[125] Y. Shamis, A. Taube, N. Mitik-Dineva, R. Croft, R.J. Crawford and E.P. Ivanova, "Specific Electromagnetic Effects of Microwave Radiation on Escherichia coli," *Applied and Environmental Microbiology*, vol. 77, no. 9, pp. 3017–3023, May, 2011.

[126] S.E. Singleton, "Radiofrequency ablation of breast cancer", *American Journal of Surgery*, vol. 69, pp. 37-40, 2003.

[127] T. Kroger, I. Altrogge, T. Preusser, P.L. Pereira, D. Schmidt, A. Weihusen and H.O. Peitgen, "Numerical Simulation of Radio Frequency Ablation with State dependent material parameters in three space dimensions," *Springer*, *LNCS*- 4191, pp. 380–388, 2006.

[128] A.H. Peralta and S.N. Goldberg, "Review of Radiofrequency Ablation for Renal Cell Carcinoma," *Clinical Cancer Research*, vol. 10, pp. 6328s–6334s, September 2004.

[129] J. Cheng and S. Abdi, "Complications of joint, tendon, and muscle injections," *National Institute of Health*, Public Access, vol. 11, no. 3, pp. 141–147, July. 2007.

[130] S.A. Bridgman and M. Kate, "Has endometrial ablation replaced hysterectomy for the treatment of dysfunctional uterine bleeding? National figures," *BJOG*: *An International Journal of Obstetrics & Gynaecology*, vol. 107, no. 4, pp. 531–534, April 2000.

[131] A.A. Nemcek, "Complications of Radiofrequency Ablation of Neoplasms," *Seminars in Interventional Radiology*, vol. 23, no. 2, pp. 177-187, 2006.

[132] A. Abdelalim, M.S. Ali and A. Elgammal, "Study of the Efficacy of Combined Radio Frequency Ablation and Percutaneous Acetic Acid Injection in the Management of Hepatocellular Carcinoma," *Journal of American Science*, vol. 9, no. 6, pp. 622-631, 2013.

[133] H. Rhim, S.N. Goldberg, G.D. Dodd, L. Solbiati, H.K. Lim, M. Tonolini and On Koo Cho, "Essential Techniques for Successful Radiofrequency Thermal Ablation of Malignant Hepatic Tumors," *Radio Graphics*, vol. 21 (Special issue), pp. S17–S39, October 2001.

[134] T. Livraghi, "Radiofrequency ablation, PEIT, and TACE for hepatocellular carcinoma," *Journal of Hepatobiliary Pancreat Surgery*, vol. 10, pp. 67–76, 2003.

[135] S.N. Goldberg, L. Solbiati, E.F. Halpern, G.S. Gazelle, "Variables affecting proper system grounding for radiofrequency ablation in an animal model," *Journal Vasc. Interv. Radiology*, vol. 11, pp. 1069–1075, 2000.

[136] V. Quaranta, G. Manenti, F. Bolacchi, E. Cossu, C.A. Pistolese, O.C. Buonomo, L. Carotenuto, C. Piconi and G. Simonetti, "FEM Analysis of RF Breast Ablation: Multiprobe versus Cool-tip Electrode," *Anticancer Research*, vol. 27, pp. 775-784, 2007.

[137] S. Mulier, G. Marchal and Y. Ni, "Electrodes and multiple electrode systems for radiofrequency ablation: a proposal for updated terminology," *Eur. Radiology*, vol. 15, pp. 798–808, 2005.

[138] S. Tungjitkusolum, S.T. Staelin and D. Haemmerich, "Three-dimensional finite element analyses for radio-frequency hepatic tumor ablation," *IEEE Trans. Biomed. Eng.*, vol. 49, pp. 3-9, 2002.

Chapter 3

Development of Numerical analysis tools for study on interaction of Non-Ionizing EM radiation with Human Being and Environment

3.1 Introduction

With the advancement of scientific knowledge and engineering practice, computational techniques based on numerical analysis are now regarded as an almost equal and requisite partner to theory and experiment. These techniques allow the study of complex systems and natural phenomena that would be too expensive in terms of cost or time, dangerous, or even impossible, to study directly by experimentation. Such significant progress has resulted from rapid and powerful advances in computer algorithms and architecture in respect of increases in speed and memory. These techniques enable scientists and engineers to solve, with relative accuracy, large-scale problems which were once thought intractable.

To calculate EM fields including dosimetric parameters, different type of computational and numerical EM methods play significant roles because it is difficult to actually measure these values inside living body or complex structure. This chapter briefly introduces different type of available computational and numerical EM methods which are suitable for study on interaction of non-ionizing EM radiation with biological tissues. Some of these methods are very general in nature and are capable enough to accurately predict effects of EM radiation on biological tissues. Numerical codes for such techniques are sometimes freely available but most of these codes are not suitable enough to incorporate simulation models based on available resources. Thus modifications of methodologies are required to include certain considerations and capabilities. A fully working numerical tool based on FDTD is developed in-house with some modifications to take care of very large simulation model data. This tool has been finally verified in time and frequency domain separately using some commercially

available simulators for some standard simulation models. Step by step development methods, its modifications and test results are also included in this chapter.

3.2 Available methods of analysis

Direct measurement of EM field components and SAR is very difficult inside a living human head or other body parts using the experimental technique. Moreover, in the experimental method, actual phone with the equivalent homogeneous head or other body parts are used for the measurement of the dosimetric parameters, but these homogeneous models are not a faithful representation of the complex heterogeneous human organs because actual electrical properties of different tissues are not considered. Therefore, the numerical techniques are used to calculate EM field components and SAR inside human head or body parts [1]. A large number of numerical methods have been widely used in the time and frequency domains to solve EM problems [2]-[4]. For each one, there are some advantages and also some drawbacks depending on specific applications. A brief overview of some existing and emerging numerical methods is presented in this section with an emphasis on their advantages and drawbacks [5].

Today, most of the popular numerical methods used in electromagnetics are:

a. Finite Element Method (FEM),
b. Method of Moments (MoM),
c. Finite-Difference Time-Domain Method (FDTD),
d. Finite Integration Technique (FIT).

Most of the popular commercial EM field simulation software packages have been developed based on: FEM, MoM, FDTD and FIT methods. At the same time, there is also some software available which applies more than one numerical method, i.e., hybrid method. The SFDTD method is most recently developed where as the hybrid FDTD method is developed by the author and his supervisor themselves. The FEM, MoM, FDTD and FIT are described briefly in the following sections, whereas the SFDTD method and hybrid FDTD method are described in detail.

3.2.1 Finite Element Method (FEM)

In 1943, mathematical treatment of the FEM was first proposed by Courant [6]. Initially the FEM was used for most of the applications of mechanical and civil engineering but not

applied to EM problems until 1968. Since then the method has been employed in such diverse areas as waveguide problems, electric machines, semiconductor devices, microstrips, and absorption of EM radiation by biological bodies [2].

Mathematically, FEM is used for finding an approximate solution of Partial Differential Equations (PDE) as well as of integral equations. Starting point of the FEM method is the subdivision of the total region or domain into a number of non overlapping small sub regions or sub domains called finite elements, which is described by its vertices and one point on each edge. These points are called the nodes. The FEM analysis of any problem involves basically four steps [7]:

a. Discretizing the solution region into a finite number of sub regions or elements,
b. Deriving governing equations for a typical element,
c. Assembling of all elements in the solution region and
d. Solving the system of equations obtained.

Line elements are used as the finite elements in one-dimensional space and polygons are used as the finite elements in the two and three-dimensional spaces. Simplest form of polygons used in two-dimensional space is triangles, squares and quadrilaterals and that is used in three-dimensional space is tetrahedron, pentahedron and hexahedron. Other elements, like rectangular patches, bricks etc., are also used as finite elements. Basic finite elements used in typical one, two and three-dimensional spaces are shown in Figure 3.1 [8].

In order to divide the region, sometimes, combination of different finite elements becomes more useful [9]. Division of a region using combination of triangles and squares is shown in Figure 3.2 (a). But using only triangles an arbitrary region can be fairly divided as shown in Figure 3.2 (b).

The major advantage of FEM is the flexibility of its discretised elements. Other benefit of FEM is that its coefficient matrix generated from the finite element equation system is sparse and symmetric, which is suitable for solution of the algebraic equations system [10].

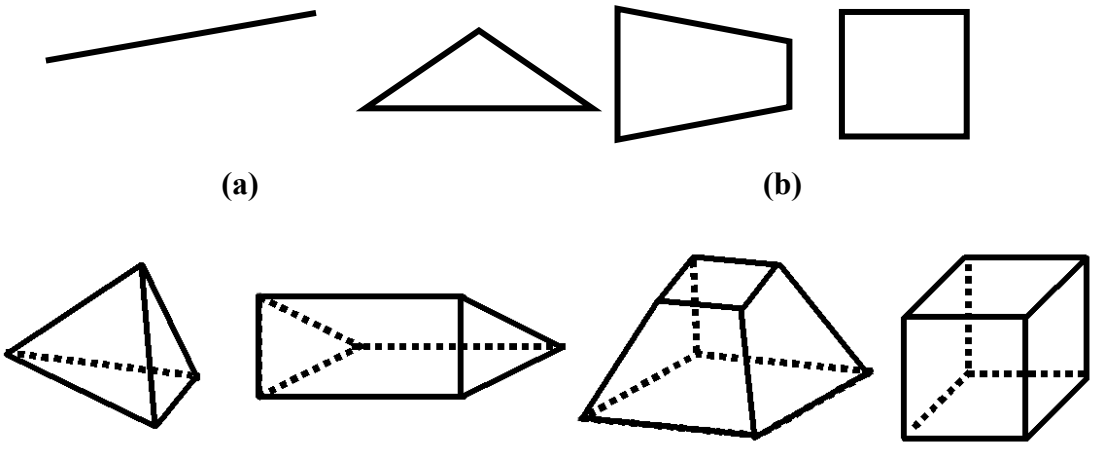

Figure 3.1. Basic Finite Elements: (a) 1D: line element, (b) 2D: triangle, quadrilateral, square and (c) 3D: Tetrahedron, pentahedron, hexahedron and cubical.

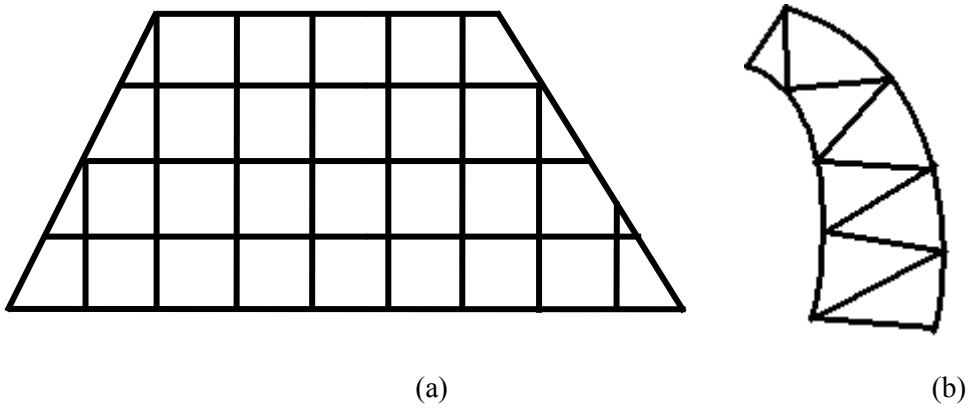

Figure 3.2. (a) Division of a region into triangles and squares and (b Division of an irregular region into triangles.

3.2.2 Method of Moments (MoM)

The MoM or boundary element method (BEM) is one of the efficient full-wave numerical methods used for EM compatibility (EMC) and antenna applications. It is essentially the method taking moments by multiplying with appropriate weighting functions and integrating, which can be used for solving both differential and integral equations. Use of MoM to solve the EM problems has become popular since the work of Richmond in 1965 and Harrington in 1967 [11], [12]. MoM is fairly efficient for the problems with appropriate properties but during the last few years, where computer performance has increased

dramatically, the importance of MoM has decreased while the use of other techniques like FDTD or FEM has increased. Yet, the MoM still provides advantages for certain complex structures, like metal objects and wires.

All moment method solutions are found from the solution of integral equations over boundary conditions [13]. The boundary conditions can be either the tangential *E* field or *H* field components given by the following equations or a combination applied using an integral scalar product:

$$\hat{n} \times \left(E_2 - E_1 \right) = -M_s \tag{3.1}$$

$$\hat{n} \times \left(H_2 - H_1 \right) = J_s \tag{3.2}$$

where, $\hat{n}$ is a unit normal vector which points from region 1 to region 2. M_S is magnetic and J_S is electric current densities exist on the surface where the fields *E* and *H* can be discontinuous at the interface between the two regions 1 and 2.

3.2.3 Finite-Difference Time Domain Method (FDTD)

FDTD is a widely used numerical computational method in the range of a few MHz to several GHz [14]. The main advantages of the FDTD-based techniques for solving EM problems are simplicity and the ability to handle complex geometries. Compare to other computational methods FDTD is more efficient in terms of computer time and memory as there is no matrix to fill and solve [15],[16]. Derivation from Maxwell's equations is based on traditional mathematical methods of approximating derivatives by finite differences and approximating line integrals, surface integrals, and volume integrals by summations [17]. It involves basic arithmetic operations: addition, subtraction, multiplication and division. FDTD can model material through parameter averaging or in case of a more sophisticated approach, choosing grids to conform to the geometries of the material boundaries [18]. An in-house simulation tool is developed based on FDTD for the studies carried out and reported in next chapters in this thesis.

3.2.4 Finite Integration Technique (FIT)

FIT is a method that is closely related to the FDTD method. But in this method, the integral form of Maxwell's equations is solved by one-to-one translation from the integral form of Maxwell's Equations to a discrete space formulation. FIT was first introduced in

1977 by T. Weiland [19]. Like FDTD method, formulation of the FIT algorithm is based on enclosing the computational volume with a numerical region representing the outer boundary condition. The next stage involves decomposition of the computational volume into a finite number of simplified material-filled homogeneous cell volumes defined as voxels. The resulting matrix equations for the EM integral quantities obtained from the FIT maintain the inherent properties of Maxwell's equations with respect to charge and energy conservation.

Conventional FDTD method uses Yee-type Cartesian meshing scheme which introduces inaccuracy to the geometry representation due to a staircase approximation of the curved structure surface. To overcome the difficulty, a fine mesh is usually necessary around critical points leading to an overall fine mesh in the whole structure. Therefore, various meshing techniques, such as variable meshing, non-orthogonal, or sub-girding techniques, have been used to improve the performance of the FIT method. FIT can be used for efficient numerical simulations on modern computers. FIT guarantees an especially favourable stability and convergence behaviour in the execution of numerical simulation. This method provides a universal spatial discretization scheme which is applicable to various EM problems ranging from static field calculations to high frequency applications in time or frequency domain.

Standard Cartesian computational grid does not have to be conformal in case of the round boundaries. So, several techniques have been introduced in FIT method to model more than one material within the same cell, such as the Perfect Boundary Approximation (PBA) and the Thin Sheet Technology (TST) [20],[21]. Like FDTD method, stability is another issue in the time domain simulation of FIT. To maintain the computational stability, in any one iteration the field must not change significantly from one point to another, and a wave must not propagate more than one spatial field point. Therefore, an up limit has been put on the time-step called Courant stability criterion, which is given by equation 3.20 and related to the size of the smallest mesh-cell. CST Microwave Studio® is a general purpose 3-D EM simulator has been developed based on the FIT. As a powerful software package for EM problem simulation, CST Microwave Studio® is used.

3.3 Details of FDTD technique for development of in-house EM simulation tool

The FDTD method starts with Maxwell's time-dependent curl equations:

$$\vec{\nabla} \times \vec{E} = -\mu \frac{\partial \vec{H}}{\partial t} \tag{3.3}$$

$$\vec{\nabla} \times \vec{H} = \sigma \vec{E} + \varepsilon \frac{\partial \vec{E}}{\partial t} \tag{3.4}$$

The parameters σ, μ and ε are conductivity, permeability and permittivity respectively. $\vec{E}$ and $\vec{H}$ are the vectors in three dimensions so the solutions of equations (3.3) and (3.4) produce a set of six scalar equations in the rectangular Cartesian co-ordinate system (x, y, z):

$$\frac{\partial E_x}{\partial t} = \frac{1}{\varepsilon}\left(\frac{\partial H_z}{\partial y} - \frac{\partial H_y}{\partial z} - \sigma E_x \right) \tag{3.5}$$

$$\frac{\partial E_y}{\partial t} = \frac{1}{\varepsilon}\left(\frac{\partial H_x}{\partial z} - \frac{\partial H_z}{\partial x} - \sigma E_y \right) \tag{3.6}$$

$$\frac{\partial E_z}{\partial t} = \frac{1}{\varepsilon}\left(\frac{\partial H_y}{\partial x} - \frac{\partial H_x}{\partial y} - \sigma E_z \right) \tag{3.7}$$

$$\frac{\partial H_x}{\partial t} = \frac{1}{\mu}\left(\frac{\partial E_y}{\partial z} - \frac{\partial E_z}{\partial y} \right) \tag{3.8}$$

$$\frac{\partial H_y}{\partial t} = \frac{1}{\mu}\left(\frac{\partial E_z}{\partial x} - \frac{\partial E_x}{\partial z} \right) \tag{3.9}$$

$$\frac{\partial H_z}{\partial t} = \frac{1}{\mu}\left(\frac{\partial E_x}{\partial y} - \frac{\partial E_y}{\partial x} \right) \tag{3.10}$$

FDTD method uses a leapfrog scheme on staggered Cartesian grids where a component of *E* field is offset spatially and temporally from the *H* field component. Components of *E* and *H* field are implemented for a lattice of sub volumes known as Yee cells that may be cubical or parallelepiped with identical or different dimensions of Δx, Δy, and Δz in the x, y, and z directions, respectively as shown in Figures 3.3 (a-b) [22]. Basis of FDTD method is the orientation of the *E* and *H* fields and is represented by the Yee cell. Conventional FDTD method considers cubic Yee cells with Δx = Δy = Δz as shown in Figure 3.3 (a) and the non-uniform FDTD (NU-FDTD) method consisting of brick shaped modified Yee cells with Δx ≠ Δy ≠ Δz. In both FDTD methods, *E* field components are located on the edges and the *H* field

components are positioned on the faces of the Yee cell as shown in Figures 3.3 (a-b). The details of the method are available in the literature [16],[23].

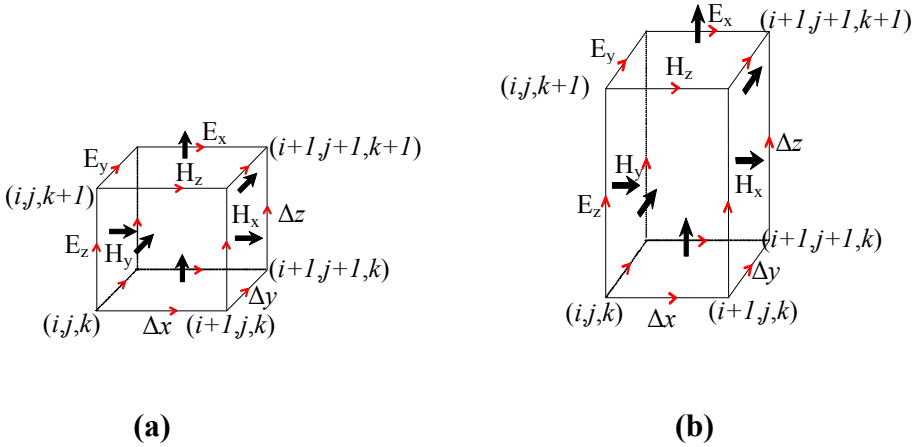

Figure 3.3. (a) Cubic Yee cell [Δx = Δy = Δz] and (b) parallelepiped Yee cell [Δx ≠ Δy ≠ Δz].

3.3.1 Discretization of Maxwell's Equations

In order to implement FDTD code in software, Maxwell's equations in partial differential form (equations 3.5 – 3.10) are modified into the corresponding central finite difference equations of space and time derivatives, discretized and solved according to leapfrog manner to obtain the explicit finite difference approximation are shown in Appendix 3A by equations 3A.1-3A.6 [8],[18],[24].

In NU-FDTD method, the spatial derivatives in x, y and z direction are modified with the following respective modification factors [25]:

$$ra\_x = \frac{\Delta y}{\Delta x} \tag{3.11}$$

$$ra\_y = \frac{\Delta y}{\Delta y} \tag{3.12}$$

$$ra\_z = \frac{\Delta y}{\Delta z} \tag{3.13}$$

where, *ra_x*, *ra_y* and *ra_z* are modification factors in the x, y and z direction assuming Δy as the basic cell size, respectively. Considering the modification factors, the generalized computer equations of the field components (equations 3A.1 – 3A.6) can be written as:

$$D_x(i,j,k) = D_x(i,j,k) + 0.5 \times ra\_x \times \begin{pmatrix} H_z(i,j,k) - H_z(i,j-1,k) - \\ H_y(i,j,k) + H_y(i,j,k-1) \end{pmatrix} \quad (3.14)$$

$$D_y(i,j,k) = D_y(i,j,k) + 0.5 \times ra\_y \times \begin{pmatrix} H_x(i,j,k) - H_x(i,j,k-1) - \\ H_z(i,j,k) + H_z(i-1,j,k) \end{pmatrix} \quad (3.15)$$

$$D_z(i,j,k) = D_z(i,j,k) + 0.5 \times ra\_z \times \begin{pmatrix} H_y(i,j,k) - H_y(i-1,j,k) - \\ H_x(i,j,k) + H_x(i,j-1,k) \end{pmatrix} \quad (3.16)$$

$$H_x(i,j,k) = H_x(i,j,k) + 0.5 \times ra\_x \times \begin{pmatrix} E_y(i,j,k+1) - E_y(i,j,k) - \\ E_z(i,j+1,k) + E_z(i,j,k) \end{pmatrix} \quad (3.17)$$

$$H_y(i,j,k) = H_y(i,j,k) + 0.5 \times ra\_y \times \begin{pmatrix} E_z(i+1,j,k) - E_z(i,j,k) - \\ E_x(i,j,k+1) + E_x(i,j,k) \end{pmatrix} \quad (3.18)$$

$$H_z(i,j,k) = H_z(i,j,k) + 0.5 \times ra\_z \times \begin{pmatrix} E_x(i,j+1,k) - E_x(i,j,k) - \\ E_y(i+1,j,k) + E_y(i,j,k) \end{pmatrix} \quad (3.19)$$

where, $D = \varepsilon E$ is the electric flux density. The above FDTD equations are formulated for lossless medium. For lossy medium, electric and magnetic tapered damping functions should be incorporated with the respective equations.

3.3.2 Accuracy, Convergence and Stability

In case of FDTD method, accuracy depends on the cell size or spatial increment which is dependent on many factors [16],[23]. Usually, the basic FDTD algorithm is formulated to second-order accuracy, however, higher order accuracy can also be achieved by reducing the cell size which would incur additional computational cost and could be insignificant. Therefore, it is seen that the selection of cell size to be used in an FDTD formulation plays an important role to define the accuracy of the computed results. To ensure the accuracy of the computed results obtained by FDTD method, the spatial increment or cell size must be small compared to the wavelength (λ). However, a good rule of thumb is cell size ≤ λ/10 or minimum dimension of the scatterer [8] It has been tested that adequate inaccuracies in the FDTD result appear if the cell size is more than the thumb rule defined value. At very high frequency component holding frequencies with a wavelength shorter than few cells may experience what is known as the *ringing effect* which prevents normal propagation of the EM waves through the model [26].

Numerical stability needs to be ensured to maintain the convergence of the FDTD solution. To make sure the stability of the FDTD analysis, time step (Δt) must be limited relative to the lattice space increments Δx, Δy, Δz by the following Courant stability criterion [27]:

$$\Delta t \le \frac{\left(\frac{1}{\Delta x^2}+\frac{1}{\Delta y^2}+\frac{1}{\Delta z^2}\right)^{-1/2}}{c} \tag{3.20}$$

where, c is the speed of light in free space. The principle of this stability factor is based on the assumption that the EM wave cannot transverse across more than one cell per time step.

For equilateral cubic Yee cell i.e., $\Delta x = \Delta y = \Delta z = \delta$, the above stability criterion could be simplified to:

$$\Delta t \le \frac{\delta}{c\sqrt{n}} \tag{3.21}$$

where, n is the number of space dimensions. For practical reasons, it is best to choose the ratio of the time increment to spatial increment to be as large as possible yet satisfying (3.20). If the time step (Δt) does not satisfy relation (3.20), then the FDTD simulation will not be converged to stable. In an unstable condition, the computed E and H field components will increase without limit as the simulation progress.

Number of steps (*NSTEPS*) the FDTD program iterated is obtained by the relation [28]:

$$NSTEPS = N \cdot \frac{1}{f\Delta t} \tag{3.22}$$

where, f is the frequency and N is number of period of oscillations or time cycles required for the internal E fields to reach the steady state condition or the input pulse has died out.

3.3.3 Lattice Truncation

A basic problem encountered in applying the FDTD method to an EM scattering problems is that the domain in which the field is to be computed is open or unbounded. Because of limited computer storage, a finite difference scheme over the whole domain is impractical as the lattice cannot cover a sufficiently large portion of space so that the scattered wave at the lattice truncation might be closely approximated [29]. Therefore, it is

necessarily required to terminate the lattice close to the scatterer in a region where the nature of the scattered wave is unknown.

Proper truncation of the lattice requires in such a way that any outgoing wave disappear at the lattice boundary without reflection during the continuous time stepping of the algorithm else results in error for all time steps after the boundary wave reflections return to the vicinity of the scatterer. To achieve this, an artificial boundary must be enforced to create the numerical illusion of an infinite space. The solution region must be large enough to enclose the scatterer and suitable boundary conditions on the artificial boundary must be used to simulate the extension of the solution region to infinity.

3.3.4 Boundary Conditions

Unpredictable reflections of the EM waves from the edges of the problem space are encountered during the simulation by the FDTD method which spread out over the whole simulation domain. At the boundary of the simulation domain, special boundary conditions have to be defined, since the domain cannot be extended to infinity due to limited computer storage. The special boundary conditions eliminate the outgoing EM waves by absorbing them as they reach the boundary, defined as absorbing boundary condition (ABC). With the use of an ABC, the computational domain can be truncated.

In the early days, ABC was developed using the concept of impedance matching of the materials represented by:

$$\frac{\sigma}{\varepsilon} = \frac{\sigma^*}{\mu} \tag{3.23}$$

where, σ^* denotes the magnetic conductivity. σ^* is a fictitious term and is added to facilitate the continuity of wave impedance across the boundaries.

When the equation (3.23) is satisfied then it is implied that the impedance due to lossy and free-space medium equals to that of the lossless vacuum. Under this condition, no reflection will occur when a plane wave is incident normally across the two materials. Material-based ABCs are constructed so that fields are dampened as they propagate into an absorbing medium. But it is found that the characteristic impedance of the free space and the matching material is only matched at certain incident angle which yields a high level of reflection [30],[31]. Later on, Mur ABC was developed based on differential method which

uses differential wave operators on the scalar wave equation to predict and approximate the fields at the boundary [32]. Such methods are based on the factorisation of the wave equation and allow one solution which permits only outgoing waves.

The PML has been known to be one of the most successful, flexible and efficient ABCs ever developed. The concept of a PML medium was introduced by Berenger in 1994 [33]. The basic characteristic of the PML is the splitting of the *E* and *H* fields in the absorbing boundary region to account for the individual losses to be assigned. This creates a non-physical absorbing medium that has its wave impedance independent of the frequency, polarization and angle of incident of the incoming wave. The basic idea of PML is that when a wave is propagating through a medium (A) and it impinges upon other medium (B) then a portion of the wave is reflected from the interface of the two media. The amount of reflection is dictated by the intrinsic impedances of the two media is given by [25]:

$$\Gamma = \frac{\eta_A - \eta_B}{\eta_A + \eta_B} \tag{3.24}$$

where, η_A and η_B are the intrinsic impedances of two media A and B respectively, and are determined by the dielectric constants ε and permeability μ of the two media:

$$\eta = \sqrt{\frac{\mu}{\varepsilon}} \tag{3.25}$$

PML is available in two different versions: split step and unsplit step [34],[35]. Both of these produce a very low reflection when used to truncate the FDTD lattice, but the split step PML is more complex and requires less memory compare to unsplit step PML. To avoid complexity, in this research work the unsplit step PML has been used as ABC in the in-house FDTD simulation.

3.3.5 Initial Fields

Every FDTD calculation requires the initial single or multiple field components as excitation which are called *source* [16],[25]. These sources are obtained by simulating either an incident plane wave pulse or single-frequency plane wave. In FDTD calculations, two types of sources are used. One is called *hard source* and other is called *soft source*. When a specific value is imposed as the initial field component or components, the corresponding source is called a hard source [25]. On the other hand, when a specific value is added with the initial field component or components, the corresponding source is called a soft source. With

the soft source, a propagating pulse will just pass through it but the hard source will be looked like a metal wall and the propagating pulse will be reflected by it.

Hard voltage source is used in FDTD for antenna and microstrip transient calculations [36]. A common choice is a Gaussian pulse, but other functions can also be used as per requirement. In case of dosimetry calculations, generally a sinusoidal pulse is used as excitation of the radiating antenna [37]. Switch over from one function to another is easily obtained by changing the pulse parameter.

During FDTD simulation, the propagation of waves from the source either hard or soft, is simulated by time stepping, i.e. repeatedly implementing Yee's finite difference algorithm on a lattice of points. Time stepping is continued until the steady state condition is achieved at each point. At a particular frequency, number of steps to be iterated to attain the steady state condition is given by the equation (3.22).

3.3.6 In-house FDTD code development

An in-house FDTD based simulation tool has been developed for the studies carried out and reported in this thesis due to the following reasons:

- Wide frequency range from a few MHz to several GHz,
- Simplicity and ability to handle complex geometries,
- Compared to the other numerical computational methods FDTD is more efficient in terms of computer time and memory and
- FDTD supports material modelling through parameter averaging or, in case of a more sophisticated approach, choosing grids to conform to the geometries of the material boundaries.

3.3.6.1 Development of 1-D, 2-D and 3-D Yee cell

1-D, 2-D and 3-D simulations for a point source of a Gaussian pulse using FDTD method have been developed using the MATLAB software [38]. *E* field distributions obtained by the simulations are shown in Figure 3.4 (a-c).

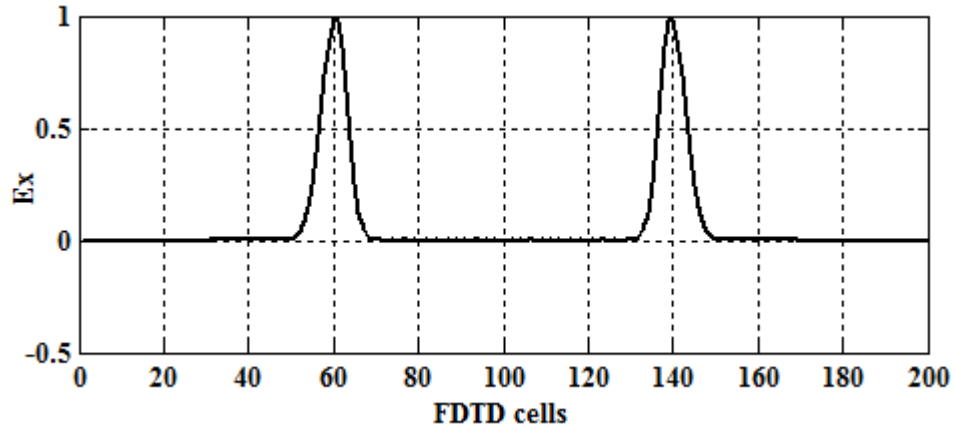

(a)

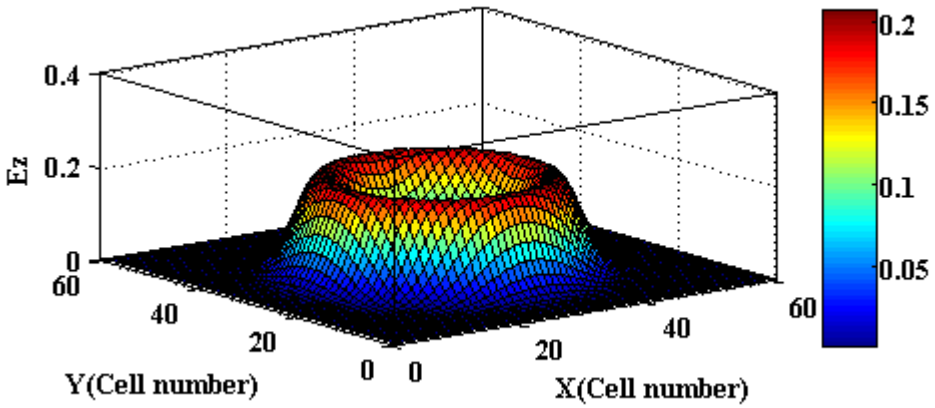

(b)

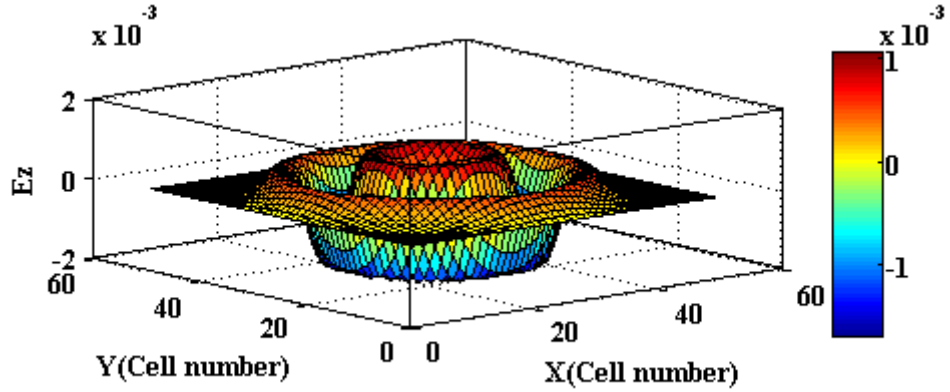

(c)

Figure 3.4. *E* field distributions for (a) 1-D, (b) 2-D and (c) 3-D simulations.

3.3.6.2 Multi layer Unsplit PML implementation

5-point unsplit PML has been implemented for a 3-D problem space of dimension: 40×40×40 Yee cells and its effectiveness are illustrated in Figures 3.5 and 3.6. The simulation has been performed with a Gaussian pulse source placing at the centre for 40, 50 and 100 time step. Resulting surface and contour plots of the E_z component show that as the wave reaches the PML which is 5 cells on every side, it is absorbed. Up to 40 time step, the out going contours would remain concentric circles only when the waves get within the PML i.e. five points of the edge but not reflected as shown in Figures 3.5 (a-b). But as the number of time step is increased, the out going waves are partially reflected from the edges which enter inside the PML and distortion starts to occur. Because of the distortion the contours would not be concentric circles as shown in Figures 3.6 (c-f). From Figures 3.6 (c-f), it is seen that distortion of the waves increases with the increase of time step. Distortion of the waves can be decreased by increasing the distance of PML from scatterer as shown in Figure 3.6 (g-h) for the same PML but problem space of dimension: 50×50×50 Yee cells. But this method would not yield an optimum implementation. In order to optimize the computational time and cost, PML layer should be placed as close as possible to the scatterer [20].

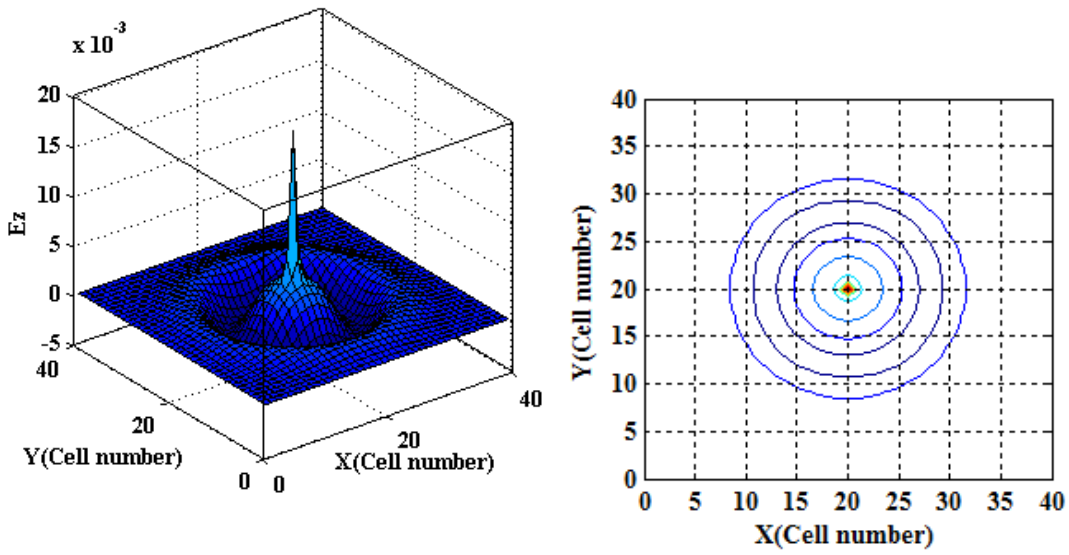

(a) **(b)**

Figure 3.5. Varaiation of E_z in 2-D space for Time step = 40 (a) surface plot and (b) contour plot.

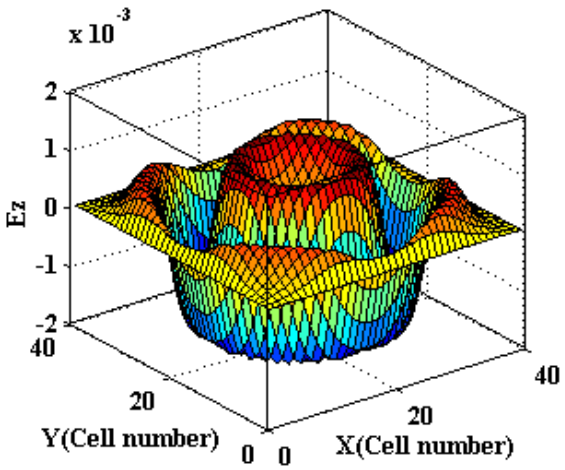

(c)

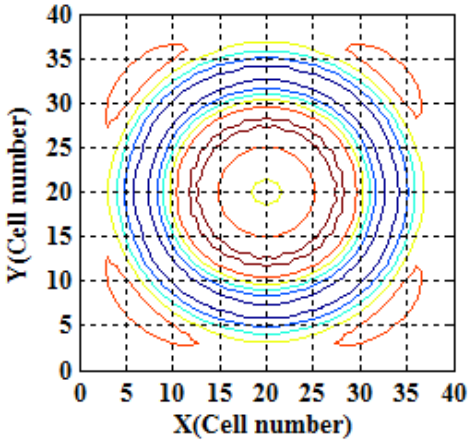

(d)

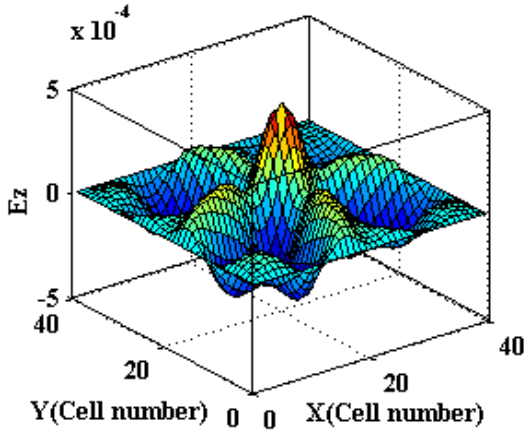

(e)

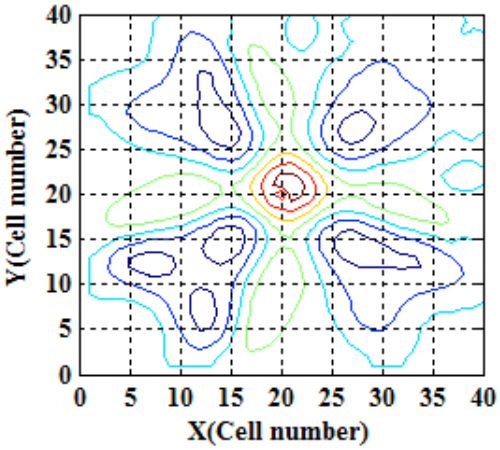

(f)

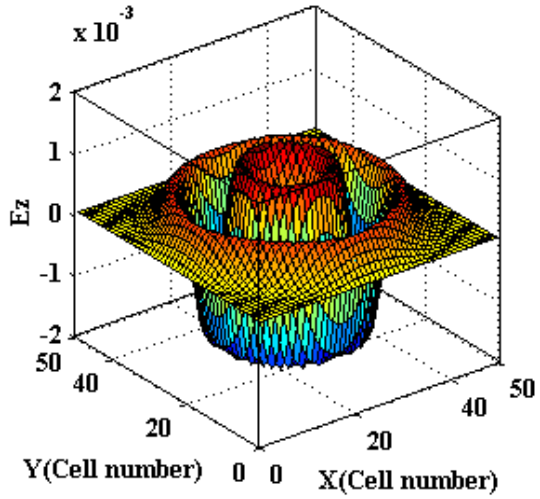

(g)

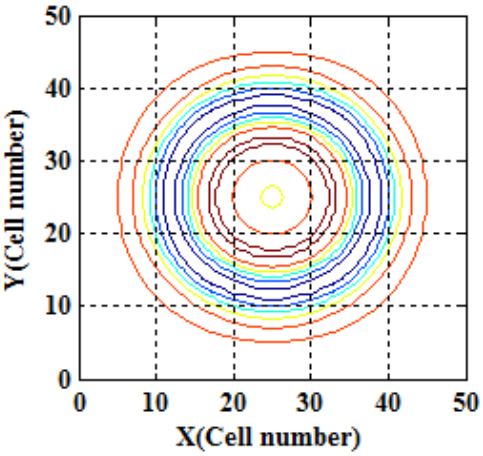

(h)

Figure 3.6. Varaiation of E_z in 2-D space for Time step = 50 (c) surface plot and (d) contour plot, for Time step = 100 (e) surface plot and (f) contour plot and Time step = 50 (g) surface plot and (h) contour plot.

The physical and the numerical approximation can further be made transparent by using the integral forms of Maxwell's equations. The disadvantages of FDTD include the requirement of a large computer memory when the linear dimension of the scattering objects is large compared to the wavelength and the error is introduced by the numerical dispersion of the algorithm. When an object is large (compared to wavelength), the effect due to the interaction of distance points in the object is not accurate because of the error introduced by the numerical dispersion.

3.4 Segmented FDTD Method (SFDTD)

Using FDTD method for modelling EM wave propagation was first proposed by Yee in 1966 [18]. Since then FDTD method has been successfully used to design and analyse both the guiding and scattering structures. But as the computer memory limits the number of mathematical cells so it is impractical to achieve desired details in large areas using FDTD method. Subgridding and multigrid FDTD codes have been developed in order to overcome the problem of FDTD [39],[40]. But the subgridding method has two limitations. First, the numerical dispersion varies considerably with the density of the mesh and second, the computational efficiency of the method is compromised by the need to use the time step corresponding to the smallest grid throughout the computational space [41]. On the other hand, when the multigrid FDTD method is used for the simulation containing dielectric materials inside the fine-grid region, the simulation begins to diverge and becomes unstable [42]. It is also observed that multigrid FDTD method becomes unstable when the fine grid region contains complex geometries. To solve large scale problems using FDTD method, a nonuniform FDTD technique has been developed where non uniform cells are used to form the problem space which reduces computational burden but stored only four field components in the whole domain [43]. SFDTD method divides large problem space into different segments to reduce the computational requirements and enhances the practicability of running the simulation on a PC [44].

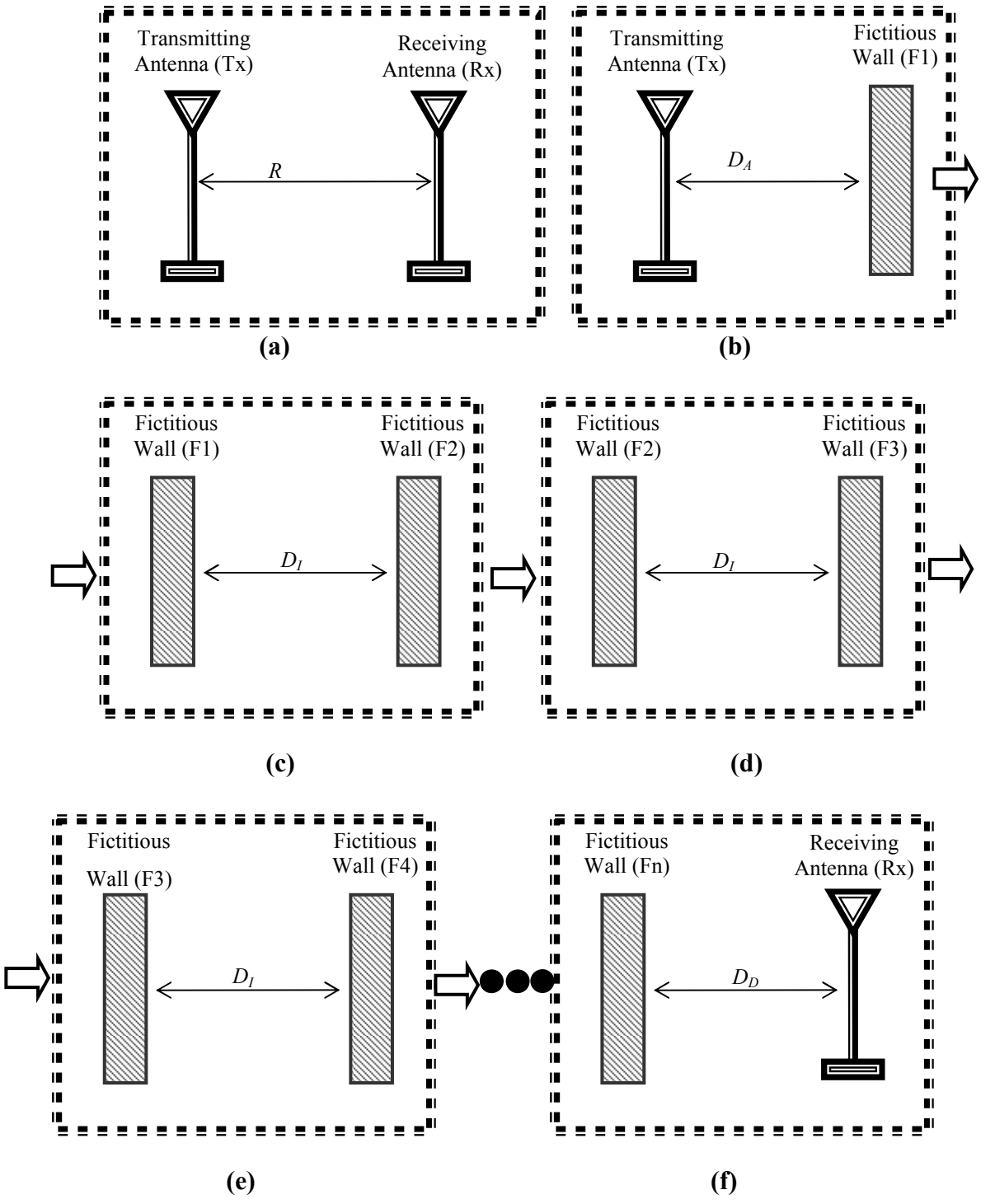

Figure 3.7. Geometry of the (a) actual problem space, (b) source segment, (c-e) intermediate segments and (f) destination segment.

3.4.1 Basics of SFDTD method

In the application of SFDTD method, ignoring the overheads due to the space taken up by other factors, e.g., the absorbing boundaries, the actual problem space is splitted into three

different segments. Geometry of the actual problem space consisting of a transmitting antenna (Tx) and a receiving antenna (Rx) separated by a distance *R* is shown in Figure 3.6 (a). The following procedures are applied to realise the SFDTD concept for the problem shown in Figure 3.7 (a) as illustrated in Figures 3.7 (b-f):

Step 1: Actual problem space is splitted into different segments: source segment, *n* number of intermediate segments and destination segment as shown in the Fig. 3.7 (b-f). Source segment contains the Tx and fictitious wall (F1), each intermediate segment contains a pair of fictitious walls (F1-F2, F2-F3,…..Fn-1-Fn) while the destination segment contains the fictitious wall Fn and the Rx.

Step 2: Segmentation is done in such a way that $R = D_A + n\ D_I + D_D$.

Step 3: Start the conventional FDTD iteration in source segment with the signal source Tx.

Step 4: When the source segment reaches its steady state, i.e., all the multipath signals have arrived at each individual cell of F1. In each time step at each cell of the fictitious wall F1, all the *E* and *H* field components are picked up and stored.

Step 5: The prestored values of the *E* and *H* field components obtained from source segment are retrieved into the corresponding cell of the fictitious wall F1 in the first intermediate segment and when the segment reaches its steady state, the field components at each cell of the fictitious wall F2 are picked up to store in each time step.

Step 6: Follow the same step to complete the simulations in the intermediate segments 2, 3, 4 and up to *n*.

Finally, in the destination segment, the fictitious wall Fn acts as a source and the prestored values of the *E* and *H* field components are retrieved into the corresponding cell of the fictitious wall Fn in each time step.

3.4.2 Application of SFDTD method in 3-D simulation

SFDTD method has been applied only for a 2-D problem [44]. But it can also be used in 3-D problem by slightly modification of the intermediate fictitious walls. In case of 3-D problem, dimension of the fictitious walls play a significant role. To study the effect of fictitious wall, a pair of half wave resonating dipole antennas each having length of 14.5 cm

and separated by a distance 20 cm, one of them is acting as Tx and other as Rx, has been simulated using conventional FDTD and SFDTD method. Detailed geometry has been shown in Figure 3.13 of section 3.7.1. Received voltages at Rx due to a 930 MHz sinusoidal input signal at Tx for 1-D, 2-D and 3-D fictitious walls are shown in Figure 3.8.

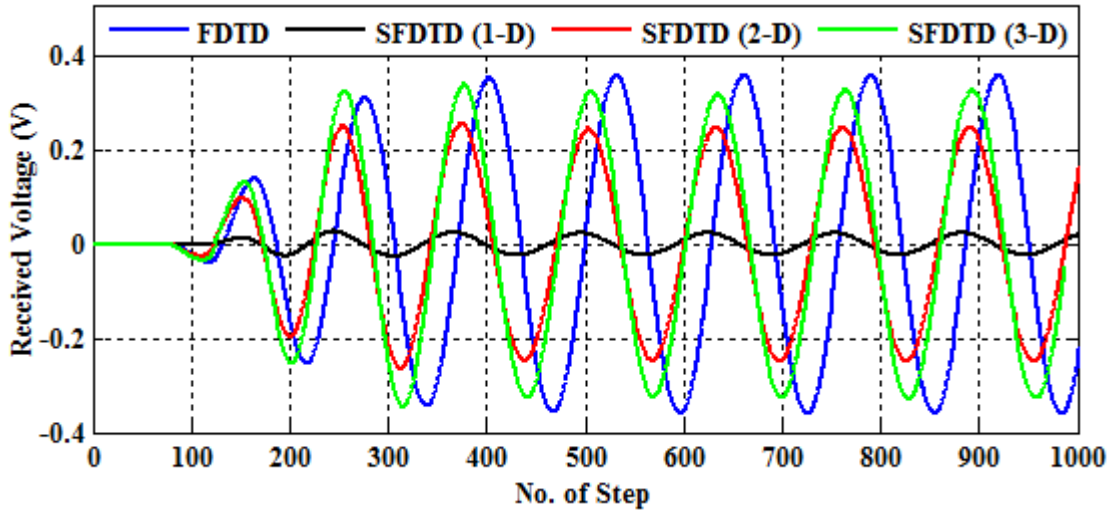

Figure 3.8. Received voltages for FDTD and SFDTD with different fictitious walls.

3.5 Development of in-house hybrid EM simulator based on Friis transmission equation and FDTD technique

During dosimetry calculation, some hybrid numerical EM techniques have been adopted to reduce the computational resource requirements. A mixed FDTD-integral equation approach is used to evaluate SAR inside a human model for the radiation from BSAs and the SAR values obtained with mixed FDTD-integral equation are found close to that obtained using the full FDTD simulations [45]. FDTD method combined with the MoM in the Time Domain (MoMTD) is used to calculate the SAR induced in a homogeneous phantom model placing at a distance of 10.0 cm from a BSA [46],[47]. Green's integral equation combined with FDTD method has been reported for SAR calculation in human head model due to radiation from a BSA [48]. Hybrid FDTD method is newly developed by combining Friis transmission equation with FDTD method. In this method, EM modelling of the simulating elements is prepared using either conventional or non-uniform FDTD method and power calculation of the source required for the simulation is made by Friis transmission formula [49]:

$$\frac{P_r}{P_t} = \frac{A_{er} A_{et}}{R^2 \lambda^2} = \frac{G_t A_{er}}{4\pi R^2} \tag{3.26}$$

where, P_r = received power (W), P_t = transmitted power (W), A_{et} = effective aperture of transmitting antenna (m^2), A_{er} = effective aperture of receiving antenna (m^2), R = distance (m), G_t = gain of the transmitting antenna and λ = wavelength (m).

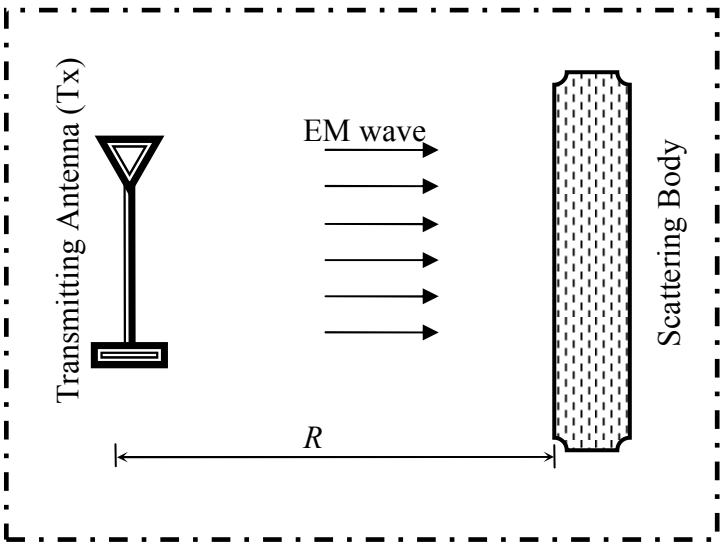

Figure 3.9. Geometry of a simulation model for scattering body along with a Transmitting Antenna (Tx) [*R* may vary from fraction to few tens of meter].

After a distance in the order of tens of wavelengths, the field from most antennas behaves like a plane wave [25]. For that reason the simulation model as shown in Figure 3.9 is divided into two sub domains namely domain 1 and 2 as shown in Figure 3.10. Domain 1 is used to compute the characteristics of resultant fictitious plane wave source. This plane wave source is actually a replacement of the radiating Tx placed at a distance R from the scattering body and its properties are calculated from equation (3.26) considering the value of transmitted power P_t. Width of the fictitious plane wave source regulates the accuracy of the simulation result. Normally, plane wave source of width two Yee cells provides result with sufficient accuracy. For distance more than the far field distance in free space, E and H field used for the local plane wave generator wall with effective aperture A_{er} in the FDTD solution domain can be related with Poynting vector as [48],[49]:

$$\vec{S} = \vec{E} \times \vec{H} = \frac{\vec{E}^2}{\eta_0} = \eta_0 \vec{H}^2 = \frac{P_r}{\vec{A}_{er}} \tag{3.27}$$

where, $\eta_0 = 120\pi\ \Omega = 377\ \Omega$.

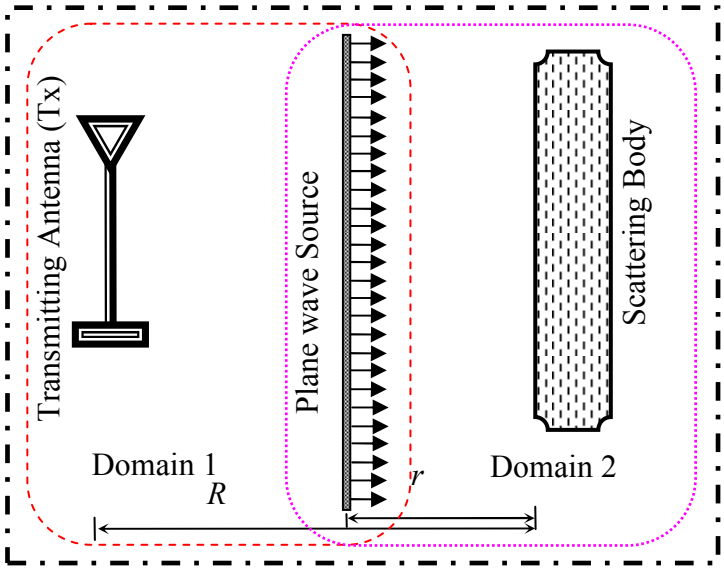

Figure 3.10. Geometry of a simulation model for scattering body along with a Transmitting Antenna (Tx) [*r* = few mm].

Using equations (3.26) and (3.27), the amplitude of the *E* field intensity i.e. E_0 at a distance *R* from the Tx can be calculated with the following relation:

$$E_0 = \sqrt{\eta_0 \frac{P_r}{A_{er}}} = \frac{1}{R}\sqrt{120\pi \frac{P_t G_t}{4\pi}} = \frac{\sqrt{30 P_t G_t}}{R} \tag{3.28}$$

Similarly, magnitude of *H* field intensity i.e. H_0 can also be calculated by the following equation:

$$H_0 = \frac{E_0}{\eta_0} \tag{3.29}$$

Values of E_0 and H_0 obtained from the equations (3.28) and (3.29) are used to construct the fictitious plane wave generating wall at a distance *R* from the Tx in a local FDTD solution domain using auxiliary one dimensional buffer. This buffer is also known as incident array and is described in available literature [25]. Solution for *E* and *H* fields for a linearly polarized plane wave travelling in the x direction are functions of only x and *t* and constrained to the y and z directions using following relations [50]:

$$E(x,t) = E_o \cos(kx - 2\pi ft) \tag{3.30}$$

$$H(x,t) = H_o \cos(kx - 2\pi ft) \tag{3.31}$$

where, f is operating frequency, λ is wave length and wave number $k = 2\pi/\lambda$. In domain 2, the fictitious plane wave is placed at a distance r from the scattering body and the required parameters are calculated by the equations (3.30) and (3.31).

3.6 Simulation using commercially available softwares

In recent years, both computer power and software capabilities have increased substantially, and there are now a variety of general purpose EM simulation tools commercially available for the analysis and design of antennas, microwave components, communication devices, etc. Moreover, some of these packages have the ability to solve bio-electromagnetic problems and BHE. Today, the general purpose EM field simulation software packages are much more cost effective. Nevertheless, not all simulators have the same capabilities or performance, and each may be best suited for a particular type of problem. Factors including accuracy, speed of execution and setup time, may play important roles in selecting the proper simulator. Table 3.1 lists nine of the most well-known commercial EM field simulators with their adopted numerical methods and applications. Among them CST Microwave Studio® of version 2010, IE3D and Fidelity have been used in this research work to validate the performance of the in-house FDTD.

3.6.1 CST Microwave Studio®

CST Microwave Studio® is a powerful and easy to use FIT based EM field simulation software package [21]. It combines both a user friendly interface and simulation performance in an incomparable manner. Process of inputting the structure has been simplified by using the ACIS kernel based powerful solid modelling front-end and strong graphic feedback further simplifies the definition of the structure. After the component has been modelled, a fully automatic meshing procedure (based on an expert system) is applied before the simulation engine is started. The simulators feature the Perfect Boundary Approximation (PBA™ method) and its Thin Sheet Technique (TST™) extension, which increases the accuracy of the simulation by an order of magnitude in comparison to conventional simulators. This simulator is equipped with the new Multilevel Subgridding Scheme (MSS™) which helps to improve the meshing efficiency and thus can significantly speed up simulations especially for complex devices. The usage of advanced signal processing

techniques (AR-filters) provided by CST Microwave Studio® allows the speeding up these simulations by orders of magnitude compared to standard time domain methods.

There is no method which works equally well in all application domains. So, for best fitting with different type of applications CST Microwave Studio® contains seven different solvers. They are transient solver (T), frequency domain solver (F), eigenmode solver (E), integral equation solver (I), asymptotic solver (A), thermal stationary solver (THs) and thermal transient solver (THt). The transient solver has been used frequently in this research work. Among the rest of the six solvers only the thermal stationary solver has been used one time for temperature calculation.

The transient solver is the most flexible time domain solver and it is capable of solving any kind of S-parameter or antenna problem within the entire desired broadband frequency range and optionally, the EM field patterns at various desired frequencies can be obtained from only one calculation run. This solver is also very efficient for most kinds of high frequency applications such as connectors, transmission lines, filters, antennas and many more. Typical areas of application of the transient solver are:

- S-parameter calculation.
- EM field distributions at various frequencies.
- Antenna radiation patterns and relevant antenna parameters.
- Signal analysis such as rise times, cross talks etc.
- Structure design by using the optimizer or the parameter sweep.
- Time domain reflectometry.
- Radar Cross Section (RCS) calculations using far field.
- Simulation of dispersive materials.

The thermal stationary solver can be used to simulate temperature distribution problems. In this study, it has been used in conjugation with the transient solver.

Table 3.1: Description of nine of the most well-known commercial EM simulators and their adopted numerical methods.

Simulator	Method	Type	Application	Provider / Web Link
HFSS	FEM	Frequency domain	3D Full-Wave-EM Field Simulation	ANSYS Inc., USA http://www.ansoft.com
CST Microwave Studio®	FEM/FIT	Time domain	3D Full-Wave-EM Field Simulation	CST Computer Simulation Technology AG. http://www.cst.de
Super NEC	MoM	Frequency domain	3D antenna design and analysis	Pointing Software (Pty) Ltd. http://www.supernec.com
Fidelity	FDTD	Time domain	3D Full-Wave-EM Field Simulation	Zeland Software Inc. http://www.zeland.com
IE3D	MoM	Frequency domain		
MDSpice	----------	Mixed domain		
FEKO	MoM and Hybrid MoM/FEM	Frequency domain	3D Full-Wave-EM Field Simulation	EM Software & Systems-S.A. (Pty) Ltd. http://www.feko.info
XFDTD	FDTD	Time domain	3D Full-Wave-EM Field Simulation	Remcom (USA) State College, PA. http://www.remcom.com
SEMCAD	FDTD and ADI-FDTD	Time domain	3D Full-Wave-EM Field Simulation	Schmid & Partner Engg. AG (SPEAG), Switzerland. http://www.semcad.com

3.6.2 Zeland IE3D, Fidelity and MDSpice

Zeland Software, Inc. was founded in 1992 to develop powerful and practical EM design tools [51]. After that, Zeland software has been recognized as a leading developer to

provide unparalleled high-frequency EM simulation and design tools for microwave, semiconductor, wireless and telecom industries. Zeeland version 14.0 is powered by the seven products among them only the following three have been used in this research work:

- IE3D
- Fidelity
- MDSpice.

IE3D is a powerful full-wave MoM based high accuracy and high efficiency EM tool for the design of general 3D and planar structures. It is used in the high frequency applications. It is based upon Maxwell's equation in integral form. IE3D is not only used for planar structures but it can also handle full-3D structures elegantly. It is not limited by uniform grids and shape of the structures. It is much more capable, accurate, efficient and flexible than other EM simulators.

Fidelity is a FDTD based full wave 3D EM simulator. It can be used in any field in which EM effects are the major concerns, for example microwave engineering, HF electronic component and circuitry design, EMC/EMI, electronic device packaging, bio-electromagnetic signal analysis etc. As the Fidelity is primarily based on FDTD method which has already been proven to be an effective and efficient method for EM simulation and analysis in case of:

- Visualize EM field in both time and frequency domains.
- Yields simulation results in full frequency band by a single simulation.
- Represents structures in full three dimensions.
- Be capable of solving extremely complex structures.
- Easy to implement
- Consumes less computer memory compared to MoM and FEM

Due to the above unique advantages, Fidelity adopts FDTD method as its primary numerical technique for solving EM problems. Combined with other numerical techniques and structure modelling schemes, Fidelity is capable of solving a wide range of complex structures in both time and frequency domains while maintains its simplicity, versatility and usability.

MDSpice is a Mixed-Domain SPICE simulator combing a time-domain simulation engine with a frequency-domain simulation engine. The most significant feature of MDSpice is that it can perform robust, accurate and efficient time-domain simulation based upon

frequency domain S-parameters. It also has a broadband SPICE model extraction capability for coupled transmission lines and interconnects. MDSpice is particularly useful in modelling high-speed digital circuits and high-frequency nonlinear devices.

3.7 Modelling and Validation

In this research work the FDTD method has been used as a master tool to design various types of simulation models. The necessary FDTD code has been developed using the MATLAB software [38]. Then the commercially available softwares CST Microwave Studio®, IE3D and Fidelity have been used to validate the performance of the in-house FDTD code. Typical radiating antennas applied in this research work as RF source have been designed using in-house FDTD code and to validate their characteristics, commercially available softwares CST Microwave Studio®, IE3D and Fidelity have been used as shown below:

3.7.1 Half wave Dipole Antenna

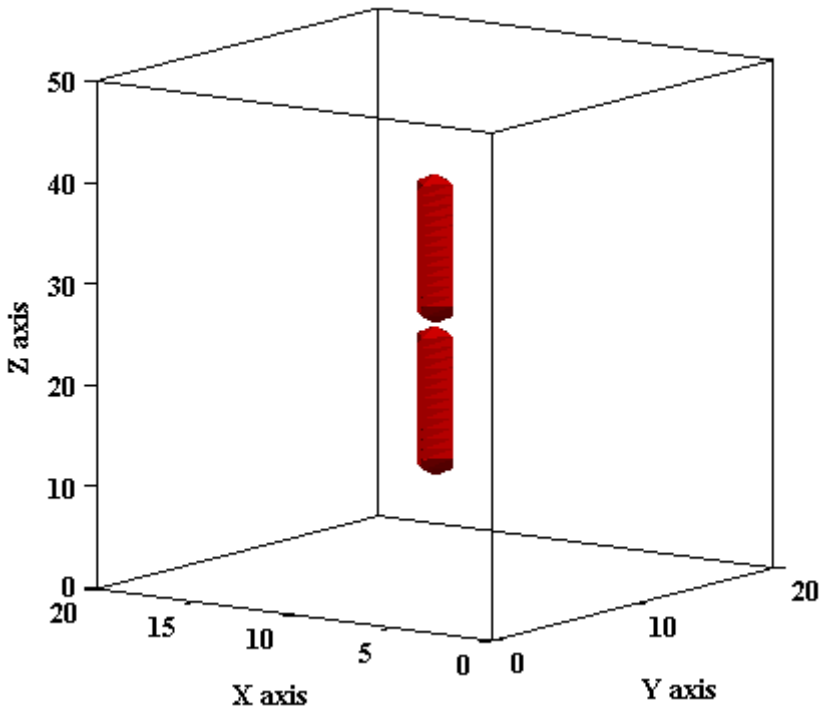

Figure 3.11. Geometry of a half wave dipole antenna placed in free space [length = 14.5 cm].

A metal made half wave dipole antenna of length 14.5 cm and diameter 0.5 cm placed in free space has been designed by FDTD method in MATLAB as shown in Figure 3.11. Reflection coefficient (S_{11}) of the dipole antenna as a function of frequency is determined from the ratio of the Discrete Fourier transform (DFT) of the transient waveforms by:

$$S_{11} = \frac{DFT\left[E_{ref}\right]}{DFT\left[E_{inc}\right]} \tag{3.32}$$

where, E_{inc} = incident electric field and E_{ref} = reflected electric field. The value of S_{11} is computed in dB by:

$$S_{11}\big|_{dB} = 20\log_{10}(|S_{11}|) \tag{3.33}$$

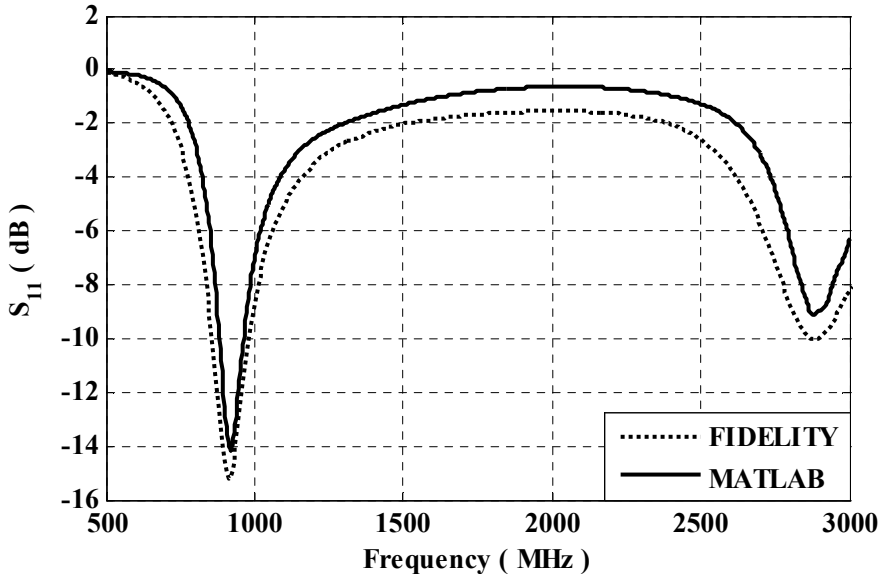

Figure 3.12. Variation of S_{11} with frequency for the half-wave dipole antenna of length 14.5 cm in free space.

Variation of S_{11} with frequency for the half wave dipole antenna placed in free space is obtained using FDTD code developed in MATLAB and compared with that obtained using FIDELITY as shown in Figure 3.12. The curve obtained using the MATLAB program is in close agreement with that obtained from FIDELTY. At the fundamental mode, the antenna resonates at 930 MHz and the value of S_{11} remains below –10 dB within GSM 900 band. Values of S_{11} at the fundamental resonance frequency obtained from MATLAB program and FIDELITY are -14.14 dB and -15.17 dB, respectively.

A pair of half wave resonant dipole antennas of each having length equal to 14.5 cm and separated by a distance of 20.0 cm placed in free space as shown in Figure 3.13 has been

simulated to carry out investigation on scattering parameters S_{11} and S_{21} of the dipole antennas. One of the antennas is acting as a Transmitter (Tx) while the other as a Receiver (Rx). First, SFDTD method has been applied to obtain S_{11} and S_{21} of the Tx-Rx pair in the frequency range of 500 MHz to 3.5 GHz. Then, the results obtained by SFDTD method are compared with that obtained from unsplitted actual problem space using conventional FDTD method and commercially available MoM based EM simulation software IE3D.

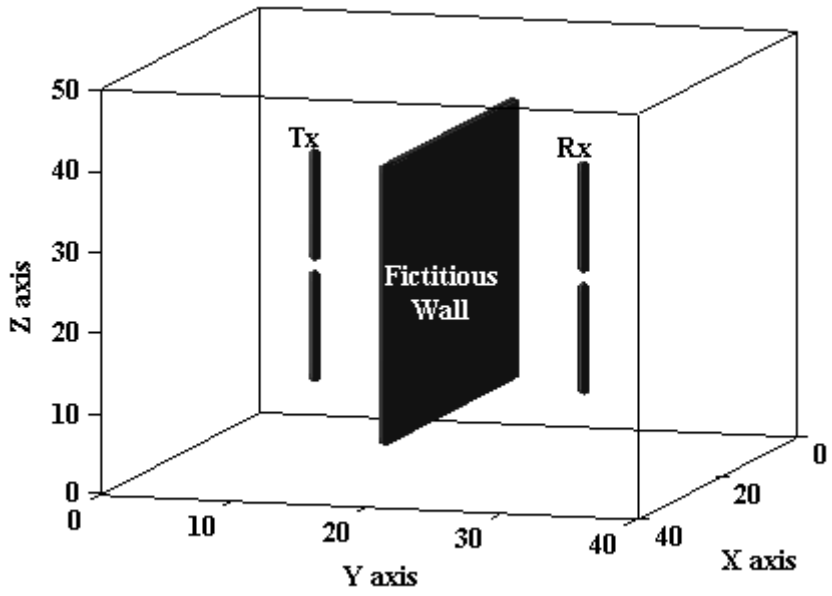

Figure 3.13. Geometry of a pair of half wave dipole antennas placed in free space.

A fictitious wall is assumed to be at the position in the free space midway between the Tx and Rx antenna. Now the actual space is splitted into two different three dimensional segments as shown in the Figure 3.14 (a-b). One of the segments contains Tx and fictitious wall defined as Tx antenna segment and the other contains the same fictitious wall and Rx defined as Rx antenna segment.

Taking the reference resistances correspond to the characteristic impedance of Tx and Rx, the scattering or S parameters S_{11} and S_{21} can be obtained by using the following equations [52]:

$$a_1 = \frac{V_1(f) + Z_0 I_1(f)}{2\sqrt{Z_0}} \tag{3.34}$$

$$b_1 = \frac{V_1(f) - Z_0 I_1(f)}{2\sqrt{Z_0}} \tag{3.35}$$

$$a_2 = \frac{V_2(f) + Z_0 I_2(f)}{2\sqrt{Z_0}} \tag{3.36}$$

$$b_2 = \frac{V_2(f) - Z_0 I_2(f)}{2\sqrt{Z_0}} \tag{3.37}$$

where, $V_1(f)$ = input pulse at Tx, $I_1(f)$ = input current at Tx, $V_2(f)$ = received voltage at Rx, $I_2(f)$ = received current at Rx and Z_0 = characteristic impedance of Tx and Rx (50 Ω). Then the S parameters are calculated by:

$$S_{11} = \left.\frac{b_1}{a_1}\right|_{a_2=0} \tag{3.38}$$

$$S_{21} = \left.\frac{b_2}{a_1}\right|_{a_2=0} \tag{3.39}$$

S_{11} and S_{21} are computed in dB by:

$$S_{11} = 20\log_{10}(|S_{11}|) \tag{3.40}$$

$$S_{21} = 20\log_{10}(|S_{21}|) \tag{3.41}$$

S parameters (S_{11} and S_{21}) vs. frequency of the Tx-Rx pair separated by a distance of 20.0 cm obtained by using SFDTD, FDTD and IE3D methods are shown in Figure 3.15. From Figure 3.15, it is seen that the agreement of the results obtained by the different methods are quite good. At the fundamental mode, both the antennas resonate near 930 MHz and the value of S_{11} remains below –10 dB within GSM 900 band. Values of S_{11} at the fundamental resonance frequency obtained from SFDTD, FDTD and IE3D methods are -11.75 dB, -12.46 dB and -13.52 dB respectively. Whereas, the values of S_{21} at the fundamental resonance frequency obtained from SFDTD, FDTD and IE3D methods are -22.83 dB, -20.83 dB and -14.63 dB, respectively.

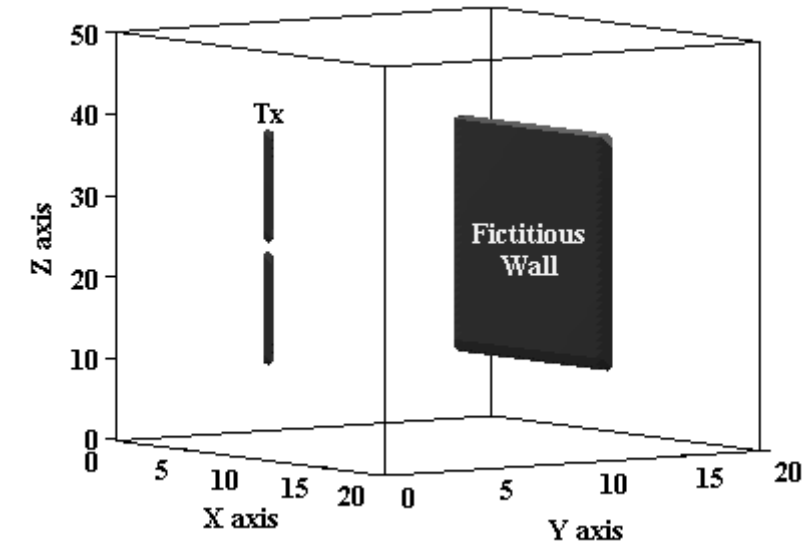

(a)

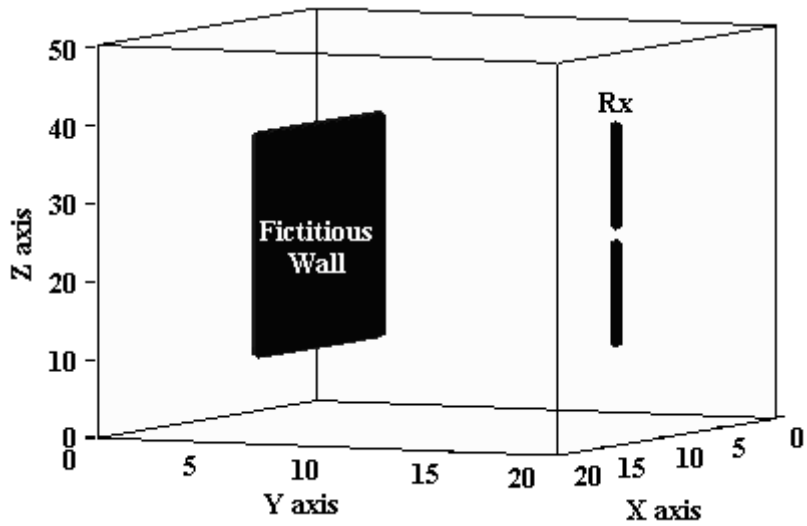

(b)

Figure 3.14. Schematic illustration of (a) Tx antenna segment and (b) Rx antenna segment.

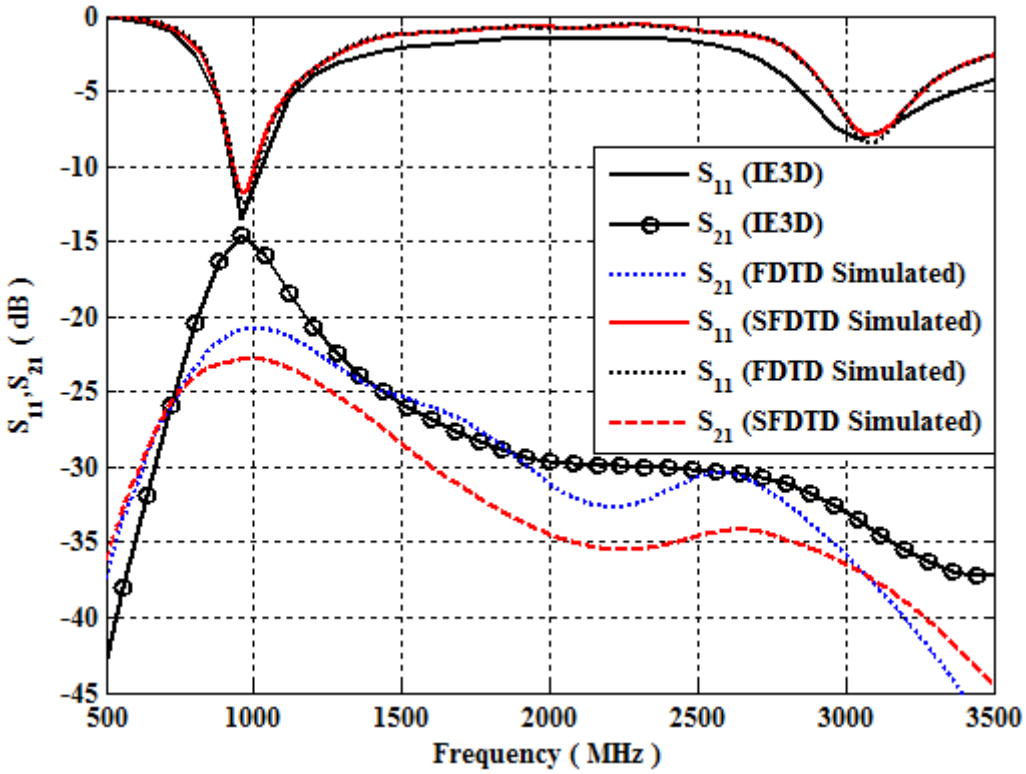

Figure 3.15. Variations of S_{11} and S_{21} of Tx-Rx pair separated by 20.0 cm calculated using SFDTD, FDTD and IE3D methods.

3.7.2 Monopole Antenna mounted Mobile Phone model

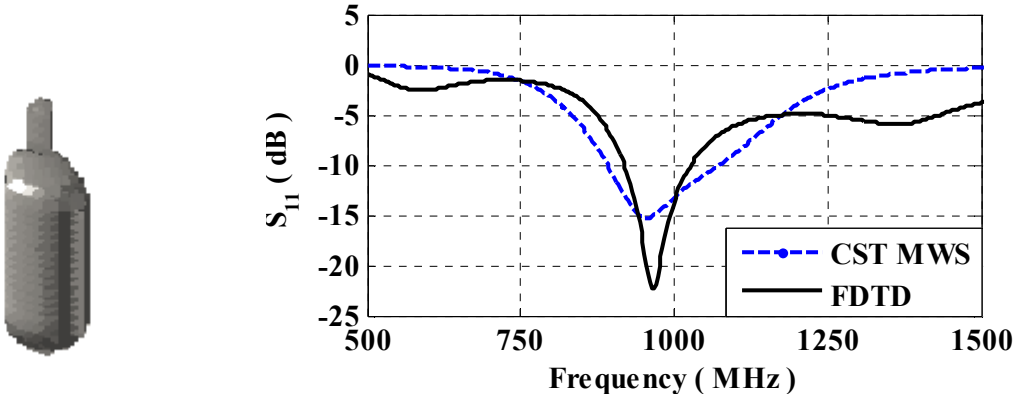

(a) **(b)**

Figure 3.16. (a) Mobile phone model and (b) it's return loss characteristics.

A simple mobile phone has been designed which consists of a monopole antenna made with aluminium having length of 4.0 cm and 5 mm × 5 mm cross sectional area placed on a metallic rectangular box of dimension: 3.2 cm × 4.6 cm × 9.9 cm as shown in the Figure 3.16. The classical one-cell gap model or delta gap model feeding used for thin-wire antenna has

been applied in the design of the mobile phone. *H* field components around the gap of the feeding point are given by [53]:

$$H_x^{n+1/2}(i,j+1/2,k+1/2) = H_x^{n-1/2}(i,j+1/2,k+1/2) + \frac{\Delta t}{\mu_0 \Delta}[\{E_y^n(i,j+1/2,k+1) - E_y^n(i,j+1/2,k)\} - \{E_z^n(i,j+1,k+1/2) + V^n/\Delta\}] \quad (3.42)$$

where, $(i,j,k+1/2)$ is location of the gap and V is an ac input voltage.

Return loss (S_{11}) of the mobile phone is computed using FDTD method in MATLAB and compared that with CST Microwave Studio®. Variations of S_{11} with frequency for the mobile phone placing in free space computed using MATLAB and CST Microwave Studio® are shown in Figure 3.16 (b). Nature of variation of S_{11} obtained using in-house FDTD based MATLAB program follows closely with that obtained using CST Microwave Studio®. For both the cases, at the fundamental mode, the mobile phone antenna resonates at 930 MHz and the value of S_{11} remains below –10 dB within GSM 900 band. Value of S_{11} at the fundamental resonance frequency obtained by the MATLAB program and CST Microwave Studio® are found to be –22 dB and –15 dB, respectively.

3.7.3 Compact Dual-Band PIFA mounted Mobile Phone model

The mobile phone is consisted of a compact dual-band Planar Inverted Folded Antenna (PIFA) design for GSM mobile. Three dimensional geometry of the PIFA which has been imported from CAD file available in literature is shown in the Figure 3.17 (a) [21]. The PIFA is encapsulated within a mobile handset housing of dimension 72 mm × 169 mm × 20 mm as shown in the Figure 3.17 (b).

Return loss of the mobile phone antenna (PIFA) is computed using the MATLAB program and compared with CST Microwave Studio® results. Variations of S_{11} with frequency for the mobile phone antenna computed using MATLAB and CST Microwave Studio® are shown in Figure 3.18. The result obtained using the MATLAB program shows close agreement with that obtained from CST Microwave Studio®. At the fundamental mode, the antenna resonates at 925 MHz and the value of S_{11} remains below –10 dB within GSM 900 band. Values of S_{11} at the fundamental resonance frequency obtained from MATLAB program and CST Microwave Studio® are –22.21 dB and –27.42 dB, respectively.

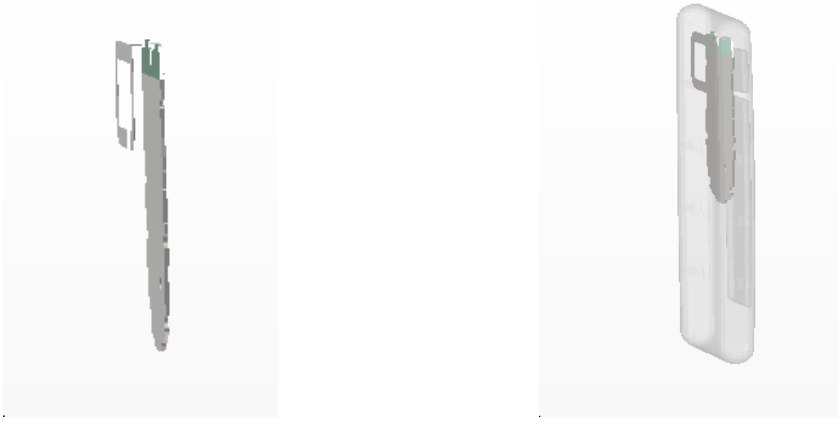

(a) (b)

Figure 3.17. (a) PIFA and (b) PIFA encapsulated within handset housing.

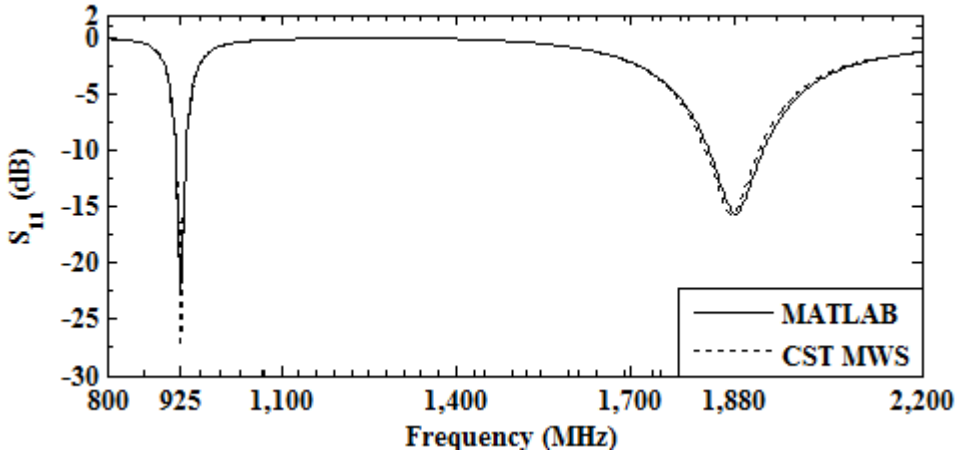

Figure 3.18. Variation of S_{11} vs. Frequency of the mobile phone antenna (PIFA) placed in free space.

3.7.4 Base Station Antenna model

Two generic BSA models have been designed in this study based on available commercial antenna models working within the GSM 900 band. One of them is the representative for the "Eurocell Panels" family of BSAs for vertical polarization offered by Kathrein working in the frequency range from 870 MHz to 960 MHz. Geometry of the antenna model is shown in Figure 3.19 which is reasonably close to that of the K730370 antenna and available in the literature [54],[55]. The BSA is an array of four collinear dipoles each having length of 14.5 cm and placed in front of a perfectly electrical conducting reflector of dimensions (height × width) 1280 mm × 240 mm. Horizontal conducting separators are used to reduce mutual coupling between radiating elements subdividing the

antenna into four segments that will be referred to as the unit cells. Transmitted power from BSA is equal to 20 W/carrier.

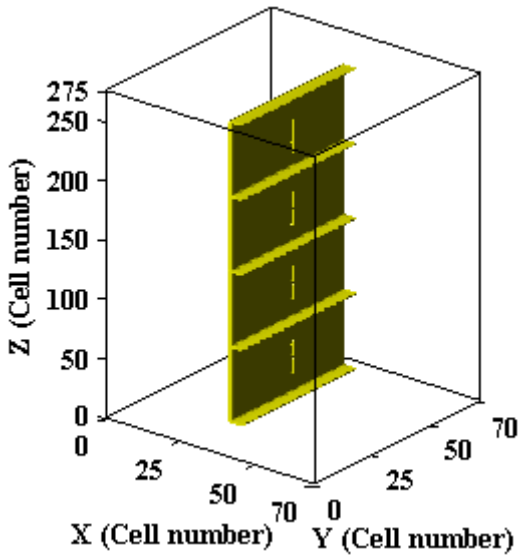

Figure 3.19. Three dimensional geometry of the Base Station Antenna (BSA).

Variations of S_{11} in dB and Gain in dBi with Frequency for a single dipole antenna and the BSA obtained by CST Microwave Studio® are shown in the Figures 3.20-3.21. From Figure 3.20, it is found that at the fundamental mode, the single dipole antenna and the BSA resonate at 928.9 MHz and 925.0 MHz with S_{11} value of -42.00 dB and -41.75 dB respectively. Value of S_{11} is below -20 dB within GSM 900 band. From Figure 3.21, it is found that maximum values of the gain are equal to 1.67 dBi and 6.37 dBi at 1000 MHz for the single dipole antenna and the BSA consists of cavity backed dipole array. At 925 MHz 5.75 dBi gain has been achieved for this BSA.

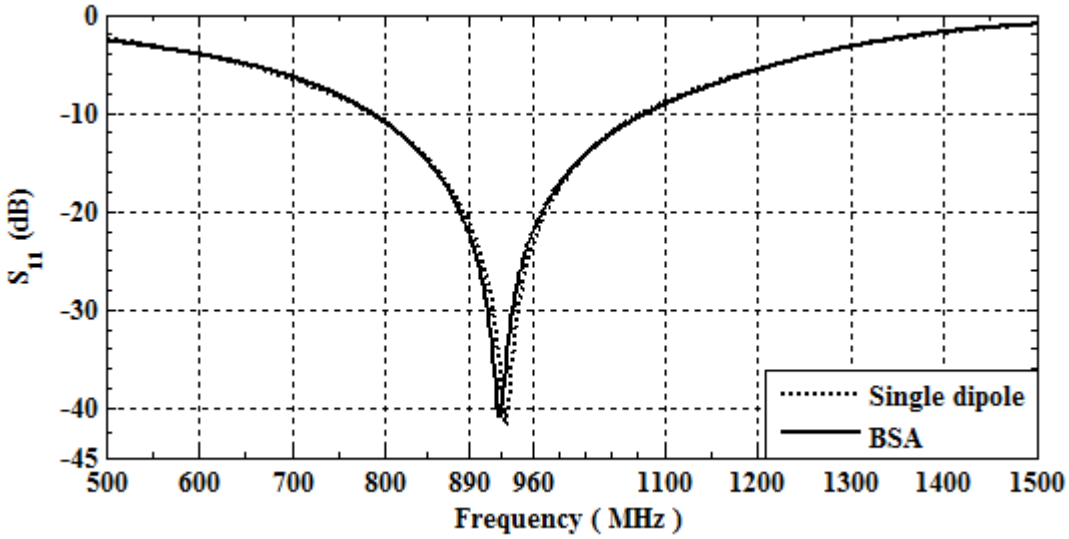

Figure 3.20. S_{11} vs. Frequency of single dipole antenna and BSA.

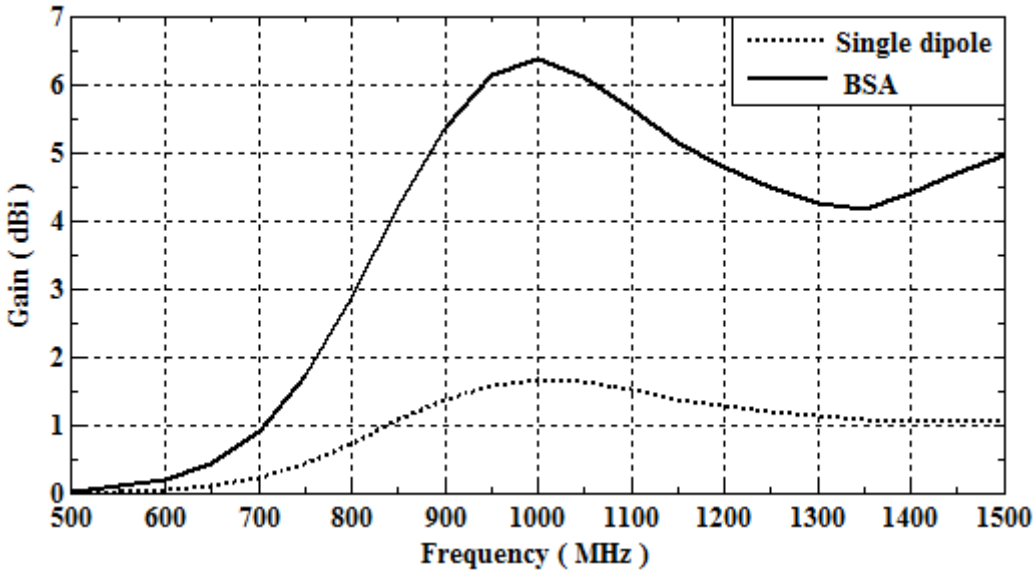

Figure 3.21. Gain vs. Frequency of single dipole antenna and BSA.

The other BSA is consisting of four optimized centre shorted suspended microstrip antenna. The designed of this BSA is described as follow:

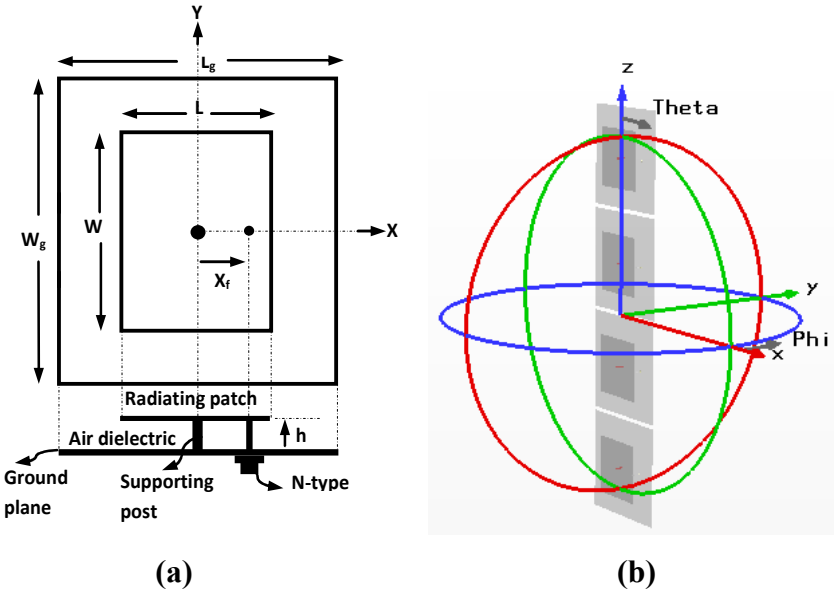

Figure 3.22. (a) Suspended microstrip antenna Configuration and (b) its linear array.

A centre shorted suspended microstrip antenna has been optimized for 925 MHz, using commercially available CST Microwave Studio® [21]. The antenna structure is shown in Figure 3.22 (a), where a shorting post of 1.0 cm diameter has been used to provide mechanical support to the suspended radiating patch. For an optimized antenna, the values of L_g, W_g, L, W, X_f and h are 250.0 mm, 250.0 mm, 140.0mm, 146.0 mm, 67.0 mm and 20.0 mm, respectively and it provides 14.02 dBi gain at 925 MHz. Once the high gain antenna is optimized, a BSA is designed using four optimized antenna placing vertically, maintaining 10.0 mm spacing between the elements as shown in Figure 3.22 (b). The optimized antenna is fabricated and its S-parameter is measured using Agilent ENA Series - E5071B (300 KHz - 8.5 GHz) Network Analyzer (NA) [56] shown in Figure 3.23.

Variations of simulated and measured values of S_{11} with frequency for the suspended microstrip antenna are shown in the Figure 3.24. Simulated S_{11} vs. frequency for the BSA is also included. At the fundamental mode, the antenna resonates at 925 MHz and the value of S_{11} remains below –10 dB within GSM 900 band. For the case of array, the minimum return loss frequency shifts slightly to 916 MHz which is possibly due to the mutual coupling between individual elements. However, at 925 MHz the designed array is still found to be suitable for this study.

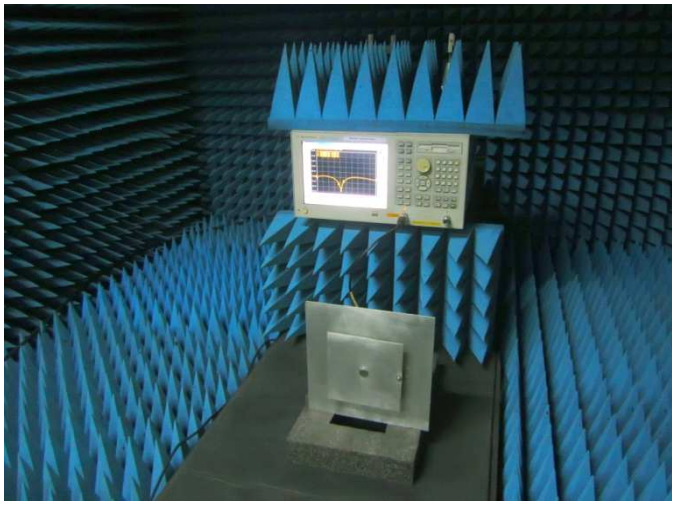

Figure 3.23. Fabricated suspended microstrip antenna and its S-parameters measurement setup.

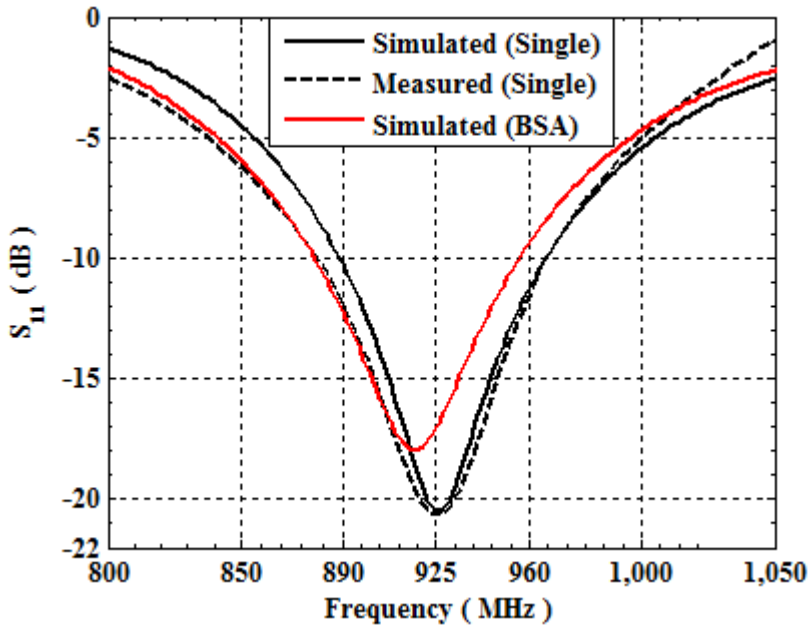

Figure 3.24. S_{11} vs. Frequency of the suspended microstrip antenna and BSA in free space.

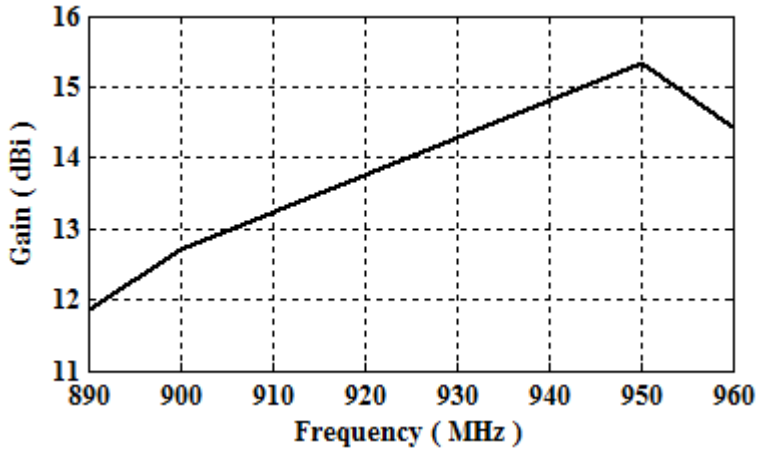

Figure 3.25. Gain vs. Frequency of the BSA in free space.

Gain vs. frequency plot for the BSA obtained using CST Microwave Studio® is shown in Figure 3.25. Maximum value of the gain is found to be 15.34 dBi near 950 MHz. At 925 MHz 14.02 dBi gain has been achieved. For this study 5 W of RF power has been applied to each element of this array to achieve total 20 W input power.

3.8 Conclusions

A brief review of the fundamentals of different type of standard computational and numerical EM methods which are used to calculate EM fields and other dosimetric parameters in this research work, has been summarised in this chapter.

An overview of SFDTD method and newly developed hybrid FDTD method by combining Friis transmission equation with FDTD method have also been presented in this chapter for solving large scale problems. In the hybrid FDTD method, EM modelling of the simulating elements is prepared using either conventional or non-uniform FDTD method and power calculation of the source required for the simulation is made by Friis transmission formula.

At the end of this chapter, typical radiating antennas applied in this research work as RF source have been designed using in-house FDTD code in MTALAB and to validate their characteristics, commercially available softwares CST Microwave Studio®, IE3D and Fidelity have been used.

References

[1] J.M. Osepchuk and R.C. Petersen, "Safety Standards for Exposure to RF Electromagnetic Fields," *IEEE, Microwave Magazine*, vol. 2, pp. 55-69, June 2001.

[2] M.N.O. Sadiku, Numerical Techniques in Electromagnetics, Second Edition, by, CRC Press LLC, 2001.

[3] A. Bondeson, T. Rylander, P. Ingelstrom, Computational Electromagnetics, *Springer*, 2005.

[4] S. Bilbao, "Wave and Scattering Methods for Numerical Simulation," *Wiley Interscience*, 2004.

[5] R. Talhi, "Computational Techniques and Numerical Analysis in E.M Wave Propagation and Scattering: An Overview and Trends," in proceeding of EMTS 2007 - International URSI Commission B - Electromagnetic Theory Symposium, Ottawa, ON, Canada, July 2007.

[6] R. Courant, "Variational methods for the solution of problems of equilibrium and vibrations," *Bull. Am. Math. Soc.*, vol. 49, pp. 1–23, 1943.

[7] M.N.O. Sadiku, "A simple introduction to finite element analysis of electromagnetic problems," *IEEE Transaction on Education*, vol. 32, No. 2, pp. 85–93, May-1989.

[8] S.I.Y. Al-Mously, Design and performance enhancement of cellular handset antennas and assessment of their EM interaction with a human, [Ph.D. thesis], Department of Electrical and Computer Engineering, School of Applied Sciences and Engineering Academy of Graduate Studies, Janzoor-Tripoli-Libya, August 2009.

[9] Richard.C. Booton, "Computational Methods for Electromagnetics and Microwaves," New York: *John Wiley & Sons*, 1992.

[10] J. Jin, "The Finite Element Method in Electromagnetics," New York: *John Wiley*, 1993.

[11] J.H. Richmond, ''Digital computer solutions of the rigorous equations for scattering problems," *Proc., IEEE*, vol. 53, pp. 796-804, Aug. 1965.

[12] R.F. Harrington, "Matrix methods for field problems," *Proc. IEEE*, vol. 55, No. 2, pp. 136-149, February 1967.

[13] Thomas.A. Milligan, "Modern Antenna Design," 2nd Edition, John Wiley & Sons, Inc., Hoboken, Published simultaneously in New Jersey and Canada, 2005.

[14] P. Stavroulakis, "Biological effects of electromagnetic fields," *Springer*-V erlag Berlin Heidelberg 2003, ISBN 3-540-429891.

[15] D. Krstic, "The influence of electromagnetic radiation in GHz bend on biological tissue," [PhD thesis], Nis: University of Nis, Faculty of Occupatinal Safety, Serbia, April 2010.

[16] K.S. Kunz, R.J. Luebbers, "The Finite-Difference Time-Domain Method," Boca Raton, FL: CRC., pp. 448, 1993.

[17] K.S. Yee and J.S. Chen, "The Finite-Difference Time-Domain (FDTD) and the Finite-Volume Time-Domain (FVTD) Methods in Solving Maxwell's Equations," *IEEE Trans. Antennas Propagation*, vol. 45, No. 3, pp. 354-363, March 1997.

[18] K.S. Yee, "Numerical solution of initial boundary value problems involving Maxwell' s equations," *IEEE Trans. Antenna Propagation*, vol. 14, No. 3, pp. 302-307, May 1966.

[19] T. Weiland, "A discretization method for the solution of Maxwell's equations for six-components fields," *Electronics and Comms.* AEU, vol. 31, No. 3, pp. 116-120, 1977.

[20] B. Krietenstein, P. Thoma, R. Schuhmann, and T. Weiland, "The perfect boundary approximation technique facing the big challenge of high precision computation," Proceedings of the 19th *LINAC* conference, Chicago, 1998.

[21] CST Microwave Studio Suite 2010, Available at: http://www.cst.com.

[22] O.P. Gandhi, "ELECTROMAGNETIC FIELDS: Human Safety Issues," *Annual Reviews Biomedical Engineering*, vol. 4, pp. 211–34, 2002. doi: 10.1146/annurev.bioeng.4.020702.153447.

[23] A. Taflove and S.C. Hagness, "Computational Electrodynamics: The Finite-Difference Time-Domain Method," Norwood, MA: Artech House, 2nd edition, pp. 852, 2000.

[24] F. Gustrau and D. Manteuffel, "EM Modelling of Antennas and RF Components for Wireless Communication Systems," *Springer*-Verlag Berlin Heidelberg, Germany, pp. 48-54, 2006.

[25] D.M. Sullivan, "Electromagnetic Simulation Using the FDTD Method," IEEE Press Series on RF and Microwave Technology, New York, 2000.

[26] Yasir Alfadhl, "Numerical evaluations on the interaction of electromagnetic fields with animals and biological tissues," [PhD thesis], Queen Mary, University of London, November 2005.

[27] K.L.Shlager and J.B.Schneider, "A selective survey of the finite-difference time-domain literature", *IEEE Antenna & Prop. Magazine*, vol. 37, No. 4, pp. 39-57, 1995.

[28] D.M.Sullivan, D.T.Broup and O.P.Gandhi, "Use of the Finite-Difference Time-Domain Method in Calculating EM Absorption in Human Tissues," *IEEE Trans. Biomedical Engineering*, vol. BME – 34, pp. 148-158, February1987.

[29] A.Taflove and M.E.Brodwin, "Numerical Solution of Steady-state Electromagnetic Scattering Problems Using the Time-Dependent Maxwell's Equations," *IEEE Trans. Microwave Theory Tech.*, vol. MTT – 23, No. 8, pp. 623-630, August 1975.

[30] C.M.Rappaport and L.J.Bahrmasel, "An absorbing boundary condition based on anechoic absorber for EM scattering computation," *Journal of Electromagnetic Waves & Applications*, Vol. 6, No. 12, pp. 1621-1633, 1992.

[31] C.M.Rappaport and L.J.Bahrmasel, "Reducing the computational domain for FDTD scattering simulation using the sawtooth anechoic chamber ABC," *IEEE Trans. on Magnetic*, vol. 31, No. 3, pp. 1546-1549, 1995.

[32] G.Mur, "Absorbing boundary conditions for the Finite-Difference Time- Domain electromagnetic-field equations", *IEEE Trans. on Electromagnetic Compatibility*, vol. 23, No. 4, pp. 377-382, November 1981.

[33] J.P.Berenger, "Perfectly Matched Layer for the FDTD Solution of Waves-Structure interaction problems", *IEEE Trans. Antenna Propagation*, vol. APT-44, No. 1, pp. 110-117, January 1996.

[34] J.P.Berenger, "A perfectly matched layer for the absorption of electromagnetic waves", *Journal Computer Physics*, Vol. 114, pp. 185-200, 1994.

[35] S.D.Gedney, "An Anisotropic PML Absorbing Media for FDTD Solution of Fields in Lossy Dispersive Media," *Electromagnetics*, vol. 16, pp. 399-415, 1996.

[36] R.J.Luebbers and H.S.Langdon, "A simple feed model that reduces time steps needed for FDTD antenna and microstrip calculations," *IEEE Trans. Antenna Propagation*, vol. APT- 44, No. 7, pp. 1000-1005, July 1996.

[37] H.Y. Chen and H.H.Wang, "Current and SAR induced in a human head model by the electromagnetic fields irradiated from a cellular phone," *IEEE Trans. Microwave Theory Tech.*, vol. MTT – 42, No. 12, pp. 2249-2254, December 1994.

[38] MATLAB, The MathWorks, Inc., Available at http://www.mathworks.com.

[39] S.S. Zivanovic, K.S. Yee and K. Mei, "A subgridding method for the time domain finite difference method to solve Maxwell's equations," *IEEE Trans. Microwave Theory Tech.*, vol. MTT – 39, No. 3, pp. 471-479, March 1991.

[40] M.E. Okoniewski, and M.A. Stuchly, "Three dimensional subgridding algorithm for FDTD," *IEEE Trans. Antenna Propagation*, vol. APT- 45, No. 3, pp.422-429, March 1997.

[41] M.J. White, M.F. Iskander and Z. Huang, "Development of a multigrid FDTD code for three dimensional applications," *IEEE Trans. Antenna Propagation*, vol. APT- 45, No. 10, pp. 1512-1517, October 1997.

[42] J. Svigelji, and R. Mitra, "Grid dispersion error using the nonuniform orthogonal finite difference time domain method," *Microwave Opt. Tech. Letter*, vol. 10, pp. 199-201, September 1995.

[43] D. White, M. Stowell, J. Koning, R. Rieben, A. Fisher, N. Champagne and N. Madsen, "Higher-oredr mixed finite element methods for time domain electromagnetics," Feb. 2004 [Online]. Available: http://www.llnl.gov/tid/lof/documents/pdf/304775.pdf.

[44] Y. Wu, and I. Wassell, "Introduction to the Segmented Finite-Difference Time-Domain Method," *IEEE Trans. on Magnetics*, vol. 45, No. 3, pp. 1364-1367, March 2009.

[45] G. Lazzy and O.P. Gandhi, "A Mixed FDTD-Integral Equation Approach for On-Site Safety Assessment in Complex Electromagnetic Environment," *IEEE Trans. Antenna Propagation.*, vol. 48, pp. 1830-1836, December 2000.

[46] D. Lautru, J. Wiart, W. Tabbara and R. Mitra, "A MoMTD/FDTD Hybrid method to Calculate the SAR induced by a Base Station Antenna," *IEEE* Antennas and Propagation Society International Symposium, vol. 2, pp. 757-760, 2000.

[47] A.R. Bretones, R.G. Martin and A. Salinas, "DOGTIGI, a Time Domain Numerical Code for the Study of the Interaction of Electromagnetic Pulse with Thin-Wire Structures," *COMPEL*, vol. 8. No. 1, pp. 39-61, 1989.

[48] L. Nonidez, M. Martinez, A. Martin, M.De. Mier and R. Villar, "Using FDTD and High Frequency Techniques in the Time Domain for SAR Assesment in Human Exposure to Base-Station Antennas," URSI International Union of Radio Science 2002, Proc. GA02, 08-July, 2002.

[49] John.D. Kraus and Ronald.J. Marhefka, "Antennas for All Applications," Tata Mc.Graw-Hill Publishing Company Limited, New Delhi, India, Third Reprint, 2003.

[50] L. Williams and S. Rosa, "Simple Derivation of Electromagnetic Waves from Maxwell's Equations," [Online] Available at: http://www.santarosa.edu/~lwillia2/42/WaveEquationDerivation.pdf.

[51] Zeland Software, Inc., Available at: http://www.zeland.com.

[52] H.S. Langdon and R. Luebbers, "Efficient FDTD calculation of Multi-ports S Parameters for Microstrip and Stripline Circuits," *IEEE Trans. Microwave Theory Tech.*, vol. MTT – 50, No. 9, pp. 998-1001, 1997.

[53] M.T. Islam and M.R.I. Faruque, "Reduction of Specific Absorption Rate (SAR) in the Human Head with Ferrite Material and Metamaterial," *Progress In Electromagnetic Research C*, vol. 9, pp. 47-58, 2009.

[54] A. Karwowski, "Comparison of simple models for predicting radiofrequency fields in vicinity of base station antennas," *Electronics Letters*, vol. 36, No. 10, pp. 859-861, May 2000.

[55] A. Loula, "Open BTS: Installation and Configuration Guide," vol. 0.1, 2009.

[56] Agilent [Home], http://www.home.agilent.com.

Chapter 4

Study on SAR analysis inside Human Body

4.1 Introduction

The study of interaction between biological elements with EM fields is referred to as bio-electromagnetics based on several established mechanisms for each of the EM field components. The *E* fields are associated with forces exerted by electric charges whereas the *H* fields exist as a result of the physical movement of electric charges defined as electric currents. Under the influence of EM field exposure, the time varying *E* field changes the orientations of the dipoles within the biological tissue and modifies their intermolecular structure. The reorientation of the dipoles creates a flow of electric charges that forms the electric current flow. The time varying *H* field components are, however, responsible for inducting internal *E* fields and circulating electric currents. The magnitudes of dipole polarisation, charge induction and electric current flow are related with EM properties of the tissue i.e. permittivity and conductivity, the strength and polarisation of the applied field, and the dimensions of the body. A huge amount of research on the biological effects caused by exposure to RF radiation is available in the literature [1]-[5].

Interaction of EM fields with the biological objects is a complicated subject due to the complex nature of the biological objects. This EM interaction due to the presence of the biological objects closed to the EM sources can be looked at from two different points of view. Firstly, the EM source has an impact on the biological object, which is often understood as the exposure of the biological object to the EM field of the radiating device. Secondly, the biological object has an impact on the EM source parameters. Impedance, radiation characteristic, radiation efficiency and Total Isotropic Sensitivity (TIS) of the EM source will be affected by the properties of the biological tissue.

In order to understand the effects of EM fields on biological tissues, it is necessary to determine the magnitude of the exposed EM fields within the various parts of the biological object which depends on the many parameters like dielectric properties of the different types

of biological tissues, signal type, field strengths etc [6],[7]. But the small size and thickness of cells and their thin membranes cause great difficulty in experimental and numerical dosimetry.

In this chapter several new studies have been carried out to explore the effects of non-ionizing EM radiation on human body and body parts considering different models and techniques. Many new methodologies have been proposed and compared with existing methodologies. Some new methodologies like number or density of hot spots are also proposed and discussed in the next chapter.

4.2 Existing Methodologies for Assessment of the EM field interaction with Human Body

Direct measurement of the EM field components and other dosimetric parameters inside a living body is very difficult. Equivalent homogeneous head or other body models are used in the experimental method with the actual phone for the measurement of the dosimetric parameters, but these homogeneous models are not a faithful representation of the complex heterogeneous human organs because actual electrical properties of different tissues are not considered. Therefore, the numerical EM techniques are used to calculate EM field components and other dosimetric parameters inside human head or other body parts which involve careful specification of the human body and the irradiation conditions. There are different types of numerical EM methods available to calculate the required parameters, discussed in detail in Section 3.2. Each of these techniques provides information over a limited range of parameters with certain level of accuracy.

4.2.1 Concept of Dosimetry

Dosimetry is generally defined as the fundamental process of quantifying the EM energy absorbed inside biological materials. Measurements of the EM energy absorption within the biological objects can be carried out finding averaged field strength considering the tissue electrical properties at the specific location. Commonly used dosimetric parameters to assess the EM exposure of biological systems are: specific absorption (SA), SAR, power density, E field, H field etc. The dosimetric parameters can be evaluated using either experimental measurements or numerical computations required EM sources to expose the biological objects. Experimental measurements make use of the actual EM sources such as

mobile phone, BSA or any other wireless mobile communication devices together with a simple homogeneous model of human head/full body or other living subject consisting of two or three type tissues acting as biological object. Whereas, numerical computational methods e.g., FDTD method, MoM method etc., are capable of using simple homogeneous model to complicated MRI and DICOM data based heterogeneous anatomically correct voxel type human head/full body model consisting of more than thirty different tissues as biological object and similarly, various type of EM sources such as half-wave resonating dipole antenna, monopole antenna etc., can be modelled to obtain desired enhanced characteristics [8]-[9].

In this chapter, FDTD, hybrid FDTD, SFDTD and FIT methods are used to study the EM interaction of the human head and body only. Different type of human head/body models, i.e., homogeneous, heterogeneous and voxel based distributed, and different handset models, i.e., simple and semi-realistic models of cellular handset and BSA are used in computations of EM energy absorption. The prediction of the EM interaction is mainly based on evaluating the SAR and EM power absorbed in tissues. Half-wave resonating dipole or monopole antennas with the semi-realistic CAD based cellular mobile phone and BSA designed at GSM 900 band are considered in different dosimetric calculations. Homogeneous box type, three layered spherical type human head models, freely available MRI-based heterogeneous anatomically correct human head model and DICOM data based voxel type human head models have been involved in simulations. DICOM data based human hand model consisting of three different tissues (bone, muscle and skin) has also been included in the simulations. Primarily, an FDTD-based platform is used to evaluate the EM wave interaction. Then to validate the results obtained using FDTD method, commercially available FDTD based EM simulation software FIDELITY and FIT based CST Microwave Studio® have been used. Hybrid FDTD method has been used to calculate SAR_{WB} induced within the full human body model exposed to a BSA at GSM 900 band for a distance in the range of 0.5 m to 5.0 m between the human body and the BSA, and compared that with the results obtained by SFDTD method for multiple number of carrier frequencies.

4.2.2 Specific Absorption Rate (SAR)

The dose rate at which EM energy at RF imparted into the human head and other body parts is measured in terms of SAR. It is defined as the rate at which a person absorbs EM energy per unit mass and is expressed in watts per kilogram (W/kg) of biological tissue [11].

It has also been internationally accepted that SAR is the most appropriate metric for determining EM energy exposure in the very near field of a RF source [12]-[20]. For safety evaluation, SAR is generally quoted as a figure averaged over a tissue volume which is still not harmonized among the different countries and states [21]. SAR averaged over *X*-g of tissue can be denoted by *X*-g SAR. In this way, local peak SAR averaged over 1-g of tissue is called peak 1-g SAR. In USA, the SAR limit is specified as 1.6 W/kg, averaged over one gram of tissue in the shape of a cube [19], [22],[23]. But in Europe and Japan, the SAR limits are specified as 2.0 W/kg, averaged over ten gram of tissue [24].

There are two separate recommended ways to measure SAR. One is based on experimental technique and the other based on numerical EM technique [25]. Robot-controlled miniature field probes are used to scan the *E* field inside a homogeneous tissue-simulating liquid filled anthropomorphic human body model in the experimental technique [26]. On the other hand in numerical technique full wave numerical methods like FDTD method, FEM or MoM are used to solve Maxwell's equations in a homogeneous/heterogeneous representation of the human head or other body parts developed from CT or MRI scans of human head or other body parts, respectively. In the experimental technique, the homogeneous body model is not a faithful representation of the actual human head or other body parts. On the other hand, direct measurement of SAR is not possible inside a living human head or other body parts using the experimental techniques. Therefore, generally the numerical technique is used to calculate EM field components and SAR inside human head or body parts. But numerical technique can be costly and can take as long as several hours [26]. Typical experimental SAR measurement setups are shown in Figure 4.1.

In the FDTD method, *E* fields are calculated at each Yee cell and consequently, the *x*, *y* and *z*-directed components associated with a cell are defined in different spatial locations. These components are combined to calculate SAR in the cell. From the converged solutions the local SAR at $(i,j,k)^{\text{th}}$ cell inside the scattering object is obtained from the following relation [27]:

$$\text{SAR}(i,j,k) = \frac{\sigma(i,j,k)\left|\hat{E}(i,j,k)\right|^2}{2\rho(i,j,k)} = \frac{\sigma(i,j,k)\left\{\left|\hat{E}_x(i,j,k)\right|^2 + \left|\hat{E}_y(i,j,k)\right|^2 + \left|\hat{E}_z(i,j,k)\right|^2\right\}}{2\rho(i,j,k)} \quad \text{(W/kg)} \qquad (4.1)$$

where, $\hat{E}_x$, $\hat{E}_y$ and $\hat{E}_z$ are the peak values of the electric-field components (V/m), σ = conductivity (S/m) and ρ = mass density of the head/body tissue (kg/m³).

(a) **(b)**

Figure 4.1. Experimental SAR measurement setups: (a) IndexSAR company, http://www.indexsar.com and (b) SPEAG (DASY5), http://www.speag.com.

There are three possible approaches to calculate the SAR: the 3-, 6-, and 12-field components approaches. Among them the 12-field components approach is the most complicated but it is also the most accurate and appropriate from the mathematical point of view [28]. For these reasons, the 12-field components approach is preferred by IEEE-Std. 1529.

4.2.2.1 Spatial Averaging SAR

Safety guidelines or standards for protecting human head and other body parts from the adverse biological effects due to RF exposure have been issued in various countries and states, in which the basic safety limits are being set in terms of SAR. In theses safety guidelines or standards, a tissue volume over which the SAR should be averaged is required for safety evaluation. As the animal bodies consist of a vast number of tissue types distributed inside the body forming regions (or organs) of different shapes, sizes, and mass densities so, averaging data over a fixed volume is therefore very difficult and even not possible over an inhomogeneous volume of tissues. Moreover, the tissue volume required for SAR average is still not harmonized among the different countries and states [29]. SAR averaged over *X*-g of tissue can be denoted by *X*-g SAR. In this way, peak SAR averaged over 10-g and 1-g of

tissue are called peak 10-g SAR and peak 1-g SAR, respectively. In USA, IEEE [12],[14],[22] and FCC [19],[23] have recommended peak 1-g SAR not exceeding 1.6 W/kg as the upper safety limit. But in Europe and Japan, ICNIRP [21] has recommended peak 10-g SAR not exceeding 2.0 W/kg as the upper safety limit.

The derivation of the average SAR values needs some post-processing of the calculated SAR. Normally, a simple cubic tissue can be used for evaluating gram average SAR provided that the calculated SAR has conservative values relative to the safety guidelines/standards of RF exposure. But it has been observed that in case of the strongly curved and irregular surfaces large differences occur depending on the averaging procedure. There are two commonly used SAR averaging procedures to get 1-g or 10-g SAR [30]:

(a) Considerations on the Cube Averaging,

(b) Considerations on the Irregular Volume Averaging.

4.2.2.1.1 Considerations on the Cube Averaging

The IEEE averaging procedure recommends considering a tissue sub-volume such that it does not extend exterior surfaces of the body, but may have pockets of air within it [31]. The above IEEE recommendation has been defined for 1-g SAR but it can also be applied to evaluate 10-g SAR [32],[33] .The mass of each sub-volume may not be smaller than the averaging mass of 1-g or 10-g but preferably as close to it as possible. In this method, averaging of SAR over the 1-g or 10-g mass of tissue in the body should be considered separately for each type of tissue. Any other tissue type contained within the cube volume should be treated as air (mass = 0 and SAR = 0).

In this technique, selection of the averaging volume for the derivation of average SAR distributions is crucial. According to the European Committee for Electrotechnical Standardization (CENELEC), shape of the averaging volume is a cube and must exactly contain 10-g of tissue for calculating 10-g SAR. The cube volumes used for calculating the 10-g SAR are shown in Figure 4.2 [33].

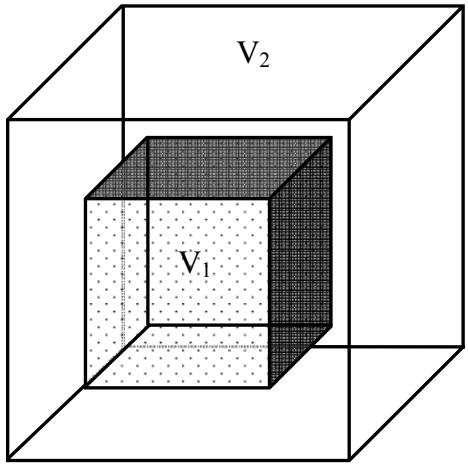

Figure 4.2. The cube volumes used for calculating the 10-g SAR.

10-g SAR is subsequently calculated considering the contribution of the smaller cube (V_1 = 10-g) and the contribution of the cubical shell around it each with a predefined weighting coefficient using equation (4.2):

$$SAR_{10} = \frac{\sum_{v1} (SAR)_i \, m_i + \sum_{v2-v1} (SAR)_j \, m_j}{\sum_{v1} m_i + \sum_{v2-v1} m_j} \qquad \text{(W/kg)} \qquad (4.2)$$

where, $m_i = \rho_i \Delta V$ and $m_j = P_j \Delta V \frac{10\text{-}V_1}{V_2\text{-}V_1}$ [32]. Index *i* refers to the lattice cells inside the inner cube and index *j* to those around it. Similarly, 1-g SAR can be calculated by the equation (4.2) with the predefined weighting coefficient V_1 = 1-g.

4.2.2.1.2 Considerations on the Irregular Volume Averaging

In irregular volume averaging technique, 1-g SAR is obtained by finding the maximum value of local SAR in an FDTD cell and then finding the neighbour cell with next higher local SAR, and so on [30]. The process is repeated until total mass of the FDTD cells becomes equal to the required mass of 1-g. Similarly peak 10-g SAR is calculated. In this technique, the volume of the scattering medium should be coherent which itself makes the procedure slightly complicated. Unlike, the cube averaging procedure use of the irregular volume averaging procedure is not limited to symmetrical SAR distributions, but can be applied to any situation. In case of a curved and irregular shaped object, irregular volume averaging procedure provides better result compare to the cube averaging procedure. In this research work, to find the gram average SAR the irregular volume averaging procedure has been applied.

4.2.2.2 Time Averaging SAR

More realistic averaging times are incorporated in the 1991 standard in order to address a number of issues including exposure to short high peak power pulses. The averaging time included in the following way:

a. In the frequency region where surface heating predominates, the averaging times decrease with increasing frequency and vice-versa.
b. For exposures in controlled environments, the averaging time decreases from a value of 0.1 hr or 6 minutes at 15 GHz to 10 s at 300 GHz and decreases from 0.5 hr or 30 minutes at 15 GHz to 10 s at 300 GHz for exposures in uncontrolled environments.
c. The shorter averaging time mitigates against conditions where skin burns could occur from short but intense exposures to small areas of the skin, which would be permitted with the longer averaging times found in the National Council on Radiation Protection and Measurements (NCRP) recommendations and the 1982 ANSI C95.1 standard.

The most universal averaging time is 6 minutes but in specific standards there can be a number of variations. As the SAR limits are averaged over a time period of 6 minutes with a safety margin of 3 to 4 [34]. So, a person should not use cell phone for more than 18 to 24 minutes per day. This information is not known to the common people in India, so crores of people who are using their cell phones for more than an hour per day without realizing its associated health hazards may be seriously affected.

4.2.2.3 Localised and whole-body Averaged SAR (SAR_{WB})

The SAR_{WB} is defined as the total power absorbed averaged over the total absorbing body mass. SAR_{WB} is calculated in those cases where the averaging mass is very small and SAR_{WB} can be expressed as the total SAR averaged over the total mass of the body part of concern [35]. In this research work, to find the SAR_{WB} the irregular volume averaging procedure has been applied.

After calculation of SAR at each FDTD cell of the absorbing body, Maximum local SAR (MLSAR) is calculated. MLSAR is obtained by finding the maximum value of SAR for the whole absorbing body at each frequency and the location of MLSAR may or may not be same for different frequency.

4.2.3 SAR Exposure Limits

Safety limits for EM exposure in the RF band defined by various national and international organisations are commonly assessed in terms of SAR. These guidelines indicated by the different agencies are based on the current evidence suggesting non-adverse biological effects below these restrictions and on the established frequency-dependent coupling mechanisms through which time-varying fields interact with living matter [36].

The ICNIRP has specified in its safety guidelines that the maximum permitted SAR values for occupational exposure are five times higher for the general public exposure as shown in Table 4.1 [21],[37]. For the frequency range 100 kHz to 10 GHz, basic restrictions on exposure are considered to prevent whole-body heat stress and excessive localised tissue heating. Most regions, such as Europe, Korea, Japan and India, are adopting or intending to adopt the ICNIRP guidelines.

Table 4.1: Occupational and public SAR limits considered by ICNIRP

Frequency range (100 kHz – 10 GHz)	SAR (W/kg)		
	Whole-body Average	Spatial peak in the head and trunk	Spatial peak in Limbs
General Public	0.08	2	4
Occupational	0.4	10	20

The FCC and the IEEE (Standard C95.1 –1999) have adopted stricter peak SAR limits for the frequency range 10 KHz to 6 GHz are shown in Table 4.2 [22],[23],[38]. Under controlled environments, the maximum permitted SAR_{WB} has been restricted to 0.4 W/kg whereas, peak localised SAR values averaged over 1-g were restricted to 8 W/kg for all type of tissues, except for the hands, wrists, feet, and ankles where the peak SAR averaged over 10-g of tissue was permitted to reach up to 20 W/kg. For uncontrolled environments, the SAR_{WB} has been allowed up to 0.08 W/kg, and the spatial peak SAR was restricted up to 1.6 W/kg (1-g averaged) for all type of tissues, except for the hands, wrists, feet, and ankles where the peak SAR was permitted up to 4 W/kg (10-g averaged).

Table 4.2: FCC and IEEE SAR guidelines for controlled and uncontrolled exposure

Frequency range (10 kHz – 6 GHz)	SAR (W/kg)		
	Whole-body average	Spatial peak in the head and trunk	Spatial peak in Limbs
Controlled Environment	0.4	8	20
Uncontrolled Environment	0.08	1.6	4

In the UK, NRPB specified the maximum occupational and general public SAR limits for the frequency range 10 MHz to 10 GHz are shown in Table 4.3 [39]. The survey work described in this guideline is concerned only with exposure to EM fields with frequencies above 10MHz. Compliance with NRPB guidelines is demonstrated by showing that none of the basic restrictions is exceeded. The restrictions permit short-term time-averaging so transient exposures may be averaged over specified periods before comparison with the restrictions.

Table 4.3: Occupational and general public SAR limits assigned by NRPB

Frequency range (10 kHz – 6 GHz)	SAR (W/kg)		
	Whole-body average	Spatial peak in the head and trunk	Spatial peak in Limbs
Occupational	0.4	10	20
General Public	0.4	10	20

4.2.4 Additional Investigation/Reference levels

There is no practical way of measuring the SAR in a living human being. In order to make calculations of SAR, either computer modelling or practical experiments with dummy persons using substances which simulate the electric characteristics of human tissues are undertaken. In addition, degree of absorption of RF energy by the human body varies with frequency and can be divided into four frequency ranges [39]. From about 100 kHz to less than about 20 MHz, absorption in the trunk decreases rapidly with decreasing frequency and significant absorption may occur in the neck and legs. Relatively high absorption can occur in the whole body for the range from about 20 MHz to 300 MHz and to even higher values if partial body (e.g. head) resonances are considered. For the frequency range from about 300

MHz to several GHz, significant local, non-uniform absorption occurs. Frequencies above about 10 GHz, absorption occurs primarily at the body surface. So, three additional investigation/reference levels: *E* field, *H* field and power density (P_d) have been introduced by the safety guidelines which can be measured separately.

Layout of the criteria for deriving the four reference values with the actual frequency ranges are shown in Figure 4.3. Below 100 kHz, electrical effect predominates and above 10 GHz, absorption occurs primarily at the body surface due to skin effect. So, in those frequency ranges calculation of all type of SARs are avoided. But SAR calculations are preferred in the frequency range between 100 kHz to 10 GHz. It should not be thought that the division lines imply exact limits of influence, but rather, that they imply the predominance of an effect. The ICNIRP has specified the maximum values of the additional three references for the general public and occupational exposures in the frequency range from 10 MHz to 300 GHz are shown in Table 4.4 where *f* is the frequency in MHz.

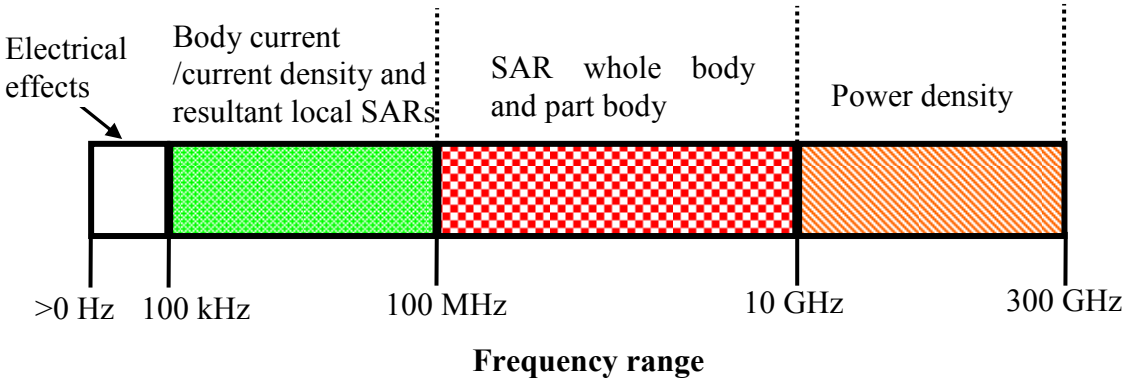

Figure 4.3. Layout of the criteria for deriving reference values.

Table 4.4: Electromagnetic exposure reference levels assigned by ICNIRP

Frequency Range	Electric field strength (V/m)		Magnetic field strength (A/m)		Power density (W/m^2)	
	General public	Occupational	General public	Occupational	General public	Occupational
10-400 MHz	28	61	0.073	0.16	2	10
400-2000 MHz	$1.375f^{1/2}$	$3f^{1/2}$	$0.0037f^{1/2}$	$0.008f^{1/2}$	$f/200$	$f/40$
2-300 GHz	61	137	0.16	0.36	10	50

The three references used for investigating compliance with NRPB guidelines are related to each other and in certain instances it is only necessary to measure one of them. Maximum values (rms) of the three references for the frequency range from 12 MHz to 300 GHz specified by the NRPB are shown in Table 4.5 where f is the frequency in GHz.. The FCC and IEEE/ANSI have produced a lot of detailed guidance in a series of documents which are available in the literature [19],[22],[23],[38]. FCC limits for general application in assessing installations, differs markedly from the IEEE99 standard.

Table 4.5: Electromagnetic exposure reference levels assigned by NRPB

Frequency range	Electric field strength (V/m)	Magnetic field strength (A/m)	Power density (W/m^2)
12-200 MHz	50	0.13	6.6
200-400 MHz	$250f$	$0.66f$	$165f^2$
400-800 MHz	100	0.26	26
0.8-1.55 GHz	$125f$	$0.33f$	$41f^2$
1.55-300 GHz	194	0.52	100

4.3 Assessment of the EM field Interaction with Human body

Assessment of biological effects due to the EM energy absorption in the human head and other body parts is quickly becoming the area of interest of many researchers. The

interest has been accentuated after the launching of second-generation mobile communication systems in 1991. Numerical simulations hold very significant role since it is not possible to actually measure the distribution of EM fields or SAR values inside a living human head/body. So, during the last several years, there have been increasing interests in the application of different numerical methods, different human head models, different cellular handset models, different hand models, and different standard and non-standard usage patterns to calculate the intensity of EM fields. This causes variation of results. The causes of discrepancies in computations have been well investigated [40],[41]. Figure 4.4 shows a layout by means of block diagram representation of the numerical computation procedure for calculations of EM fields, SAR, temperature and the antenna performance due to the EM interaction of realistic usage of a cellular handset, BSA and plane wave using different numerical methods. Proposed newly developed methodologies, models and parameters are shown in *bold* front. Assessment accuracy of the EM interaction depends on the following:

a. EM source modelling. This includes simple mobile handset model (i.e., half-wave resonating dipole antenna, monopole antenna mounted over a metal box), BSA (e.g., Kathrein K730370 [42]), realistic mobile phone (e.g., compact dual-band PIFA) and plane wave source.
b. Human head modelling (i.e., homogeneous box and heterogeneous three layered sphere). For the realistic head model (i.e., CT scan based e.g., Zubal phantom, DICOM head and MRI based DICOM head), the number of tissues, resolution, slice thickness and tissue parameters definition, all playing an important role in computing the EM interaction.
c. Human hand modelling (i.e., CT scan based DICOM hand).
d. Realistic full body modelling (i.e., CT scan based Zubal phantom).
e. Positioning of handset and BSA with respect to head, hand and full body models.
f. Electrical properties definition of the handset material and human tissues.
g. Numerical method (e.g., FDTD, SFDTD and hybrid FDTD methods). Applying the FDTD method, the grid-cell resolution and unsplit step PML acting as ABC should be specified in accordance with the available hardware for computation. Higher resolution and higher ABC needs a faster CPU and larger memory.
h. EM simulator e.g., FDTD based FIDELITY, FIT based CST Microwave Studio®, MOM based CAD-FEKO and IE3D have been applied for validation of the results obtained by the numerical methods.

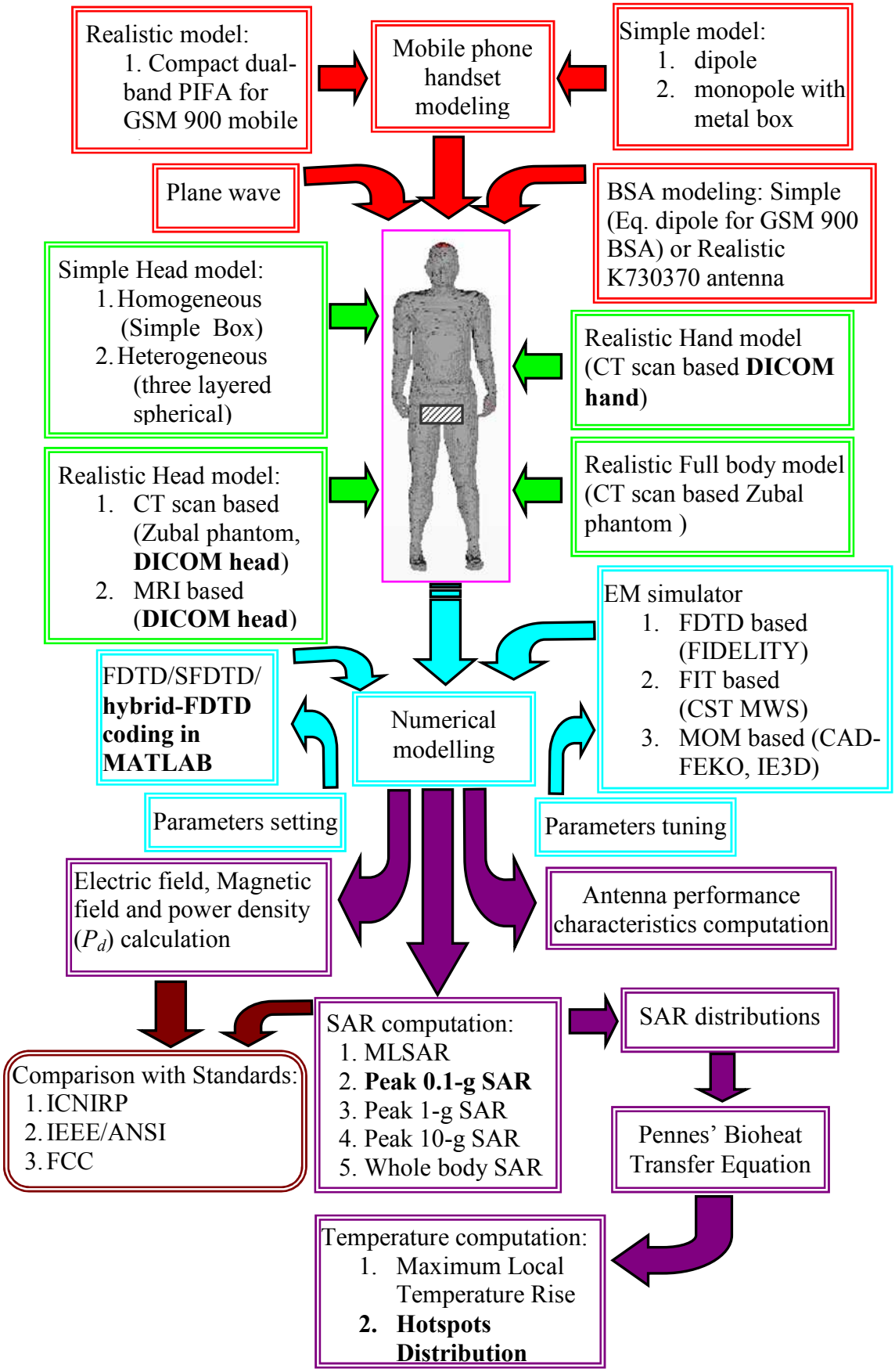

Figure 4.4. Block diagram illustrating the numerical computation of the EM interaction of RF source and human being.

4.3.1 SAR Evaluation in a homogeneous box type head model

SAR induced inside a human head exposed to EM waves radiated from a half-wave dipole antenna with input power of 0.6 W at the frequency range from 500 MHz to 5 GHz has been calculated using FDTD method. For simplicity, the human head is modelled as a rectangular cube consists of 40×40×50 Yee cells and the dielectric constant and conductivity of human head are assumed to be homogeneous, where Yee cell length is δ = 0.5 cm. A metal made half-wave dipole antenna having length of 15.5 cm and diameter of 0.5 cm is chosen as the radiating element. The geometry of the dipole antenna along with human head model used for the simulation is shown in Figure 4.5.

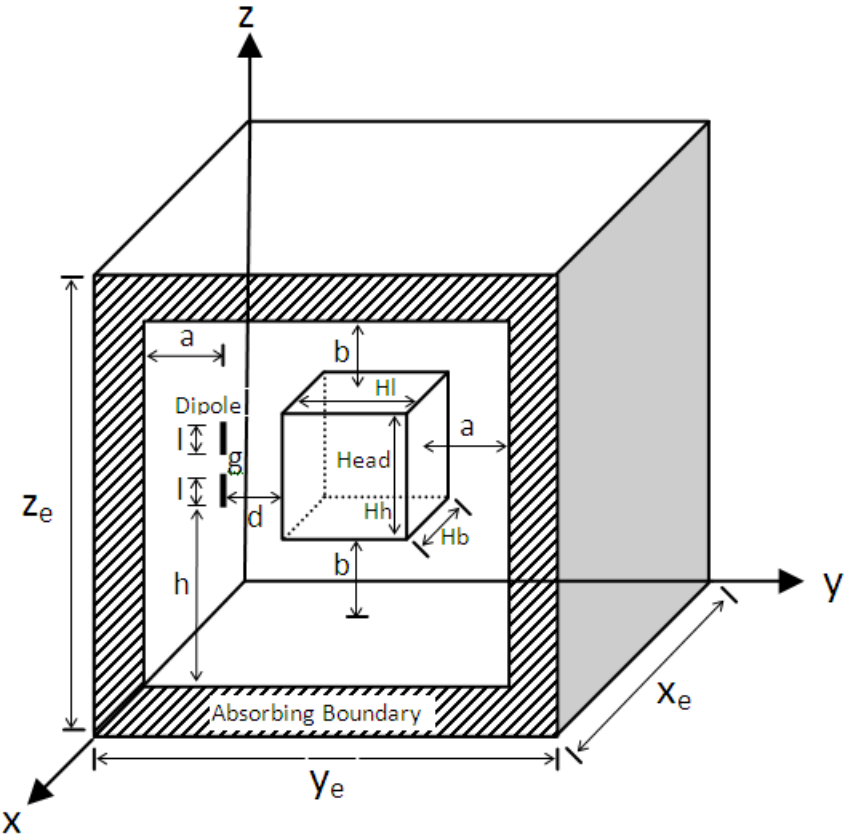

Figure 4.5. Geometry of the dipole antenna and the human head model used for simulation by the FDTD method [*Xe* = 54δ, *Ye* = 58δ, *Ze* = 62δ, a = b = 2δ, *l* = 15δ, *g* = 1δ, *Hl* = 40δ, *Hb* = 40δ, *Hh* = 50δ].

Human head is inhomogeneous in nature but in this simulation it is considered to be homogeneous for simplicity. The mass density ρ of the human head is taken as 1050 kg/m^3. Variation of dielectric constant (ε_r) and conductivity (σ) of human head at the different frequencies have been taken into consideration to calculate SAR. Average values of ε_r and σ of the human head at the desired frequency range were interpolated from the Table 4.6 [43]-

[45]. Distance (*d*) between the head and dipole antenna is varied in the range of 1.0 cm to 3.0 cm to calculate MLSAR. It is found that MLSAR induced in the head is below the FCC and IEEE's upper safety limit when distance of the head from the dipole antenna is more than 1.0 cm for the entire frequency range. Instead of SAR, MLSAR induced in the human head model had been calculated which gives more information regarding the biological effects of the EM fields inside head. MLSAR induced in human head obtained for the frequency range of 500 MHz to 5 GHz for a set of distances in the range of 1.0 cm to 3.0 cm is shown in the Figure 4.6. When the distance '*d*' is less than or equal to 1.0 cm then the MLSAR becomes more than the FCC and IEEE's upper safety limit (1.6 W/kg) [22],[23]. It is also obtained that as the distance increases over 1.0 cm the value of the MLSAR goes below the upper safety limit. For all '*d*', due to significant amount of energy transfer from antenna to head, the peak value of MLSAR has been found near the fundamental mode of operation of the antenna. But at the other resonating frequencies the value of MLSAR doesn't rise significantly due to higher reflection of EM wave from the surface of the head which results in smaller absorption. MLSAR also decreases faster in higher frequency range due to smaller penetration depth.

Table 4.6: Relative dielectric constant (ε_r) and conductivity (σ) of the human head at the different frequencies

Frequency (MHz)	Dielectric Constant (ε_r)	Conductivity σ (S/m)
100	82.0	0.53
350	60.0	0.65
900	56.8	1.1
1800	51.8	1.5
2450	48.9	1.81
6000	30.0	5.3

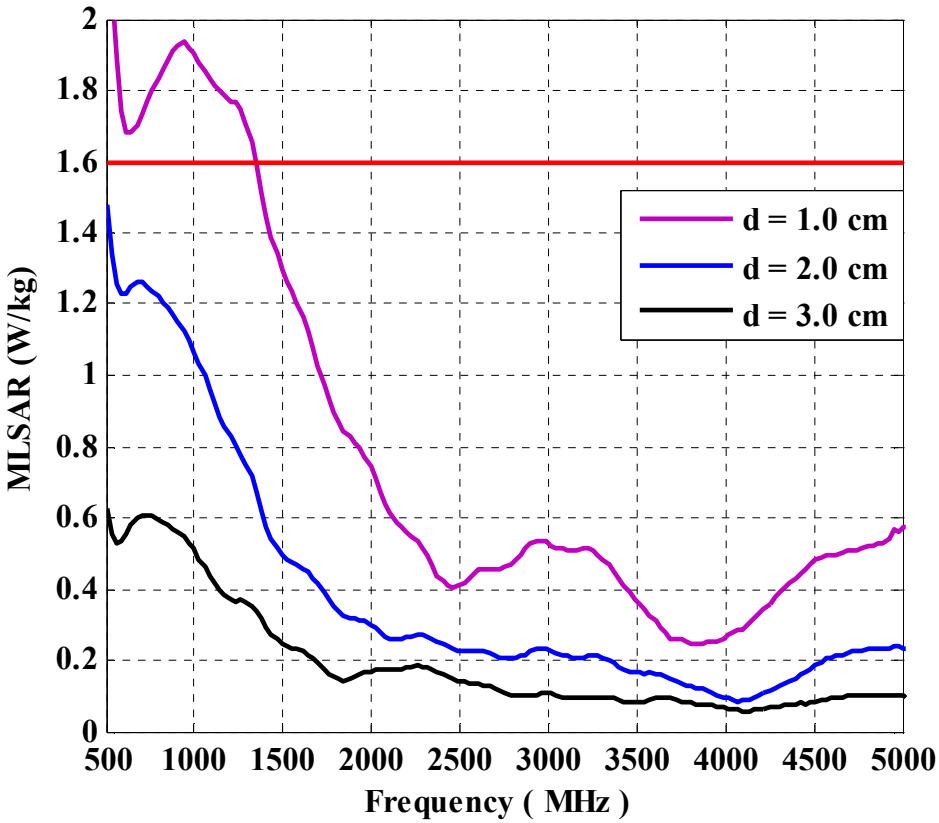

Figure 4.6. MLSAR distributions in the box type human head model for various distance '*d*'.

4.3.2 SAR Evaluation in a three layered spherical head model

A more realistic model is developed where a three layered inhomogeneous sphere of 38 Yee cells diameter consisting of a uniform core surrounded by two spherical shells representing brain, skull and skin respectively with their respective EM properties is considered for FDTD simulation. Exposing the head model by the same dipole antenna used in the previous section, MLSAR induced inside the head model at the frequency range 500 MHz to 3 GHz using FDTD method is calculated for a set of distances in the range of 1.0 cm to 3.0 cm. The geometry of the dipole antenna along with human head model used for the simulation is shown in Figure 4.7. Average values of ε_r and σ of brain, bone and skin of human head at the desired frequency range have been interpolated from the Table 4.7 [46].

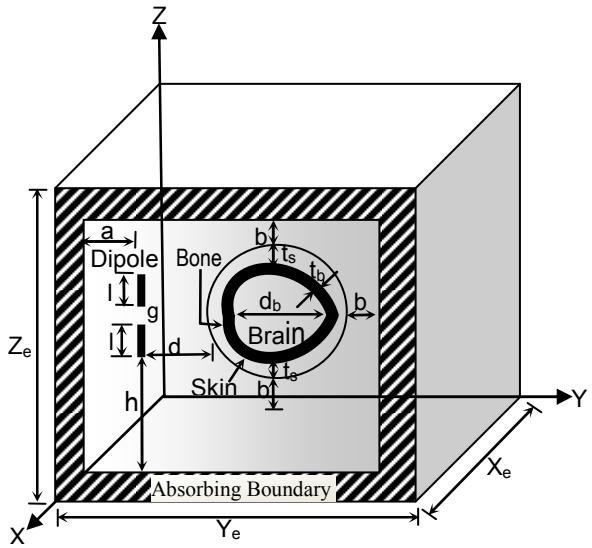

Figure 4.7. Geometry of the dipole antenna and the human head used for simulation by the FDTD method. [$Xe = 54\delta$, $Ye = 58\delta$, $Ze = 62\delta$, a = $b = 2\delta$, $l = 15\delta$, $g = 1\delta$, $d_b = 34\delta$, $t_s = 1\delta$, $t_b = 1\delta$, $d = (4 - 6)\delta$].

Table 4.7: Relative dielectric constant (ε_r) and conductivity (σ) of the human brain, bone and skin at the different frequencies.

Frequency (MHz)	Brain		Bone		Skin	
	Dielectric Constant (ε_r)	Conductivity σ (S/m)	Dielectric Constant (ε_r)	Conductivity σ (S/m)	Dielectric Constant (ε_r)	Conductivity σ (S/m)
100	82.0	0.53	7.50	0.067	24.50	0.55
350	60.0	0.65	5.70	0.072	17.60	0.44
900	56.8	1.10	20.90	0.340	41.41	0.87
1800	51.8	1.50	19.34	0.590	38.87	1.88
2450	48.9	1.81	18.55	0.820	38.01	1.46
6000	30.0	5.30	6.00	0.300	23.00	2.60

Variation of S_{11} with frequency for the half wave dipole antenna placed in free space and at 2.0 cm distance from the head model is shown in Figure 4.8. When the head model is placed closed to the radiating antenna, it behaves like a parasitic component and acts as a part of the antenna. As a result, the effective dimension of radiating structure increases and the

resonant frequencies for both fundamental and higher order modes move toward lower frequencies during the presence of head. In this study, length of the antenna is 15.5 cm and for the fundamental mode with and with out head it resonates at 835 MHz and 890 MHz respectively. Thus the shifting of resonant frequency towards left is 55 MHz due to presence of the head in front of the antenna at the distance of 2.0 cm. Value of S_{11} are -12.18 dB and -11.28 dB at the resonant frequencies 835 MHz and 890 MHz respectively. From the Figure 3.7, it is also seen that the value of S_{11} remains below -10 dB in the GSM band (890MHz – 960MHz) for both with and with out head.

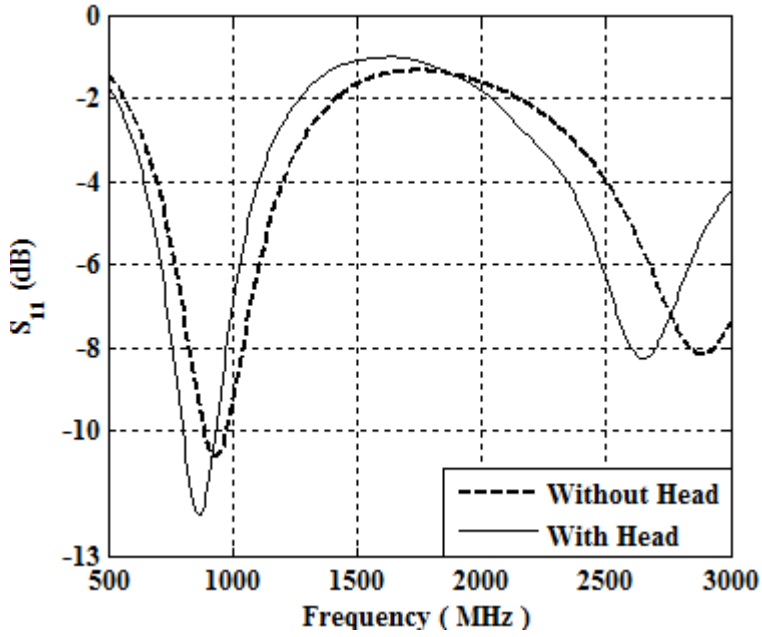

Figure 4.8. Variation of S_{11} vs. Frequency of the dipole antenna of length 15.5 cm for with and with out head.

Figure 4.9, shows the MLSARs induced in the human head are in the range of 1.8 W/kg to 0.15 W/kg for the frequency range from 500 MHz to 3 GHz for a set of distances '*d*' in the range of 1.0 cm to 3.0 cm. When *d* is less than or equal to 1.0 cm then the MLSAR (1.8 W/Kg) is above FCC and IEEE's upper safety limit (1.6 W/kg). As the distance increases over 1.0 cm then the value of the MLSAR goes below the upper safety limit. The curve shows three major peaks near the resonant frequencies. For all *d*, peak value of MLSAR has been found at fundamental resonant frequency near GSM band (890MHz – 960MHz) due to large amount of energy transfer from antenna to head for good impedance matching. But at the other resonant frequencies the value of MLSAR doesn't rise significantly due to higher

reflection of EM wave from the surface of the head which results in smaller absorption. MLSAR also decreases faster in higher frequency range due to smaller penetration depth.

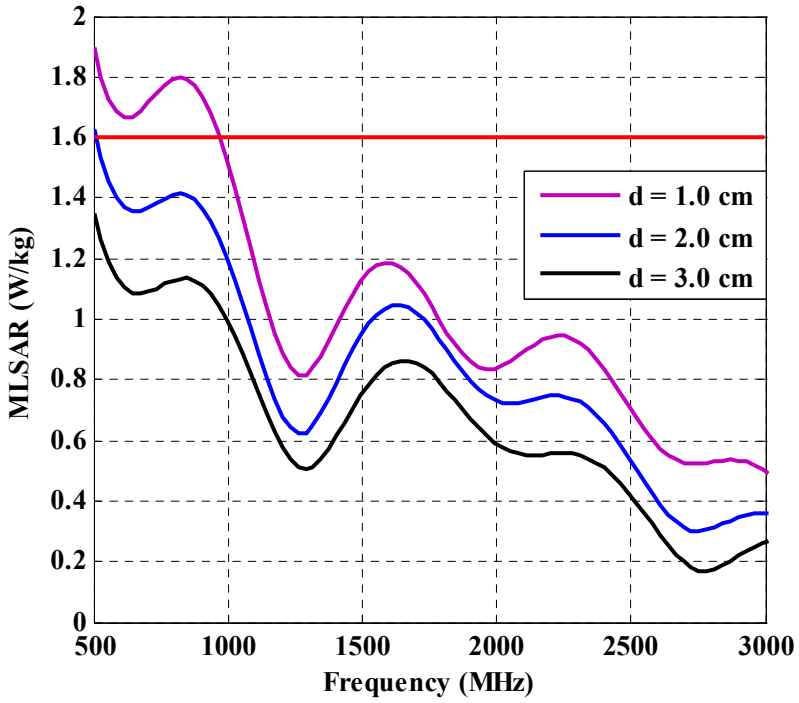

Figure 4.9. MLSAR distributions in the spherical human head model for various distance '*d*'.

The human head is coupled with radiation antenna to represent accurate FDTD simulations of real-life communication scenarios and also provide information concerning the SAR for power absorbed in human head. A metallic material having length L and diameter of 0.5 cm is used as the radiating dipole antenna. The value of L of the resonant dipole antenna is appropriately varied corresponding to several spot frequencies following the relation:

$$f_{res} = \frac{c}{2L} \tag{4.3}$$

where, f_{res} = resonant frequency of the dipole antenna and c = speed of light in free space (3×10^8 m/s). The values obtained for L are 18.5 cm, 14.5 cm, 10.5 cm and 5.5 cm for approximate resonating frequencies 700 MHz, 1.0 GHz, 1.6 GHz and 2.5 GHz, respectively.

MLSARs induced in the spherical human head model by the half wave resonant dipole antennas having different values of L near their resonance frequencies for a set of d are shown in Figure 4.10. It is seen that for all antennas MLSARs are obtained near their

resonance frequencies. For L = 10.5 cm and L = 5.5 cm, the values of MLSARs remain lower than the FCC and IEEE's upper safety limit of 1.6 W/kg even when d = 1.0 cm.

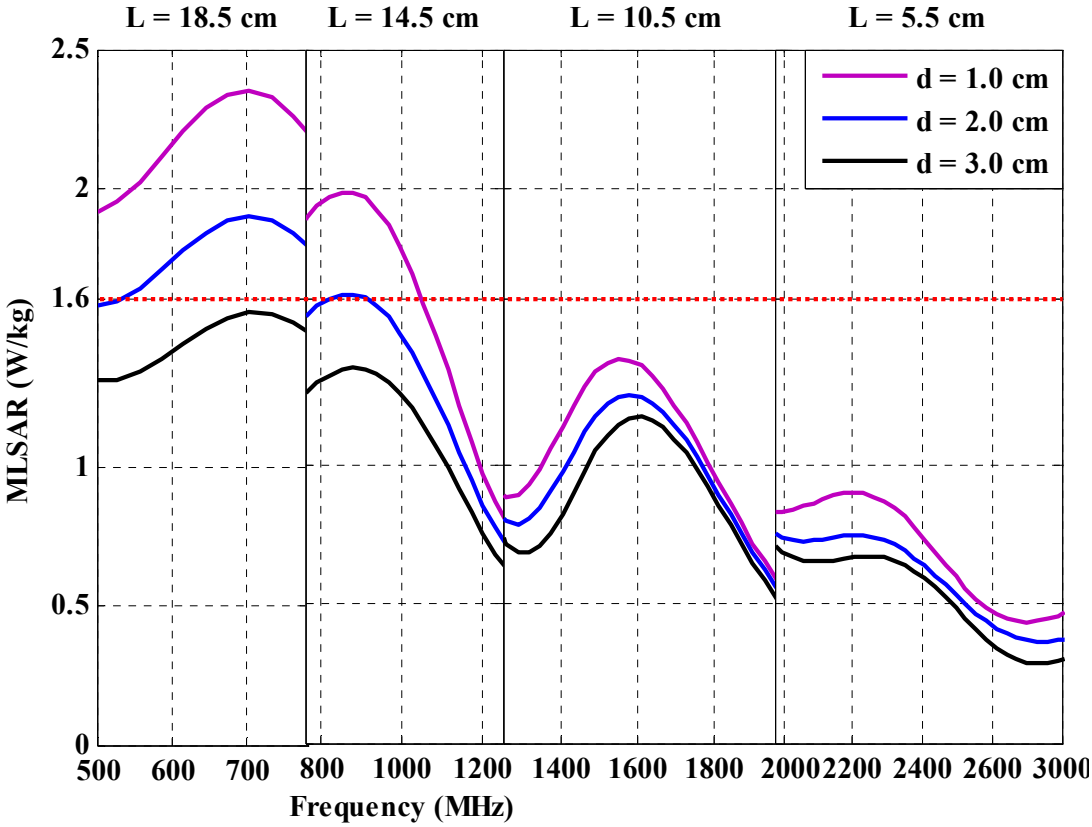

Figure 4.10. MLSAR distributions in the human head model for different '*d*' and *L*.

4.3.2.1 SAR Evaluation in child and adult head models

MLSARs induced in the head models of children and adult exposed to a half-wave radiating dipole antenna of length 14.5 cm at 500 MHz to 3 GHz frequency band have been calculated for different d using FDTD method. Three head models, one male adult and two child head models, aged 3 and 7 years, have been down-scale modelled as inhomogeneous three layered sphere of different diameters as shown in Table 4.8 [47].

Table 4.8: Physical parameters for different head models.

Head model	Mass (kg)	Diameter (cm)
3-year-old child head	3.321	17.0
7-year-old child head	3.434	18.0
Adult male head	4.679	21.0

Calculated MLSAR vs. Frequency for a set of distances *d* and different head models are shown in Figure 4.11 (a-c). It can be observed from Figures 4.11 (a-c) that MLSAR reaches its maximum value near the fundamental resonance frequency of the dipole antenna for all the cases due to large amount of energy transfer from antenna to head for good impedance matching. At *d* equal to 0.5 cm values of MLSAR obtained for 3-year-old child, 7-year-old child and adult male head models are 2.5 W/kg, 2.4 W/kg and 2.3 W/kg respectively. For frequency higher than 700 MHz, the value of MLSAR is larger for smaller head models for the same *d* and frequency which shows that smaller head absorbs more RF energy with compared to larger head for same *d* and frequency. Again for all the head models with increase of *d* and frequency, value of MLSAR decreases due to smaller penetration depth and higher reflection of EM wave from the surface of the head, at higher frequencies which results in smaller absorption.

4.3.3 SAR Evaluation in the Realistic Human head models

CT or MRI scanned voxel based anthropomorphic phantom data are available for EM modelling of human head or other body parts. Full wave numerical methods like FDTD, FEM or MoM are utilized to solve Maxwell's equations in a heterogeneous representation of the human head or other body parts developed from voxel based anthropomorphic phantom data considering the electrical parameters of different anatomical internal structures of the human body. The biological voxel-based computational models constructed from the medical imaging types like CT and MRI provide high resolution cross-sectional digital images of internal anatomy. The head model is exposed to EM waves radiated from a half wave dipole antenna made with aluminium having length L = 14.5 cm and width of 0.4 cm.

During SAR calculation excitation source voltage (V) applied at the feeding point of the dipole antenna is obtained by the following equation [48]:

$$V = \sqrt{8 \times P \times R} \tag{4.4}$$

where, P = 0.6 W and R = 50 Ω. MLSAR is obtained by finding the maximum value of SAR within the whole head model.

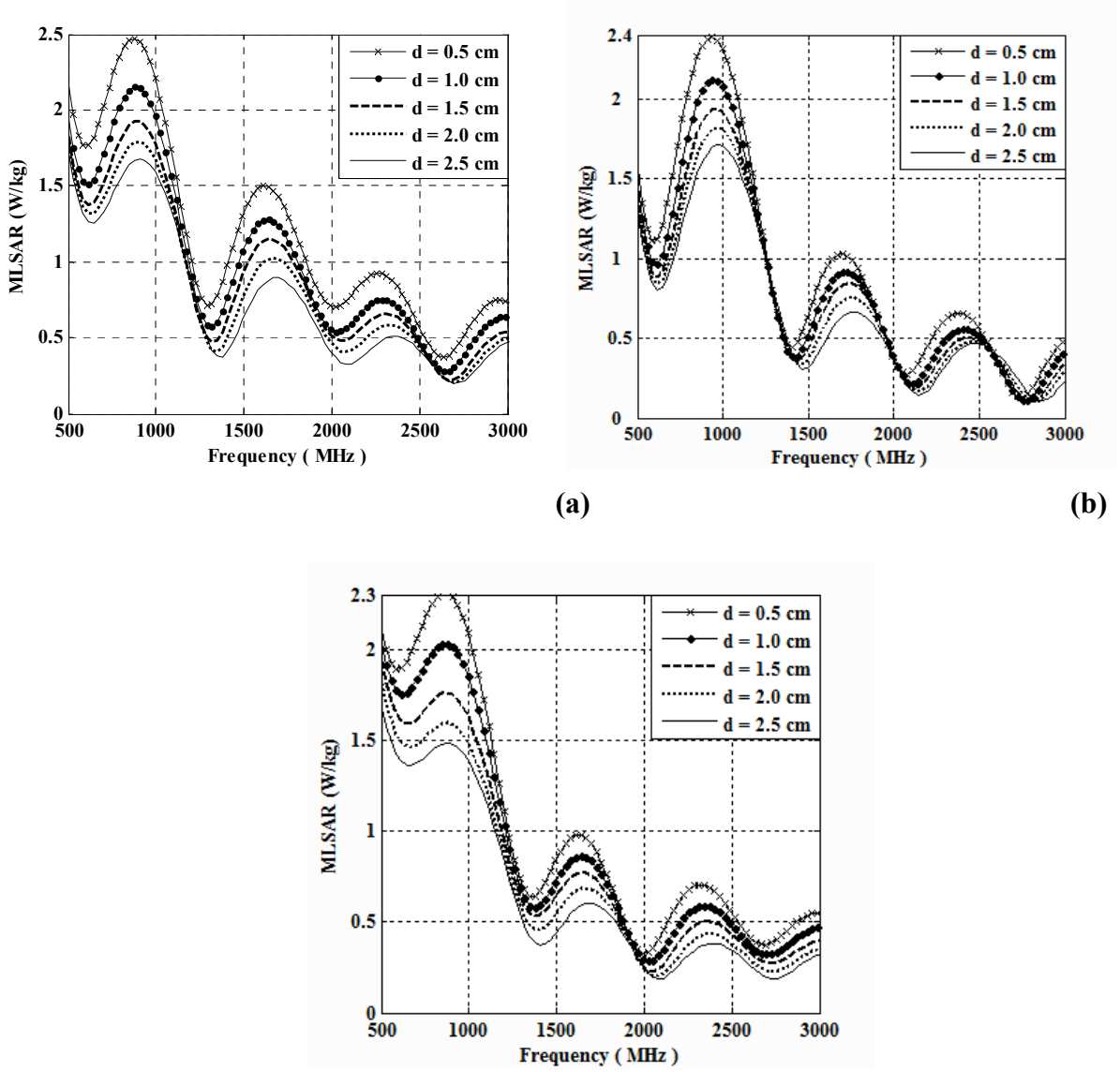

Figure 4.11. MLSAR vs. Frequency for (a) 3 year old child, (b) 7 year old child and (c) adult male head models.

4.3.3.1 Zubal head model

The human head model has been constructed from Zubal phantom which is based on CT scan data of a 35 year old male weighing 155 lbs or 70.31 kg and measuring 5′10″ or 1.778 m in height [49]. Midsaggital, midcoronal and three dimensional geometry of the Zubal phantom are shown in Figure 4.12 (a-c). The man has been considered to be clinically normal and had no head abnormalities. MATLAB program is used to read, resample and reshape the phantom volume data consists of 128×128×243 cubic cells. To simplify the numerical

calculations, resolution of volume is reduced by 50% and other parts of the human body except the head are excluded in the simulation.

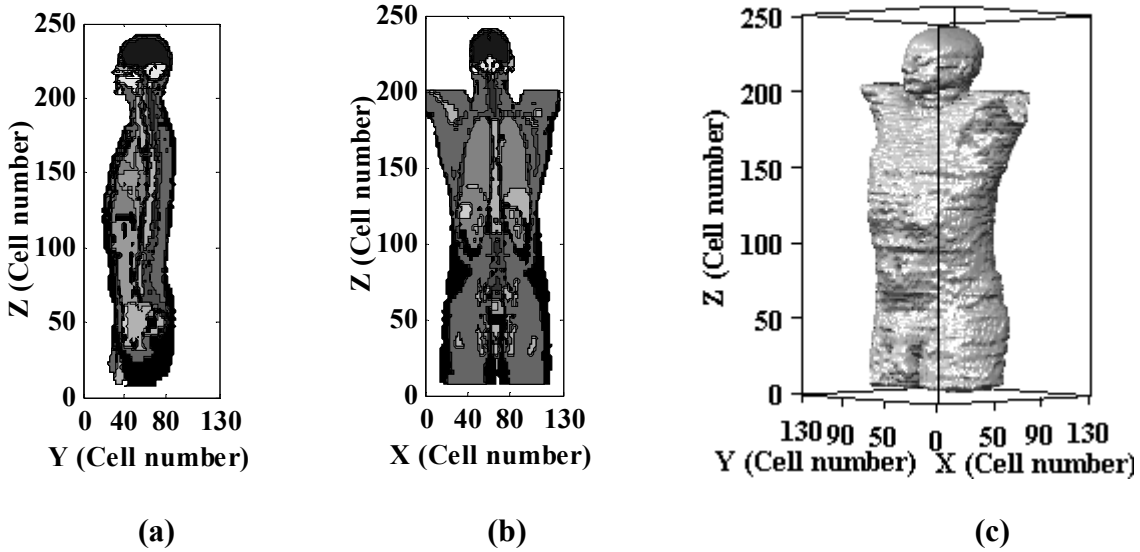

Figure 4.12. (a) Midsaggital, (b) midcoronal and (c) three dimensional geometrical view of the Zubal phantom.

4.3.3.1.1 Development of Simulation model

Due to huge complexity of the human head, limitations of FDTD method and computational resources, many assumptions have been made in calculations of SAR. For this head model SAR has been calculated considering only twenty two types of head tissues but it is actually consisting of several types of tissue of varying dielectric properties. Except head other parts of human body have been excluded in the simulation and the hand-held cellular phone is modelled as an equivalent half-wave dipole antenna. Midsaggital, midcoronal and three dimensional geometry of the human head model along with the mobile handset used in the simulation are shown in Figure 4.13 (a-c). The head is comprised of twenty two types of tissues; i.e., brain, cerebellum, skin, bone, muscle, fat, lens, eyeball, tongue, blood, cartilage, cerebral falx, parotid gland, retina, teeth, trachea, spinal chord, nerve, eye sclera, bone marrow, pituitary gland and mouth cavity/sinuses. Values of ρ, ε_r and σ of different tissues are obtained from the literature [46]. Relative dielectric constant, conductivity, mass density and mass of one 4 mm × 4 mm × 5 mm volume cell for different tissues are shown in Table 4.9. During simulation, frequency dependent ε_r and σ are determined by interpolating the available data.

Table 4.9: Dielectric constant (ε_r), conductivity (σ), mass density (ρ) and mass of one cell of the human head Tissues.

Tissue Type	Dielectric Constant (ε_r) [930 MHz]	Conductivity σ (S/m) [930 MHz]	Mass density ρ (kg/m^3)	Mass of one cell (g)
Brain	50.6800	0.9295	1030	0.0824
Cerebellum	57.5980	1.0020	1030	0.0824
Skin	48.0980	0.6657	1010	0.0808
Bone	13.2700	0.0869	1850	0.1480
Muscle	57.5960	0.7834	1040	0.0832
Fat	5.6000	0.0403	920	0.0736
Lense	48.4900	0.6580	1100	0.0880
Eye	74.1000	1.9700	1010	0.0808
Tongue	58.2090	0.7590	1040	0.0832
Blood	64.8200	1.3320	1000	0.0800
Cartilage	46.0430	0.5690	1100	0.0880
Cerebral Falx	71.7090	2.2380	1010	0.0808
Esophagus	68.0200	0.9875	1030	0.0824
Pons	58.5500	0.7150	1050	0.0840
Teeth	13.2770	0.0869	1850	0.1480
Trachea	44.6850	0.6237	1040	0.0832
Spinal Chord	36.0650	0.4329	1040	0.0832
Nerve	36.0650	0.4329	1040	0.0832
Dens of axis	47.2140	0.8155	1040	0.0832
Bone Marrow	5.7099	0.0283	1000	0.0800
Thyroid	61.9430	0.8641	1040	0.0832
Mouth cavity/sinuses	1.0000	0.0000	1.200	0.0001

Human head floating in free space is not a realistic situation. In reality, head is connected to dielectric body mass and ground plane is beneath the body mass. To simplify the numerical calculations other parts of the human body except the head are excluded so in order to approach towards a more practical condition a conductive ground plane is added at the bottom of the human head model. MLSAR has been computed using FDTD method induced inside the grounded human head model for a set of distance between head model and radiating dipole antenna (d) in the range of 0.4 cm to 1.2 cm and plotted against distance (D) measured from the end of antenna side.

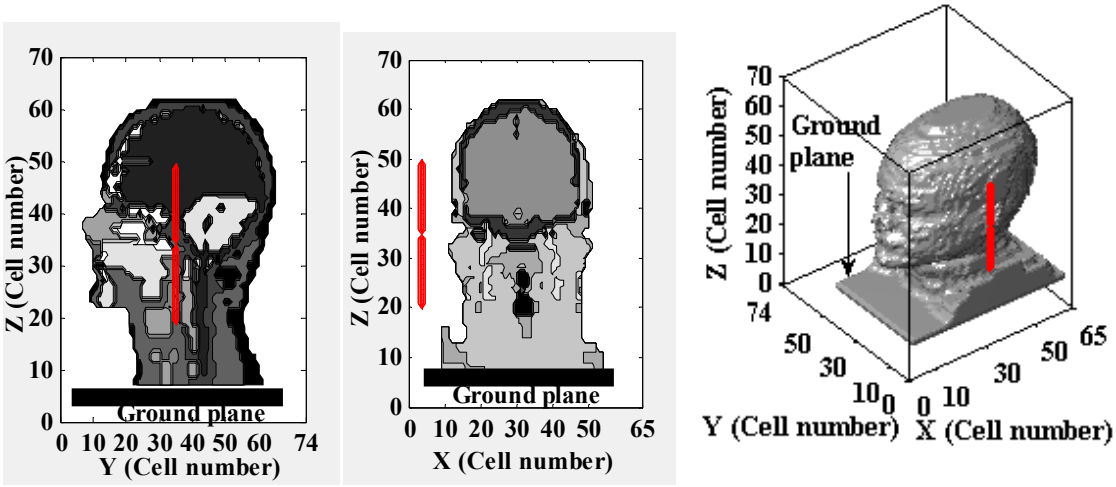

(a) **(b)** **(c)**

Figure 4.13. (a) Midsaggital, (b) midcoronal and (c) 3-dimensional geometrical view of human head model along with dipole antenna.

Figures 4.13 (a-c) illustrate the geometry of a grounded realistic human head model along with a dipole antenna used for the simulation by FDTD method to calculate MLSAR. The human head is composed of 1,51,200 Yee cells of dimension: 0.4 cm × 0.4 cm × 0.5 cm. MLSAR vs. D obtained for L = 14.5 cm and d equal to 0.4 cm, 0.8 cm, and 1.2 cm is shown in Figure 4.14. From the Figure 4.14, it is seen that when d is equal to 0.4 cm then the value of MLSAR is 1.96 W/kg, above ANSI/IEEE's upper safety limit. As d increases over 0.8 cm then the value of the MLSAR goes below the upper safety limit. For each value of d, value of MLSAR increases towards the direction of antenna side and decreases significantly away from the antenna side due to smaller penetration of EM waves through the head model.

4.3.3.1.2 SAR Calculation

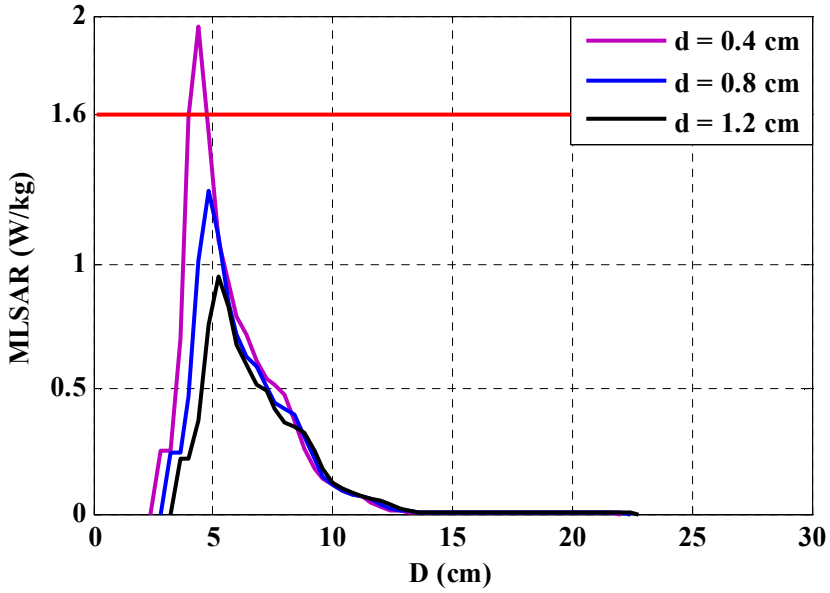

Figure 4.14. MLSAR vs. *D* induced in the human head model for a set of *d* in the range of 0.4 cm to 1.2 cm at 930 MHz.

4.3.3.1.3 Evaluation of additional EM field parameters

FDTD method is used to calculate the induced current (*I*), *E* field, *H* field and absorbed power density (P_{asb}) inside the grounded Zubal head model exposed to a half-wave radiating dipole antenna designed at GSM 900 band as shown in Figure 4.13 (a-c). Keeping a fixed distance (*d*) of 4.0 mm between the antenna and head model, maximum local *I*, *E* field, *H* field and P_{abs} inside the head model have been calculated. From the converged solutions the local *E* field, *H* field, *I* and P_{abs} at the i^{th} layer inside the human head are obtained from following equations [50]-[52]:

$$E(i,j,k)=\sqrt{E_x(i,j,k)^2+E_y(i,j,k)^2+E_z(i,j,k)^2}\ \text{(V/m)} \qquad (4.5)$$

$$H(i,j,k)=\sqrt{H_x(i,j,k)^2+H_y(i,j,k)^2+H_z(i,j,k)^2}\ \text{(A/m)} \qquad (4.6)$$

$$I(i)=\sum_j\sum_k ABS\left[\sigma(i,j,k)+j\omega\varepsilon_r(i,j,k)\right]\times\frac{\left[E_{\max}(i,j,k)-E_{\min}(i,j,k)\right]\delta^2}{2\sqrt{2}}\ \text{(A)} \qquad (4.7)$$

$$P_{abs}(i)=\sum_j\sum_k\left[\frac{1}{2}\sigma(i,j,k)\times\left\{E_x(i,j,k)^2+E_y(i,j,k)^2+E_z(i,j,k)^2\right\}\right]$$

$$\text{(mW/cm}^2\text{)} \qquad (4.8)$$

where, E_x , E_y and E_z are the magnitudes of the electric field components (V/m), $\sigma(i,j,k)$ is the conductivity (S/m) of the $(i,j,k)^{th}$ FDTD cell, $E_{max}(i,j,k)$ and $E_{min}(i,j,k)$ are the peak of positive and negative electric field values respectively, ε_r is the relative dielectric constant of the human head tissue, δ is the Yee cell length, f = operating frequency (930 MHz) and $\omega = 2\pi f$.

Variation of maximum local electric field, magnetic field, induced current and power density with distance D measured from the end of antenna side for d = 4.0 mm are shown in the Figure 4.15-4.18. From Figure 4.15, it is seen that the value of maximum local electric field is 40.64 V/m. While the value of maximum local magnetic field is 0.121 A/m as seen in Figure 4.16. From Figure 4.17, it is seen that value of maximum local induced current is 2.674 mA. From Figure 4.18, it is seen that the value of maximum local power density is 2.197 mW/cm^2. The values of maximum local electric field, magnetic field and absorbed power density obtained by the calculation are found to be below to their corresponding ICNIRP recommended upper safety limits shown in Table 4.4.

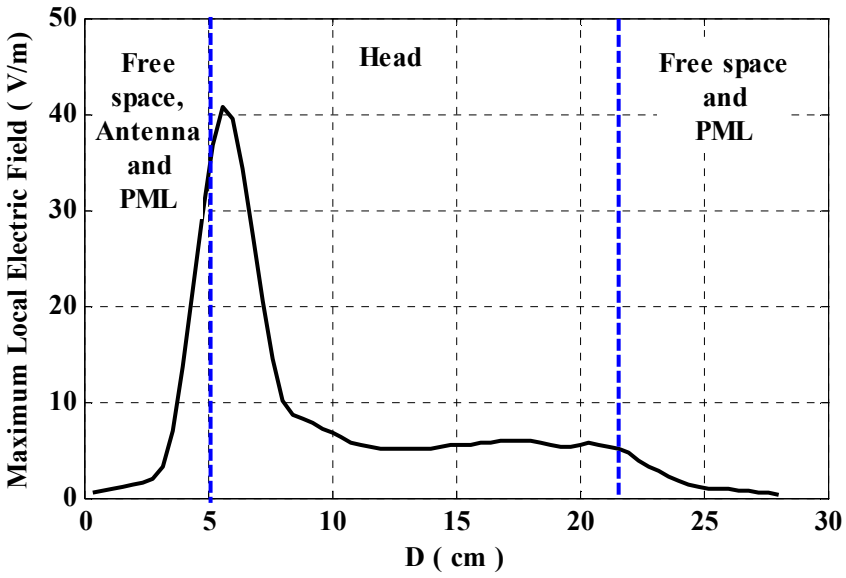

Figure 4.15. Maximum local electric field vs. *D*.

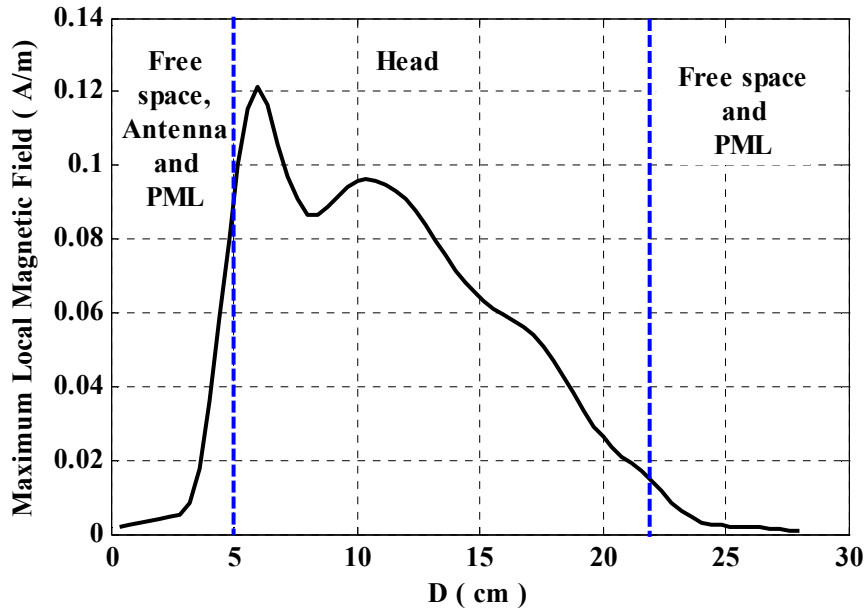

Figure 4.16. Maximum local magnetic field vs. *D*.

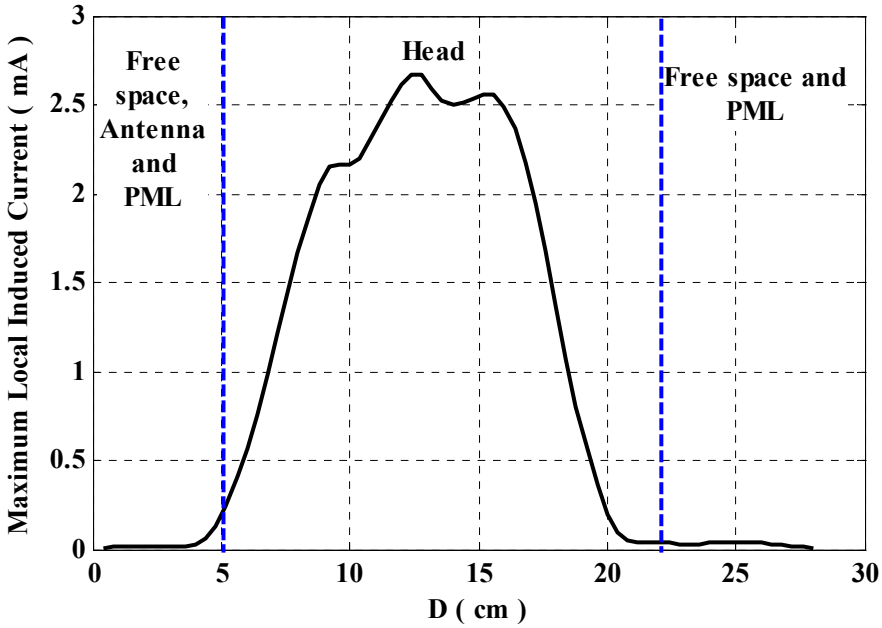

Figure 4.17. Maximum local induced current vs. D.

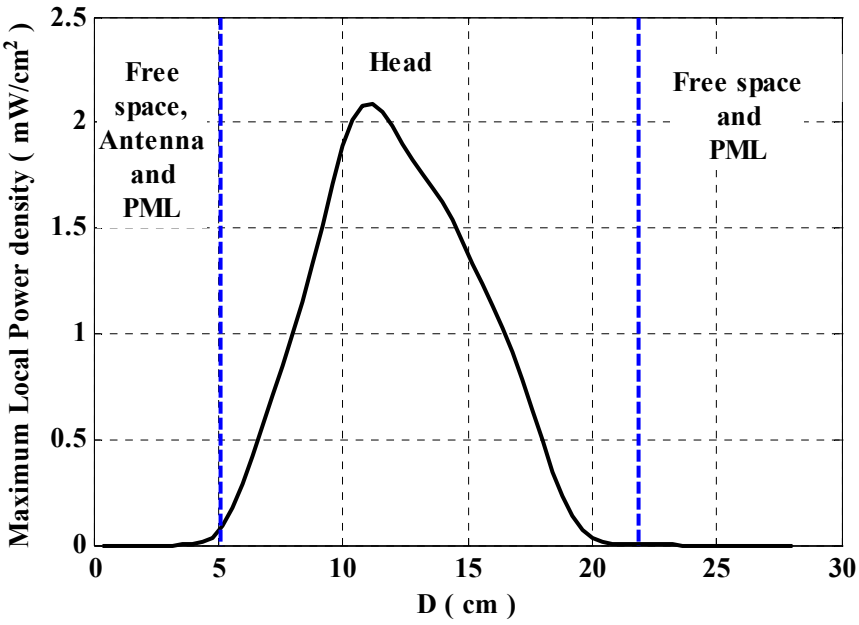

Figure 4.18. Maximum local power density vs. *D*.

4.3.3.2 DICOM head model

DICOM format is used extensively in CT, MRI and ultrasound devices and combines images and metadata to create a rich description of a medical imaging procedureand it has been widely adopted by hospitals around the world [53]. DICOM is a standard for handling, storing, printing, and transmitting information in medical imaging and it integrates different scanners, servers, workstations, printers and network hardware from multiple manufacturers into a Picture Archiving and Communication System (PACS). It includes a file format definition and a network communications protocol. The National Electrical Manufacturers Association (NEMA) holds the copyright of DICOM standard. Voxel-based computational models of the human head and hand can also be constructed from DICOM files [54]. Each DICOM file contains a header. Useful informations required for voxelization of the metadata available in the DICOM file are obtained from the header of that DICOM file. The head contains a Service-Object Pair (SOP) instance related to Information Object Definition (IOD). The construction way of the tomographic voxel-based computational models is starting by stacking up the medical images within the DICOM files without modification the order of the DICOM files [55],[56].

4.3.3.2.1 Construction of Voxel models using CT scan DICOM files

In this study the required computational electrical models have been constructed from CT and PET-CT 64 image data set available in DICOM format. A 278 MB, PET-CT 64

whole body scan data for alias subject MELANIX and a 40 MB, CT head scan data for alias subject MANIX are obtained from Osirix samples [53]. The method is general in nature and can be applied to any subject.

The header of the DICOM file used for modelling the human head is shown in the Table 4.10 [53],[55],[56]. The examination was performed with a CT scan machine (Philips). The data is stored as a 512 × 512 × 460 two-byte pixel array with slice thickness of 1.5000 mm and 0.7000 mm spacing between slices. Original 3-D geometry of the human head model obtained from the DICOM files is shown in the Figure 4.19 (a).

The header of the DICOM file, used for modelling the hand is shown in the Table 4.11 [53],[55],[56]. The examination was performed with a CT scan machine (SIEMENS). The data is stored as a 512 × 512 × 134 two-byte pixel array with slice thickness of 2 mm and 0.7000 mm spacing between slices. Original 3-D geometry of the hand model obtained from the DICOM files is shown in the Figure 4.19 (b).

Table 4.10: Information samples obtained from Header of DICOM file used for head model

Rows	512
Columns	512
Dimensions	[512 512 460]
Slice Thickness	1.5000
Spacing Between Slices	0.7000
Rescale Slope	1
Pixel Dimensions	[0.4883 0.4883 0.7000]
Rescale Intercept	-1000

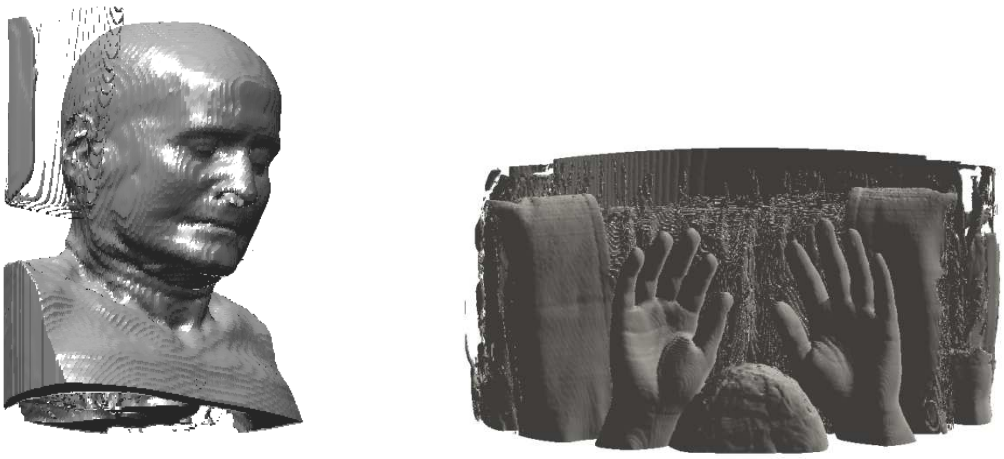

(a) **(b)**

Figure 4.19. Three-dimensional geometrical view of (a) human head and (b) hand model.

Table 4.11: Information samples obtained from Header of DICOM file used for hand model

Rows	512
Columns	512
Dimensions	[512 512 134]
Slice Thickness	2
Spacing Between Slices	0.7000
Rescale Slope	1
Pixel Dimensions	[0.9766 0.9766 1.5000]
Rescale Intercept	-1024

4.3.3.2.2 Tissue Identification from DICOM data

Image pixel data is stored as the value of the pixel data element within the DICOM file in the form of pixel cell. A pixel cell is the container for a pixel sample value and optionally additional bits. A pixel cell exists for every individual pixel sample value in the pixel data. As the sample pixel cells are encoded in byte streams so to construct voxel-based computational models the pixel cells are decoded using in-house MATLAB program.

Pixels in an image obtained by CT scanning are displayed in terms of relative radio density. Hounsefield scale proposed in 1972 by Godfrey Newbold Hounsefield is a quantitative measure of radio-density [57]. The pixel corresponds to the mean radio attenuation by the tissue is represented on a Hounsfield scale using a value from -1024 to +3071. Using a linear transformation, the pixel values found in CT data can be converted in the Hounsefield Units (HU) [58]-[60]:

$$\mathrm{HU} = \left(\mathrm{pixel\_value} \times \mathrm{slope}\right) + \mathrm{intercept} \tag{4.9}$$

where, slope and intercept are the Rescale Slope and Rescale Intercept respectively obtained from the header shown in the Tables 4.10-4.11.

Each different type of tissue has different values of HU and the pixels correspond to a particular tissue can be identified and distinguished from pixels belonging to other tissues. HU used in the simulation corresponding to the tissues are listed in the Table 4.12 [57]-[61]. Due to huge complexity of the human head and hand, limitations of FDTD method and computational resources, many assumptions have been made during modelling of head and hand models. The head model is assumed to be consisted of only eleven types of tissues i.e., skin, bone, muscle, fat, blood, cartilage, CSF, white matter, grey matter, water and mouth cavity/sinuses whereas, the hand model is assumed to be consisted of only three types of tissues i.e., skin, bone and muscle.

4.3.3.2.3 Development of Simulation model

To simplify the numerical calculations raw data obtained from the DICOM files for both the head and hand models has been processed using in-house MATLAB program. The metallic parts of the CT scam machines as shown in Figures 4.19 (a-b) are removed completely. Resolutions of the volume of head and hand models are reduced by 10% and 20%, respectively. Excluding the left hand, the right hand is placed at the side of the right ear of the head model holding the mobile phone.

Sagittal, coronal and three-dimensional geometry of the human head model along with the mobile phone holding with right hand used in the simulation are shown in Figures 4.20 (a-c). Values of ρ, ε_r and σ of different tissues are obtained from the literature are shown in Table 4.13 [46]. Frequency dependent ε_r and σ are determined by interpolating the available data.

Table 4.12: HU of the tissue used for head and hand models

Tissue Type	HU	
	Lower limit	Upper limit
Skin	-100	+200
Bone	+400	+3000
Muscle	+5	+40
Fat	-100	-50
Blood	+40	+40
Cartilage	-140	-120
CSF	+15	+15
White Matter	+20	+30
Grey Matter	+37	+45
Water	0	0
Mouth cavity/sinuses	-1000	-1000

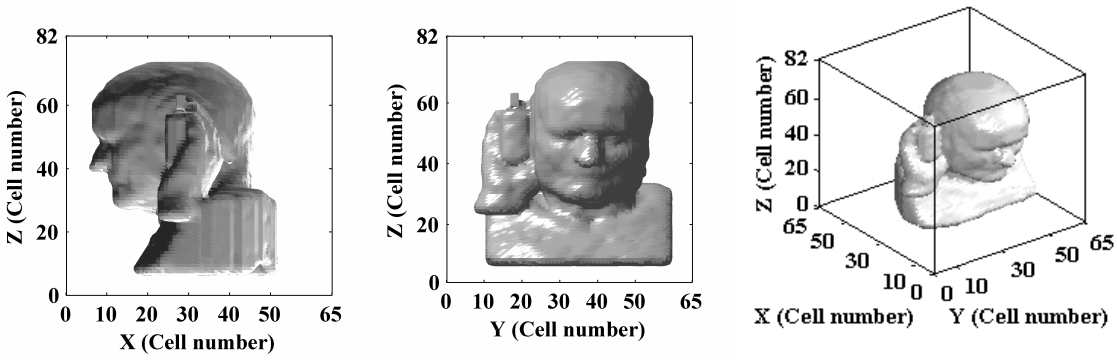

(a) **(b)** **(c)**

Figure 4.20. (a) Sagittal plane, (b) coronal plane and (c) three-dimensional geometrical view of DICOM based human head model along with hand and mobile phone.

4.3.3.2.4 SAR Calculation

Commercially available software CST Microwave Studio® and in-house FDTD code developed in MATLAB have been used to calculate SAR induced in the DICOM data based head and hand models for a hand held mobile phone shown in Figure 3.15 (a) due to applied input power of 0.6 W [62]. During calculation of SAR in MATLAB, a sinusoidal signal with

amplitude V is applied as the excitation of the mobile phone antenna. The value of V is obtained using the following equation:

$$V = \sqrt{4R_a P} \tag{4.10}$$

where, P = radiated power from the antenna (0.6 W), R_a = equivalent antenna input impedance (50 Ω), V = peak value of voltage.

Table 4.13: Dielectric constant (ε_r), conductivity (σ) and mass density (ρ) of the human head and hand tissues

Tissue Type	Dielectric Constant (ε_r) [930 MHz]	Conductivity σ (S/m) [930 MHz]	Mass density ρ (kg/m^3)
Skin	48.0980	0.6657	1010
Bone	13.2700	0.0869	1850
Muscle	57.5960	0.7834	1040
Fat	5.6000	0.0403	920
Blood	64.8200	1.3320	1060
Cartilage	46.0430	0.5690	1100
CSF	36.0650	0.4329	1040
White Matter	42.8100	0.4290	1030
Grey Matter	58.5500	0.7150	1050
Water	78.00	1.59	1000
Mouth cavity/sinuses	1.0000	0.0000	1.300

In FDTD method, peak 1-g and 10-g SARs have been obtained considering irregular volume averages [30]. Whereas, in CST Microwave Studio®, SAR is calculated as a post-processing step after the simulation setting the power loss density monitor to calculate the SAR values and fields. It is also recommended to use the FPBA mesh type for SAR simulations. For the local SAR calculation, specify the mass in gram over which the SAR

should be averaged. Typical values are 1-g or 10-g. Applied input power of the mobile phone antenna is rescaled using the SAR Special Settings Dialog Box option.

SAR distributions at the midsagittal and midcoronal planes for DICOM data based model with handheld mobile phone at 930 MHz are shown in the Figure 4.21 (a-b). In midsagittal plane, SAR holds higher value in the central parts. No SAR is induced in the mouth cavity, sinuses and throat as they are filled with air. Average level of SAR decays gradually towards outer region. In midcoronal plane SAR is found maximum near the outer region of head but inner region of the hand close to antenna and then decreases and increases periodically with continuous decrease in the average level with the increases of distance from the mobile phone.

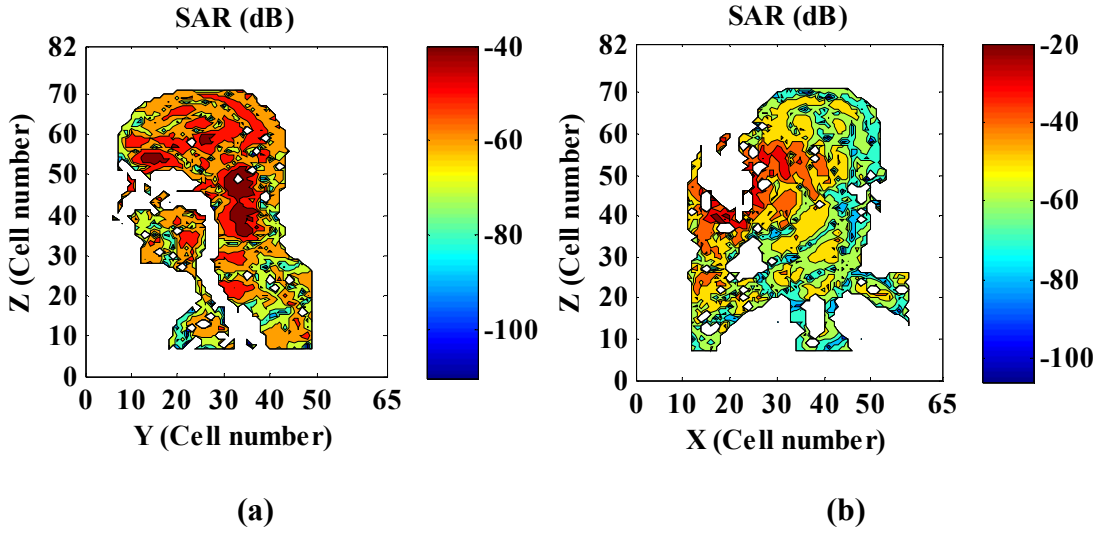

Figure 4.21. SAR distribution in the (a) midsagittal and (b) midcoronal planes.

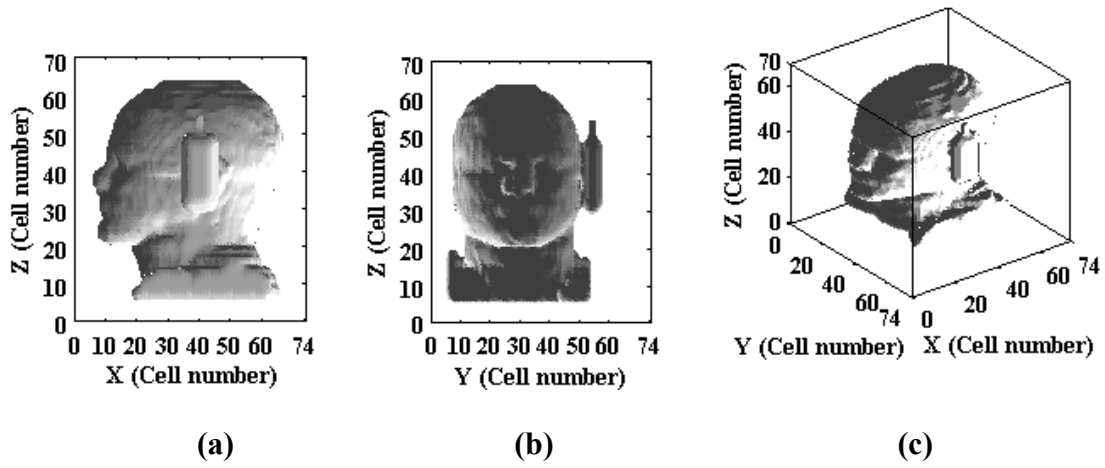

Figure 4.22. (a) Sagittal plane, (b) coronal plane and (c) three-dimensional geometrical view of Zubal head model along with mobile phone.

To calculate peak 10-g and 1-g SAR induced in the DICOM data based head model along the mobile phone is simulated for 800 MHz to 1.1 GHz. Variation of peak 10-g and 1-g SAR with frequency for DICOM data based human head model with and without hand is shown in Figure 4.23. For comparison, variation of peak 10-g and 1-g SAR with frequency for the Zubal head model without hand due to the same mobile phone as shown in Figure 4.22 is also included in Figure 4.23.

From Figure 4.23, it is found that the nature of variation of peak gram averaged SARs with frequency obtained using the DICOM data based human head model agrees with that obtained from Zubal head model. For all resolutions, peak SAR value initially increases with increase of frequency and attains to maximum near the antenna resonance frequency then decreases with further increase of frequency within both head models. The maximum values of peak 10-g and 1-g SARs induced in the DICOM data based head model for without hand are, 0.30 W/kg and 1.01 W/kg, whereas that for the Zubal head model are 0.37 W/kg and 0.78 W/kg, respectively. For 1-g SAR, DICOM data based model shows higher MLSAR than that of Zubal model but for 10-g SAR, MLSAR for DICOM data based model becomes lower than that of Zubal model. MLSAR depends upon the size, shape and internal structures of body organs and its value for 1-g SAR should be higher than that of 10-g SAR. In this study, the difference between maximum values of peak 10-g and 1-g SARs for these models are within 0.07 W/kg and 0.23 W/kg, respectively. These results show that the absorbed power for DICOM data based model at the frequency band of study is not arbitrary in nature. The SAR values obtained for DICOM data based model are close to that obtained using Zubal model but hold different values due to the difference in the size, shape, internal structure and types of tissues considered during construction of these two head models. MLSAR for 10-g and 1-g mass average in the DICOM data based head model for handheld mobile phones are 0.37 W/kg and 1.54 W/kg, respectively. It can be noted that for DICOM data based model, the MLSAR for handheld mobile phone is 0.53 W/kg more than that without hand. So in this case, maximum energy dissipation occurs in hand instead of head for 1-g mass average.

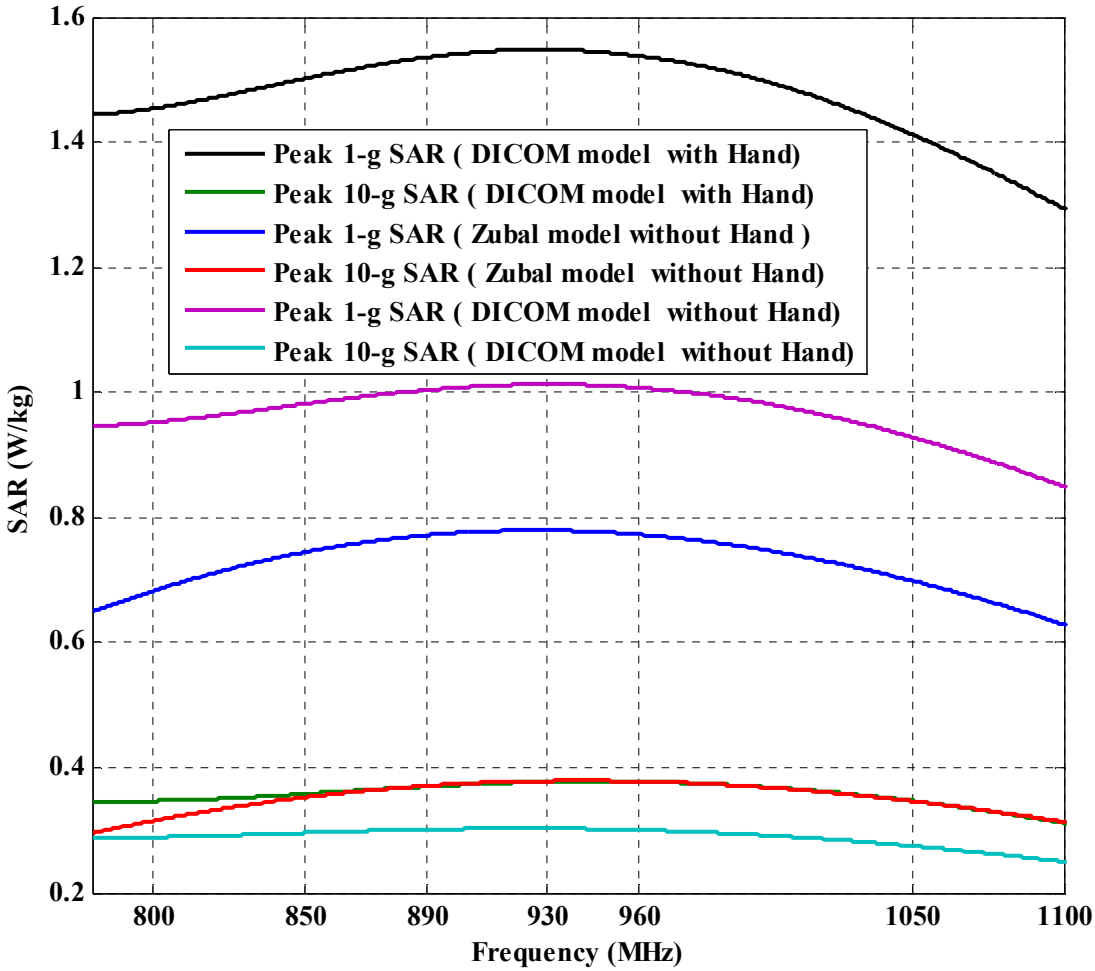

Figure 4.23. Peak 10-g and 1-g SAR vs. Frequency induced in the DICOM data based head model including right hand and Zubal head model without hand.

Three-dimensional 1-g and 10-g SAR distributions inside the DICOM data based human head model including hand model at 930 MHz obtained by CST Microwave Studio® are shown in the Figures 4.24 (a-b). Higher value of 1-g and 10-g SAR are found in the vicinity of the mobile phone antenna and their value decreases periodically with continuous decrease in the average level for the increase of distance from the mobile phone antenna and vice-versa.

Variations of peak 1-g and 10-g SARs with distance *D* measured along Y-axis in the mid-coronal plane at 930 MHz obtained using CST Microwave Studio® are shown in Figures 4.25 (a-b). The stem plots of peak gram averaged SAR vs. *D* contain a number of hotspots. From the Figures 4.25 (a-b), it is seen that the density of the hotspots decreases with increase of SAR value and vice-versa. Only one hotspot is found corresponding to each maximum peak 1-g and 10-g SAR with the value of 1.33 W/kg and 0.38 W/kg respectively.

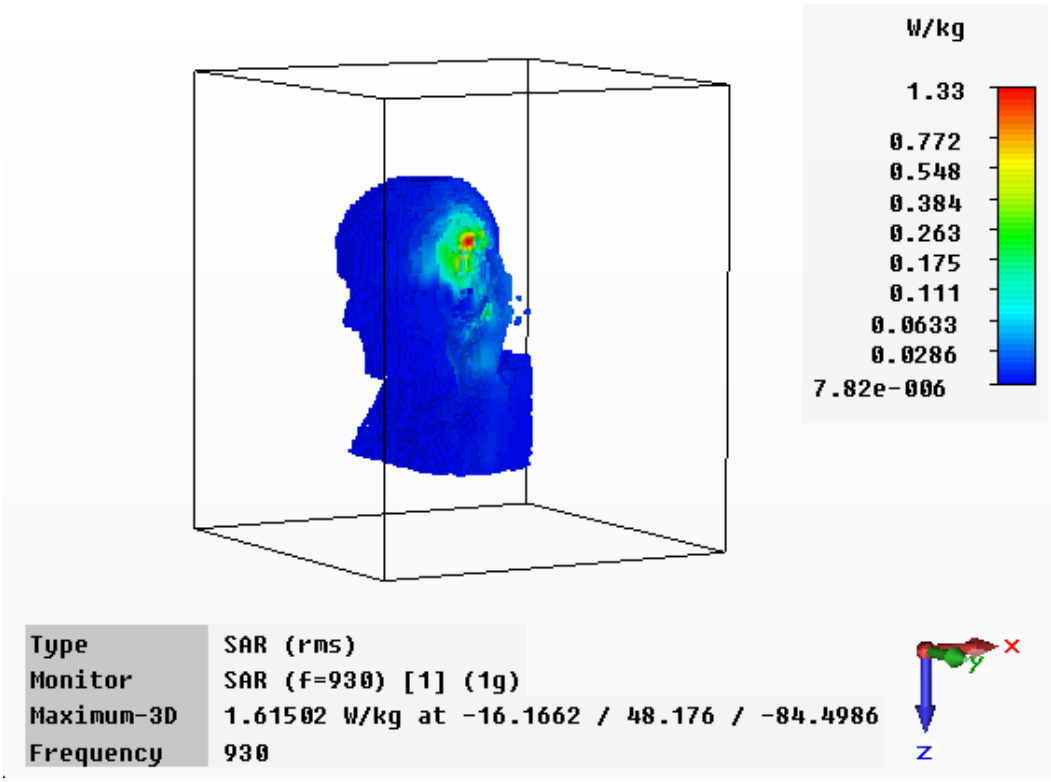

(a)

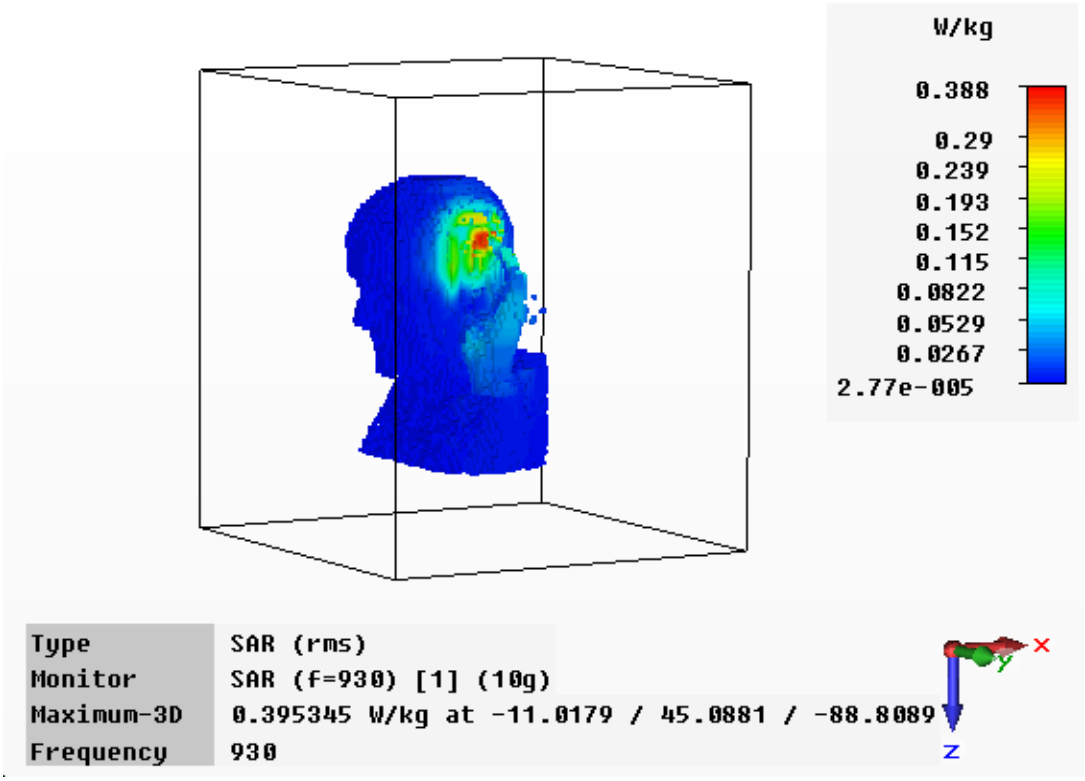

(b)

Figure 4.24. Three-dimensional (a) 1-g and (b) 10-g SAR distributions inside the DICOM data based human head model using CST Microwave Studio®.

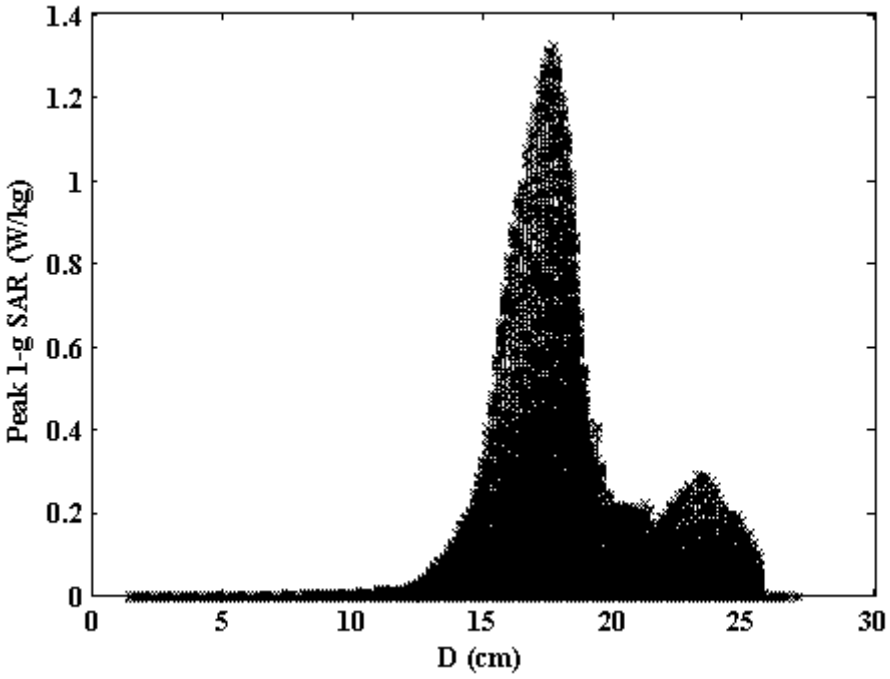

(a)

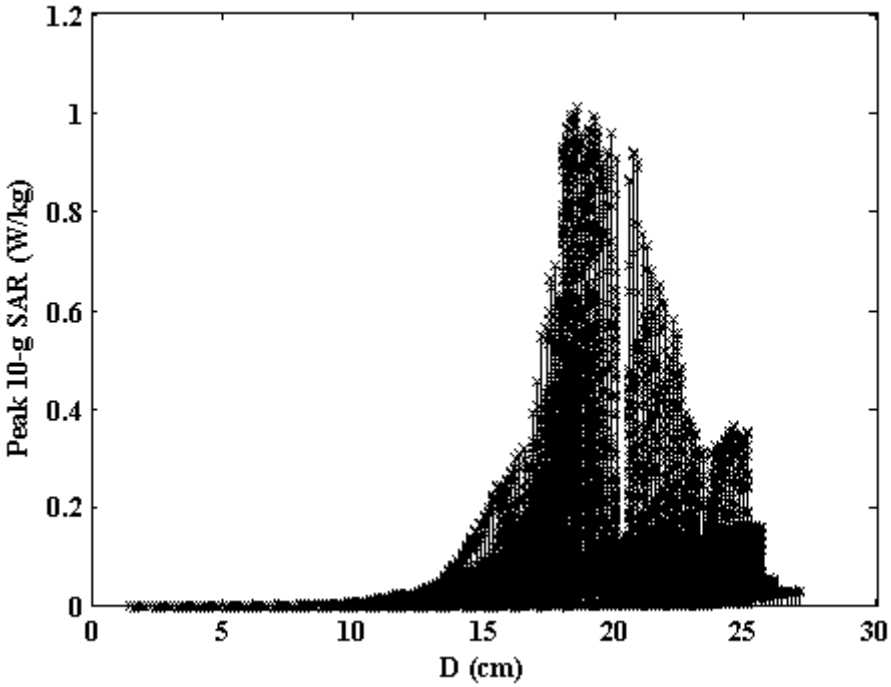

(b)

Figure 4.25. Variations of Peak (a) 1-g and (b) 10-g SARs vs. *D* at 930 MHz.

Maximum value of peak 1-g and 10-g SARs for different type of tissues at 930 MHz obtained using MATLAB are listed in the Table 4.14. From the table, it is seen that maximum peak 1-g and 10-g SARs obtained in skin are 1.3238 W/kg and 0.3882 W/kg respectively. The minimum peak 1-g and 10-g SARs obtained in CSF are 0.0084 W/kg and 0.0014 W/kg respectively. Mouth or sinuses cavities are filled with air and therefore have zero conductivity so no SAR is induced in it.

Table 4.14: Peak 1-g and 10-g SAR induced in the human head and hand tissues at 930 MHz

Tissue Type	Peak 1-g SAR (W/kg)	Peak 10-g SAR (W/kg)
Skin	1.3238	0.3882
Bone	0.0168	0.0028
Muscle	0.7803	0.1323
Fat	0.0176	0.0029
Blood	0.0465	0.0078
Cartilage	1.0512	0.1783
CSF	0.0084	0.0014
White Matter	0.0779	0.0132
Grey Matter	0.0503	0.0085
Water	0.0339	0.0057
Mouth cavity/sinuses	0.0000	0.0000

Measured values of peak 1-g and 10-g SAR at GSM 900 band for a typical commercial handheld mobile phone have been obtained from the literature [63]. Comparison between the available measured and simulated values of the gram averaged SARs for DICOM data based models are shown in the Table 4.15. From the table, it is observed that the peak 1-g and 10-g SARs obtained by simulation are close to each other and lower than the corresponding Measured values within the ANSI/IEEE and FCC safety limits [22],[23]. The differences between simulated and measured data obtained are possibly due to the head and antenna model differences.

Table 4.15: Comparison of simulated SAR with measured SAR

SAR	Simulated	Measured
Peak 1-g SAR (W/kg)	1.3238	1.41
Peak 10-g SAR (W/kg)	0.3882	0.96

4.3.3.3 SAR Calculation for Compact Dual-Band PIFA mounted Mobile phone model

SAR induced inside the grounded Zubal head model in the near-field of a compact dual-band PIFA designed for GSM mobile phone shown in Figure 3.16 has been investigated for three different SAR resolutions using FDTD method at GSM 900 band. Voxel based anthropomorphic Zubal head model has been used to calculate the peak SAR values averaged over 10-g, 1-g and 0.1-g mass. In-house FDTD code is developed using commercially available MATLAB software to carry out EM simulations. For all simulations the antenna is placed in the close vicinity of the head model. 3-D geometry of the human head model along with the mobile handset used in the simulation is shown in Figure 4.26.

In real case, for normal use value of radiated power from cellular phone is 250 mW but it can reach to 1 W or 2 W when the phone is far away from the mobile base station [64]. For this calculation, the PIFA is fed with 0.6 W power and placed in closed vicinity of the human head model.

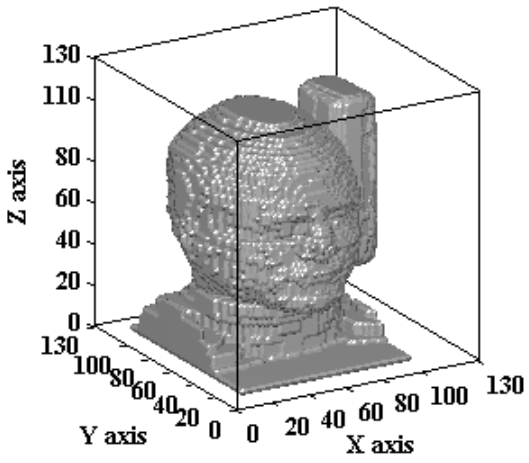

Figure 4.26. Three dimensional geometrical view of human head model along with mobile handset.

SAR distributions at the midsagittal YZ, midcoronal XZ and transverse XY planes in dB scale at 925 MHz are shown in the Figure 4.27 (a-c). The distribution of SAR inside the head model for all sectional planes shows similarity with propagating wave field pattern. In

midsagittal plane, SAR holds higher value in the central parts and the average level decays gradually towards outer region. In midcoronal plane, SAR is found maximum near the outer region of head close to antenna and then decreases and increases periodically with continuous decrease in the average level with the increases of distance from antenna. In transverse plane, SAR is found maximum in the vicinity of right ear close to antenna and then decreases periodically with increase of distance from antenna.

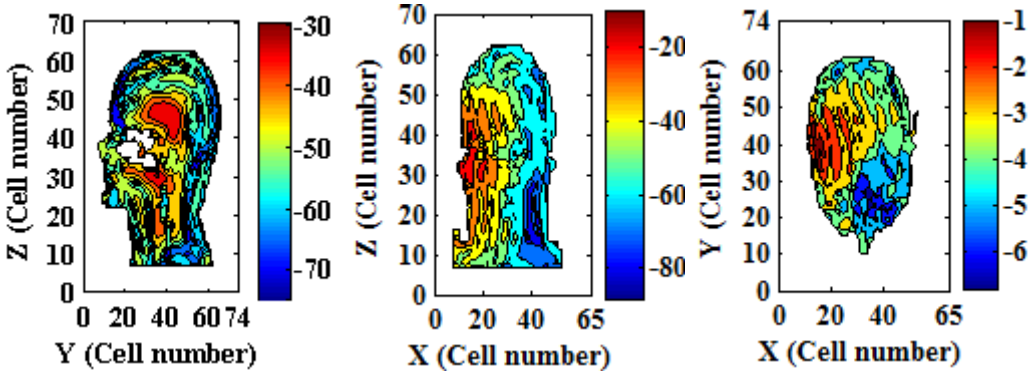

(a) **(b)** **(c)**

Figure 4.27. SAR distribution in the (a) midsagittal plane, (b) midcoronal plane and (c) transverse plane of the human head model.

Maximum value of peak 10-g, 1-g and 0.1-g SARs obtained at 925 MHz in different type of head tissues are listed in the Table 4.16. From the table, it is seen that maximum value of peak gram averaged SARs for all resolutions are obtained in skin tissue. Whereas, minimum value of peak gram averaged SARs for all resolutions are obtained in bone marrow tissue. Mouth or sinuses cavities are filled with air and therefore have zero conductivity so no SAR is induced in it. Calculation of peak 0.1-g SAR within the bone and teeth tissues is not possible using the irregular volume averaging technique because the mass of one cell for these tissues is 0.148 g which is greater than 0.1 g. So, using the cube averaging technique, peak 0.1-g SAR is calculated within the bone and teeth tissues where mass of one cell is not been considered. Corresponding SAR values obtained are 0.0471 W/kg and 5.4255×10^{-4} W/kg, respectively.

Table 4.16: Maximum value of peak gram average SARs induced in the human head tissues at 925 MHz

Tissue Type	Maximum Peak 0.1-g SAR	Maximum Peak 1-g SAR	Maximum Peak 10-g SAR
Brain	0.5620	0.2555	0.1342
Cerebellum	0.0492	0.0333	0.0164
Skin	3.7629	2.7649	0.8951
Bone	0.0471	0.0490	0.0291
Muscle	2.3434	1.5917	0.7448
Fat	0.3419	0.1922	0.0310
Lense	2.6203e-004	1.6395e-004	8.2176e-005
Eye	0.0033	0.0027	9.0376e-004
Tongue	0.0262	0.0168	0.0038
Blood	0.4633	0.3374	0.1001
Cartilage	2.5529	1.2733	0.4048
Cerebral Falx	0.0149	0.0047	9.2749e-004
Esophagus	8.3832e-004	3.2804e-004	1.0390e-004
Pons	0.0194	0.0149	0.0064
Teeth	5.4255e-004	3.2381e-004	8.5599e-005
Trachea	0.0026	0.0013	4.4126e-004
Spinal Chord	0.0017	0.0014	8.4875e-004
Nerve	0.0028	0.0015	3.4515e-004
Dens of axis	0.0049	0.0032	0.0026
Bone Marrow	1.9832e-004	1.4191e-004	5.3735e-005
Thyroid	7.5321e-004	5.0310e-004	3.5714e-004
Mouth cavity/ Sinuses	0.0000	0.0000	0.0000

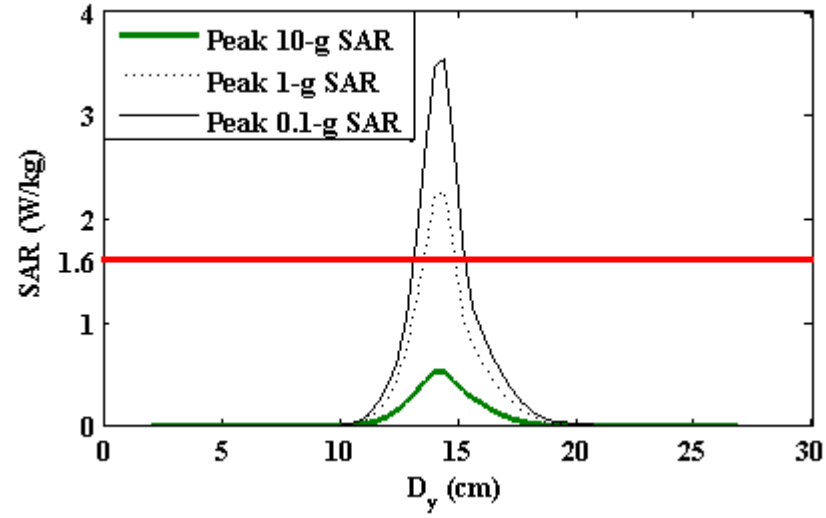

(a)

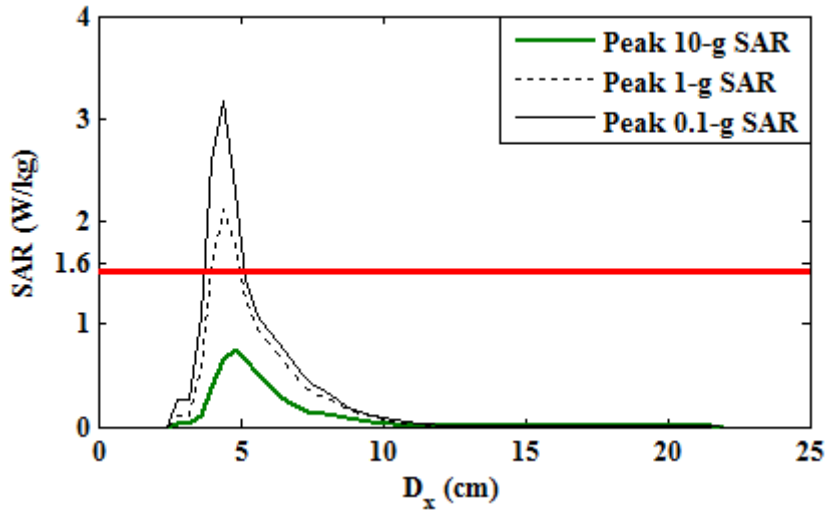

(b)

Figure 4.28. Peak 10-g, 1-g and 0.1-g SAR vs. distance in the (a) saggital and (b) coronal planes of the human head model at 925 MHz.

Variation of peak SAR with distance for 10-g, 1-g and 0.1-g mass in saggital and coronal planes at 925 MHz are shown in Figure 4.28 (a-b), where D_x and D_y are the measured distances along X and Y-axis respectively. In saggital plane for all resolutions, peak SAR value attains to maxima near the position of the antenna and decreases exponentially with either increase or decrease of D_y. But in coronal plane for all resolutions, peak SAR value attains to maxima in the position close to the antenna and decreases exponentially with increase of D_x. The maximum value of peak 10-g, 1-g and 0.1-g SARs obtained in the saggital plane are 0.53 W/kg, 2.26 W/kg and 3.53 W/kg and that obtained in the coronal

plane are 0.74 W/kg, 2.11 W/kg and 3.18 W/kg respectively. In the both planes, value of peak 10-g SAR is below the recommended safety limit of 2.0 W/kg whereas the value of peak 1-g SAR is more than the recommended safety limit of 1.6 W/kg.

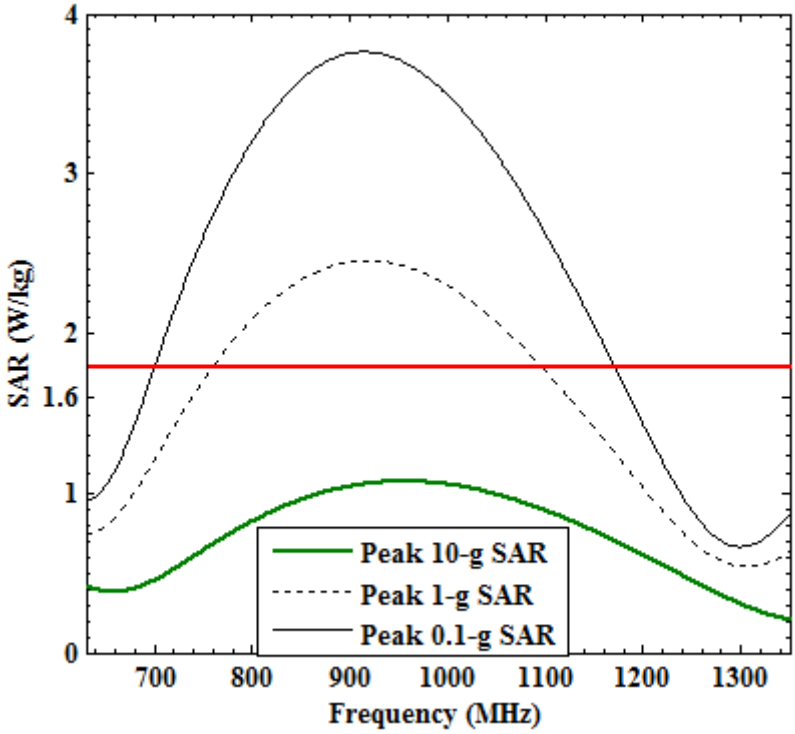

Figure 4.29. Peak 10-g, 1-g and 0.1-g SAR vs. Frequency induced in the realistic grounded human head model.

Variation of peak SAR with frequency in the range of 700 MHz to 1.3 GHz for 10-g, 1-g and 0.1-g mass is shown in Figure 4.29. For all resolutions, peak SAR value initially increases with increase of frequency and attains to maximum near the antenna resonance frequency then decreases with further increase of frequency. Because at the antenna resonance frequency maximum power is transmitted from the antenna to head model due to good impedance matching. The maximum value of peak 10-g, 1-g and 0.1-g SARs induced in the head are 1.07 W/kg, 2.45 W/kg and 3.75 W/kg, respectively. These result shows that the absorbed power at the frequency band of study is not uniform throughout the 10-g or 1-g mass of the head tissues. The absorbed power at any frequency within the band of study is concentrated to smaller mass in the form of node.

It is seen that maximum value of peak 10-g, 1-g and 0.1-g SARs induced in the head model obtained by variation of peak SAR with frequency are higher than that obtained in saggital and coronal planes at 925 MHz. This unwanted mismatch occurs due to

inhomogeneous nature of realistic human head model and the averaging technique. In case of saggital and coronal plane, peak gram average SARs are obtained by finding the value of maximum local SAR in 2-D but in the case of variation of peak SAR with frequency, peak gram average SARs are obtained by finding the value of maximum local SAR in 3-D.

4.3.4 Effect of GSM 900 band Mobile BSA on human body

With the introduction of digital mobile phone systems, number of mobile phone users has been increased rapidly. As a result, to support these large numbers of mobile phones the number of base stations is also increased proportionately. When the EM waves radiated from the transmitting mobile telephone BSA directly pass through the human body then a significant portion of the radiated power is absorbed by the body tissues [65]. Human body is non-homogeneous and anisotropic in nature. Absorption of EM waves at RF inside the human body creates standing waves, which causes localized hot spots [66]. The energy absorptions due to localized hot spots may result in boils, drying up the fluids around eyes, brain, joints, heart, abdomen, etc. Higher level of non-ionizing radiation may damage DNA of the living tissues [67]. Large number of investigations on the hazardous effects of mobile telephone BSAs are available in the literature but very few of that are available on the effects on wellbeing [68]. The current international safety guidelines or standards have been established for avoiding or limiting the potentially hazardous exposures of human head and other body parts from the adverse biological effects due to RF exposure [21]-[23].

In this study, SAR, MLSAR and SAR_{WB} induced within the human head and full body model exposed to a BSA at GSM 900 band have been calculated using hybrid FDTD and SFDTD methods.

4.3.4.1 SAR calculation in human head

Using hybrid FDTD method, SAR induced inside a three layered spherical human head model exposed to a 100 W mobile BSA at GSM 900 band has been investigated in order to find out the safety distance of head from the mobile BSA and compared that with SFDTD method. MLSAR has been calculated at 925 MHz, keeping distance (R) between head and BSA in the range of 0.5 m to 5.0 m. Geometry of the human head model along with BSA is shown in Figure 4.30 (a) where Yee cell length δ = 0.5 cm. The three layered spherical human head model has a uniform content at its core representing the human brain of diameter

19.0 cm. Core is surrounded by two spherical shells each having width of 0.5 cm. The inner shell is representing the skull (bone) and the outer shell is representing the skin.

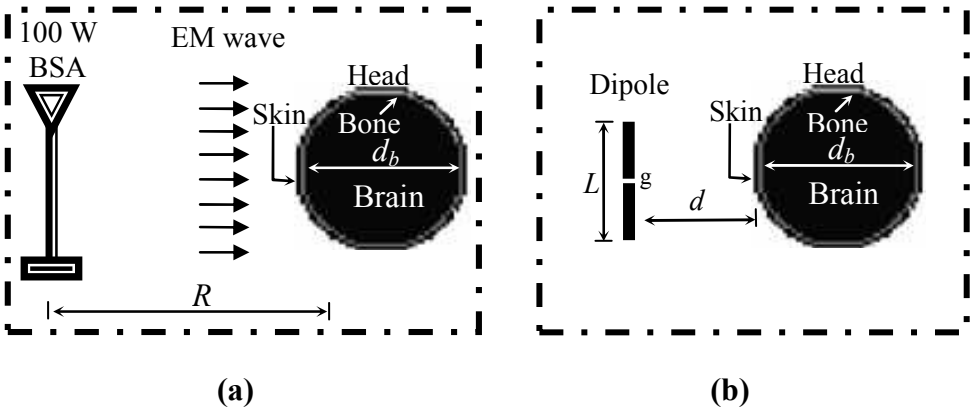

Figure 4.30. Geometry of (a) BSA and (b) fictitious dipole antenna along with the human head model. [R = 0.5 m – 5.0 m, $g = 1\delta$, $L = 29\delta$, $d_b = 38\delta$ and $d = 2\delta$].

In the hybrid FDTD method, the BSA is replaced by an equivalent half-wave fictitious dipole antenna of length 14.5 cm as shown in Figure 4.30 (b). The fictitious dipole antenna is assumed to receive microwave power from the BSA and relays the received power toward the head model. Distance d between head and fictitious dipole antenna is maintained constant at 1.0 cm for a set of R in the range of 0.5 m to 5.0 m. VSWR of the BSA is below 1.4 for GSM 900 band. Effective aperture A_{et} of it is 0.151 m^2 [69]. Effective aperture of the fictitious dipole antenna is obtained by [70]:

$$A_{er} = 0.13\lambda^2 \tag{4.11}$$

Using Friis transmission equation (3.26), received power P_r at the head which is at a distance of R from BSA is calculated considering transmitted power P_t = 100 W. Using equations (3.26 and 4.11), power to be relayed from the fictitious dipole antenna is calculated substituting the value of P_r.

In the application of SFDTD method, the actual space is splitted into three different 3-D segments: antenna segment, intermediate segment and head segment as shown in the Figure 4.31 (a-c) [71]. Antenna segment contains the equivalent half-wave dipole antenna and fictitious wall (F1), intermediate segment contains two fictitious walls (F1-F2) while the head segment contains the fictitious wall (F2) and the human head model. Here, the dipole antenna is assumed to transmit directly same power (100 W) as the BSA and Friis transmission equation is not required. Simulation using SFDTD is performed in the three segments separately. First, in antenna segment in each time step at each cell of the fictitious wall F1, all

the *E* and *H* components are picked up and stored. Then, in the intermediate segment the fictitious wall F1 acts as a source. The prestored values of the *E* and *H* components of antenna segment are retrieved into the corresponding cell of the fictitious wall F1 and the field components at each cell of the fictitious wall F2 are picked up to store at each time step. At last, in the head segment, the fictitious wall F2 acts as a source and the prestored values of the *E* and *H* components are retrieved into the corresponding cell of the fictitious wall F2 in each time step.

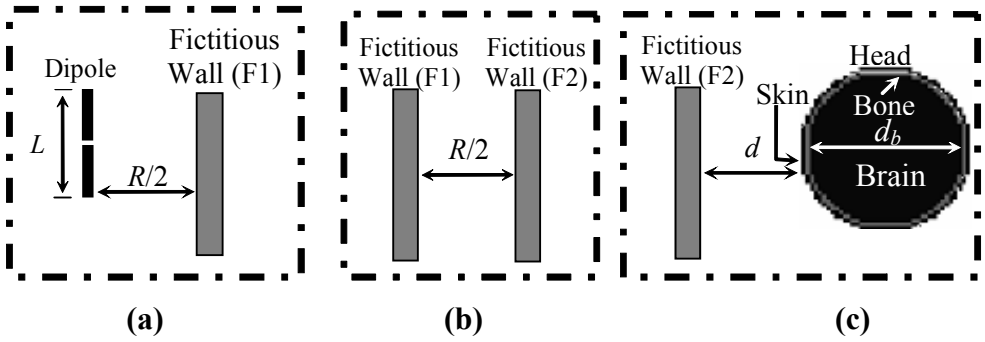

Figure 4.31. Geometry of the (a) antenna segment, (b) intermediate segment and (c) head segment.

Figure 4.32 shows the MLSAR obtained by hybrid FDTD and SFDTD methods in the human head model at frequency of 925 MHz for a set of *R* in the range of 0.5 m to 5.0 m. From the figure, it is seen that MLSAR is obtained in the range of 4.65 W/kg to 0.05 W/kg for hybrid FDTD method and 4.22 W/kg to 0.05 W/kg for SFDTD method. When *R* is less than 1.0 m then MLSAR is above FCC and IEEE's upper safety limit (1.6 W/kg) [22],[23]. For *R* greater than or equal to 1.0 m, MLSAR goes below the upper safety limit.

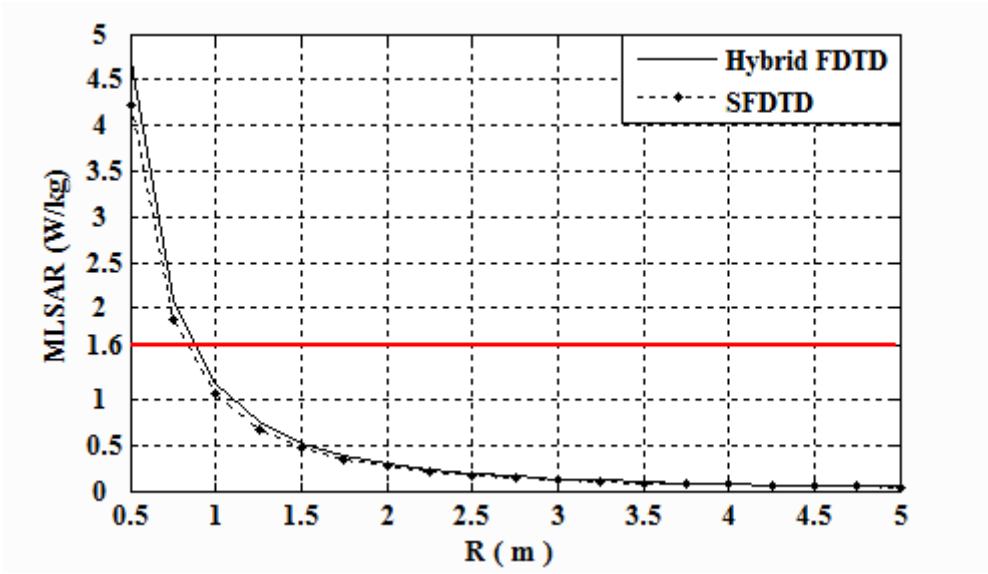

Figure 4.32. MLSAR vs *R* in human head model at frequency of 925 MHz.

SAR distribution obtained by SFDTD and hybrid FDTD methods at the middle layer of YZ plane inside the human head model for R = 1.0 m at frequency of 930 MHz are shown in Figure 4.33 (a-b). From the figures, it is seen that higher values of SARs are induced in the outer section of head consisting of skin and bone tissues nearer to the antenna side. Lower values of SARs are induced in the core region of head consisting of brain tissue.

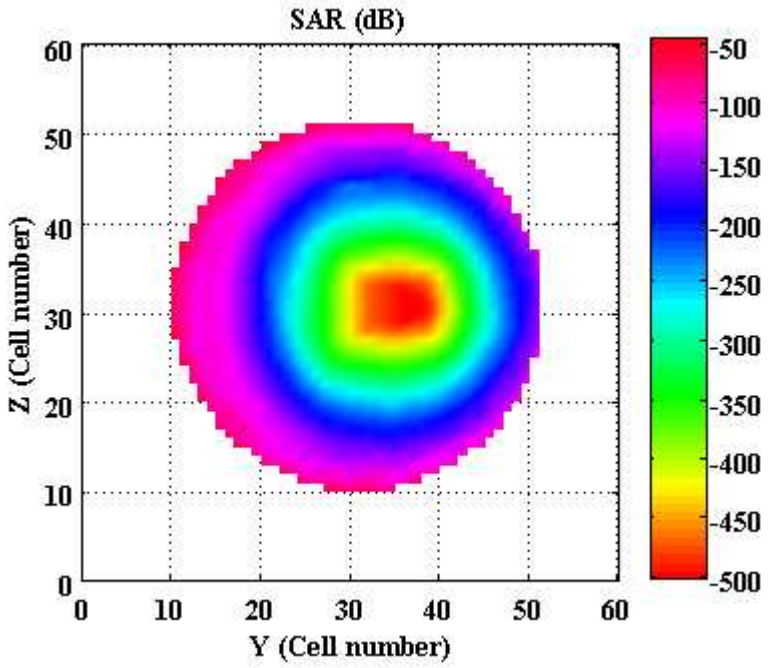

(a)

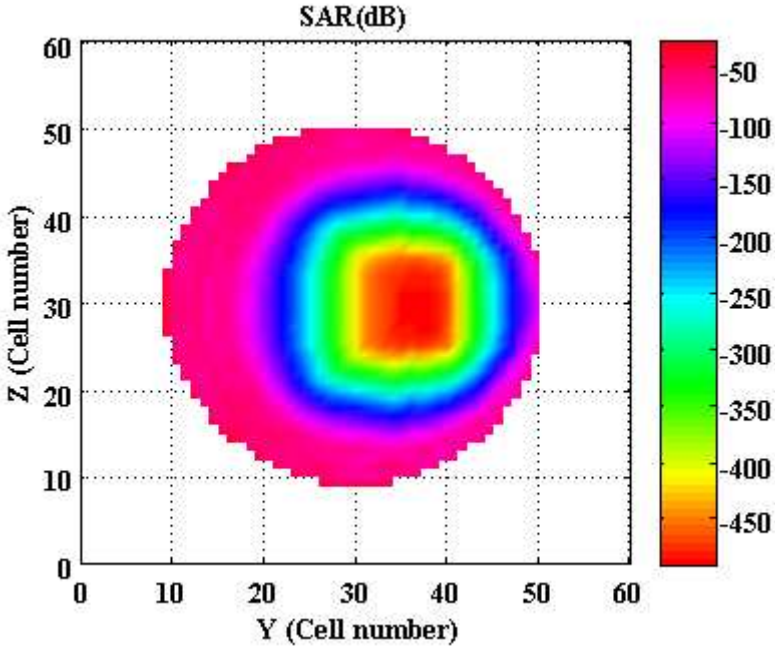

(b)

Figure 4.33. SAR distribution at the middle layer of YZ plane obtained by (a) SFDTD and (b) hybrid FDTD methods.

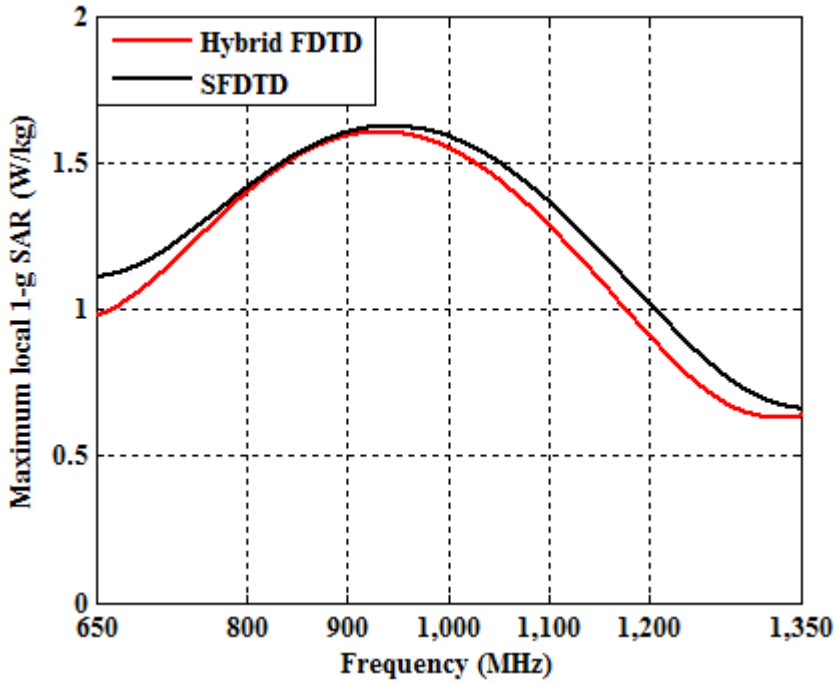

Figure 4.34 Maximum local 1-g SAR vs. frequency obtained by SFDTD and hybrid FDTD methods.

Variations of maximum local 1-g SAR with frequency in the range of 650 MHz to 1.35 GHz obtained by SFDTD and hybrid FDTD methods are shown in Figure 4.34. For both methods, maximum local 1-g SAR initially increases with increase of frequency and attains to maximum near the antenna resonance frequency near 930 MHz then decreases with further increase of frequency. Because at the antenna resonance frequency maximum power is transmitted from the antenna to head model due to good impedance matching. The peak value of maximum local 1-g SAR induced in the head obtained using SFDTD and proposed hybrid FDTD methods are 1.60 W/kg and 1.59 W/kg, respectively.

4.3.4.2 Estimation of Whole-body average SAR in Human Body

EM wave absorption inside the full human body has been investigated using hybrid FDTD and SFDTD methods. The human body has been modelled using 3- D voxel based dataset considering different electrical parameters. At GSM 900 band, SAR induced inside the human body model exposed to a radiating BSA has been calculated for multiple numbers of carrier frequencies and input power of 20 W/carrier. Distance (R) of human body from BSA is varied in the range of 0.5 m to 5.0 m. Modelling of the BSA is described in detail in Section 3.7.4 and the corresponding 3-D geometry is shown in Figure 3.18.

4.3.4.2.1 Development of simulation model

The full human body model has been constructed from voxel based Zubal phantom which is based on CT scan data of a 35 year old physically normal male weighing 70.31 kg and measuring 1.78 m in height [49]. MATLAB program is used to read, resample and reshape the phantom volume data consists of 192 × 96 × 498 voxels, each having dimensions of 3.6 mm × 3.6 mm × 3.6 mm. To simplify the numerical calculations, resolution of the human body is reduced to 75 × 75 × 245 voxels, each of dimensions: 5.0 mm × 5.0 mm × 5.0 mm. Geometry of the human body model along with BSA is shown in Figure 4.35. The human body is comprised of eighty seven types of tissues. Mass density ρ (kg/m^3), relative dielectric constant ε_r and conductivity σ (S/m) of the eighty seven tissues at GSM 900 band are obtained from the literature [46].

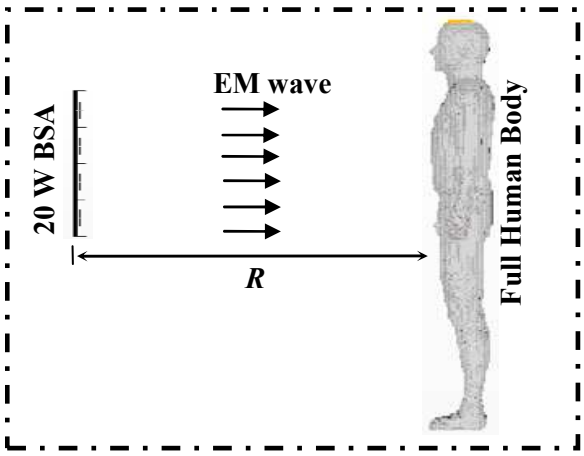

Figure 4.35. Geometry of the BSA along with the human body model.

In India, BSA acting in the GSM 900 band transmits in the frequency range of 935 MHz - 960 MHz (base station to handset) providing 124 RF channels (channel numbers 1 to 124) spaced at 200 KHz [72]. The method chosen by GSM is a combination of Time- and Frequency-Division Multiple Access (TDMA / FDMA). The FDMA part involves the division by frequency of (maximum) 25 MHz bandwidth which is divided into twenty sub-bands of 1.2 MHz and is allocated to various operators. There may be several number of carrier frequencies (1 to 5) allotted to one operator with upper limit of 6.2 MHz bandwidth. Each carrier frequency may transmit 10 to 20 W of power. So, one operator may transmit 50 to 100W of power. There may be 3-4 operators on the same roof top or tower; therefore, total transmitted power may be 150 to 400W.

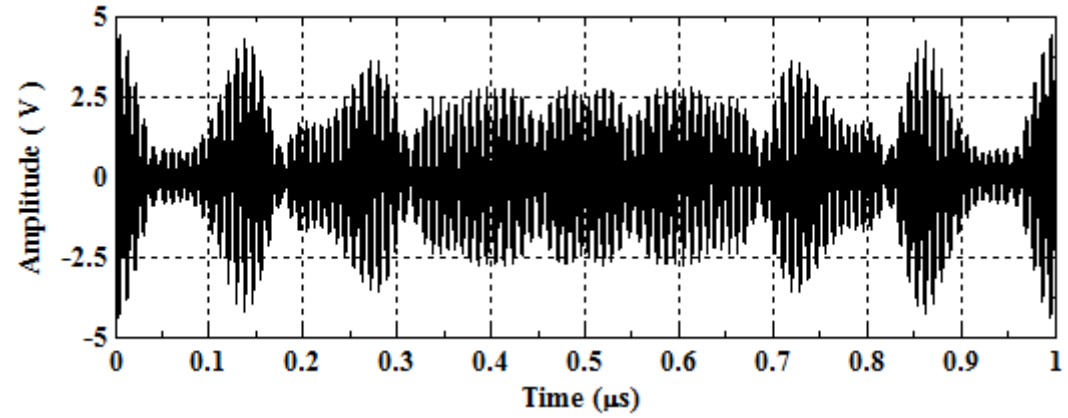

(a)

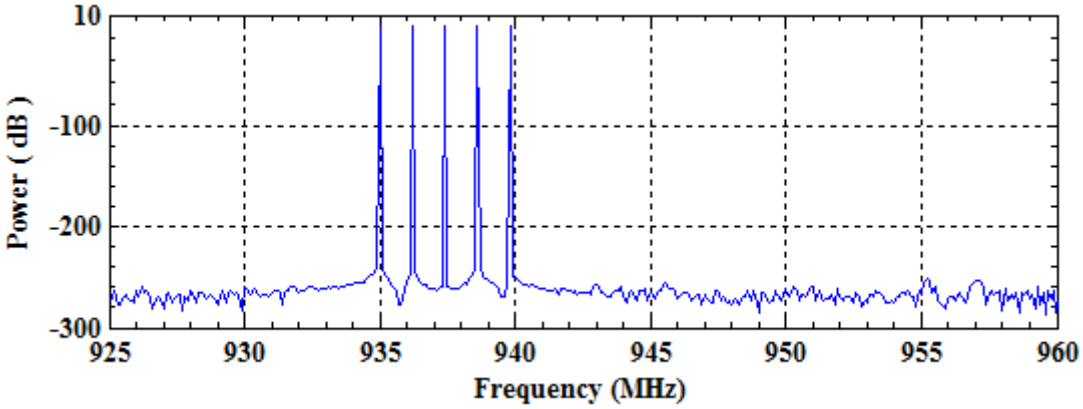

(b)

Figure 4.36. Spectrum of 5 carrier frequencies in (a) time domain and (b) frequency domain.

Time and frequency domain GSM 900 band downlink spectrum for five carrier frequencies are shown in Figure 4.36 (a-b). The spikes as shown in Figure 4.36 (b) are corresponding to the frequencies (carriers) used by the operator.

The distributions of *E* field and *H* field intensity in free space for distance up to 5.0 m from BSA have been computed using CST Microwave Studio®. Distributions of *E* field and *H* field intensity at 925 MHz in the mid YZ-plane and XY-plane for BSA are shown in Figures 4.37-4.38. Peak value of *E* and *H* field intensity at 5.0 m away from the BSA antenna are found to be 24.1 V/m and 0.06 A/m respectively. The peak value of *E* and *H* field at 5.0 m away from the BSA can also be calculated using the equations (3.28) and (3.29), and becomes approximately equal to 23.5 V/m and 0.06 A/m which closely agrees with the value obtained using CST Microwave Studio®.

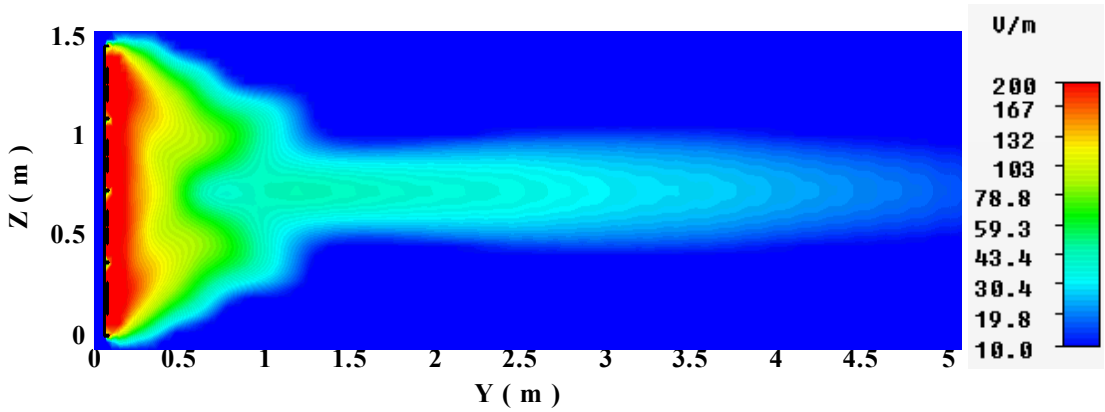

(a)

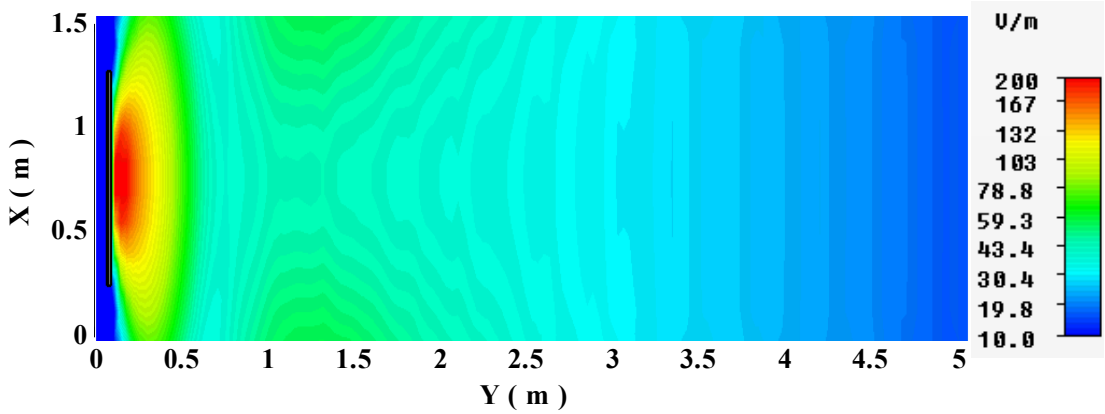

(b)

Figure 4.37. *E* field distributions at 925 MHz in (a) YZ-plane and (b) XY-plane in free space.

In SFDTD method, the actual problem space is divided into different segments to reduce the computational requirements and enhances the practicability of running the simulation on a PC [71]. To carry out the required numerical evaluation of SAR and EM field distributions inside the human body model using SFDTD method, the actual space is splitted into three different 3-D segments: antenna segment, intermediate segment and body segment as shown in the Figure 4.39 (a-c).

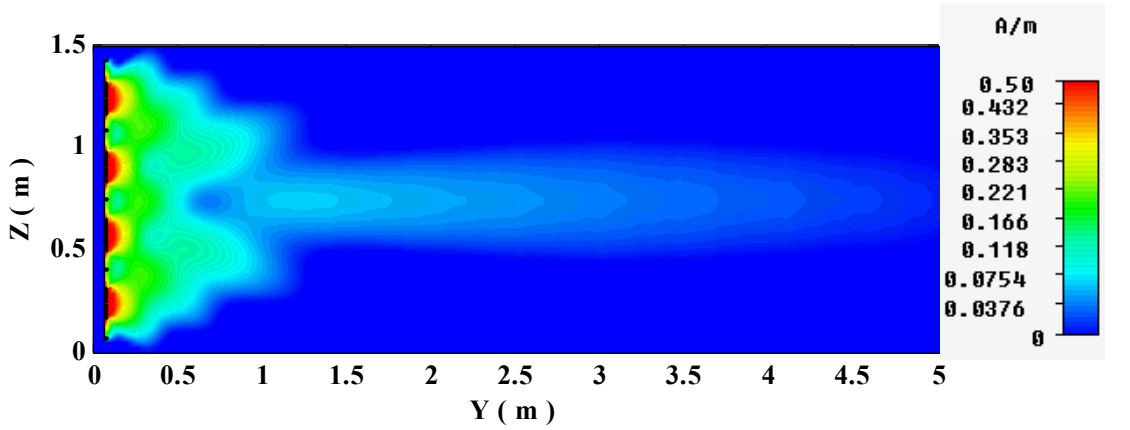

(a)

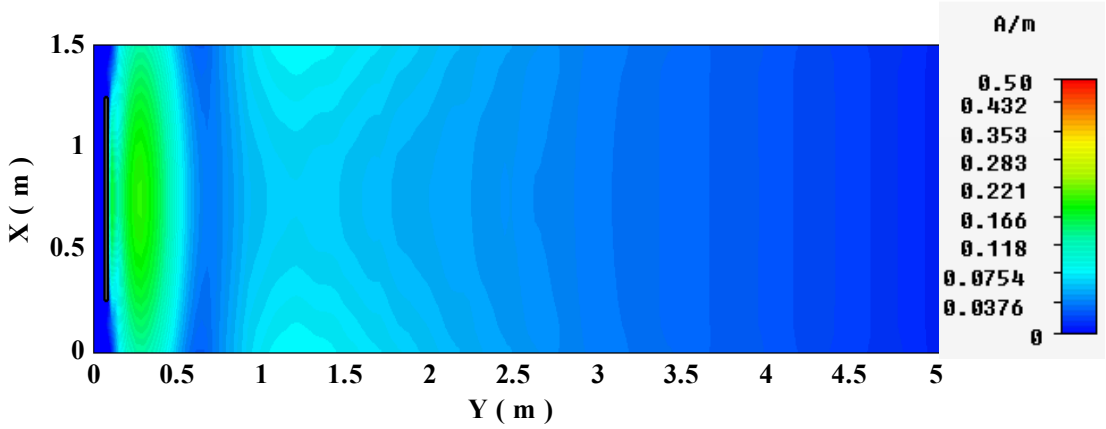

(b)

Figure 4.38. *H* field distributions at 925 MHz in (a) YZ-plane and (b) XY-plane in free space.

After a distance in the order of tens of wavelengths, the field from most antennas behaves like a plane wave [73]. Therefore, for the convenience of simulation in hybrid FDTD method, the simulation model shown in Figure 4.35 is divided into two sub domains namely domain 1 and 2 as shown in Figure 4.40. Domain 1 is used to compute the characteristics of resultant fictitious plane wave source. This plane wave source is actually a replacement of the radiating BSA placed at a distance R from the human model and its properties are calculated from equation (3.26) considering transmitted power P_t = 20 W/carrier. In domain 2, the fictitious plane wave is placed at a distance of r = 25 mm away from the human model and the required E field and H field intensity at a distance R from the antenna can be calculated from equations (3.28) and (3.29) respectively.

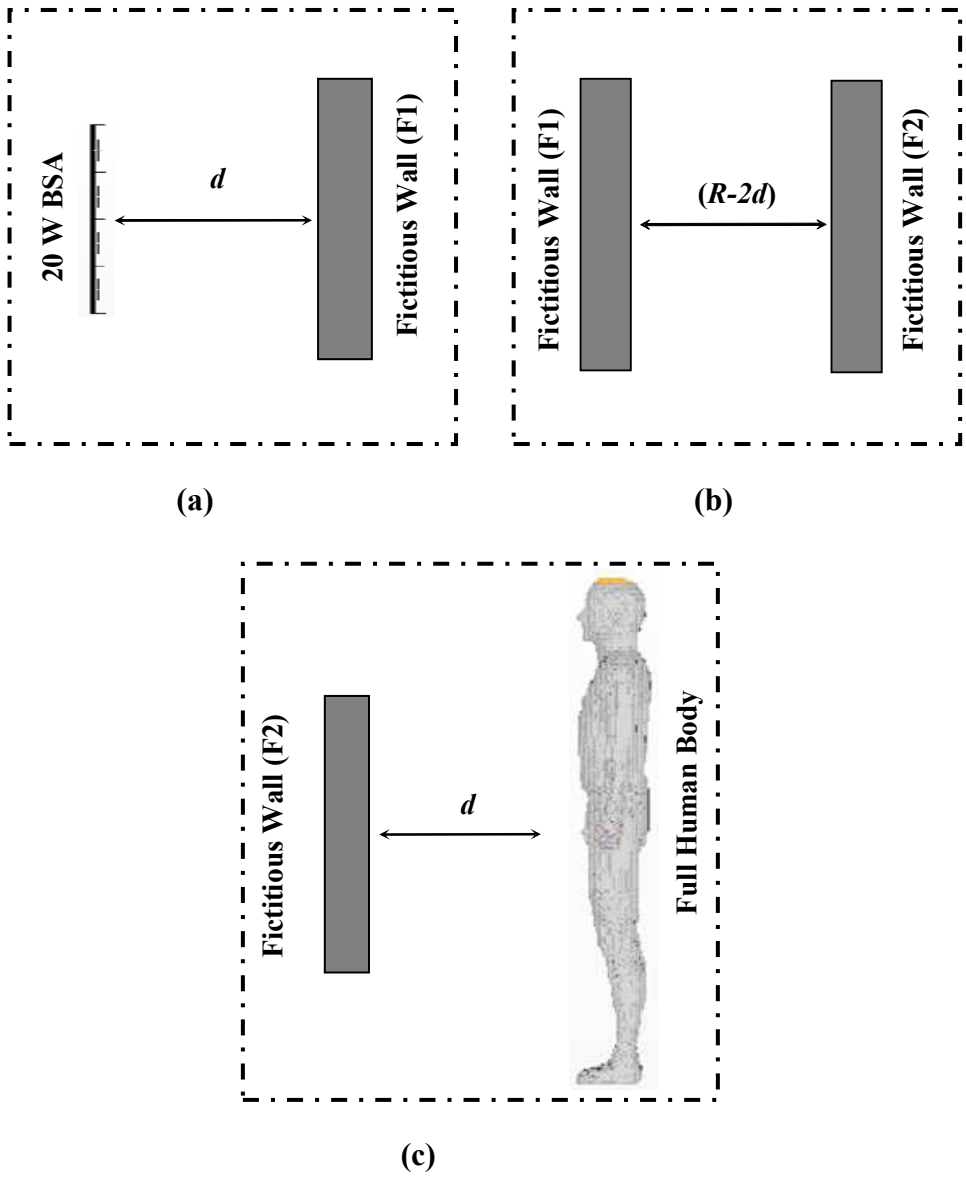

Figure 4.39. Geometry of the (a) antenna segment, (b) intermediate segment and (c) body segment.

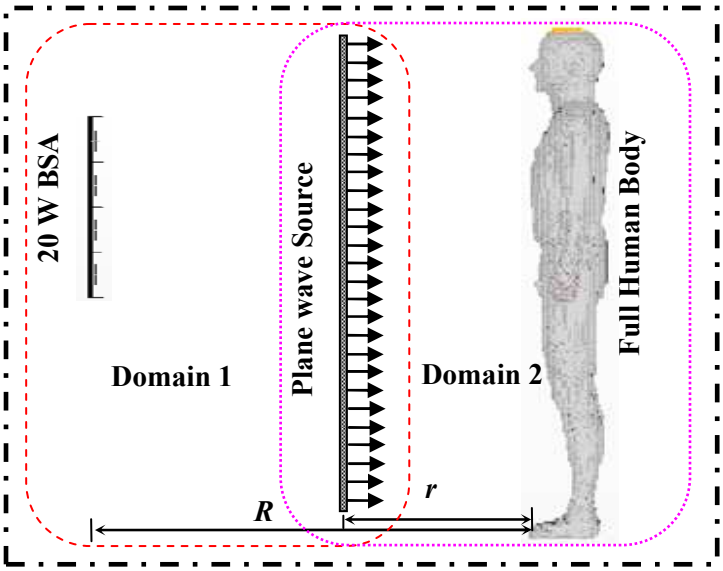

Figure 4.40. Geometry of human model along with BSA [*R* = 0.5 m to 1.5 m and *r* = 25 mm].

4.3.4.2.2 SAR Calculation

SAR distributions in dB scale inside the human body model at the mid-saggital and mid-coronal planes for *R* = 0.5 m due to 5 carrier are shown in Figure 4.41 (a-b). From Figure 4.41, it is seen that higher value of SAR is found in the superficial region of the human body model consisting of mainly skin tissue. But lower value of SAR is induced in thoracic and abdominal cavity region of the human body model, major portion of which is filled with air.

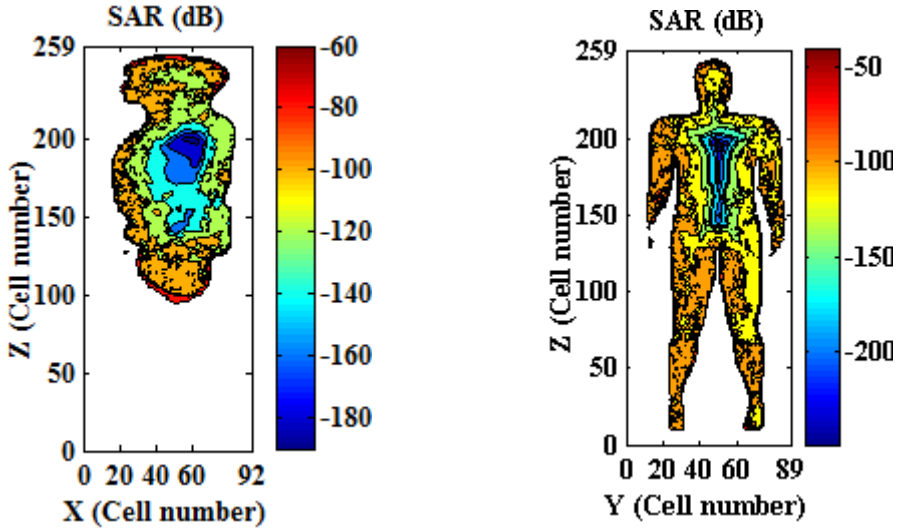

(a) **(b)**

Figure 4.41. SAR distributions in (a) mid-saggital plane and (b) mid-coronal plane for *R* = 0.5 m and five carrier frequencies.

Variations of SAR_{WB} with R for multiple numbers of carrier frequencies obtained by hybrid FDTD and SFDTD methods are shown in the Figure 4.42. From Figure 4.42, it is found that SAR_{WB} obtained by hybrid FDTD method closely matches with that obtained by the SFDTD method. Either due to increase of R or decrease the number of carrier frequencies, SAR_{WB} decreases. For number of carrier frequency equal to five and R = 0.5 m, maximum value of SAR_{WB} obtained by both hybrid FDTD and SFDTD method is found to be 0.69 W/kg which exceeds the occupational exposure safety limit but for R more than 1.5 m, value of SAR_{WB} is below the general public exposure safety limit. From the simulation it is found that the value of safety distance for general public is 1.5 m due to five number of carrier frequencies but its value decreases with lowering the number of carrier frequencies.

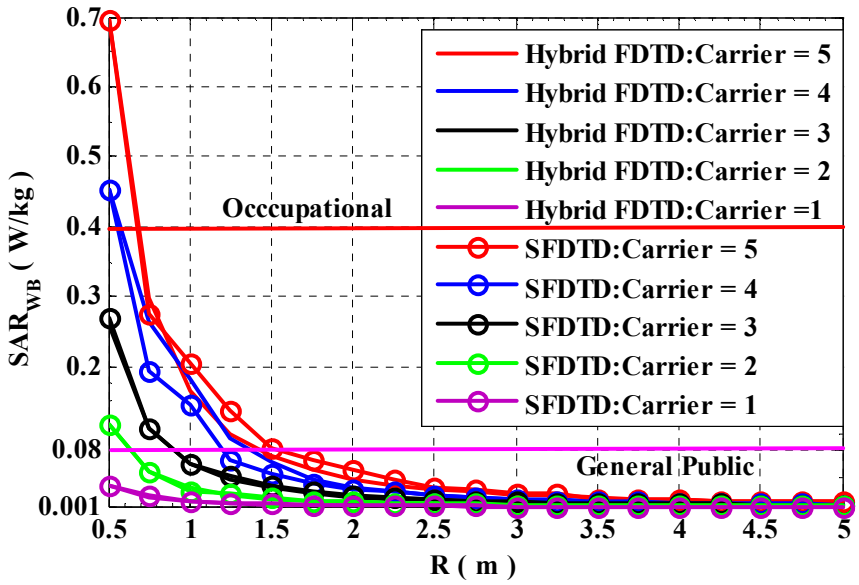

Figure 4.42. Variations of SAR_{WB} with R for multiple numbers of carrier frequencies.

Variations of SAR_{WB} with Time for multiple numbers of carrier frequencies and R = 1.0 m obtained by hybrid FDTD method are shown in Figure 4.43. From the figure it is found that after 0.2 μs settling time, with increase of time SAR_{WB} increases exponentially for very short period of time then it becomes almost constant for each number of carrier frequencies. Steady-state value of SAR_{WB} increases with increase of number of carrier frequencies and vice-versa.

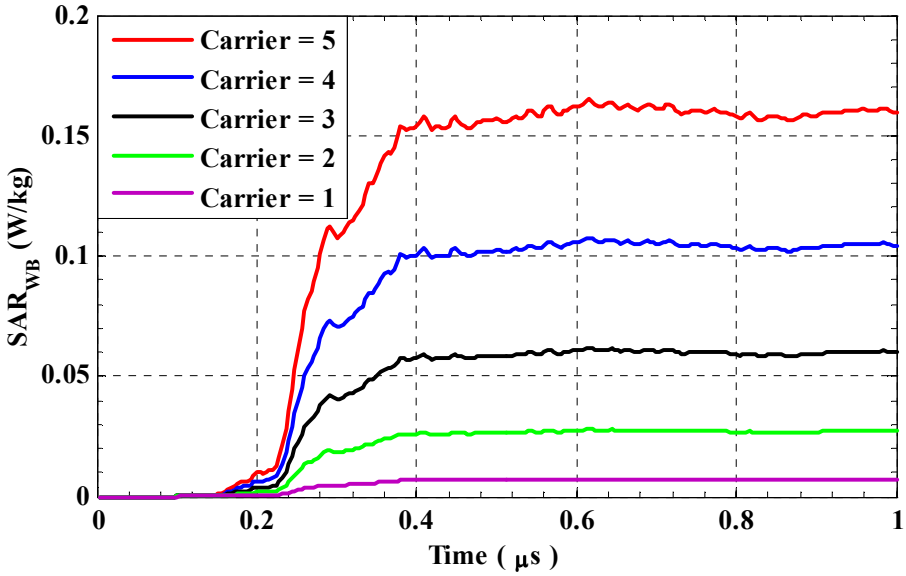

Figure 4.43. Variations of SAR_{WB} with Time obtained by hybrid FDTD method for multiple numbers of carrier frequencies and R = 1.0 m.

4.4 Conclusions

In this chapter, the concept of dosimetry has been discussed in details. Important of SAR correspond to the dosimetric concept and different EM numerical methods have been particularly highlighted for assessment of SAR. The current safety levels and EM exposure guidelines with respect to different dosimetric parameters have been reviewed shortly. Finally, assessment of the EM field interaction with human body has been discussed.

Using in-house FDTD code developed in MATLAB, SAR analysis has been started to evaluate the MLSAR induced inside a homogeneous box type and a three layered inhomogeneous spherical human head models exposed to a half-wave radiating dipole antenna. It has been found that the MLSAR reaches its maximum value near the fundamental resonance frequency of the dipole antenna due to large amount of energy transfer from antenna to head model for good impedance matching.

Then the simplified geometrical head models are replaced by realistic anatomical human head models (Zubal and DICOM head model) obtained from CT or MRI scanned voxel based anthropomorphic phantom data. FDTD based simulation has been carried out to calculate induced MLSAR in addition with the current, electric field, magnetic field and absorbed power density inside the grounded Zubal head model exposed to a half-wave radiating dipole antenna designed at GSM 900 band.

The half-wave resonating dipole antenna is replaced by a hand held mobile phone which is consisted of a monopole antenna mounted on a metallic rectangular box. Commercially available software CST Microwave Studio® and FDTD method have been used to calculate peak gram averaged SAR induced in the DICOM data based head and hand models for a hand held mobile phone. Variation of peak 10-g and 1-g SAR with frequency for DICOM data based human head model with and without hand is compared with that for the Zubal head model without hand due to the same mobile phone. It has been found that the nature of variation of peak gram averaged SARs with frequency obtained for the DICOM data based human head model agrees with that obtained from Zubal head model. For all resolutions, peak SAR value initially increases with increase of frequency and attains to maximum near the antenna resonance frequency then decreases with further increase of frequency within both head models.

The hand held mobile phone is replaced by a compact dual-band PIFA designed for GSM mobile phone to calculate the peak SAR values averaged over 10-g, 1-g and 0.1-g mass induced inside the grounded Zubal head model. Maximum value of peak 10-g, 1-g and 0.1-g SARs at 925 MHz in different type of head tissues are calculated and it has been found that maximum value of peak gram averaged SARs for all resolutions are obtained in skin tissue. Whereas, minimum value of peak gram averaged SARs for all resolutions are obtained in bone marrow tissues. Variation of peak SAR with frequency in the range of 700 MHz to 1.3 GHz for 10-g, 1-g and 0.1-g mass shows that for all resolutions, peak SAR value initially increases with increase of frequency and attains to maximum near the antenna resonance frequency then decreases with further increase of frequency due to maximum power transmission from the antenna to head model for impedance matching.

In order to find out the safety distance of human head from the mobile BSA, SAR induced inside a three layered spherical human head model exposed to a 100 W mobile BSA at GSM 900 band has been investigated using hybrid FDTD method and compared that with SFDTD method. It has been found that when the distance of human head from the mobile BSA is less than 1.0 m then MLSAR is above FCC and IEEE's upper safety limit but when the distance is greater than or equal to 1.0 m, MLSAR goes below the upper safety limit.

SAR_{WB} induced inside a full human body has been investigated using hybrid FDTD and SFDTD methods. The human body has been modelled using 3-D CT scan voxel based Zubal phantom dataset considering different electrical parameters. At GSM 900 band, SAR induced inside the human body model exposed to a radiating BSA has been calculated for

multiple numbers of carrier frequencies and input power of 20 W/carrier. Distance of the human body from BSA is varied in the range of 0.5 m to 5.0 m. It has been found that either due to increase of the distance or decrease of the number of carrier frequencies, SAR_{WB} decreases.

References

[1] P. Bernardi, "Power absorption and temperature elevations induced in the human head during a dual-band monopole-helix antenna phone," *IEEE Trans. Microwave Theory Tech.*, vol. 49, No. 12, pp. 2539-46, 2001.

[2] A. Drossos, V.Santomaa and N.Kuster, "The dependence of electromagnetic energy absorption upon human head tissue composition in the frequency range of 300-3000 MHz," *IEEE Trans. Microwave Theory Tech.*, vol. 48, pp. 1988-1995, 2000.

[3] Chiang et al, "Health effects of environmental electromagnetic fields", *Journal of Bioelectricity*. 8(1), 127-131 (1989). EPI2064.

[4] J.E.H. Tattersall, I.R. Scott, S.J. Wood, J.I. Nettell, M.K. Bevier, Z. Wang, N.P. Somasiri and X. Chen, "Effects of low intensity radiofrequency electromagnetic fields on electrical activity in rat hippocampal slices," *Brain Research*, vol. 904, pp. 43-53, 2001.

[5] G. Emili, A. Schiavoni, M. Francavilla, L. Roselli, and R. Sorrentino, "Computation of electromagnetic field inside a tissue at mobile communications frequencies," *IEEE Trans. Microwave Theory Tech.*, vol. 51, No. 1, pp. 178-186, 2003.

[6] M. Sancho, G. Martinez and C. Martin, "Accurate dielectric modelling of shelled particles and cells," *Journal of Electrostatics*, vol. 57, pp. 143-156, 2003.

[7] N.S. Stoykov, J.W. Jerome, L.C. Pierce and A. Taflove, "Computational modelling evidence of nonthermal electromagnetic interaction mechanism with living cells: Microwave nonlinearity in the cellular Sodium ion channel," *IEEE Trans. Microwave Theory Tech.*, vol. 52, No. 8, pp. 2040-2045, 2004.

[8] N. Chavannes, R. Tay, N. Nikoloski and N. Kuster, "Suitability of FDTD-based TCAD tools for RF design of mobile phones," *IEEE Antennas & Propagation Magazine*, vol. 45, No. 6, pp. 52-66, 2003.

[9] N. Chavannes, P. Futter, R. Tay, K. Pokovic, and N. Kuster, "Reliable prediction of mobile phone performance for different daily usage patterns using the FDTD method," in Proceedings of the IEEE International Workshop on Antenna Technology (IWAT '06), pp. 345–348, White Plains, NY, USA, Mar. 2006.

[10] P. Futter, N.Chavannes, R. Tay, et al., "Reliable prediction of mobile phone performance for realistic in-use conditions using the FDTD method," *IEEE Antennas and Propagation Magazine*, vol. 50, No. 1, pp. 87–96, 2008.

[11] H. Shabani, M.R. Islam, AHM Z. Alam and H.E. Abd EI-Raouf, "EM Radiation from Wi-LAN Base Station and Its' Effects in Human Body," 5th International Conference on Electrical and Computer Engineering, Dhaka, Bangladesh, pp. 86-91, 2008.

[12] IEEE Recommended Practice for Determining the Peak Spatial-Average Specific Absorption Rate (SAR) in the Human Head from Wireless Communications Devices: Measurement Techniques, IEEE Standard-1528, Dec. 2003.

[13] S.G. Allen, "Radiofrequency field measurements and hazard assessment," *Journal of Radiological Protection*, vol. 11, pp. 49-62, 1996.

[14] Standard for Safety Levels with Respect to Human Exposure to Radiofrequency Electromagnetic Fields, 3 kHz to 300 GHz, IEEE Standards Coordinating Committee 28.4, 2006.

[15] Product standard to demonstrate the compliance of mobile phones with the basic restrictions related to human exposure to electromagnetic fields (300 MHz–3GHz), European Committee for Electrical Standardization (CENELEC), EN 50360, Brussels, 2001.

[16] Basic Standard for the Measurement of Specific Absorption Rate Related to Exposure to Electromagnetic Fields from Mobile Phones (300 MHz–3GHz), European Committee for Electrical Standardization (CENELEC), EN-50361, 2001.

[17] Human exposure to radio frequency fields from hand-held and body-mounted wireless communication devices — Human models, instrumentation, and procedures — Part 1: Procedure to determine the specific absorption rate (SAR) for hand-held devices used in close proximity to the ear (frequency range of 300 MHz to 3 GHz), IEC 62209-1, 2006.

[18] Specific Absorption Rate (SAR) Estimation for Cellular Phone, Association of Radio Industries and businesses, ARIB STD-T56, 2002.

[19] Evaluating Compliance with FCC Guidelines for Human Exposure to Radio Frequency Electromagnetic Field, Supplement C to OET Bulletin 65 (Edition 9701), Federal Communications Commission (FCC),Washington, DC, USA, 1997.

[20] ACA Radio communications (Electromagnetic Radiation— Human Exposure) Standard 2003, Schedules 1 and 2, Australian Communications Authority.

[21] International Commission on non-Ionizing Radiation Protection, "ICNIRP statement-Health issues related to the use of hand –held radiotelephones and base transmitters," *Health Phys*., vol. 70, No. 4, pp. 587-593, April-1996.

[22] American National Standard – Safety Levels with Respect to Exposure to Radio Frequency Electromagnetic Fields, 3 kHz to 300 GHz, ANSI/ IEEE C95.1 - 1992.

[23] Federal Communication Commission (FCC), Evaluating compliance with FCC guidelines for human exposure to radiofrequency electromagnetic fields", Bulletin 65, Supplement C, 1997. Home Page. http://www.fcc.gov.

[24] J. Wang and O. Fujiwara, "Numerical and Experimental Evaluation of Dosimetry in the Human Head for Portable telephones," *IEICE Trans. Communication*, vol. J84-B, No. 1, pp. 1-10, 2001.

[25] J.M. Osepchuk and R.C. Petersen, "Safety Standards for Exposure to RF Electromagnetic Fields," *IEEE, Microwave Magazine*, vol. 2, pp. 55-69, 2001.

[26] S.I.Y. Al-Mously, Design and performance enhancement of cellular handset antennas and assessment of their EM interaction with a human, [Ph.D. thesis], Department of Electrical and Computer Engineering, School of Applied Sciences and Engineering Academy of Graduate Studies, Janzoor-Tripoli-Libya, August 2009.

[27] O.P. Gandhi, Gianluca Lazzi and M.Cynthia Furse, "Electromagnetic Absorption in the Human Head and Neck for Mobile Telephones at 835 and 1900 MHz," *IEEE Trans. Microwave Theory Tech*., vol. 44, pp. 1884-1897, 1996.

[28] K. Caputa, M.Okoniewski, M.A.Stuchly, "An algorithm for computations of the power deposition in human tissue," *IEEE Antennas and Propagation Magazine*, vol. 41, pp.102-107, 1999.

[29] J. Wang and O. Fujiwara, "Dosimetry in the Human Head for Portable telephones," http://rp.iszf.irk.ru/hawk/URSI2002/rsreview/3.pdf.

[30] S. Watanabe and L. Martens, "Comparison of Averaging Procedures for SAR Distributions at 900 and 1800 MHz," *IEEE Trans. Microwave Theory Tech.*, vol. 48, No. 11, pp. 2180-2184, November-2000.

[31] Recommended Practice for Determining the Peak Spatial-Average Specific Absorption Rate (SAR) associated with the use of wireless handsets-computational techniques, IEEE-1529, draft standard.

[32] P. Stavroulakis, "Biological Effects of Electromagnetic Fields," *Springer*, 2002.

[33] S. Khalatbari, D. Sardari, A.A. Mirzaee and H.A. Sadafi, "Calculating SAR in Two Models of the Human Head Exposed to Mobile Phones Radiations at 900 and 1800MHz," Progress In Electromagnetics Research Symposium 2006, pp. 104-109, Cambridge, USA, March 2006.

[34] S.K. Huha, S. Neogi and G. Kumar, "Report on: Cell phone towers radiation hazards," Submitted to West Bengal Environment Minister, October-2011.

[35] M. Zhang and A. Alden, "Calculation of whole-body SAR from a 100 MHz dipole antenna," *Progress In Electromagnetics Research*, vol. 119, pp. 133-153, 2011.

[36] International Commission on Non-Ionizing Radiation Protection (INIRP), "Guidelines for limiting exposure to time-varying electric, magnetic, and electromagnetic fields (up to 300GHz)", *Health Physics*, vol. 75, No. 4, pp. 442, 1998.

[37] International Commission on Non-Ionizing Radiation Protection (ICNIRP). Statement on the "Guidelines for limiting exposure to time-varying electric, magnetic and electromagetic fields (up to 300 GHz)," 2009.

[38] IEEE Standard C95.1 - 1999, "IEEE standard for safety levels with respect to human exposure to radio frequency electromagnetic fields, 3 kHz to 300 GHz," 1999.

[39] Ronald Kitchen, "RF and microwave radiation safety handbook," Butterworth-Heinemann, Second edition 2001.

[40] B.B. Beard, W. Kainz, T. Onishi, et al., "Comparisons of computed mobile phone induced SAR in the SAM phantom to that in anatomically correct models of the human head," *IEEE Transaction on Electromagnetic Compatibility*, vol. 48, no. 2, pp. 397–407, 2006.

[41] B.B. Beard and W. Kainz, "Review and standardization of cell phone exposure calculations using the SAM phantom and anatomically correct head models," *Bio. Medical Engineering*, Online, 2004, 3:34, doi: 10.1186/1475-925X-3-34.

[42] A. Karwowski, "Comparison of simple models for predicting radiofrequency fields in vicinity of base station antennas," *Electronics Letters*, vol. 36, No. 10, pp. 859-861, May-2000.

[43] M. Dennis Sullivan, O.P. Gandhi and Allen Taflove, "Use of the Finite Difference Time-Domain Method for Calculating EM Absorption in Man Models," *IEEE Trans.BiomedicalEngineering*, vol. 35, No. 3, pp.179-186, March-1988.

[44] S. Khalatbari, D. Sardari, A.A. Mirzare and H.A. Sadafi, "Calculating SAR in two Models of the Human Head exposed to Mobile Phones radiations at 900 and 1800 MHz," Progress in Electromagnetics Research symposium 2006, Cambridge,USA, March, 26-29.

[45] O.P. Gandhi and Jin-Yuan Chen, "Electromagnetic Absorption in Human Head from Experimental 6-GHz Handheld Transceivers," *IEEE Trans.* Electromagnetic Compatibility, vol. 37, No. 4, pp. 547-557, November-1995.

[46] Dielectric Properties of the Human Body tissue in the Frequency Range of 10 Hz-100GHz. http://niremf.iroe.fi.cnr.it/tissprop.

[47] J. Keshvari and S. Lang, "Comparison of radio frequency energy absorption in ear and eye region of children and adults at 900, 1800 and 2450 MHz*," Physics Med. Biol*., vol. 50, pp. 4355-4369, 2005.

[48] H.Y. Chen and K.Y. Shen, "Reduction of SAR in a Human Head model wrapped in clothing Materials," *Microwave and Optical Technology Letter*, vol. 37. No. 4, pp. 305-308, May-2003.

[49] The Zubal Phantom data, MRI Head Phantom Data Description. http://noodle.med.yale.edu/phantom/getzubdesc.htm.

[50] N. Homsup and W. Homsup, "FDTD Simulation of a Mobile Phone Operating Near a Metal Wall," *Journal of Computers*, vol. 4, No. 2, pp. 168-175, February-2009.

[51] Hissing-Yi Chen and Hou-Hwa Wang, "Current and SAR induced in a human head model by the electromagnetic fields irradiated from a cellular phone," *IEEE Trans. Microwave Theory Tech*., vol. MTT – 42. No.12, pp. 2249-2254, December-1994.

[52] L. Tang and T.S. Ibrahim, "On the Radio-frequency power requirements of human MRI," *PIERS* Online, vol. 3, No. 6, pp. 886-889, 2007.

[53] DICOM files, http:// http://www.osirix-viewer.com/datasets/.

[54] Rumen Rusev, "A Module for Visualisation and Analysis of Digital Images in DICOM File Format," International Conference on Computer Systems and Technologies-CompSysTech'2003.

[55] http://www.pubimage.hcuge.ch:8080.

[56] The Matlab Central File Exchange, available at: http://www.mathworks.com/matlabcentral/fileexchange/loadFile.do?objectId=4879&objectType=file.

[57] T.M. Nassef, M. Alkhodary, M.K. Marei, N.H. Solouma and Y.M. Kadah, "Extraction of human Mandible bones from multi-slice Tomographic data," pp. 260-263, MECBME, February-2011.

[58] D.C. Dias Medora and N.E. Prashant, "Morphometric Study of the Ventricular System of Brain by Computerized Tomography," *Journal of the Anatomical Society of India*, vol. 56, No. 1 (2007-01 - 2007-06).

[59] Converting CT Data to Hounsfield Units, Fanning Consulting Services, http://www.idlcoyote.com/fileio_tips/hounsfield.html.

[60] Odelberg W: Godfred N. Hounsfield-Autobiography. The Nobel Prizes, The Noble Foundation, 1979.

[61] F. Terrier, M. Grossholz and C.D. Becker, "Spiral CT of the Abdomen," *Medical Radiology*, *Springer*, 1999.

[62] J. Wang and O. Fujiwara, "FDTD computation of temperature rise in the human head for portable telephones," *IEEE Trans. Microwave Theory Tech.*, vol. 47, pp. 1528-1534, August 1999.

[63] The Facts and Figures on Cellular Phone Radiation, (for Nokia Asha 501s Type RM-899) http://www.sarvalues.com/measuring-sar.

[64] M.T. Islam and M.R.I. Faruque, "Reduction of specific absorption rate (SAR) in the human head with ferrite material and metamaterial," *Progress in Electromagnetic Research C*, vol. 9, pp. 47-58, 2009.

[65] N. Kumar and G. Kumar, (2009, December). Biological Effects of Cell Tower radiation on Human Body. International Symposium on Microwave and Optical Technology (ISMOT). [Online]. Available: http://briarcliffheights.org/bch/wp-content/uploads/2011/12/celltowerradiationeffects-100317162351-phpapp01.pdf.

[66] H. Lennart, "Epidemiological evidence for an association between use of wireless phones and tumor diseases", *Pathophysiology*, *ELSEVIER*, PATPHY-595, 2009.

[67] H. Lai and N.P. Singh, "Melatonin and a spin-trap compound block radiofrequency electromagnetic radiation-induced DNA strand breaks in rat brain cells," *Bioelectromagnetics*, vol. 18, pp. 446-454, 1997.

[68] M. Kundi and H. Peter, "Mobile phone base stations-Effect on wellbeing and health," *Pathophysiology*, *ELSEVIER*, vol. 16, pp. 123-135, 2009.

[69] 500 W GSM Base Station Antenna, Home Page, http://www.globalsources.com/gsol/I/Base-station/p/sm/1008744388.htm.

[70] John.D. Kraus and R.J. Marhefka, "Antennas for All Applications," Tata Mc.Graw-Hill Publishing Company Limited, New Delhi, India, Third Reprint, 2003.

[71] Y. Wu and I. Wassell, "Introduction to the Segmented Finite-Difference Time-Domain Method," *IEEE Trans. on Magnetics*, vol. 45. No. 3, pp.1364-1367, March 2009.

[72] A. Loula, "Open BTS: Installation and Configuration Guide," vol. 0.1, 2009.

[73] D. M.Sullivan, Electromagnetic Simulation Using the FDTD Method, IEEE Press, New York, 2000.

Chapter 5

Study on hotspot, imaging and induced current inside Human Body

5.1 Introduction

In the previous chapter, in order to assess the RF effects due to the EM energy absorption in the human head and other body parts, EM numerical simulations have been used to calculate the distribution of EM fields or SAR values inside a living human head or body. But the localized RF energy absorption inside a living human head/body increases temperature of the human tissue. From this point-of-view, it is important to study the thresholds of thermal damages due to temperature rise.

In this chapter, temperature rise in an anatomically based human head model is calculated numerically using Pennes' BHE considering bio cooling effects for a mobile phone using FDTD method. Apart from the thermal effect, quasi optical effects of non-ionizing EM radiation inside a pregnant woman abdomen has been thoroughly explored in this chapter. At the end of this chapter, a RECTENNA based sensor is described for easy visual representation of EM field strengths at GSM 900 band.

5.2 Temperature Rise calculation

Tissue heating is not only influenced by SAR but also by the way in which the RF energy absorption is distributed in the surrounding area, by the thermal characteristics of the considered and neighbouring tissues and by the heat exchange mechanism with external environment [1]. So, the correlation between SAR values and temperature rise and between SAR and thermal distributions are not straight forward. But the thermal analysis is accompanied with SAR analysis for the assessment of safety of RF exposure as explained in Pennes' BHE [2]. In this study, maximum local temperature rise due to EM waves radiated

from a mobile phone antenna and hotspots created due to standing wave antinodes inside head cavity are investigated at the mid-GSM 900 band frequency of 930 MHz.

5.2.1 Development of simulation model

The geometry of the mobile phone and human head model used for the thermal simulation is shown in Figure 4.22 and described detail in Section 4.3.3. All the numerical computations are performed by calculating the SAR in the human head model using FDTD method and then substituting the SAR values into Pennes' BHE. The antenna input power is set to 0.6 W at 930 MHz.

The formation of thermal energy in living tissue is a complex process. It is involving of multiple phenomenological mechanisms such as conduction, convection, radiation, metabolism, evaporation and phase change. Based on the suggestion that the rate of heat transfer between blood and tissue is proportional to the product of the volumetric perfusion rate and the difference between the arterial blood temperature and the local tissue temperature, Pennes derived BHE [2], which is applied in most of the thermal simulations.

At the thermal equilibrium state of the human head model exposed to EM fields, temperature distribution inside the head model is obtained from the BHE. In this work the BHE takes into account only the heat exchange mechanisms: heat conduction, blood flow, metabolic process and EM heating [2]. The BHE is represented as:

$$\rho.C_p \frac{\partial T}{\partial t} = K\nabla^2 T + A_0 + \rho.SAR - b.\left(T - T_b\right) \tag{5.1}$$

subjected to the boundary condition:

$$K\frac{\partial T}{\partial n} = -h.\left(T - T_a\right) \tag{5.2}$$

where, T is temperature of the tissue (^{o}C), K is thermal conductivity of the tissue (W/m.^{o}C), A_0 is the heat source due to metabolic process (J/s.m^3), C_p is specific heat of the tissue (J/kg.^{o}C), b is a constant associated with blood flow (W/m^3.^{o}C), T_b is blood temperature (^{o}C), T_a is ambient temperature (^{o}C), h is convective heat-transfer coefficient (W/m^2.^{o}C), n is the unit vector normal to the surface of head and SAR is the input EM heating source into the BHE. For simplification in solving the BHE, the parameters C_p, K and b are assumed to be constant within each tissue as the temperature rise induced by the mobile phone is small.

In order to obtain numerical stability of the BHE, time step δ_t is derived from the following Von Neumann's condition [3]:

$$\delta_t \leq \frac{2\rho C_p \delta^2}{12K + b\delta^2} \tag{5.3}$$

Values of C_p, K and b of human head tissues used in this study obtained from literature are shown in Table 5.1 [4],[5]. Two values of h have been used. One is h_a = 10.5 W/m^2.^{o}C, which is used for the convective heat-transfer coefficient from the head surface to the ambient temperature [6]. The other is h_b = 50 W/m^2.^{o}C, which is used for the convective heat-transfer coefficient from the internal surface to the cavity [5]. The ambient temperature and the blood temperature have been set to be 25^{o}C and 37^{o}C respectively.

Temperature rise due to RF exposure from the mobile phone has been obtained from the difference between the temperature $T(i,j,k,t)$ and $T(i,j,k,0)$ where $T(i,j,k,0)$ is the normal temperature at the $(i,j,k)^{th}$ point inside the unexposed head (SAR = 0) at thermal equilibrium. Maximum local temperature rise is obtained by finding the maximum value of temperature rise for the whole head model at each time step.

5.2.2 Hotspots and temperature rise analysis

Distributions at the mid-saggital and mid-coronal planes of the human head model for frequency 930 MHz are shown in the Figure 5.1 (a-b). From the figures, it is found that the peak temperature rise occurs within the internal tissue rather than the skin tissue. It is observed that, in mid-saggital plane, temperature rise in the region near right ear closer to the mobile phone is relatively higher than the other regions. In mid-coronal plane, temperature rise in the region of the upper portion of brain closer to the mobile phone is higher than other regions. The whitish region in between mouth cavity and sinuses as shown in the Figure 5.1 (b) is filled with air and variation of temperature in this region is not considered.

It is observed that the rise of temperature is not uniform in nature within the head cavity and concentrated significantly at some spots with different threshold temperatures. These hotspots are created due to standing wave antinodes inside head cavity. Hotspots with different threshold values of temperature rise are shown in Figure 5.2 (a-b). In mid-saggital as well as in mid-coronal plane, threshold values of temperature rise for the hotspots of red, green, blue and magenta are corresponding to 0.02^{o}C, 0.04^{o}C, 0.05^{o}C and 0.07^{o}C, respectively. It is also observed that the hotspots with higher threshold value of temperature

rise are fewer in number than those with lower threshold values and are concentrated near right ear closer to the mobile phone. On the other hand from the hotspots with lower threshold value of temperature rise are many and also present in different regions away from the mobile phone. Density of hotspots increases with decrease of threshold values of temperature rise and vice-versa.

Table 5.1: Thermal Properties of Human Head Tissues

Tissue	C_p [J/kg.^{o}C]	K [W/m.^{o}C]	B [W/m^3.^{o}C]	A_0 [J/s.m^3]
Brain	3500	0.60	37822	10000
Cerebellum	4200	0.58	35000	10000
Skin	3500	0.50	8652	1000
Bone	1300	0.30	1401	0
Muscle	3500	0.60	3488	690
Fat	2300	0.50	816	180
Lense	3000	0.40	0	0
Eyeball	3900	0.50	0	0
Tongue	3300	0.42	13000	3700
Blood	3900	0.49	0	0
Cartilage	3400	0.45	9100	1000
Cerebral falx	3800	0.52	35000	7000
Parotid gland	3700	0.57	7000	7000
Retina	3200	0.45	0	0
Teeth	1340	0.624	0	0
Trachea	2000	0.624	1040	0
Spinal chord	4200	0.60	0	0
Nerve	3700	0.565	32760	7000
Eye sclera	3700	0.57	0	0
Bone marrow	3900	0.624	0	0
Pituitary gland	1700	0.42	17280	7000
Mouth cavity/sinuses.	1000	0.02	0	0

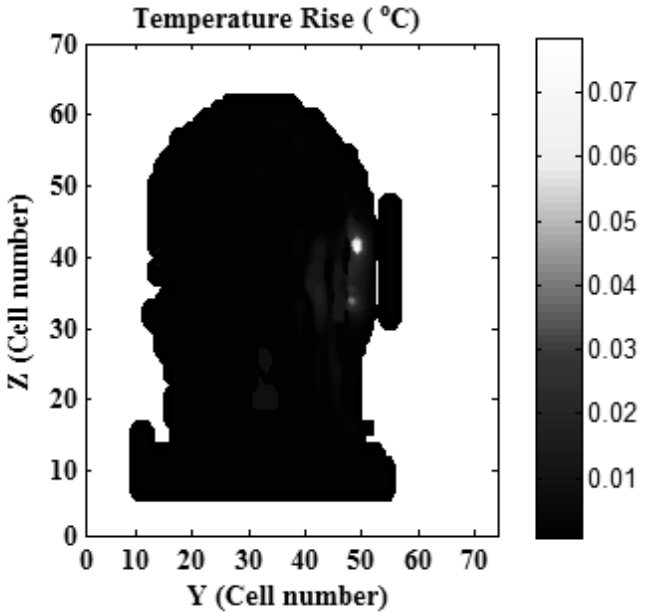

(a)

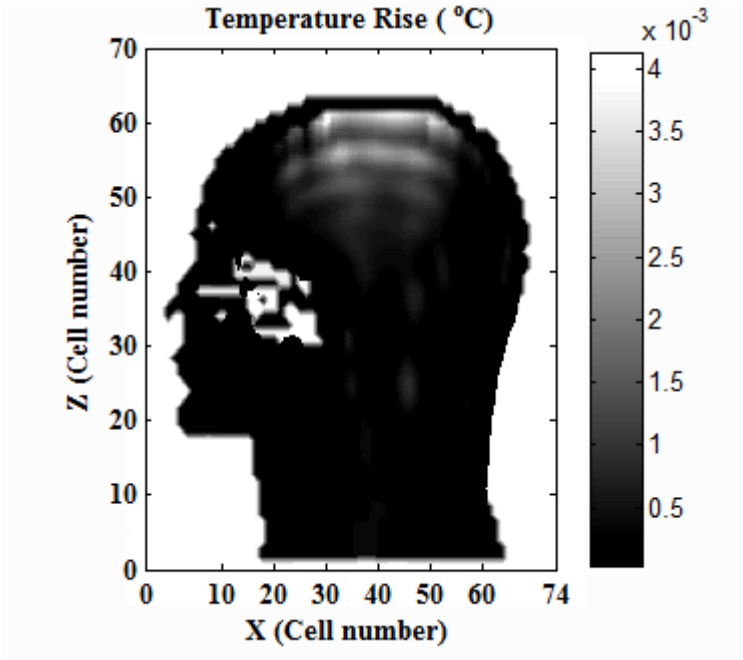

(b)

Figure 5.1. Temperature rise distributions in (a) mid saggital and (b) mid coronal planes of the human head model for mobile phone at 930 MHz.

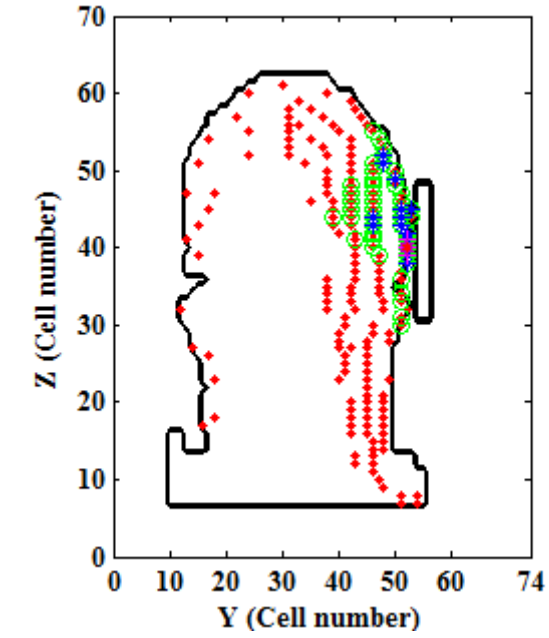

(a)

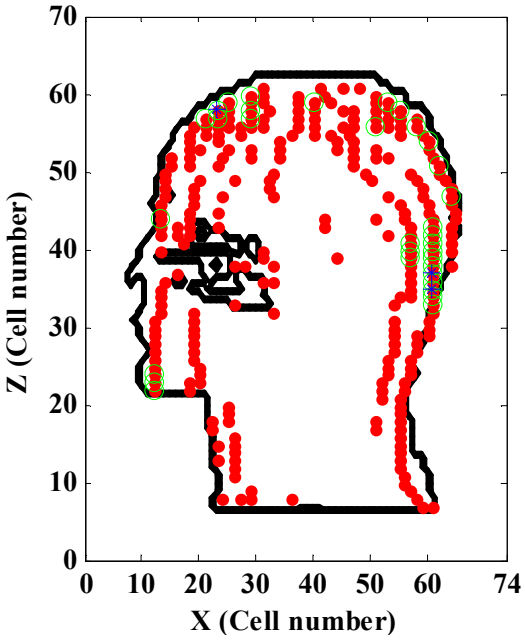

(b)

Figure 5.2. Hotspots distributions in (a) mid-saggital and (b) mid-coronal plane (red, green, blue and magenta hotspots with threshold values of 0.02°C, 0.04°C, 0.05°C and 0.07°C) of the human head model at 930 MHz.

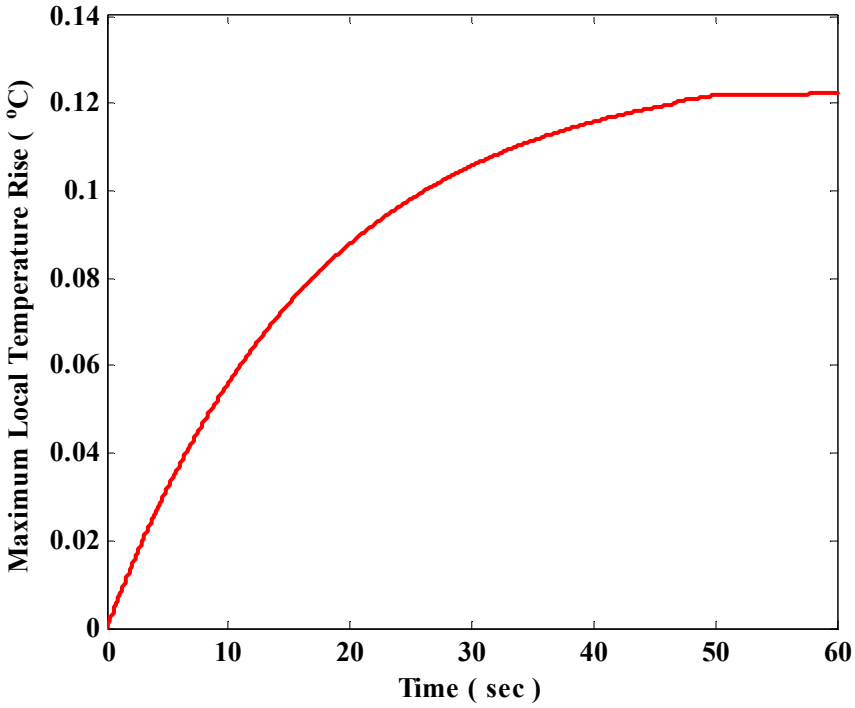

Figure 5.3. Short-term temperature rise in the human head model for mobile phone at 930 MHz.

Short-term maximum local temperature rise at frequency 930 MHz is shown in Figure 5.3. From the figure, it is seen that initially maximum local temperature rise inside the human head increases non-linearly with time and then attains to steady state value. The temperatures increase rapidly over the first 15-20 sec, then slows down and the steady state is achieved after approximately 55 sec exposure. At the thermal steady state condition, peak value of maximum local temperature rise is 0.122^{o}C.

5.3 Analysis of Quasi Optical effects inside a pregnant woman Abdomen

EM waves at microwave frequencies can be refracted, transmitted and reflected when it pass through a dielectric material object [7],[8]. Diffraction may occur from edges and corners of dielectric objects where the size of the object is similar to the wavelength. Thus, EM waves at microwave frequencies show many similarities like visible light [9]. Microwave lens is a dielectric structure which is transparent for microwave and capable of focusing or defocusing the EM energy of the microwave just like an optical lens focuses or defocuses visible light, discussed in Appendix 5A. Homogeneous dielectric materials of refractive index

different from the free space have been used for a long time in microwave lens applications [10].

5.3.1 Simulation of a pregnant woman abdomen model

The pregnant woman model has been constructed considering a 25 year old female with 65 kg weight and 5′4″ height [11]. To simplify the numerical model, other parts of the pregnant woman body except the full abdomen are excluded in the simulation. For further simplification, the pregnant body model is assumed to be comprised of only water. The abdomen of the pregnant woman model is comparable with a plano-convex lens with radius R = 17.6 cm and focal length f = 2.3 cm.

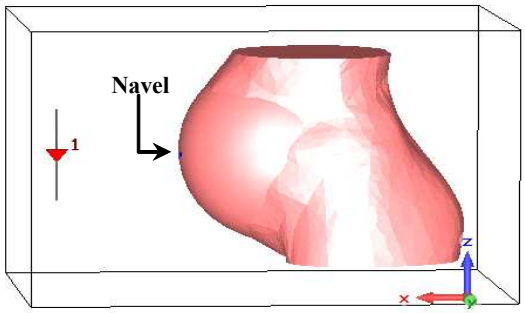

Figure 5.4. Geometry of a pregnant woman abdomen model along with a dipole antenna.

Geometry of the pregnant woman abdomen along with a half-wave dipole antenna resonating at 925 MHz used in the simulation by CST Microwave Studio® is shown in Figure 5.4. Input power of 20.0 W is considered for the simulation. The simulation performed consisting of 7,12,356 mesh cells.

5.3.2 Image analysis

Variation of peak $|H|$ with depth i.e., distance measured from the navel inside the pregnant woman abdomen model for a set of object distance (d) 10.0 cm, 20.0 cm, 30.0 cm, 40.0 cm and 50.0 cm at 925 MHz is shown in Figure 5.5. It is found that a peak corresponding to the maximum value of $|H|$ is obtained at the plane where the fields are focused. For d more than or equal to 20.0 cm, H field is focused almost at the focal plane

inside the pregnant woman abdomen and an image of *H* field corresponds to the *H* field at the centre of dipole is formed.

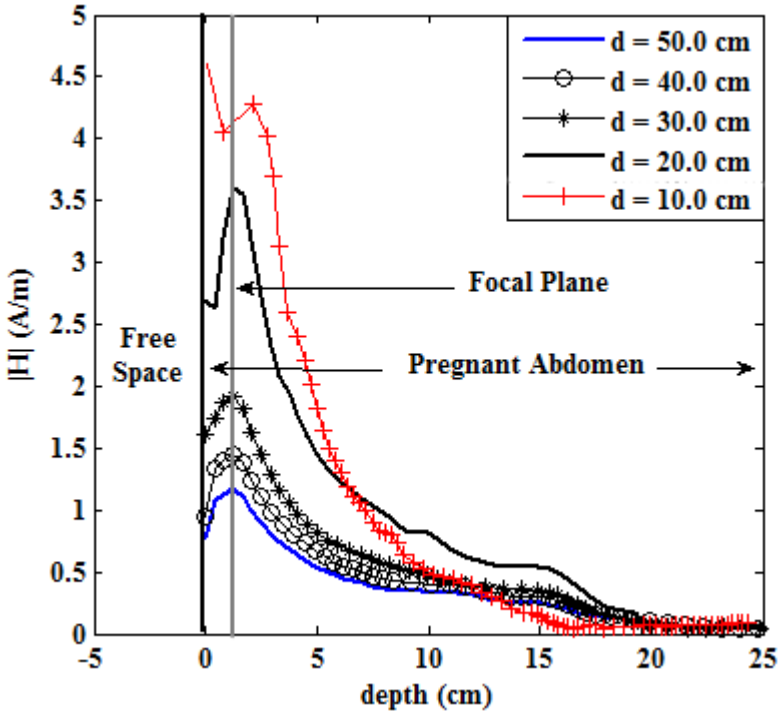

Figure 5.5. |*H*| vs. depth for different object distances at 925 MHz.

For *d* = 10.0 cm, image is obtained at the plane inside the pregnant woman abdomen model which is at the distance slightly more than the focal length. Unlike other curves this curve shows large magnetic field at skin which is possibility due to increase of diffraction due to increase of angle of incident at various part of the convex area of abdomen. Peak |*H*| decreases with the increase of *d* and vice-versa. Variation of *d* (cm) with image distance (cm) obtained from the simulation at 925 MHz for the pregnant woman abdomen model is shown in the Table 5.2. All the distances are measured from the navel of the pregnant woman abdomen. It is found from the Table 5.2 that for different object distance peak value of |*H*| with abdomen is higher than that for without abdomen due to the focusing of fields from dielectric lens. Therefore, it is seen that the pregnant woman abdomen model behaves like a plano-convex lens and follows classic principle of convex lens. For *d* more than or equal to 20.0 cm, quasi optical behaviour of microwave is prominent.

Table 5.2: Variation of object distance with image distance including peak |*H*| for with and without woman model at 925 MHz

Object distance (cm)	Image distance (cm)	Peak |*H*| With woman model (A/m)	Peak |*H*| Without woman model (A/m)
10.0	2.6	4.21	2.47
20.0	2.3	3.55	1.28
30.0	2.3	1.92	0.91
40.0	2.3	1.46	0.67
50.0	2.3	1.25	0.56

Variation of |*H*| with depth for *d* = 20.0 cm using different half-wave dipole antennas resonating at 925 MHz, 1795 MHz and 2.1 GHz respectively, is shown in Figure 5.6. From the Figure 5.6, it is found that peak |*H*| is obtained at the focal plane inside the pregnant woman abdomen model and value of peak |*H*| increases with the increase of frequency.

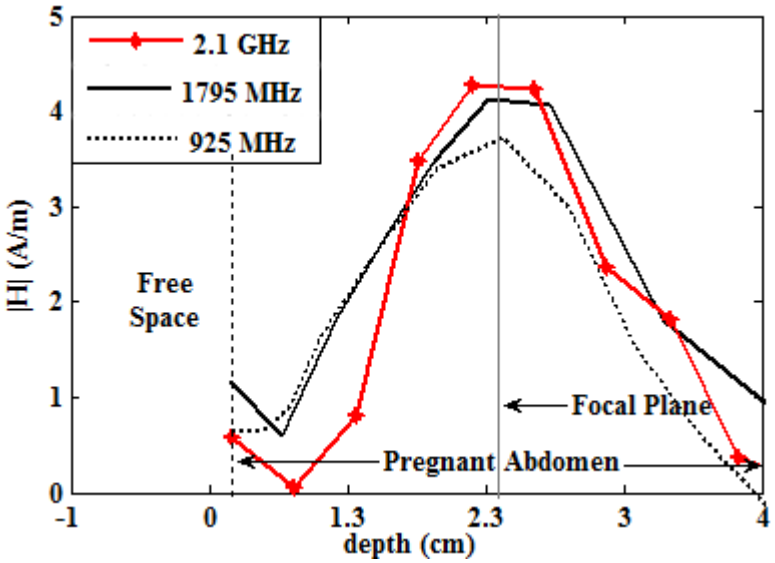

Figure 5.6. |*H*| vs. depth for *d* = 20.0 cm at 925 MHz, 1795 MHz and 2.1 GHz.

Field distribution using contour plots corresponding to *H* field obtained at the focal plane inside the pregnant woman abdomen for antenna/object distance of 20.0 cm at 925 MHz are shown the Figures 5.7 (a-b). From Figure 5.7 (a), it can be observed that like the dielectric plano-convex lens, a single high concentric spot is formed at the focal plane because of the maximum *H* field exists close to the centre of the resonating dipole antenna.

From contour line plots shown in Figure 5.7 (b), it is found that contour corresponding to the higher value of *H* filed concentrate towards the focus.

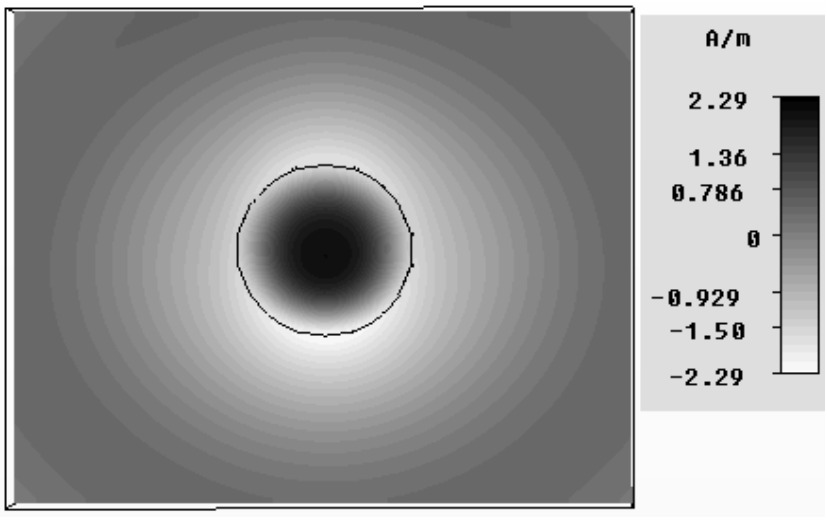

(a)

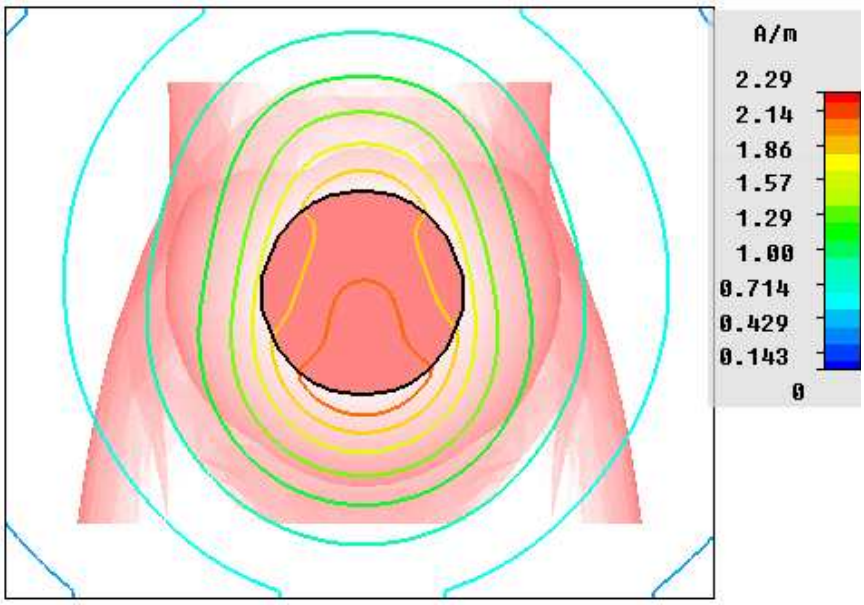

(b)

Figure 5.7. (a) Phase and (b) contour line plots of *H* field at the focal plane inside the pregnant woman abdomen model at 925 MHz.

5.4 Visual indication of EM field strength using RECTENNA based sensors

EM field is invisible but field strength can be measured using different suitable probes. So far microwave camera or scanner is not available for direct observation of the EM field inside EM tissues/cells near GSM bands. Here a RECTENNA based sensor is described for easy visual representation of field strengths.

5.4.1 RECTENNA based sensors for GSM band

RECTENNA is an acronym for Rectifying Antenna [12]. A general block diagram of a rectenna is shown in Figure 5.8. It can receive and rectify the microwave power from the EM waves into DC power.

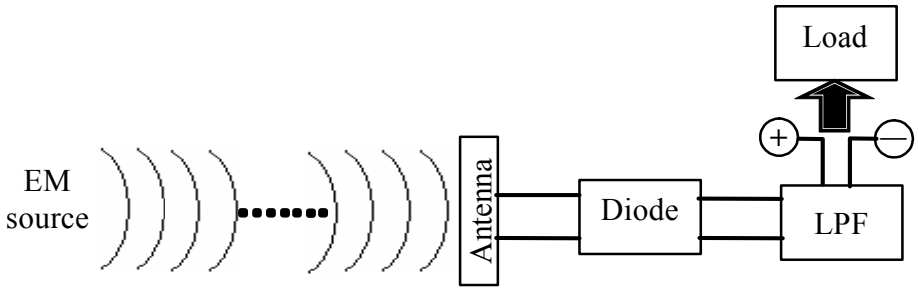

Figure 5.8. Block diagram of rectenna.

A rectenna is consisting of an antenna, a rectifier generally a Schottky diode and a Low Pass Filter (LPF). As an essential element, the antenna used in rectenna can be of any type such as dipole, Yagi-Uda antenna, microstrip antenna, monopole, loop antenna, coplanar patch, spiral antenna, or even parabolic antenna [13]. Rectenna can also take any type of rectifying circuit such as single shunt full-wave rectifier, full-wave bridge rectifier, or other hybrid rectifiers [14],[15]. The circuit, especially the diode is used to determine the RF-DC conversion efficiency. Silicon Schottky barrier diodes are very common but in these days more efficient diodes made of Silicon Carbide and Gallium Nitride (SiC and GaN) are available. The microwave energy radiated from the EM source is collected by the antenna attached with the rectifying diode. The rectifying diode converts the received microwave energy into DC power. To get better conversion of microwave energy sometime an additional filter and matching circuit is placed between the antenna and diode. The low-pass filter will match the load with the rectifier and block the high order harmonics generated by the diode in

order to achieve high energy conversion efficiency which is the most important parameter of such a device [16],[17]. In addition, the rectifier is optimized to match the antenna with a filter.

For this study several RECTENNA based sensors are designed where the output DC power of RECTENNA is connected to a low power LED for visual indication of received EM field for GSM 900 band. Some designed RECTENNA based sensors are shown in Figure 5.9 (a-c). These sensors consist of different types of antennas and Schottky diodes. Sometimes a 47 pF microwave capacitor has been connected in parallel to LED to reduce the flickering rate of LED during experiments.

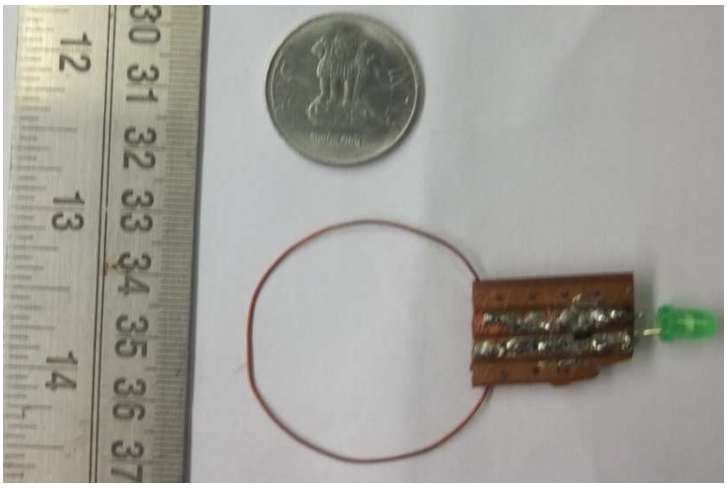

(a)

(b)

(c)

Figure 5.9. Rectenna based sensors (a) type-1, (b) type-2, (c) type-3.

5.4.2 Experiments with RECTENNA based sensors

A typical experimental setup has been adopted to study the characteristics of the RECTENNA based sensors where a GSM 900 band mobile phone as shown in Figure 5.10

(a) is used as RF source. The rectenna converts the radio wave energy from the mobile phone signal into electricity to light the respective LED. As the antenna of this mobile phone is being installed near the back side lower end, so all the rectennas are initially placed near radiating antenna as shown in Figures 5.10 (b-d). Experiment has been performed by varying the distance of the sensors when mobile phone is receiving phone calls.

(a) **(b)** **(c)** **(d)**

Figure 5.10. (a) GSM 900 mobile phone, experimental setup for (b) type-1 rectenna, (c) type-2 rectenna and (d) type-3 rectenna sensors.

Variations of brightness of the LEDs for type-1, type-2 and type-3 for different positions are shown in Figures 5.11 (a-c), respectively. For easy visualization a movie has been recorded and all frames are merged to obtain a single image.These images crudely show the variation of field strength near an operational mobile phone. As per the rating of LED, atleast 16 mA current is required to turn on the used LED.

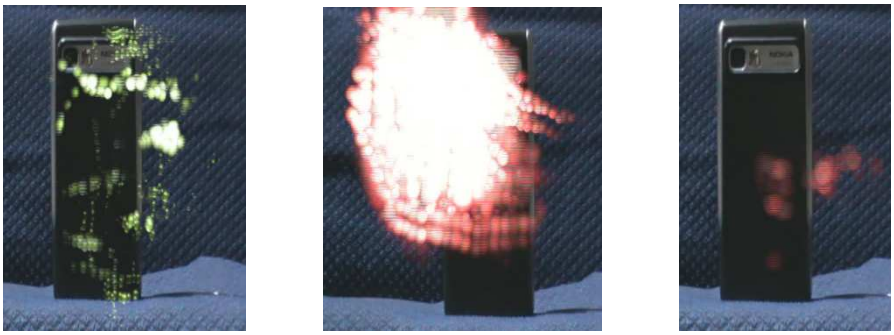

(a) **(b)** **(c)**

Figure 5.11. Variations of brightness of sensors for various positions due to (a) type-1 rectenna, (b) type-2 rectenna and (c) type-3 rectenna.

Investigations have been carried out to see the EM field strength inside a cup of water and an egg using rectenna based sensors. Most of the theoretical studies reported so far are

related to SAR and are actually based on Maxwell's equations. Sometimes temperature rise is studied considering the Pennes' BHE which is indirectly related to the EM absorption due to dielectric loss. Chemical reactions i.e. the electro-chemical changes inside the human body due to the EM fields have been totally ignored. Due to expose to the EM field, inside the complex human body, some electrically conducting internal organs like the blood vessels can behave like antenna made of ionic liquid. Ionic Liquid Antenna (ILA) is well known in the field of antenna Engineering [18]-[20]. And thus an ac current may flow in the different positions inside human body parts which may participate in electro-chemical changes directly without any thermal changes. Thus these types of changes cannot be predicted by the conventional SAR simulation methods. Again these induced current may interfere the bio-electric signal. Ionic conduction can not be predicted using wave propagation theories and may be converted into other form of energies which is not at all similar to the dielectric heating.

(a) **(b)**

Figure 5.12. Experimental setup for visualizing induced EM field inside water due to non-ionizing radiation from GSM 900 mobile phone (a) not in operating mode and (b) in operating mode.

To examine possibility of induction of EM wave inside human tissue some experiments have been carried out using rectenna based sensors. In one case induced field inside a cup of water and in another case an egg is considered for experiment as shown in Figures 5.12-13. It is true that a copper wire loop antenna can not actually represent an ionic fluid antenna but possibility of conduction through ionic fluids inside blood vessels can not be ignored. A rectenna based sensor is placed inside a cup of water as shown in Figure 5.12 (a-b). Figure 5.12 (a) shows that the LED remains off when the phone is not in operating mode. On the other hand the LED of the rectenna based sensor glows brightly when the phone is in operating mode as shown in Figure 5.12 (b). Now, the rectenna based sensor is placed inside

an egg as shown in Figure 5.13 (a). Figures 5.13 (b-c) show that the LED of the rectenna based sensor inside egg glows brightly when the phone is in operating mode. In these experiments the induced ac current has been converted to dc first to light the LED but in reality when living cells or tissues are exposed to the radiated EM field at RF, some part of it can initiate chemical changes inside body due to the flow of induced ac current.

(a) **(b)** **(c)**

Figure 5.13. (a) Experimental setup for visualizing induced EM field inside an egg due to non-ionizing radiation from GSM 900 mobile phone, (b) and (c) for operating mobile phone with different position of the egg.

5.5 Conclusions

In this chapter, temperature rise in an anatomically based human head model has been calculated using BHE due to a mobile phone using FDTD method. Temperature distributions at the mid-saggital and mid-coronal planes of the human head model for frequency 930 MHz shows that the peak temperature rise occurs within the internal tissue rather than the skin tissue. It has also been observed that, in mid-saggital plane, temperature rise in the region near right ear closer to the mobile phone is relatively higher than the other regions. It is found that temperature rise within the head cavity is not uniform in nature and concentrated significantly at some spots with different threshold temperatures-defined as hotspots. These hotspots are created due to standing wave antinodes inside head cavity. Hotspots with different threshold values of temperature rise have been shown in both mid-saggital and mid-coronal planes by different colours. It has also been observed that the hotspots with higher threshold value of temperature rise are fewer in number than those with lower threshold values and are concentrated near right ear closer to the mobile phone. But the hotspots with

lower threshold value of temperature rise are many in number and also present in different regions away from the mobile phone. Density of hotspots increases with decrease of threshold values of temperature rise and vice-versa. Short-term maximum local temperature rise at frequency 930 MHz shows that initially maximum local temperature rise increases non-linearly with time and then attains to steady state value. The temperature increases rapidly at initial state then slows down and attained the steady state after some time.

Quasi optical effects of non-ionizing EM radiation inside a pregnant woman abdomen model has been analyzed using CST Microwave Studio®. The pregnant woman abdomen model has been constructed considering a 25 year old female with 65 kg weight and 5′4″ height. It has been found that the abdomen of the pregnant woman model behaves like a plano-convex lens.

At the end of this chapter, to examine the possibility of induced current through ionic liquid in blood vessels inside human body, some experiments have been carried out using rectenna based sensors. For this purpose different types of rectenna based sensors have been designed where the output DC power of rectenna is connected to a low power LED for visual indication of received EM field for GSM 900 band. Since, significant part of human body is consisting of water; induced current in a conductor loop antenna inside a cup of water is observed. In another case an egg which can in fact represent an animal cell is considered for similar experiment. When a rectenna based sensor is placed inside a cup of water, LED connected with it glows brightly when a phone in operating mode is kept in close proximity. In similar way wnen the rectenna based sensor is placed inside an egg the LED connected with the rectenna based sensor glows brightly when the phone is in operating mode. In these experiments the induced ac current has been converted to dc first for lighting up the LED but in reality when living cells or tissues are exposed to the radiated EM field at RF, some part of it can initiate chemical changes inside body due to the flow of induced ac current. It is true that a copper wire loop antenna can not actually represent an ionic fluid antenna but possibility of conduction through ionic fluids inside blood vessels can not be ignored..

References

[1] P. Bernardi, “Power absorption and temperature elevations induced in the human head during a dual-band monopole-helix antenna phone,” *IEEE Trans. Microwave Theory Tech.*, vol. 49, No. 12, pp. 2539-46, 2001.

[2] H.H.Pennes, "Analysis of tissue and arterial blood temperature in the resting human forearm," *Journal of Applied Physiology*, vol. 1, pp. 93-102, 1948.

[3] R.D.Richtmyer and K.W.Morton, "Different Methods for Initial Value Problems," 2nd edition, New York: Wiley, 1967.

[4] A.Hirata and T.Shiozawa, "Correlation of maximum temperature increase and peak SAR in the human head due to handset antennas," *IEEE Trans. Microwave Theory Tech.*, vol. 51, pp. 1834-1841, July 2003.

[5] J.Wang and O.Fujiwara, "FDTD computation of temperature rise in the human head for portable telephones," *IEEE Trans. Microwave Theory Tech.*, vol. 47, pp. 1528-1534, August 1999.

[6] A.Taflove and M.E.Brodwin, "Computation of the electromagnetic fields and induced temperatures within a model of the microwave irradiated human eye," *IEEE Trans. Microwave Theory Tech.*, vol. 23, pp. 888-896, November 1975.

[7] D.W.Preston and E.R.Dietz, The Art of Experimental Physics, Wiley, New York, 1991.

[8] W.H.Murray, "Microwave Diffraction Techniques from Macroscopic Crystal Models," *American Journal of Physics*, vol. 42, 137, July-1974.

[9] R.Y.Kezerashvili, "Light and electromagnetic waves teaching in engineering education," *International Journal of Electrical Engineering Education*, vol. 46, no. 4, pp. 343-353, November 2007.

[10] S.Cornbleet, Microwave Optics. New York: Academic Press, 1976.

[11] Make Human™, Available: http://www.makehuman.org.

[12] S.Pradhan, G.S.Kim, P.Prasain, S.W.Kim, S.K.Noh and D.Y.Choi, "Electromagnetic Energy Harvesting for Rectenna," Advanced Science and Technology Letters, vol. 30, pp. 36-44, 2013.

[13] Y.Fujino and K.Ogimura, "A Rectangular Parabola Rectenna with Elliptical Beam for SPS Test Satellite Experiment. Proc. of the Institute of Electronics," Information and Communication Engineers, SBC-1-10, pp. S29-S20, 2004.

[14] P.Leroy, G.Akoun, B.Essakhi, L.Santandrea, L.Pichon and C.Guyot, "An efficient global analysis of a rectenna using the combination of a full-wave model and a rational approximation," Euro Physics Journal of Applied Physics, no. 29, pp.39-43, 2005.

[15] J.Zhang and Yi Huang, "Rectennas for wireless energy harvesting," 6th European Conference on Antennas and Propagation (EUCAP), 26-30 March 2012.

[16] J.O. McSpadden, Lu Fan and Kai Chang, "Design and experiments of a high-conversion efficiency 5.8-GHz rectenna," IEEE Transactions on Microwave Theory and Techniques, vol. 46, no. 12, pp. 2053-2060, 1998.

[17] Jonathan Hare, "Simple demonstration to explore the radio waves generated by a mobile phone," IOP, Physics Education, vol. 45, no. 5, pp. 481-486, 2010.

[18] Ewananovil Paraschakis, Hazem Fayad Paul Record; Ionic Liquid Antenna; Small Antennas and Novel Metal Materials, pp. 252-254, *IEEE*, 0-7803-8842-09/05/S, 2005.

[19] H. Fayad and P. Record, Broadband Liquid Antenna, *IEEE Electronics Letters*, vol. 42, Issue 3, pp. 133-134, 2006.

[20] J. H. Meloling, J.H. Schukantz and J. Fischer, "A Transmit Mast-Clamp Current Probe for Shipboard HF Communications," *IEEE* 0/7803-8883-6/05, pp. 17-20, 2005.

Chapter 6

Study on Effects of Non-Ionizing EM radiation on Environment

6.1 Introduction

EM waves radiating from mobile phone and mobile phone tower affect the birds, animals, plant and environment [1]-[5]. Ratio of the surface area to weight for a bird is relatively larger than in comparison to human body, therefore the birds absorb more radiation in terms of W/kg. Fluid content by a bird is small due to less weight, for which it gets heated up very fast and also the magnetic field disturbs their navigational skills. Generally, birds like to make their nests on the top of a tree, building or tower but they also exposed by the EM field radiated from huge number mobile phone towers [6]. An abrupt disappearance of bees has been reported due to rising EM pollution [7]. "*The huge amount of EM radiation produced by towers and mobile phones is actually frying the navigational skills of the honey bees and preventing them from returning back to their hives …* [8]" – needs to be verified.

A study from Germany reported that cows grazing near cell towers are more likely to experience still births, spontaneous abortions, birth deformities, behavioural problems and general declines in overall health. Moving cattle herds away from such towers has reportedly led to immediate health improvements [9]. Dairy cows exposed to the magnetic fields results reduction in milk yield, changed milk composition and fertility problems [10]. Similarly, impaired immune system in sheep, reproductive and developmental problems in dogs and cats, anxiety and alarm in rabbits, frequent death of domestic animals such as, hamsters, and guinea pigs living near base stations of mobile phone towers has been observed [11].

Apart from bees, birds and animals, EM radiation emanating from cell towers can also affect vegetables, crops and plants in its vicinity [12]-[14]. Studies show definitive clues that cell phone/tower radiation can choke seeds, inhibit germination and root growth, thereby affecting the overall growth of agricultural crops and plants. Trees located inside the main

lobe (beam), have much lower fruit yield, have dried tops, show slow growth and high susceptibility to illnesses and plagues [15],[16]. Also, EM radiation generates heat, which may kill micro-organisms present in the soil near it. This in turn harms those organisms which feed on them and disturbs the ecological cycle.

This chapter describes EM wave absorption and shielding characteristics of a Bonsai tree and Money plant. EM energy absorption characteristic and image formation by the pollen grains at GHz frequencies are also presented at the end of this chapter.

6.2 Assessment of the EM field interaction with green Tree

Trees and vegetables are continuously exposed to the RF radiation emanating from wireless communication towers 24 × 365 hours a year. Those trees and vegetables are also absorbing RF/microwave energy because of their high water content and chemical ionic constituents. Continuous RF/microwave energy absorption by the trees/crops can also have some effects on their growth and other physical activities as discussed above. But there is no RF exposure guideline available to protect them from the RF hazards [17]-[19]. People do not take any care for providing radiation shield to the trees but the trees provide good radiation shield to reduce the effects of EM radiation on human beings and environment. Thus, it is seen that to protect our environment trees not only absorb carbon-di-oxide and produce oxygen during photo synthesis, but along with this they also provide us radiation shield as another helpful role. In this study, an attempt has been made to estimate EM wave absorption capability of a tree in terms of maximum local *E* field, *H* field, 1-g SAR and Shielding Effectiveness (SE). Figure 6.1 shows a layout by means of block diagram representation of the numerical computation procedure for calculations of EM fields, SAR and SE due to the EM interaction of realistic usage of a BSA and plane wave with tree using different numerical methods. Assessment accuracy of the EM interaction depends on the following:

a. EM source modelling. This includes BSA (e.g., centre shorted suspended microstrip antenna working at GSM 900 band, rectangular patch antenna resonating at 2.42 GHz) and plane wave source.
b. Tree modelling (i.e., Bonsai tree [20] and Money plant).
c. Electrical properties of tree tissues.
d. Numerical method (e.g., FDTD, SFDTD and hybrid FDTD methods). Applying the FDTD method, the grid-cell resolution and PML acting as ABC should be specified in

accordance with the available hardware for computation. Higher resolution and higher ABC needs a faster CPU and larger memory.

e. EM simulator e.g., FIT based CST Microwave Studio® has been applied for validation and additional calculation of dosimetric parameters.

f. SE for a Money plant is measured by means of a handheld RF power meter.

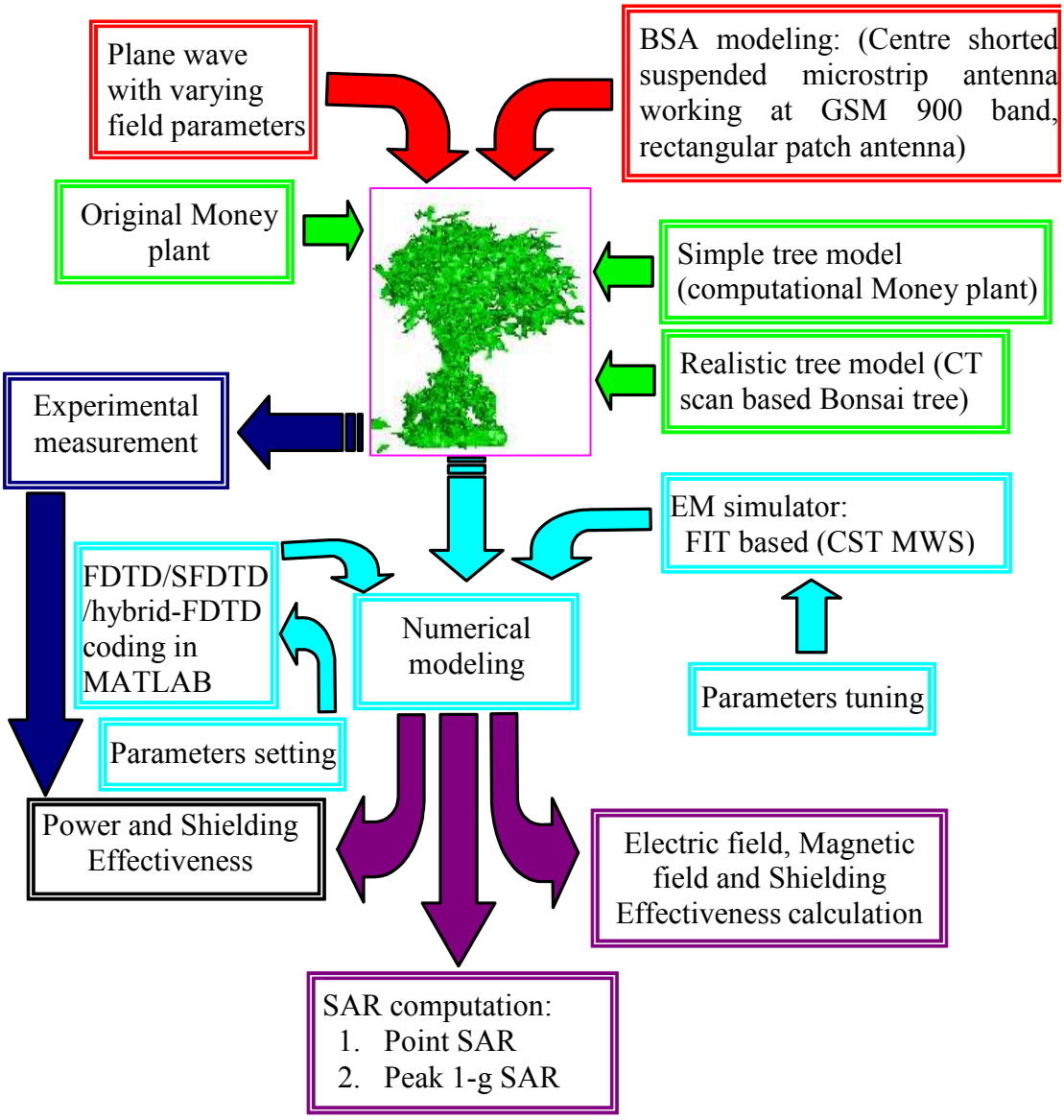

Figure 6.1. A Block diagram illustrating the numerical computation of the EM interaction of RF source and tree.

6.2.1 Evaluation of EM wave absorption characteristics for a Bonsai tree

Using hybrid FDTD method EM wave absorption characteristics for a Bonsai tree is investigated at GSM 900 band. The tree model used in this study is obtained from 3-D CT

scan Bonsai dataset considering the electrical parameters of different internal structures of the living tree. The available tree model consists of 256 × 256 × 128 voxels having 0.585938 mm × 0.585938 mm × 1.0 mm voxel dimension [20]. To simplify the numerical calculations, resolution has been reduced to 74 × 70 × 76 voxels with 2.34 mm × 1.71 mm × 4.00 mm dimensions. The tree model is assumed to be comprised of only two types of tissues; i.e., xylem and phloem. Values of relative dielectric constant (ε_r) and conductivity (σ) of tree tissues and soil at GSM 900 band are shown in Table 6.1 [21]-[23]. Geometry of the Bonsai tree along with BSA is shown in Figure 6.2. Maximum local *E* field, *H* field, 1-g SAR and SE have been calculated for the tree placing at distance R = 5.0 m away from a radiating BSA with 20 W input power. Modelling of the BSA is described in detail in Section 3.7.4 and the geometry is shown in Figure 3.21 (b).

Table 6.1: Dielectric Properties of Tree Tissue.

Tissue type	Dielectric Constant (ε_r)	Conductivityσ (S/m)
Xylem	80	0.01
Phloem	30	0.07
Soil	15	0.01

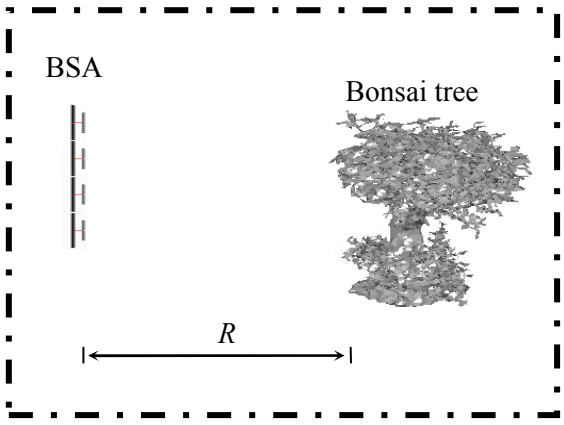

Figure 6.2. Geometry of Bonsai tree with BSA [*R* = 5 m].

SE is defined as the ratio in dB of the field without and with the shield [24]:

$$SE = 20\log_{10}\left|\frac{E_0}{E_t}\right| \tag{6.1}$$

where, E_0 = electric field without shield, E_t = electric field with shield.

In terms of power, SE is defined as the difference of power in dB of without and with the shield:

$$SE = P_0 - P_t \tag{6.2}$$

where, P_0 = power without shield and P_t = power with shield.

6.2.1.1 Development of simulation model

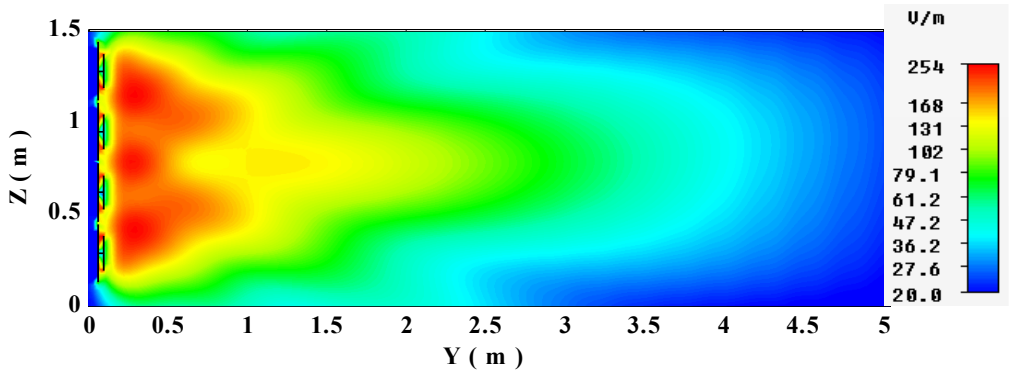

(a)

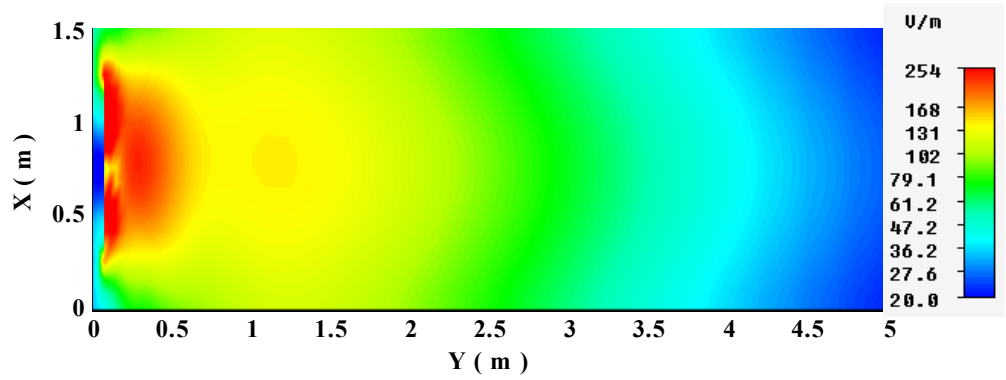

(b)

Figure 6.3. *E* field distributions at 925 MHz in (a) YZ-plane and (b) XY-plane.

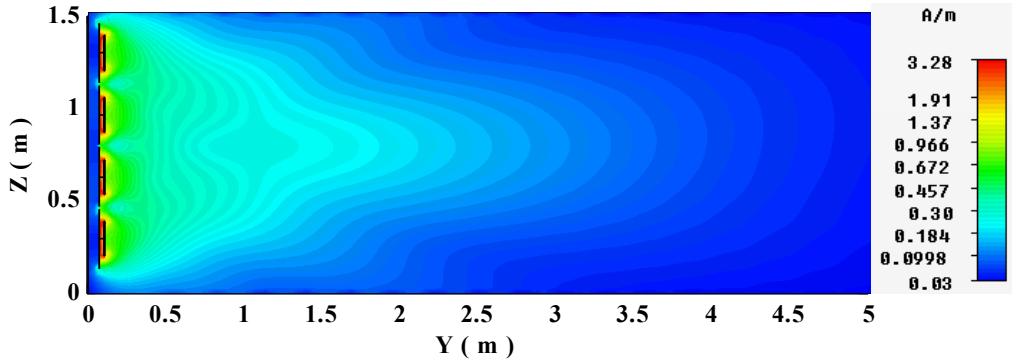

(a)

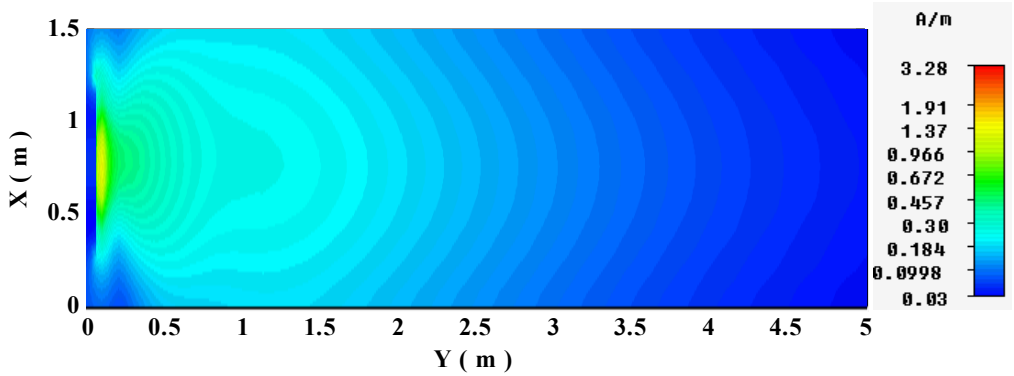

(b)

Figure 6.4. *H* field distributions at 925 MHz in (a) YZ-plane and (b) XY-plane.

The distributions of *E* field, *H* field intensity and power density for distance up to 5 m from BSA have been computed using CST Microwave Studio® using lower mesh limit of 6 cells per wavelength which is in fact very coarse meshing. The distributions of *E* field, *H* field intensity and power density at 925 MHz for the BSA in the mid YZ-plane and XY-plane are shown in Figures 6.3-6.5. Maximum *E* field intensity of 31.9 V/m, maximum *H* field intensity of 0.09 A/m and maximum power density of 1.57 VA/m^2 are observed at 5 m away from the BSA. The power density at 5 m away from the BSA can also be calculated using Friis transmission relation and it becomes approximately equal to Effective Isotropic Radiated Power (EIRP)/(4 × π × 5^2) = 1.59 W/m^2 which closely agrees with the value obtained using CST Microwave Studio®.

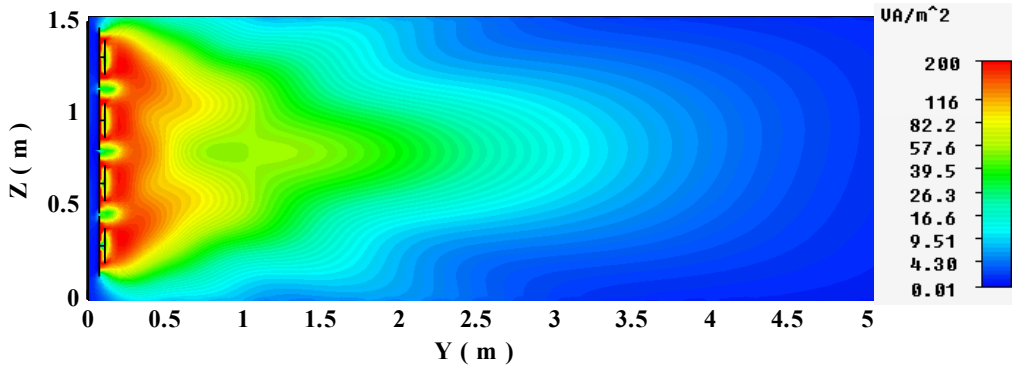

(a)

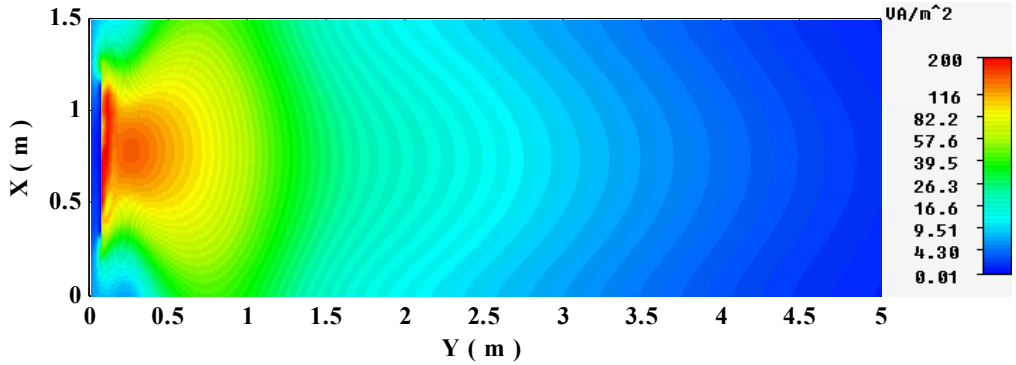

(b)

Figure 6.5. Power density distributions at 925 MHz (a) YZ-plane and (b) XY-plane.

As it is well known that after a distance in the order of tens of wavelengths, the field from most antennas behaves like a plane wave [25]. For that reason in hybrid FDTD method, the simulation model shown in Figure 6.2 is divided into two sub domains namely domain 1 and 2 as shown in Figure 6.6 for the convenience of simulation. Domain 1 is used to compute the characteristics of resultant fictitious plane wave source of two Yee cells width. This plane wave source is actually a replacement of the radiating BSA placed at 5 m away from the tree and its properties are calculated from equation (3.26) considering transmitted power P_t = 20 W. And in domain 2, the fictitious plane wave is placed at a distance of r = 2.34 mm away from the tree and the required E field and H field intensity at a distance R from the antenna can be calculated from equations (3.28) and (3.29) respectively.

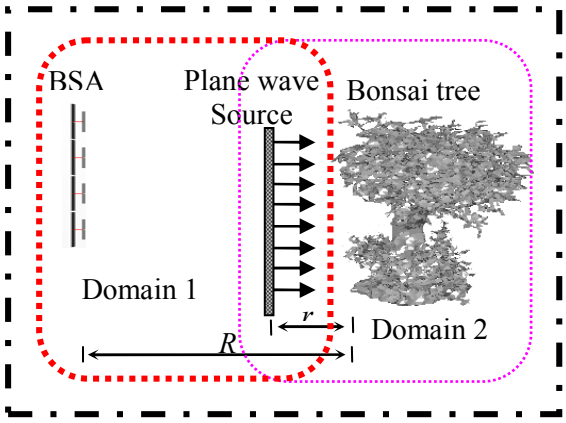

Figure 6.6. Geometry of Bonsai tree with BSA [*R* = 5 m and *r* = 2.34 mm].

This simulation domain is slightly more modified as shown in Figure 6.7 to incorporate a far field power sensor dipole antenna of 14.8 cm length. At 925 MHz, far field distance for this dipole is 13.51 cm and it is placed 14.04 cm away from the tree model to calculate SE.

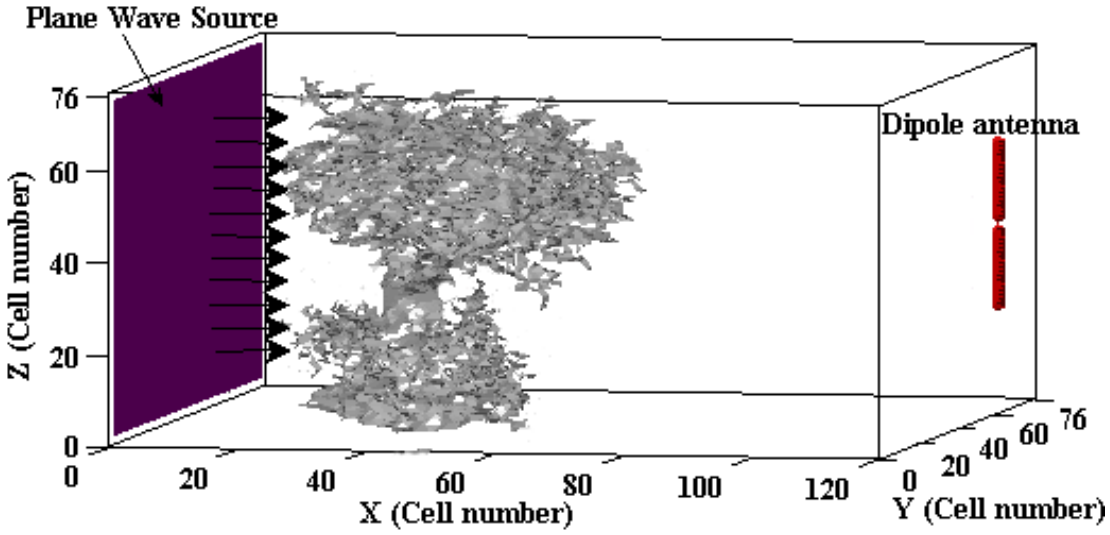

Figure 6.7. Three dimensional geometry of Bonsai tree model with plane wave source and dipole antenna.

6.2.1.2 Analysis of EM wave absorption characteristics

E field and *H* field distributions in dB scale at 925 MHz in the plane of wave propagation (YZ-plane) are shown in the Figure 6.8 (a-b). From Figure 6.8 (a), it is seen that higher value of *E* field is induced in the outer region of tree. On the other hand from Figure 6.8 (b), it is seen that higher value of *H* field is induced in the inner region of tree. Value of *H* field decreases as the distance of the region from plane wave source increases.

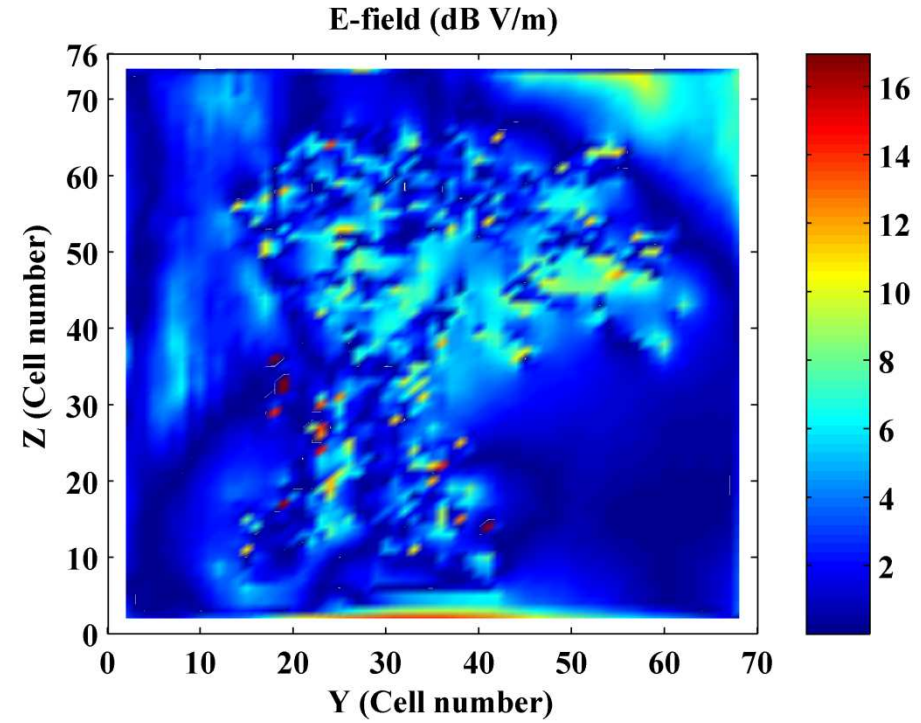

(a)

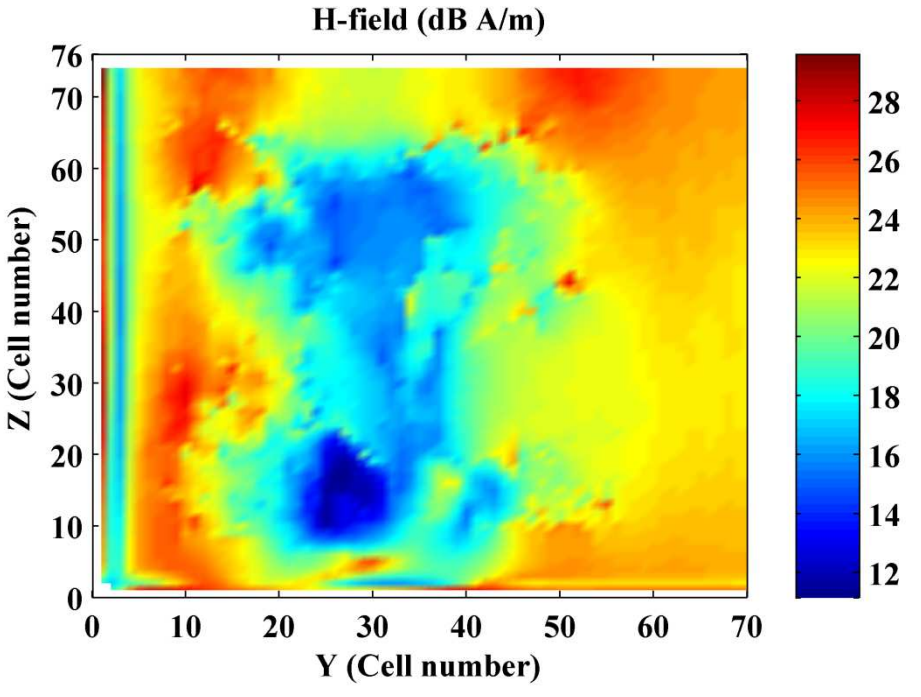

(b)

Figure 6.8. (a) *E* field and (b) *H* field distributions at 925 MHz.

Variations of maximum local *E* field, *H* field and 1-g SAR with height of tree (*h*) for *R* = 5 m at 925 MHz are shown in the Figures 6.9-6.11. From the Figure 6.9, it is seen that

initially with the increase of *h*, maximum local *E* field decreases abruptly then attains a flattened peak and after that, with further increase of *h*, maximum local *E* field increases rapidly. Peak value of maximum local *E* field is found to be 70.1 V/m. which is 2.2 times higher than the maximum *E* field obtained for free space at a distance 5 m away from the antenna as observed from Figure 6.3. This increase in field intensity is possibly due the nodes of fields generated from standing waves inside the dielectric cavity.

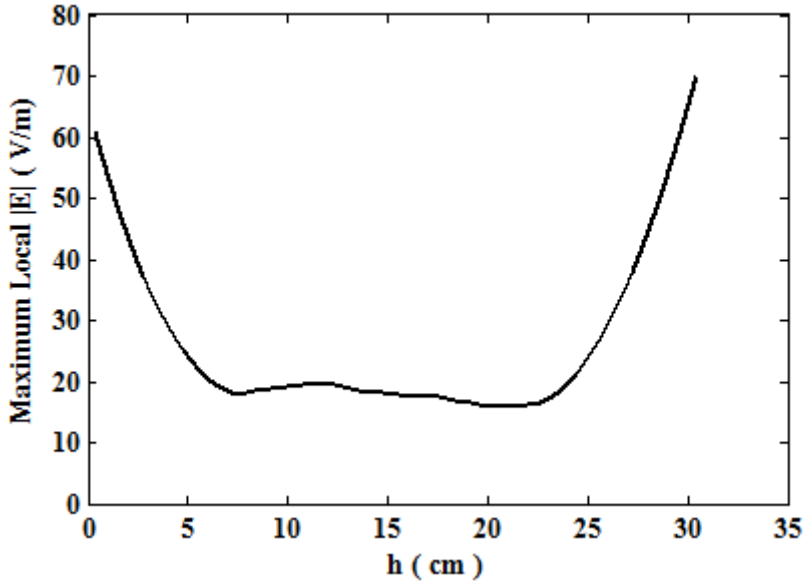

Figure 6.9. Maximum local *E* field vs. *h* at 925 MHz.

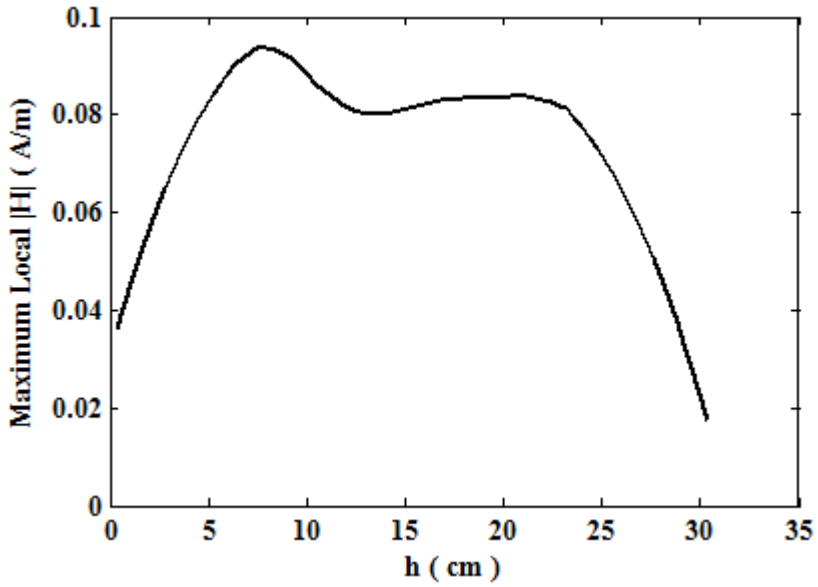

Figure 6.10. Maximum local *H* field vs. *h* at 925 MHz.

From Figure 6.10, it can be observed that, initially with the increase of *h*, maximum local *H* field increases rapidly then attains one consecutive sharp and flattened peaks and with further increase of *h*, maximum local *H* field decreases quickly. Peak value of maximum local *H* field of 0.09 A/m is observed which fairly matches with the maximum *H* field obtained for free space at a distance 5 m away from the antenna as observed from Figure 6.4.

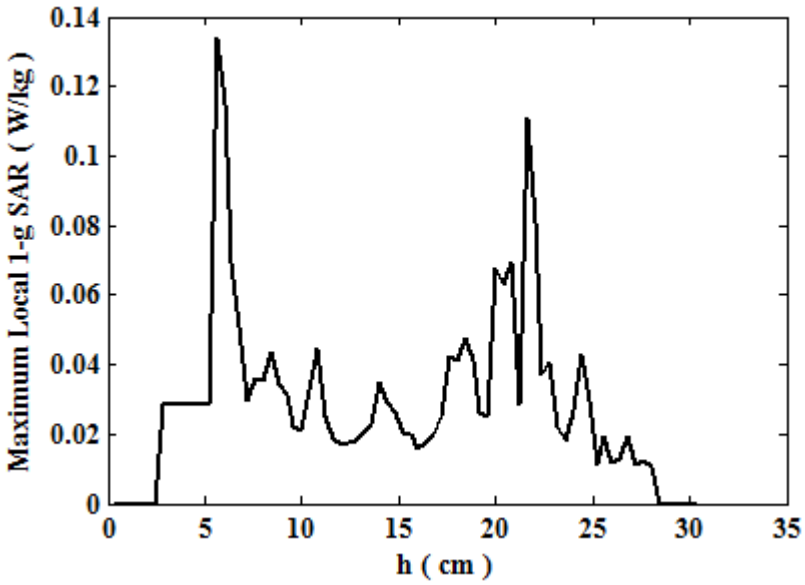

Figure 6.11. Maximum local 1-g SAR vs. *h* at 925 MHz.

Maximum local 1-g SAR vs. *h* plot is shown in the Figure 6.11. Peak value of maximum local 1-g SAR is 0.135 W/kg. Fluctuation in SAR value ensures hot spots with high energy absorption [26],[27].

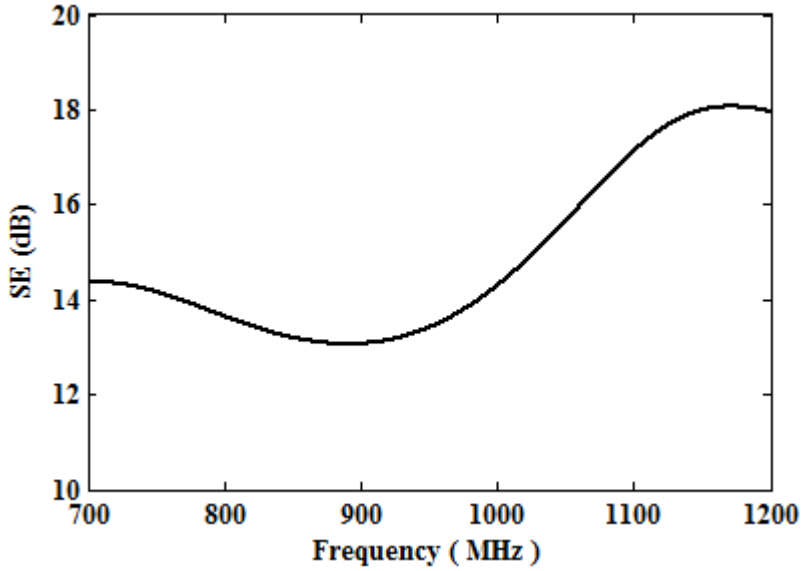

Figure 6.12. SE vs. Frequency for Bonsai tree.

Variation of SE with Frequency due to the Bonsai tree is shown in the Figure 6.12. From the figure, it is seen that at 925 MHz value of SE is 13.18 dB.

6.2.2 Evaluation of EM wave absorption characteristics for a Money plant

SAR induced inside a Money plant and SE provided by the Money plant in the frequency range of 2.35 GHz to 3.0 GHz has been calculated as well as measured experimentally by means of a handheld RF power meter. All the required simulations are developed by commercially available software CST Microwave Studio®. Money plant has been modelled considering the electrical parameters for internal and external structures of the actual Money plant. For simplification in simulation, Money plant is assumed to be comprised of only one type of tissues i.e., phloem as the major portion of Money plant are leaves which are made of phloem. At 2.4 GHz, value of relative dielectric constant (ε_r) of the phloem is obtained by measurement using Agilent 85070E dielectric probe in conjunction with E5071B NA [28],[28] as shown in Figure 6.13. Measured value of ε_r along with conductivity (σ) and mass density (ρ) of the phloem obtained from literature are shown in Table 6.2 [21],[22]. As the Money plant normally found lying within a small tub which is filled with wet soil. So in order to approach towards the realistic condition a solid tub made of soil is added at the bottom of the Money plant model. Values of relative ε_r and σ of soil used in the simulation are shown in Table 6.2 [23].

Figure 6.13. Dielectric measurement set-up.

Table 6.2: Dielectric Properties of Tree Tissue.

Tissue type	Dielectric Constant (ε_r)	Conductivity (σ) (S/m)	Mass density (ρ) (kg/m^3)
Phloem	41	0.07	950
Soil	15	0.01	—

6.2.2.1 Simulation set-up for SAR calculation

Transient analysis has been used in CST Microwave Studio® for SAR calculation inside the Money plant and the corresponding simulation set-up is sown in Figure 6.14. A plane wave with linear polarization has been used as the RF radiation source which passes through the Money plant model in separate simulation environment. A 5-layered conventional PML with 0.0001 reflection coefficient has been used as the absorbing boundary. The separation between the Money plant and the boundary wall has been kept fixed at 2.5 cm by varying the mesh-lines per wavelength for different frequency of exposure. Figure 6.14 shows the Money plant gets exposed to a plane wave propagating in Z direction whereas the *E* field and *H* field are in X and Y direction respectively. All the SAR results for Money plant model have been evaluated with the above mentioned direction of plane wave propagation for occupational as well as general public exposure levels prescribed by ICNIRP [18].

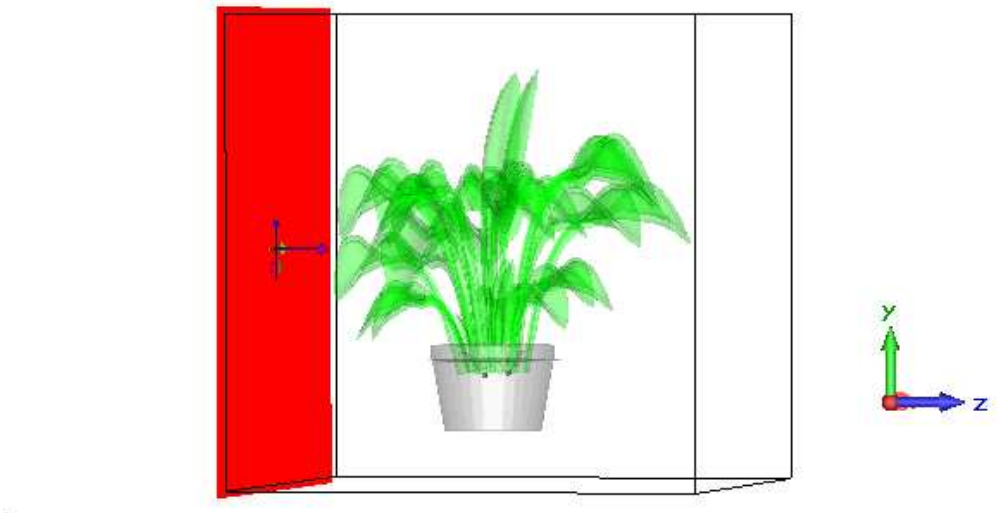

Figure 6.14. Simulation set-up for SAR calculation in Money plant gets exposed in a plane wave at 2.4 GHz with setting of ICNIRP prescribed peak *E*-fields.

6.2.2.2 Simulation and Experimental set-up for SE measurement

The plane wave source is replaced by a rectangular patch antenna made of copper resonating at 2.42 GHz and to measure SE, a far field power sensor dipole antenna of 5.5 cm length has been incorporated as shown in Figure 6.15 (a). At 2.42 GHz, far field distance for this dipole antenna is found to be 5.51 cm so it is placed 7.0 cm away from the tree model. Experimental set-up for the measurement of SE is shown in Figure 6.15 (b). In case of simulation, E_0 and E_t are obtained from the probes connected with far field RF power sensor dipole antenna then by equation (6.1), SE is calculated. On the other hand, for the experimental measurement values of P_0 and P_t are obtained directly from the handheld RF power meter [29], and then by equation (6.2), SE is calculated.

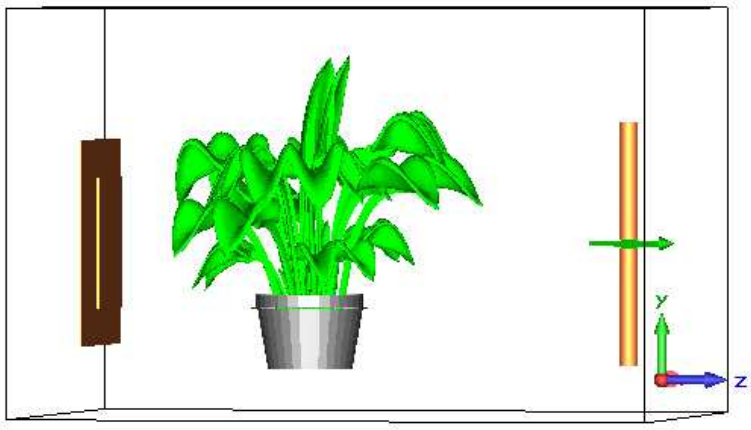

(a)

(b)

Figure 6.15. (a) Simulation and (b) experimental set-up with Money plant for computing SE.

6.2.2.3 Analysis of EM wave absorption characteristics

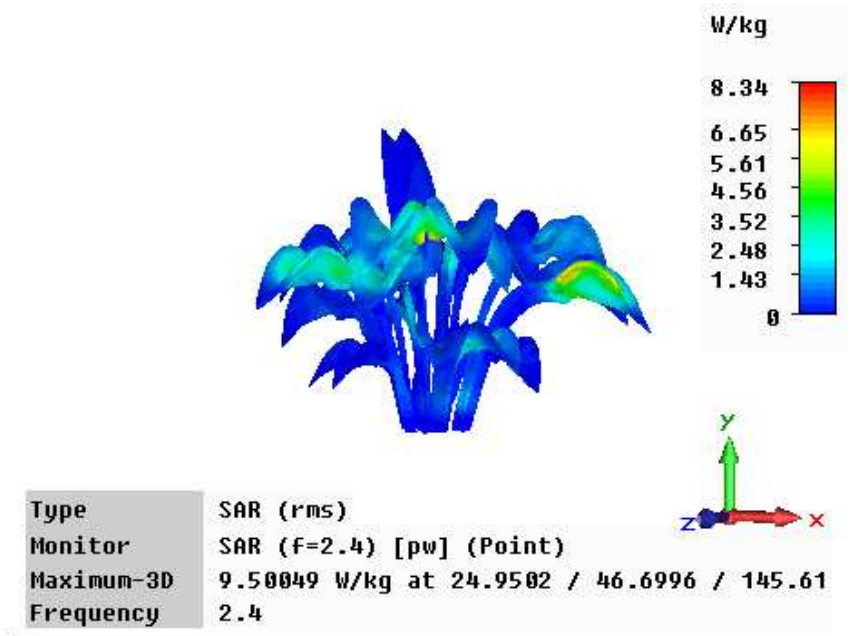

(a)

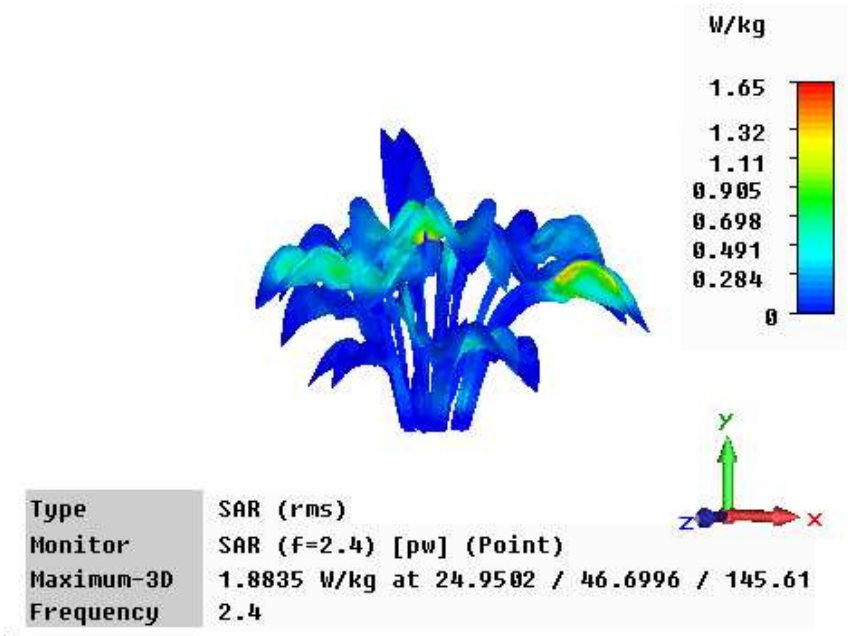

(b)

Figure 6.16. Local Point SAR distributions for (a) occupational and (b) general public exposure levels prescribed by ICNIRP at 2.4 GHz.

3-D Local Point SAR distributions inside the Money plant model exposed by a plane wave at 2.40 GHz for occupational (peak *E* field = 137 V/m) and general public exposure levels (peak *E* field = 61 V/m) prescribed by ICNIRP are shown in the Figure 6.16 (a-b). From Figures, it is seen that higher value of SAR is induced in the leaves than the stem.

Maximum value of Local Point SAR obtained for occupational and general public exposure levels are 9.50 W/kg and 1.88 W/kg respectively.

Variations of measured and simulated SE with Frequency in the frequency range of 2.35 GHz to 3.0 GHz obtained for the Money plant are shown in Figure 6.17 From Figure 6.17, maximum values of simulated and measured SE are found to be 9.48 dB and 9.01 dB respectively at 2.72 GHz. The curve corresponding to the measured value of SE follows the curve corresponding to the simulated value of SE. But there is unwanted mismatch between simulated and measured value of SE, this may be due to the assumption in modelling of the Money plant.

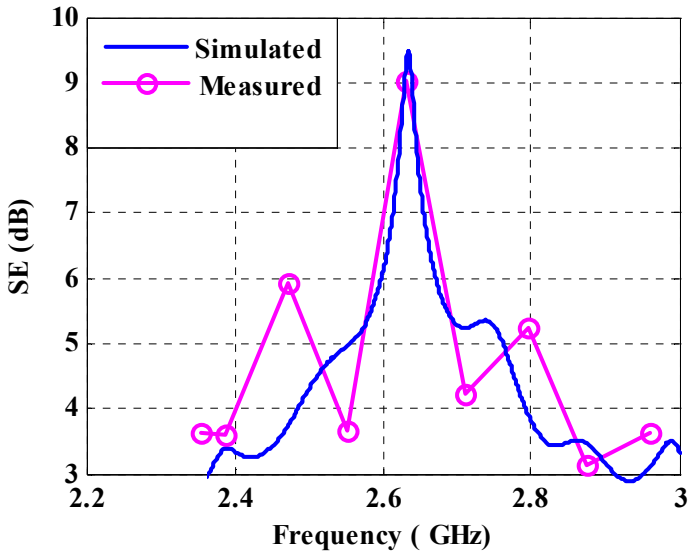

Figure 6.17. SE vs. Frequency for Money plant.

Comparison of SE obtained for Money plant at 2.4 GHz with that for Bonsai tree at GSM 900 band shows that the Bonsai tree provides more shielding than the Money plant. This is possible due to the fact that the Bonsai tree is larger in size compare to the Money plant which causes more RF power absorption and less transmission for Bonsai tree with respect to the Money plant.

6.3 Effects of non-ionizing EM radiation on Pollen grains

Theoretical investigations have been carried out on the effects of non-ionizing EM radiation inside pollen grains at GHz frequencies. To carry out the investigation, a realistic 3-D electrical model of pollen colony placed between a pair of dipole antennas designed at GHz frequencies has been simulated using CST Microwave Studio®.

6.3.1 EM modelling of Pollen cell

Pollen grains of various species can vary quite a lot in size in the order of 10 μm – 100 μm [30]. The natural colours of pollen grains are mostly white, cream, yellow or orange. The texture of the cell wall of pollen grain shows also great variations, from smooth to spiky. The wall of the pollen grain always consists of two layers: the inner intine wall and the outer exine wall. Both inner and outer cell wall of pollen grains often has a typical structure that depends on the species. The deposition of these walls begins already during meiosis and continues until final maturation of the pollen grain. The inner layer is laid by the cells themselves, the outer wall is deposited by the tapetum. The inner wall consists of cellulose and hemi-cellulose, but callose is always present. The outer wall consists mainly of sporopollenin which is a mixture of stable biopolymeres containing fatty acids. Sporopollenin protects the living vegetative and generative cell in the pollen grain against mechanical damage, chemical break-down and too rapid desiccation and it provides a shield against the aggressive ultraviolet radiation of the sun. On the surface of the outer wall and in cavities remnants of the tapetum can be found. Sometimes the grain is covered by a fatty liquid called *pollenkit*.

From biological point of view, pollen grains are micro structure of size and consisting of tapetum, cellulose, hemi-cellulose and other complex compounds, having different chemical properties [31]. But instead of the chemical details of the compounds, the effective dielectric properties of those chemicals, characterized by their permittivity and conductivity values are required in EM modelling of a pollen cell. A pollen cell like a bacterium cell is prokaryotic in nature and can be modelled as a multilayered structure, where each layer has some specific electrical properties. Also another point to be noted is the dispersive nature of the different layers, which implies that the dielectric constant and other passive electrical parameters like conductivity and resistivity are directly or indirectly dependent on frequency [32],[33]. Therefore, it is necessary to consider the frequency dependant characteristics of these electrical parameters in the frequency band of analysis.

Pollen grains produced by different species of plant have a distinctive appearance. Using a microscope, the distinctive features of different types of pollen can be observed. This helps to identify what they are. Two useful features for identifying pollen are pores and furrows. Pores are holes in the surface of a pollen grain. Furrows are slits or elongated openings on the surface of a pollen grain. From consideration of number of pores and furrows

present in the pollen grains, they can be subdivided broadly into the following categories [34],[35]:

i. Monoporate: It has only one pore and no furrow.

   Example: Grass pollen.

ii. Triporate: It has only three pores and no furrow.

   Example: Ostrya.

iii. Colpate: It has only furrows and no pore.

   Example: Quercus found in oak, has three furrows.

iv. Colporate: It has both pore and furrow on the surface of the pollen grain.

   a. Monocolporate: It has one pore and one furrow.

      Example: Wood Fern.

   b. Tricolporate: It has three pores and three furrows.

      Example: Fagus found in beech.

Typical dimensions of different categories of pollen cells are shown in the Table 6.3 [32]-[35].

Table 6.3: Dimension of different categories pollen grains.

Type of pollen	Size
Grass	30 μm to 40 μm
Ostrya	19 μm to 29 μm
Quercus	24 μm to 38 μm
Fagus	45 μm to 50 μm

(a) **(b)**

Figure 6.18. (a) Lambs Quarter pollen and (b) its approximation version for modelling.

A schematic diagram of the equivalent model of pollen cell which has been used in the simulation is shown in Figure 6.18. For this study, further simplification is made by removing the outer cell and filled with water only.

Like bacteria colony, instead of single pollen multiple pollens live together known as pollen grains. An air-borne pollen colony has been considered for this investigation. To study the EM energy absorption characteristic of the pollen grains, a pair of half-wave resonating dipole antennas each of 0.9 mm length is used as shown in Figure 6.19. To obtain real image of the phase distribution due to EM fields formed inside the pollen grains, a resonating half-wave dipole antenna of the same length is placed at a distance of 21.5 mm from the pollen grains as shown in Figure 6.20.

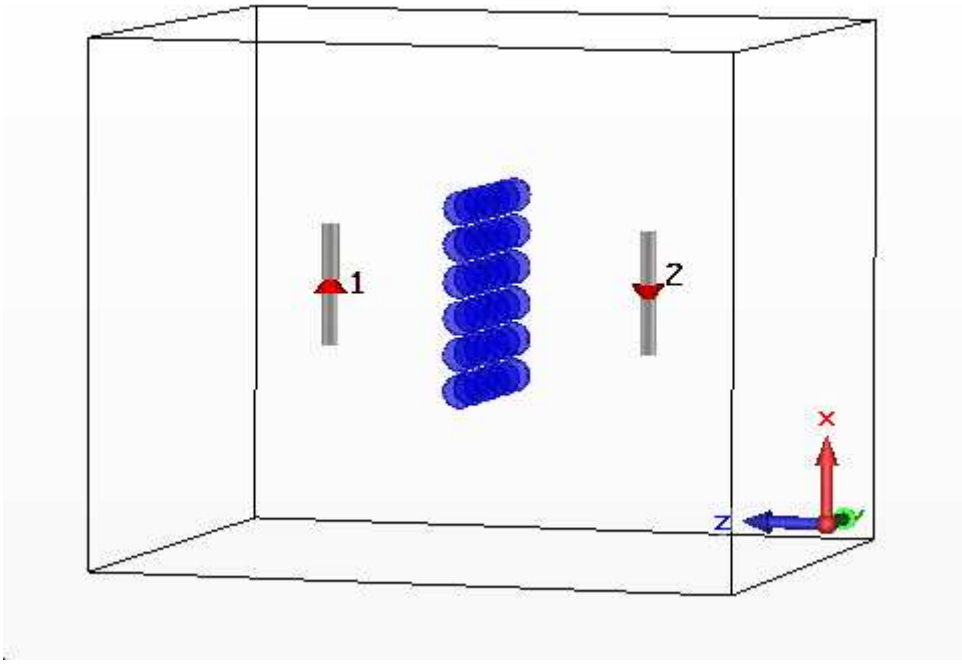

Figure 6.19. Simulation Model of pollen grains placed between two dipole antennas.

Figure 6.20. Simulation Model of pollen grains placed in front of a dipole antenna.

6.3.2 Analysis of EM energy absorption characteristics of Pollen grains

The variations of S_{11} and S_{21} with frequency for with and without pollen grains are shown in Figure 6.21. From the curve it can be observed that for without pollen grains S_{11} is below -10 dB from 143 GHz to 184 GHz. With pollen grains a dip is found in S_{11} plot at 178 GHz. On the other hand the S_{21} shows two peaks of -27 dB at 166 GHz and 176 GHz, respectively, which are possibly due to the absorptions of EM energy at electrical resonance frequencies for every individual cell or their numerical and structural combinations in the pollen grains of study.

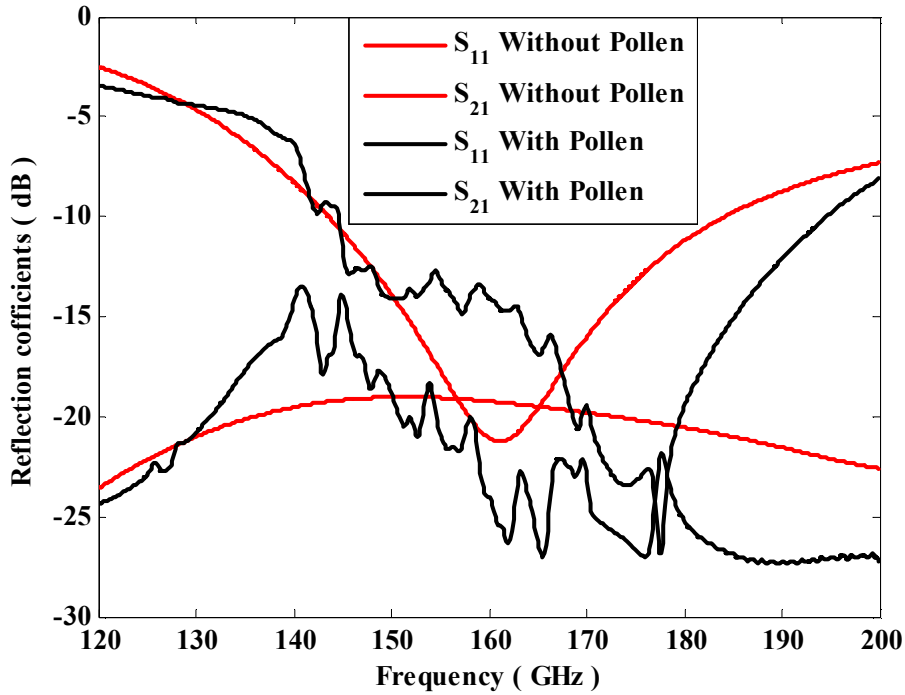

Figure 6.21. S_{11} and S_{21} vs. frequency for two with and without presence of pollen grains.

The distributions of *E* field and *H* field at the centre plane of XY as obtained from simulation are shown in Figure 6.22 (a-b). From Figure 6.22 (a), it can be observed that two high concentric spots consists of different phase are observed inside the pollen grains. The phase difference between these two *E* fields, are exactly 180 degree, like the phase difference of two poles of the source dipole. These two points represent the *E* field image of the source dipole antenna. From Figure 6.22 (b), it can be observed that a single high concentric spot is formed inside the pollen grains. This point represents the high *H* field image of the source dipole antenna. For a resonating dipole antenna, the maximum *H* field exists at the centre of the dipole antenna.

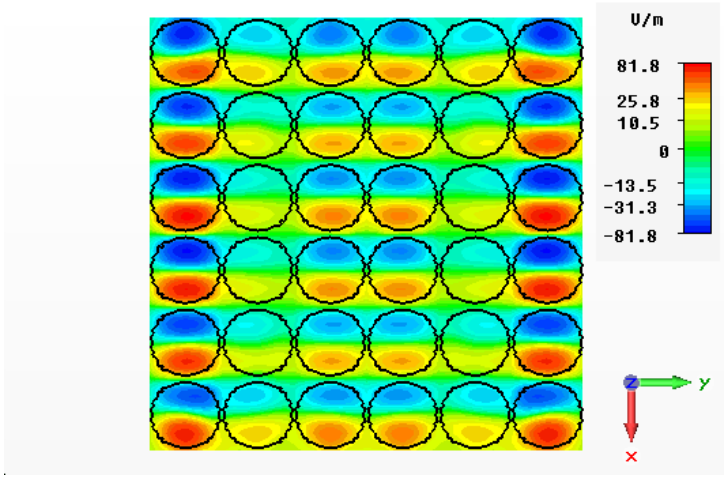

(a)

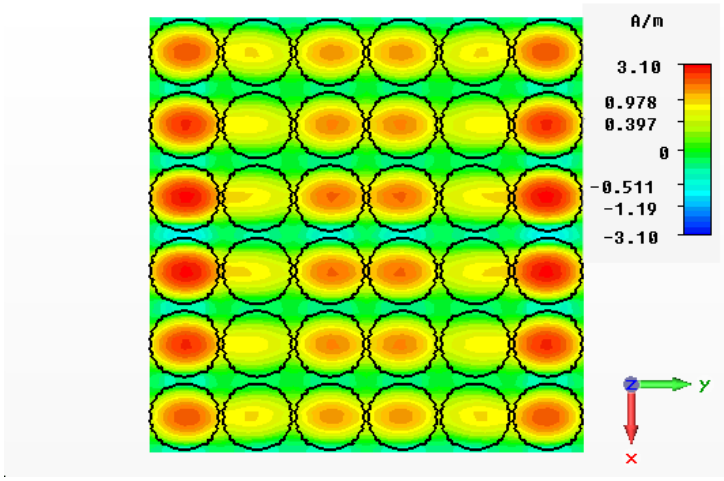

(b)

Figure 6.22. (a) *E* field and (b) *H* field distributions inside pollen grains at the centre of XY plane.

E field and *H* field distributions at ±0.05 mm from the centre of XY plane are shown in Figures 6.23-6.24. From Figures 6.23-6.24, it can be observed that both the images of *E* field and *H* field are formed in the same fashion as before but their positions are slightly shifted.

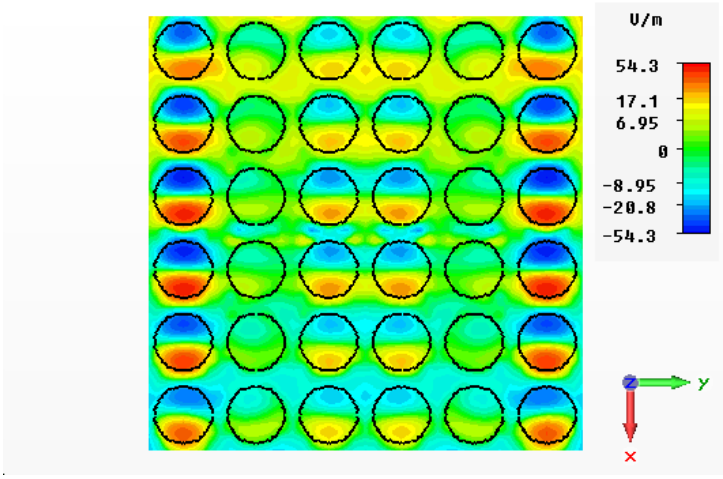

(a)

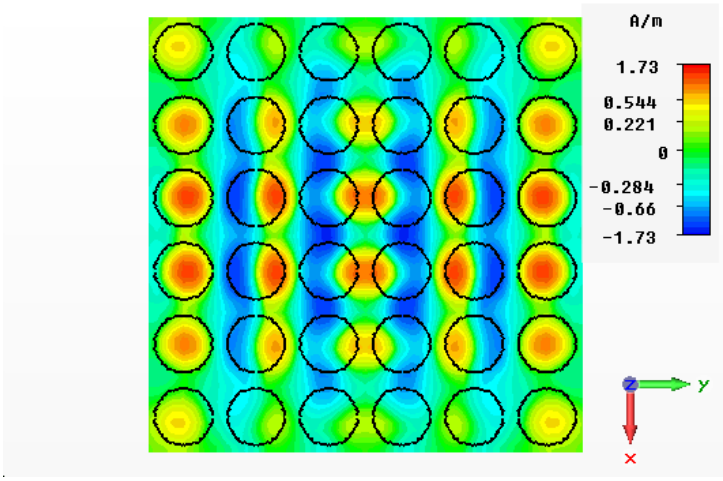

(b)

Figure 6.23. (a) *E* field and (b) *H* field distributions inside pollen grains at +0.05 mm from the centre of XY plane.

The distributions of *E* field at XZ plane for y = 0.8 mm, y = 0.85 mm and y = 0.75 mm are shown in Figure 6.25 (a-c). It is seen that the images of *E* field in the Figure 6.25 (b) are more prominent compare to others.

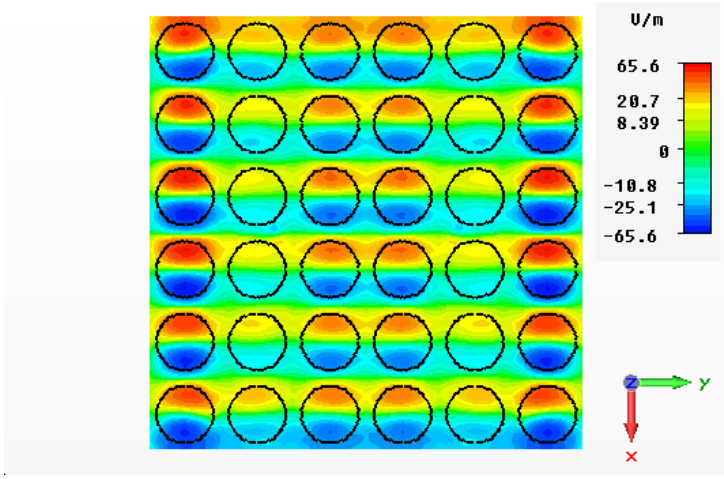

(a)

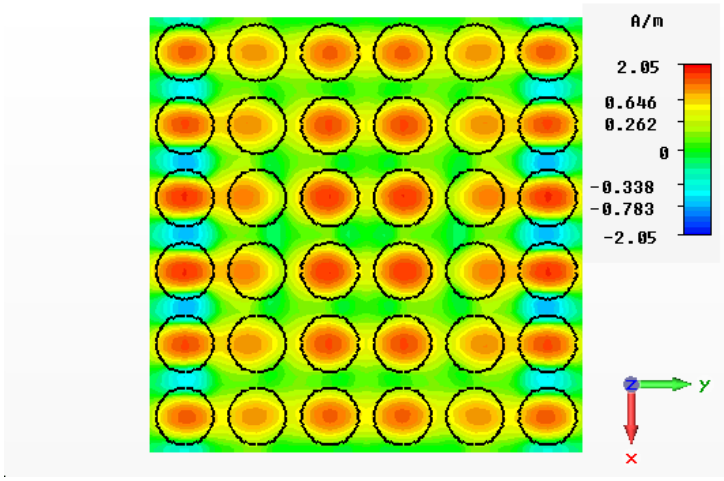

(b)

Figure 6.24. (a) *E* field and (b) *H* field distributions inside pollen grains at -0.05 mm from the centre plane of XY plane.

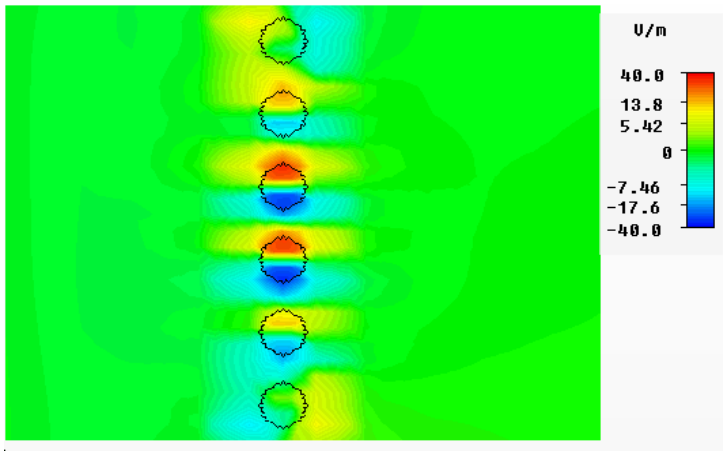

(a)

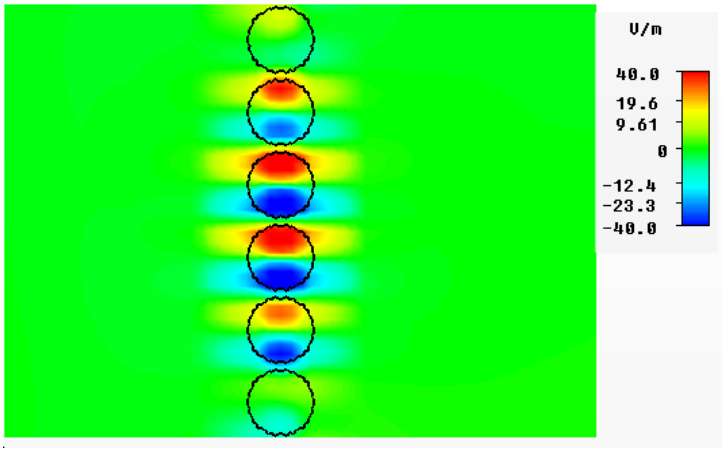

(b)

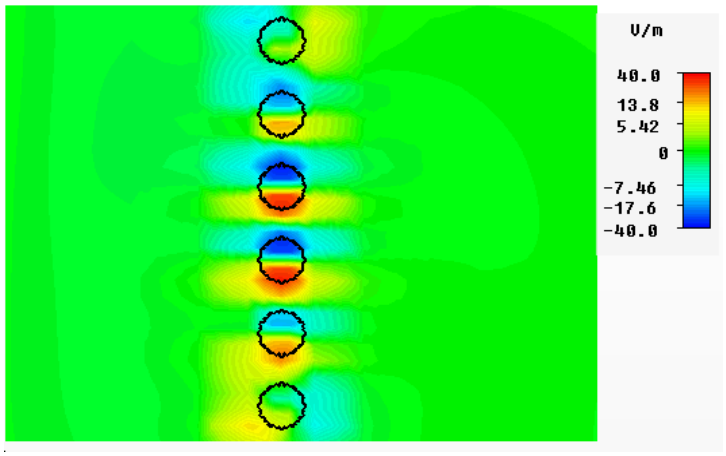

(c)

Figure 6.25. *E* field distribution at XZ plane for (a) y = 0.8 mm, (b) y = 0.85 mm and (c) y = 0.75 mm.

6.4 Conclusions

In this chapter, non-ionizing EM absorption characteristics of Bonsai tree and Money plant have been estimated in terms of maximum local *E* field, *H* field, 1-g SAR and SE. Using in-house hybrid FDTD method, EM wave absorption characteristics of the Bonsai tree has been investigated at GSM 900 band. The tree has been modelled from freely available 3-D CT scan Bonsai dataset considering the electrical parameters of different internal structures of the living tree. Maximum local *E* field, *H* field, 1-g SAR and SE have been calculated for the Bonsai tree placing at distance of 5 m away from a radiating BSA with 20 W input power. From *E* field and *H* field distributions in the plane of wave propagation, it has been found that higher value of *E* field is induced in the outer region of tree. But higher value of *H* field is induced in the inner region of tree and the value of *H* field decreases as the distance of the region from source increases. Variations of maximum local *E* field, *H* field and 1-g SAR with height of tree at 925 MHz show that initially with the increase of height, maximum local *E* field decreases abruptly then attains a flattened peak and after that, with further increase of height, maximum local *E* field increases rapidly. It can be observed that, initially with the increase of height, maximum local *H* field increases rapidly then attains one consecutive sharp and flattened peaks and with further increase of height, maximum local *H* field decreases quickly. Peak value of maximum local 1-g SAR is found to be 0.135 W/kg. Variation of SE with frequency due to the Bonsai tree shows that at 925 MHz value of SE is 13.18 dB.

SAR induced inside a Money plant and SE provided by the Money plant in the frequency range of 2.35 GHz to 3.0 GHz have been calculated as well as measured experimentally by means of commercially available software CST Microwave Studio® and a handheld RF power meter respectively. For occupational (peak *E* field = 137 V/m) and general public exposure levels (peak *E* field = 61 V/m) prescribed by ICNIRP at 2.40 GHz, it has been found that higher value of SAR is induced in the leaves compare to the stem. Maximum value of Local Point SAR induced inside the Money plant for occupational and general public exposure levels are found to be 9.50 W/kg and 1.88 W/kg respectively. For the frequency range of 2.35 GHz to 3.0 GHz it has been found that curve corresponding to the measured value of SE follows the curve corresponding to the simulated value of SE. Maximum values of simulated and measured SE are found to be 9.48 dB and 9.01 dB respectively at 2.72 GHz.

At the end of this chapter, non-ionizing EM energy absorption characteristics of pollen grains have been analyzed using FIT based commercially available software CST Microwave Studio®. The phase value distributions of *E* field and *H* field at the different planes have been obtained. Two high concentric spots of 180 degree phase difference between these two *E* fields are observed inside the pollen grains. These two points represent the *E* field image of the source of the dipole antenna. It has also been observed that a single high concentric spot is formed inside the pollen grains due to *H* field image of the source dipole antenna.

References

[1] A. Balmori, "Electromagnetic pollution from phone masts: Effects on wildlife," *Pathophysiology*, *ELSEVIER*, vol. 16, pp. 191–199, 2009.

[2] J. Everaert and D. Bauwens, "A possible effect of electromagnetic radiation from mobile phone base stations on the number of breeding House Sparrows (Passer domesticus)," *Electromagnetic Biology Med*., vol. 26, pp. 63-72, 2007

[3] C.H. Durney, H. Massoudi and M.F. Iskander, "Radiofrequency radiation dosimetry handbook," USAF School Aerospace Med., Brooks AFB, TX, USAFSAM-TR-85-73. 1986.

[4] G. Kumar, "Report on cell tower radiation," DOT, New Delhi, December 2010.

[5] A. Balmori, "The incidence of electromagnetic pollution on the amphibian decline: Is this an important piece of the puzzle?" *Toxicological & Environmental Chemistry*, vol. 88, No. 2, pp. 287–299, 2006.

[6] J.D. Summers-Smith, "The decline of the House Sparrow: a review," *British Birds*, vol. 96, pp. 439-446, 2003. [Online] http://www.ndoc.org.uk/articles/Decline%20of%20the%20House%20Sparrow.pdf.

[7] D. Vanengelsdorp and M.D. Meixner, "A historical review of managed honey bee populations in Europe and the United States and the factors that may affect them," *Journal of Invertebrate Pathology*, vol. 103, pp. (Suppl. 1): S80-95, 2010.

[8] S.S. Sahib, "Electromagnetic Radiation (EMR) Clashes with Honey Bees," *International Journal of Environmental Sciences*, vol. 1, No. 5, pp. 897-900, 2011.

[9] W.Lo ¨scher and G. Ka¨s, "Conspicuous behavioural abnormalities in a dairy cow herd near a TV and radio transmitting antenna," *Practical Vet. Surgeon*, Germany, vol. 29, pp. 437–44, 1998.

[10] J.F. Burchard, D.H. Nguyen, L. Richard and E. Block, "Biological effects of electric and magnetic fields on productivity of dairy cows," *Journal Dairy Science*, vol. 79, pp. 1549-1554, 1996.

[11] T.A. Marks, C.C. Ratke and W.O. English, "Strain voltage and developmental, reproductive and other toxicology problems in dogs, cats and cows: a discussion," *Vet. Human Toxicology*, vol. 37, pp. 163–172, 1995.

[12] V. Russello, C. Tamburello and A. Scialabba, "Microwave effects on germination and growth of Brassica drepanensis seed," Proceedings of 3rd *International Congress of the European BioElectromagnetics Association*, 89, 1996.

[13] S.K. Guha, S. Neogi and G. Kumar, "Report on: Cell phone towers radiation hazards," October 2011. Available: https://www.ee.iitb.ac.in/~mwave/Cell-tower-rad-report-WB-Environ-Oct2011.pdf.

[14] G. Soja, B. Kunsch and M. Gerzabek, "Growth and yield of winter wheat (Triticum aestivum L.) and corn (Zea mays L.) near a high voltage transmission line," *Bioelectromagnetics*, vol. 24, pp. 91–102, 2003. Available: http://www.ncbi.nlm.nih.gov/pubmed/125246755.

[15] T. Selga and M. Selga, "Response of Pinus sylvestris L. needles to electromagnetic fields, cytological and ultrastructural aspects," *Sci. Total Environ*., vol. 180, pp. 65–73, 1996.

[16] M. Tkalec, K. Malarik, M. Pavlica, B. Pevalek-Kozlina and Z. Vidakovic-Cifrek, "Effects of radiofrequency electromagnetic fields on seed germination and root meristematic cells of Alliumcepa L.," *Mut. Res.*, vol. 672, pp. 76–81, 2009. Available: http://www.ncbi.nlm.nih.gov/pubmed/19028599.

[17] American National Standard – "Safety Levels with Respect to Exposure to Radio Frequency Electromagnetic Fields, 3 kHz to 300 GHz" ANSI/ (IEEE C95.1 – 1992).

[18] International Commission on non-Ionizing Radiation Protection, "ICNIRP statement-Health issues related to the use of hand –held radiotelephones and base transmitters," *Health Phys*ics, vol. 70, No. 4, pp. 587-593, 1996.

[19] Federal Communication Commission (FCC), Home Page. http://www.fcc.gov.

[20] The volume library. Home page. http://www9.informatik.uni-erlangen.de/External/vollib.

[21] C.J. Love, S. Zhang and A. Mershin, "Source of sustained voltage difference between the xylem of a potted ficus benjamina tree and its soil," *PLoS ONE*, vol. 3, No. 8, pp. 1-5, August 13, 2008.

[22] A. Franchois, R. Lang, D. Leva1, Y.Pineiro, G. Nesti1 and A. Sieber, "Ground truth complex permittivity measurements of trees," [Online] http://www.esamultimedia.esa.int/conferences/98c07/papers/P003.PDF.

[23] Soil dielectric properties, [Online] http://pe2bz.philpem.me.uk/Comm/-Antenna/Info-905-Misc/soildiel.htm.

[24] J. Krzysztofik, R. Borowiec and B. Bieda, "Some consideration on shielding effectiveness testing by means of the nested reverberation chambers," *Radioengineering*, vol. 20, pp. 766-774, 2011.

[25] D.M.Sullivan, Electromagnetic Simulation Using the FDTD Method, IEEE Press, New York, 2000.

[26] M.A.A. Karunarathna and I.J. Dayawansa, "Energy absorption by the human body from RF and microwave emissions in Sri Lanka," *Sri Lankan Journal of Physics*, vol. 7, pp. 35-37, 2006.

[27] P.A. Masson, J.M. Ziriax, W.D. Hurt, T.J. Walters, K.L. Ryan, D.A. Nelson, K.I. Smith and J.A. D'andrea, "Recent Advancements in Dosimetry Measurements and Modeling," *NATO Science Series*, *Springer*, vol. 82, pp 141-155, 2000.

[28] T. Hanai, N. Koizumi and A. Irimajiri, "A method for determining the dielectric constant and the conductivity of membrane-bounded particles of biological relevance," *Biophys. Struct. Mech.*, vol. 1, pp. 285-294, 1975.

[29] Agilent [Home], http://www.home.agilent.com.

[30] Virtual Classroom Biology, Radboud University. [Online] http://www.vcbio.science.ru.nl/en/virtuallessons/pollenmorphology.

[31] B. Levitin, D. Richter, I. Markovich and M. Zik, "Arabinogalactan proteins 6 and 11 are required for stamen and pollen function in Arabidopsis," *The Plant Journal*, vol. 56, pp. 351–36, 2008.

[32] Salt, Arcaeology and Environment: The Study of an Ancient Industry. [Online] http://www.seillevalley.com/IdentifyingPollen.htm.

[33] The Virtual Forest Interactive: Paleoecology. [Online] http://www.blackrock.ccnmtl.columbia.edu/paleoecology/identification.

[34] A.V. Rajurkar, J.A. Tidke and G.V. Patil, "Studies on pollen morphology of Ipomoea species (Convolvulaceae)," *Research in Plant Biology*, vol. 1, No. 5, pp. 41-47, 2011.

[35] L. Amjad, and M. Shafighi, "Effect of Electromagnetic Fields on Structure and Pollen Grains Development in Chenopodium album L," *World Academy of Science, Engineering and Technology*, vol. 46, pp. 10-29, 2010.

Chapter 7

Study on some useful Applications based on interaction of microwave with Living being

7.1 Introduction

Effect of EM waves at RF frequencies can also be utilized for many useful applications. This chapter includes study on some new applications along with further study on some available applications which involve interaction of EM waves with living tissues or cells. Previously developed numerical tools or models are used for some of these studies.

7.2 Detection and Selective Destruction of Bacteria colony

Theoretical investigation has been carried out to determine the usefulness of EM wave for detection and selective destruction of bacteria colony at THz frequencies. To carry out the investigation, a realistic 3-D electrical model of bacteria colony has been developed and placed between a pair of dipole antennas designed at THz frequencies. The model is simulated using FDTD based in-house numerical code developed by commercially available MATLAB software [1].

7.2.1 EM modelling of Bacteria cell

From biological point of view, a bacterium cell is a micro structure consisting of proteins, liquids and other complex compounds, having different chemical properties. But instead of the chemical details of the compounds, the effective dielectric properties of those chemicals, characterized by their permittivity and conductivity values are required in EM modelling of a bacterium cell. General idea proposed by various researchers for modelling single prokaryotic or eukaryotic cell is to consider it as a central protoplasm-ellipsoid covered by cell-membrane and cell-wall at the outermost part [2]-[4]. A bacterium cell is prokaryotic in nature and can be modelled as a multilayered structure, where each layer has some specific

electrical properties. Also another point to be noted is the dispersive nature of cell-membrane and cytoplasm, which implies that the dielectric constant and other passive electrical parameters like conductivity and resistivity are directly or indirectly dependent on frequency [5],[6]. Therefore, it is necessary to consider the frequency dependant characteristics of these electrical parameters in the frequency band of analysis.

From consideration of shapes, bacteria cells with regular shapes can be subdivided broadly into following categories:

a. Cocci: Spherical (Example: Staphylococcus Aureus)
b. Bacilli: Rod-like or Cylindrical (Example: Bacillus Anthracis)
c. Spirillum: Spiral or Helical (Example: Treponema Pallidum)
d. Filamentous: Complex forms, like "jellybeans in a straw" (Example: Leptothrix)

Shapes of typical Cocci, Bacilli, Spirillum and Filamentous bacteria cells are shown in Figure 7.1. Typical dimensions of different categories of bacteria cells are shown in the Table 7.1 [7]-[10].

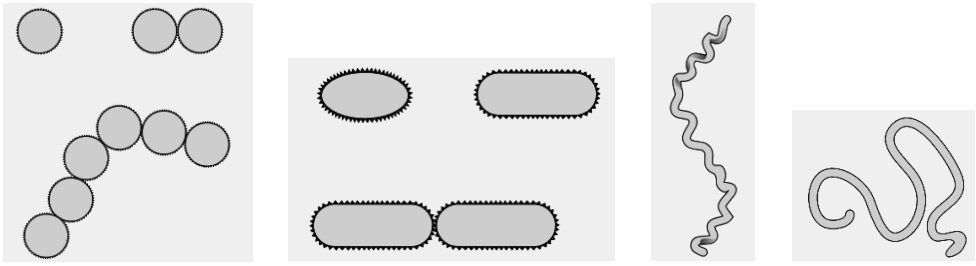

(a) **(b)** **(c)** **(d)**

Figure 7.1. Different bacteria cell structures: (a) Cocci, (b) Bacilli, (c) Spirillum and (d) Filamentous.

Table 7.1: Size of different type Bacteria Cell

Type of Bacteria Cell	Size
Bacilli	Width: 1.5 μm to 3.5 μm Length: 2.0 μm to 8.0 μm
Cocci	Diameter: 2 μm to 3 μm
Spirillum	Diameter: 1.4 μm to 1.7 μm Length: 60 μm
Filamentous	Diameter: 0.5 to 2.0 μm

The components which are present in all bacteria cells are cell-membrane, cytoplasm, nucleic acid and different other cellular components. But these components are so miniscule compared to the cytoplasm and nucleic acid volumes that contribution due to these other cellular components in the value of equivalent dielectric constant is pretty small and can be neglected. Similarly the cell wall also can be approximated as a layer with a continuous dielectric constant value. Thus equivalently a bacterium cell can be modelled as a three layered structure consists of cell wall or membrane, cytoplasm and nucleic acid. A schematic diagram of the equivalent model which has been used in the simulation is shown in Figure 7.2. For this study, further simplification is made by removing the outer cell membrane, and nucleic acid is placed at the central structure only for possible cases. For a 3 μm × 3 μm × 6 μm bacteria, central 4 Yee cells represent the nucleic acid and outer 50 Yee cells represent cytoplasm. For a 3 μm × 3 μm × 2 μm bacteria central 2 Yee cell represent nucleic acid and outer 16 Yee cells represent cytoplasm. For other bacteria considered in this study are modelled with cytoplasm only.

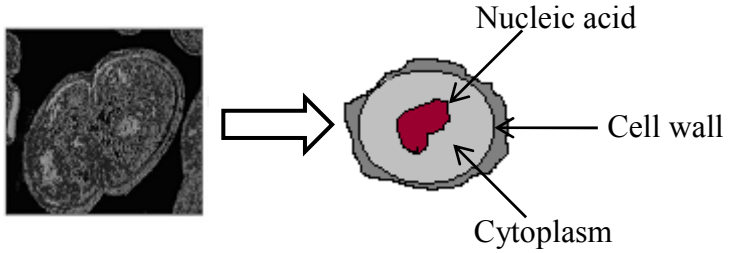

Figure 7.2. (a) Original bacterium cell and (b) its approximation version to be model.

Table 7.2: Dielectric Properties of Cell Structures

Tissue type	Dielectric Constant (ε_r)	Conductivity σ (S/m)
Cell-membrane	40	0.01
Cytoplasm	60	0.01
Nucleic-Acid	80	0.98

Relative dielectric constant (ε_r) and conductivity (σ) of cell-membrane, cytoplasm and nucleic acid used for the bacterium cell modelling are obtained from the literature listed in Table 7.2 [11]-[13]. It can be noted that, the dielectric constants for various cell components

are of very large value with compared to that of free space and the guided wavelength inside the cell is much smaller than that in free space or air. For example guided wavelength in side nucleic-acid is approximately 1/9th of that in free space or air.

7.2.1.1 Construction of Dipole antenna system

A pair of dipole antennas placed in the air media and aligned along z-axis with central feed gap on the same xy plane as shown in the Figure 7.3 has been used for all the simulations. Initially, a pair of dipole antennas of 25 μm lengths (L) with resonant frequency near 6 THz is considered for study of electromagnetic energy absorption for different number and shapes of bacteria cells. To see the effect of change in dipole length on electromagnetic energy absorption, another pair of antennas with 19 μm lengths with resonant frequency near 7.9 THz is chosen. For all cases, the separation between the dipoles is taken as 35Δ where Δ = 1 μm.

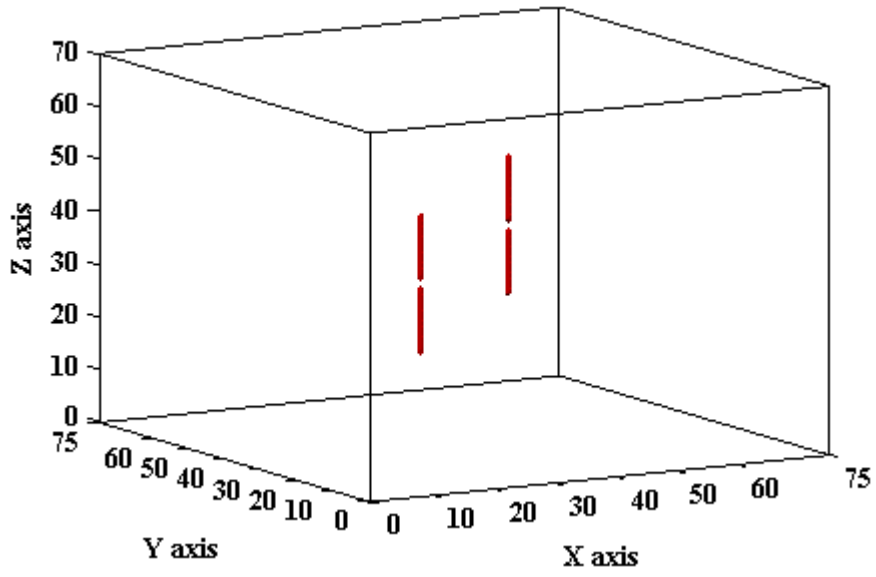

Figure 7.3. Schematic diagram of a dual dipole antenna system.

The transmitting (Tx) antenna is excited using the Gaussian pulse of unit amplitude whereas other acts as receiving (Rx) dipole antenna. The voltage at the two ports of the systems is calculated to obtain S_{21} using the equation (3.41) [14].

7.2.1.2 Generation of Bacteria colony

Practically a single bacterium seldom exists in isolated fashion rather multiple bacteria lives together to form colony. An air-borne bacterial colony has been considered for this investigation. A MATLAB sub-program is used to generate random bacteria colony within

the pre-defined problem space within the 35Δ spacing between the dipole antennas as shown in the Figure 7.4. Then the wideband Gaussian pulse is applied in the feed gap of the T_x and measure the received voltage at R_x to compute S_{21}.

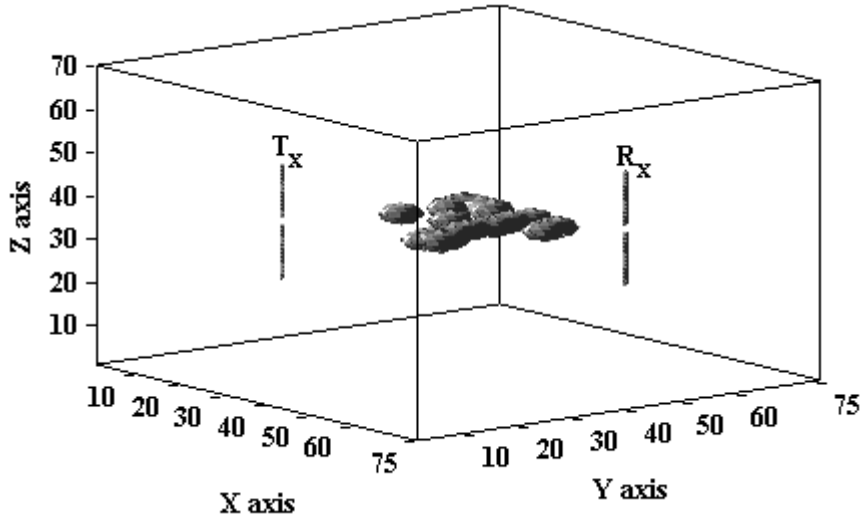

Figure 7.4. Simulation Model of bacteria colony placed between two dipole antennas.

7.2.2 Analysis of EM energy absorption characteristics of different type Bacteria cells

The variation of S_{11} and S_{21} with frequency is shown in Figure 7.5. From the curve it can be observed that the value of S_{11} is -10 dB at 6.4 THz for the reference system impedance 50 Ω. On the other hand the S_{21} shows two peaks of -34 dB at 4.6 GHz and 6.4 GHz, respectively, which is possibly due to mutual coupling, multiple reflection and interference of wave fronts. Due to the small distance of 0.7λ, it is expected that these antenna elements will maintain close coupling among them.

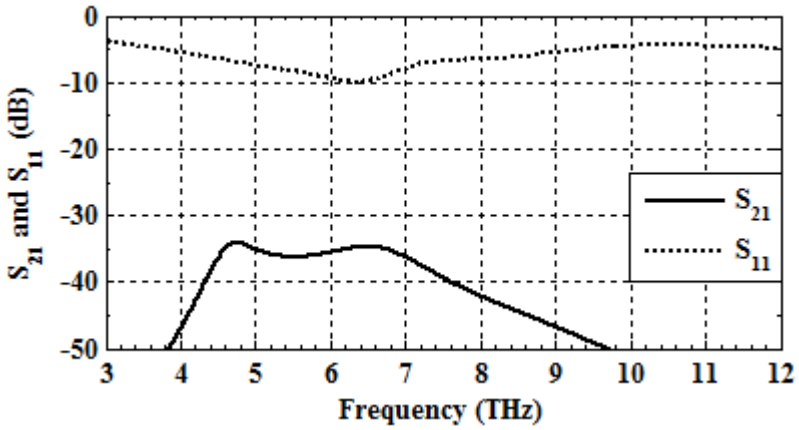

Figure 7.5. S_{11} and S_{21} vs. frequency for two dipoles without presence of bacteria cell.

The variation of energy absorbing band for different bacteria sizes is analysed. One type of cocci and thee types of bacilli are considered for this analysis. Dimensions of cocci are considered as 3 µm × 3 µm × 2 µm and modelled with 18 Yee cells. Dimensions of three types (i.e. type 1, type 2, and type 3) of bacilli are considered as 2 µm × 2 µm × 5 µm, 2 µm × 2 µm × 6 µm and 3 µm × 3 µm × 6 µm and modelled with 20, 24 and 54 Yee cells, respectively. Variations of S_{21} with frequency for different types of bacteria colony each consists of five bacteria cells are shown in Figure 7.6. Multiple dips are observed for all types of bacteria cells in the S_{21} plots, which are due to the absorptions of EM energy at electrical resonance frequencies for every individual cell or their numerical and structural combinations in the colony of study.

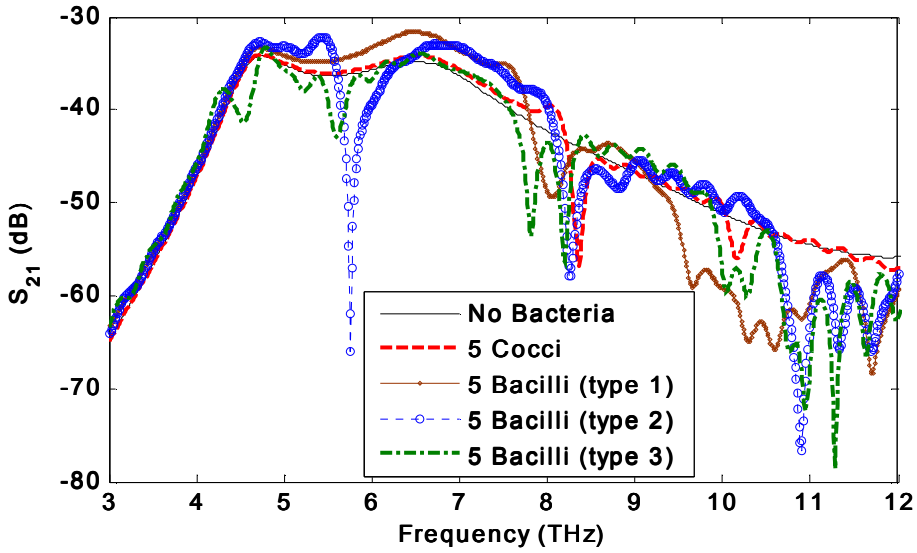

Figure 7.6. S_{21} vs. frequency for different types of bacteria cells present in the colony of study.

7.3 Detection and Identification of Caries in human Tooth

Numerical investigation has been carried out to determine the usefulness of EM wave for detection and identification of caries in a human tooth model at GHz frequencies. To carry out the investigation, a realistic 3-D electrical model of human tooth has been developed and placed between a pair of dipole antennas designed at GHz frequencies. The model is simulated using FIT based commercially available software CST Microwave Studio® [15].

7.3.1 EM modelling of human Tooth

A pair of dipole antennas made of aluminium placed in the air media and aligned along Z axis with central feed gap on the same XY plane has been used. The pair of dipole antennas having length of 2.0 mm with resonant frequency near 58.8 GHz in free space is considered for study of EM energy absorptions in normal and affected teeth. The dipole-pair is separated by a distance of 6.0 mm. A realistic 3-D electrical model of human tooth has been developed from freely available 3-D dataset of archive site [16]. An in-house program has been developed in CST Microwave Studio® where 3-D raw data from original data file of tooth model has been imported. Geometry of the human tooth model along with dipole antenna pair used in the simulation is shown in Figure 7.7. The simulation domain consisting of 64,328 mesh cells of each having length equal to 0.039 mm.The tooth model is assumed to be comprised of only one type of tissue; i.e., tooth tissue. Values of relative dielectric constant (ε_r) and conductivity (σ) of the tooth material used in this study are obtained from literature [17].

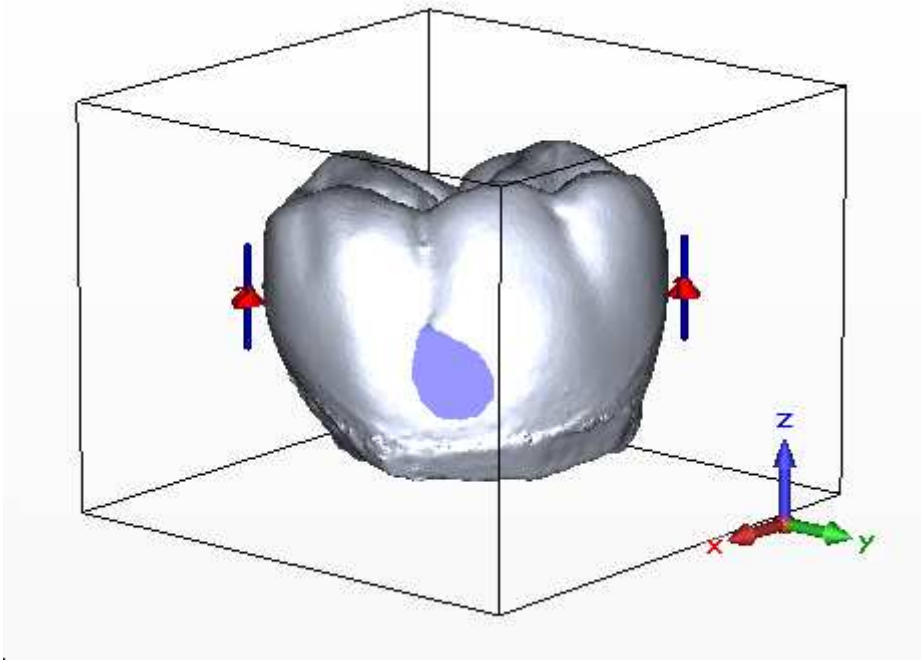

Figure 7.7. Geometry of simulation model of human tooth.

7.3.2 Analysis of EM energy absorption characteristics of different type Dental caries

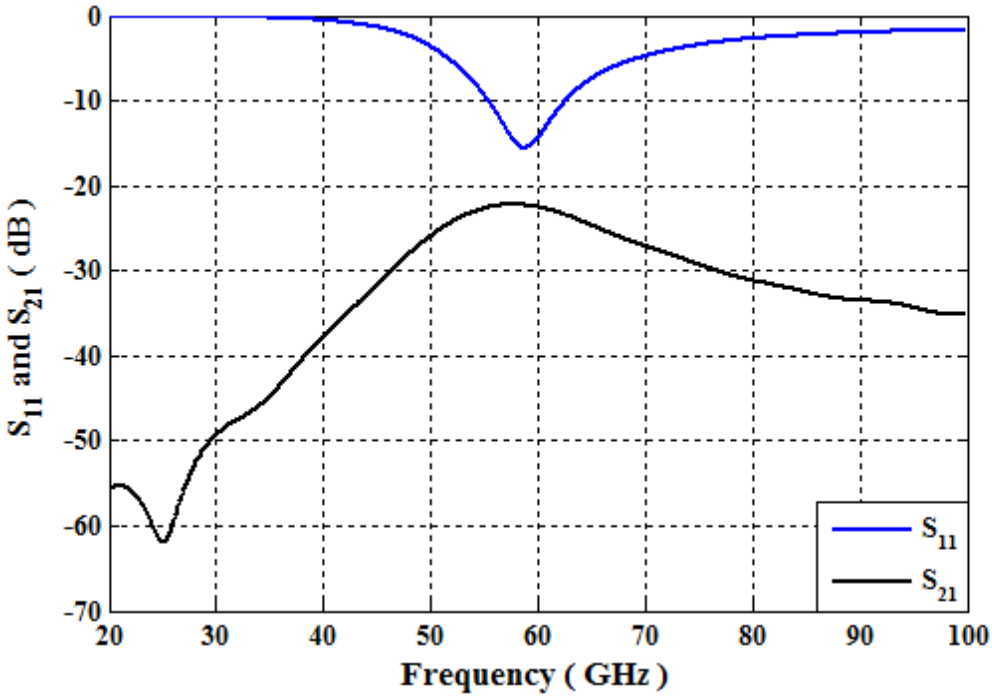

Figure 7.8. Variation of S_{11} and S_{21} with frequency for the dipole-pair in free space.

The variations of S_{11} and S_{21} with frequency for the dipole-pair without presence of tooth model are shown in Figure 7.8. From the figure it can be observed that the value of S_{11} is -15.55 dB at 58.8 GHz on the other hand the S_{21} shows peak value of -22.23 dB at 57.6 GHz, respectively for the reference system impedance of 50 Ω.

The variation of energy absorbing band for normal and affected tooth has been analysed. Variations of S_{21} with frequency for different type of caries composition are shown in Figure 7.9. From the Figure 7.9, it is found that for the normal tooth peak value of S_{21} is higher than that for the affected tooth. Again, for different carries material peak value of S_{21} are different as shown in the Figure 7.9. Peak values of S_{21} for the caries composed of water, vacuum/no material and blood are -12.18 dB, -13.64 dB and -22.37 dB respectively.

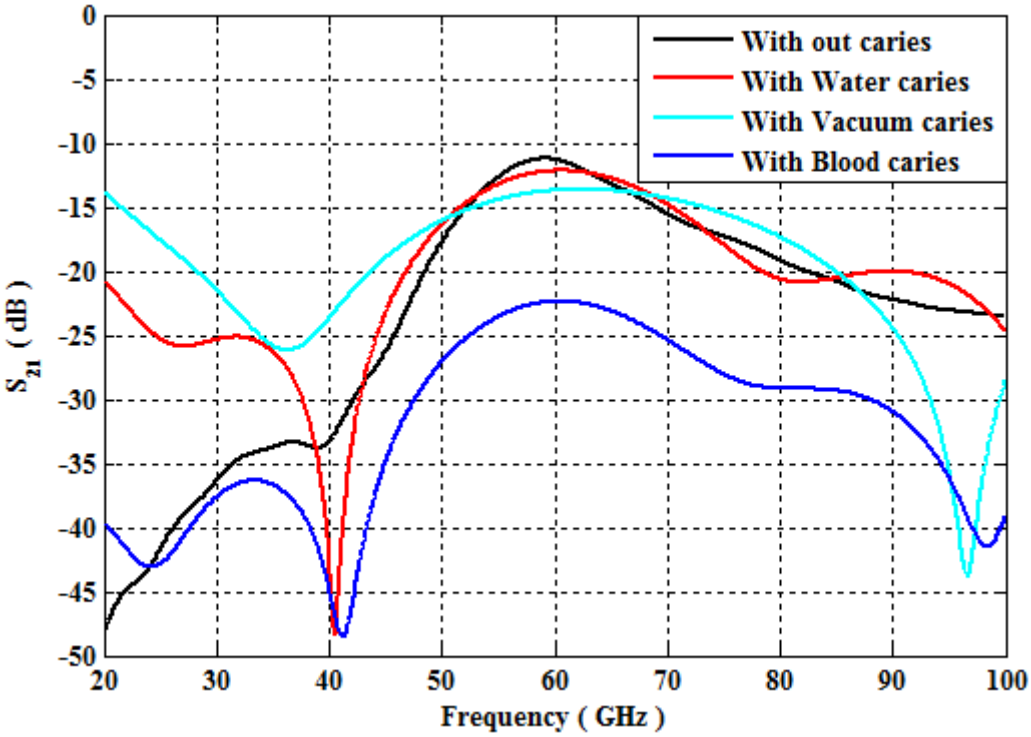

Figure 7.9. Variations of S_{21} with frequency for different type of carres.

7.4 Offline RF Thermal Ablation Planning using CT/MRI Scan data

Steady state temperature variations in human brain due to different electrical and physical changes have been studied considering different thermal ablation treatment requirements using RF probe. Initially, a subject specific voxel-based electrical model has been constructed from DICOM formatted CT or MR based image stacks with different pixel characteristics using HU extraction technique. This subject specific electrical model consists of different dielectric constant and conductivity, considering different anatomical organs and tissues is simulated using CST Microwave Studio®.

7.4.1 Subject specific RFA Planning using CT/MR based DICOM data and EM-Thermal simulation

A simplified block diagram representing the required steps for RFA planning and treatment is shown in Figure 7.10.

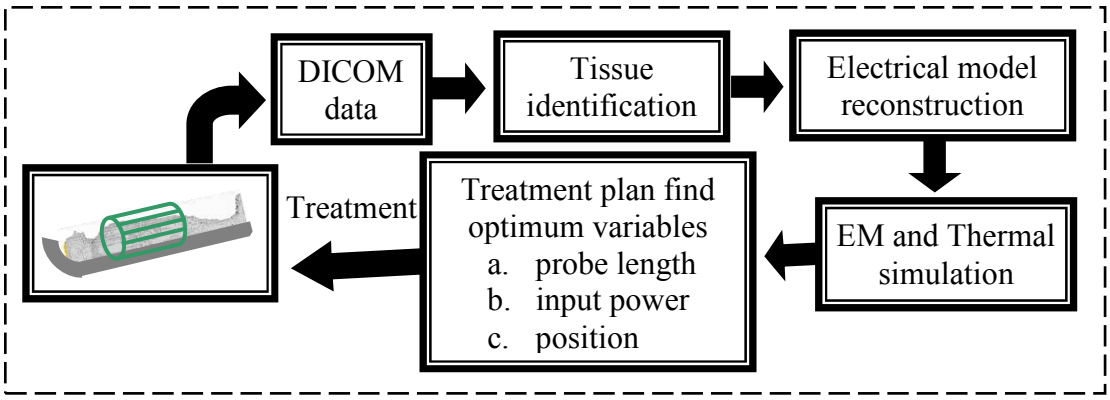

Figure 7.10. Block diagram of the EM simulation for RFA planning of body parts.

The whole planning process consists of:

a. Read CT/MR scan based DICOM data
b. Tissue identification
c. Electrical/Thermal model reconstruction
d. EM-Thermal simulation
e. Plan RFA by finding optimum probe characteristics, input power or position.

Numerical voxel-based computational models of biological structures are used to investigate the interaction between RF source and human body parts. Initially, mathematical models of adults and children were used for this purpose [18],[19]. These models were represented by equations of planes, spheres, cones, ellipsoids, elliptical cylinders or cylinders and do not conform to the shape of real anatomical organs. To obtain more accurate result, free and non-free voxel-based computational models constructed from CT/MR/ultrasound scan data came in the research domain [20],[21]. However these models are not suitable for subject specific investigations. Thus DICOM data holds crucial role in construction of subject specific electrical or thermal model.

7.4.1.1 Read CT/MRI Scan based DICOM data

It has already been mentioned in section 4.3.3.2 that DICOM is a standard for handling, storing, printing, and transmitting information in medical imaging and it integrates different scanners, servers, workstations, printers, and network hardware from multiple manufacturers into a PACS. It includes a file format definition and a network communications protocol. The NEMA holds the copyright of DICOM standard. DICOM format is used extensively for combining the images obtained by CT, MRI and ultrasound devices with metadata to create a

rich description of a medical imaging procedure and it has been widely adopted by hospitals around the world [22].

Each DICOM file contains a header which is useful for voxelization of the scanned organ. The header contains a SOP instance related to IOD [23] which is useful for voxelization of scanned organ. The voxel-based tomographic computational model can be constructed by stacking up the medical images embedded within the DICOM files.

The required computational electrical model has been constructed from PET-CT image data set available in DICOM format. A 278 MB, PET-CT 64 whole body scan data for alias subject MELANIX is obtained from Osirix samples [22]. Although the subject is a Melanoma patient, the brain of the subject is used for this study. The method is general in nature and can be applied to any subject.

Table 7.3: Structural information in the DICOM header of Melanix data

Dimensions	[512 512 507]
Slice Thickness	2
Rescale Slope	1
Rescale Intercept	-1024
Pixel Dimensions	[0.9766 0.9766 1.5000]

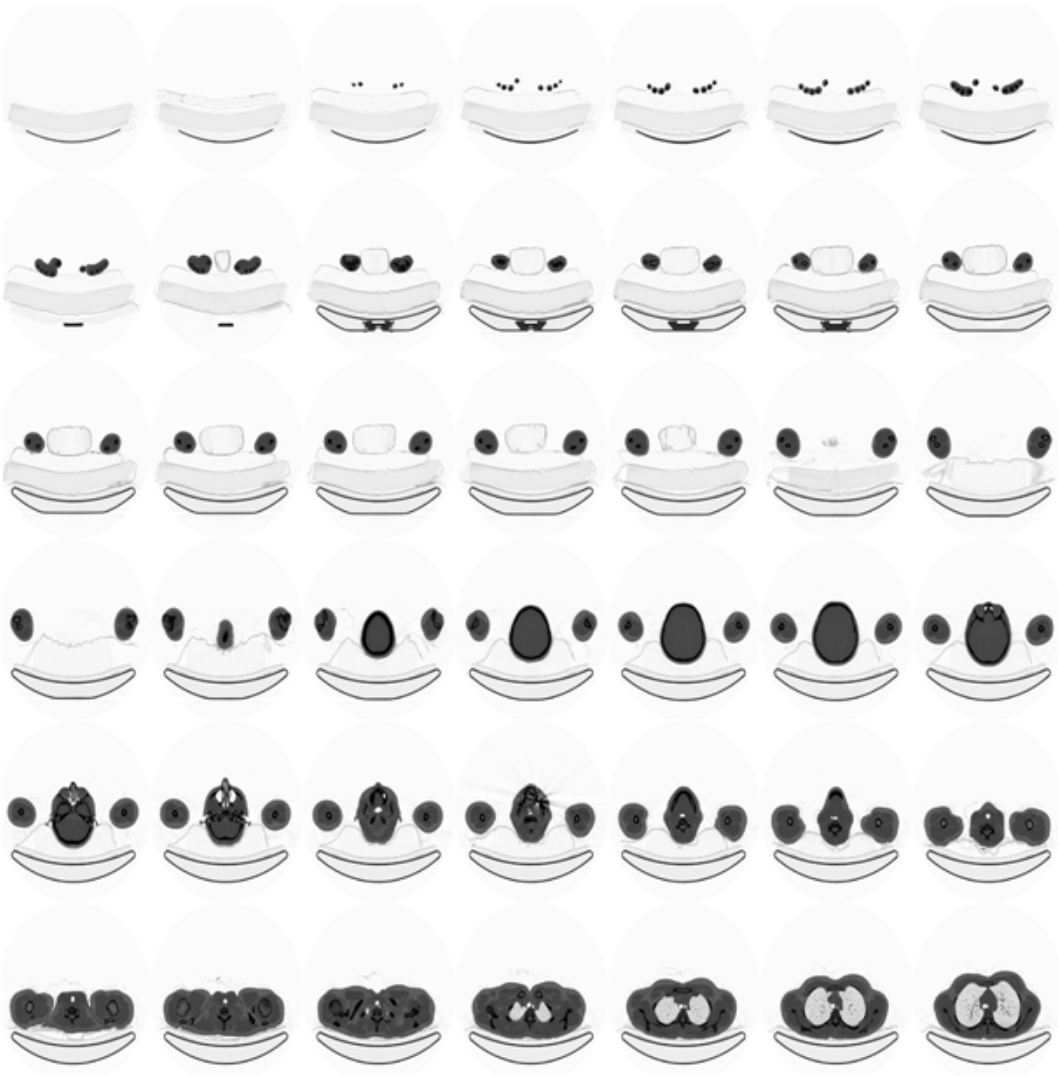

Figure 7.11. Montage of some saggital sections extracted from Melanix data.

The header of the DICOM file used for modelling the human head is shown in the Table 7.3. It is seen that the image data is stored as a 512 × 512 × 507 two-byte pixel array with slice thickness of 2.0 mm. Image data is stored within the DICOM file in the form of pixel cell. A pixel cell is the container for a pixel sample value and optionally additional bits. A pixel cell exists for every individual pixel sample value in the pixel data. As the sample pixel cells are encoded in byte streams, they can be decoded using in-house MATLAB program. The voxel-based computational model can be constructed by stacking up images using the header information. Montage of some saggital sections extracted from Melanix data is shown in Figure 7.11 which is used to construct the 3-D voxel model.

Using the header information, Melanix data is imported in MATLAB and then reshaped. A partially reconstructed three-dimensional geometry constructed using MATLAB program is shown in the Figure 7.12.

Figure 7.12. Three-dimensional geometrical view of actual DICOM head model.

7.4.1.2 Tissue identification from DICOM data

Pixels in an image obtained by CT scanning are displayed in terms of relative radio-density. A quantitative radio-density measuring scale is proposed in 1972 by Godfrey Newbold Hounsfield [24]. The pixel corresponds to the mean radio attenuation by the tissue is represented on a Hounsfield scale using a value from -1024 to +3071. Using a linear transformation equation (4.9), the pixel values found in CT data can be converted in the HU [25],[26].

Each different tissue has different values of HU by which the tissue can be identified and distinguished from other tissues. It is seen from the literature that HU defined for a tissue is not always unique. HU used in this study corresponding to the tissues are listed in the Table 4.12 [27],[28]. For this study, for simplification, the head model is assumed to be consisted of only nine types of tissues i.e., skin, bone, muscle, fat, blood, white matter, grey matter, water and mouth cavity/sinuses.

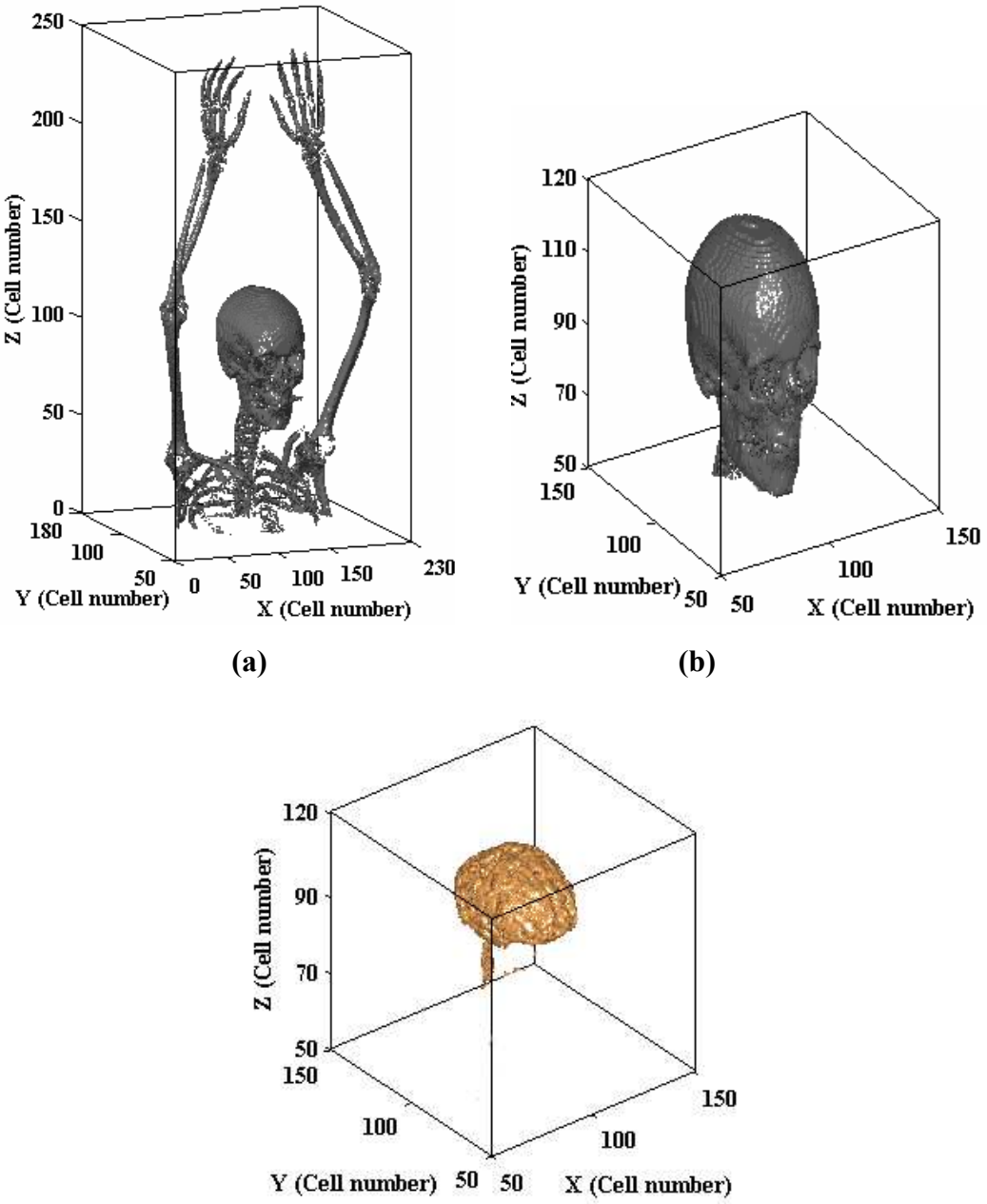

Figure 7.13. Three-dimensional voxel-based computational models of (a) skeleton, (b) CT-bones and (c) brain.

Voxel-based 3-D models of the identified skeleton, CT-bones and brain obtained by filtering other tissues using HU are shown in the Figure 7.13 (a-c). Brain is assumed to be consisted of white and grey matter tissues. During extraction of brain, upper portion of spinal cord is also extracted with brain but for simplicity in the thermal simulation the spinal chord is discarded.

By this method extraction of the voxel-based 3-D computational models for the other organs can also be done. From the literature, it is found that HU defined for a tissue is not always unique for which during extraction of an organ unwanted noise come within the organ itself. In order to eliminate the noise further filtration of the HU is required.

7.4.1.3 Construction of electro-thermal model from 3-D DICOM data

Once the tissue for a particular voxel is identified, they need to be associated with different required physical, electrical and thermal parameters. For EM simulations required electrical parameters are: dielectric constant and electrical conductivity. For thermal simulations, physical parameter like mass density and thermal parameters like thermal conductivity, specific heat is required. To take care of Pennes' BHE [29], heat source due to metabolic process and constants for cooling effect due to blood flow needs to be associated with all voxels during EM-thermal simulation. Electrical and physical properties of different human tissues are listed in Table 7.4 [17], where ε_r is relative dielectric constant, σ is conductivity (S/m) and ρ is mass density of the tissue (kg/m^3).

Table 7.4: Electrical Properties of Human tissue

Tissue Type	ε_r	σ [S/m]	ρ [kg/m^3]
Skin	38.00	1.46	1010
Bone	11.38	0.39	1850
Muscle	52.73	1.74	1040
Fat	5.28	0.11	920
Blood	58.26	2.54	1060
White Matter	36.17	1.22	1030
Grey Matter	48.91	1.81	1050
Water	78.00	1.59	1000
Mouth cavity/sinuses	1.00	0.00	1.300

Thermal property of different human tissues are listed in Table 7.5 [29],[30], where, K is thermal conductivity of the tissue (W/m.^{o}C), A_0 is the heat source due to metabolic process (J/s.m^3), C_p is specific heat of the tissue (J/kg.^{o}C) and b is a constant associated with blood flow (W/m^3.^{o}C).

Table 7.5: Thermal Properties of Human tissue

Tissue Type	C_p [J/kg.°C]	K [W/m.°C]	b [W/m³.°C]	A_0 [J/s.m³]
Skin	3500	0.50	8652	1000
Bone	1300	0.30	1401	0
Muscle	3500	0.60	3488	690
Fat	2300	0.50	816	180
Blood	3900	0.49	0	0
White Matter	3500	0.60	37822	10000
Grey Matter	3500	0.60	37822	10000
Water	4184	0.6	0	0
Mouth cavity/sinuses	1000	0.02	0	0

7.4.1.4 Thermo-EM modelling for deep RF Ablation Treatment

7.4.1.4.1 EM modelling of RF probe

A customized coaxial RF thermal probe as shown in Figure 7.14 has been used for this study [31]. Core of the coaxial RF thermal probe consists of a movable stainless steel needle with diameter and length of 1.0 mm × 20 mm. The needle is enclosed by a coaxial hollow cylinder which is 15.0 mm long and 2.5 mm in diameter. Both the core needle and the hollow cylinder are insulated, except for the portion of the tip that makes contact with tissue. During thermal ablation, the insulation prevents normal tissue from being destroyed along with pathological tissue. Epoxy-resin has been used as the insulation. The length of the tip of the needle is adjustable.

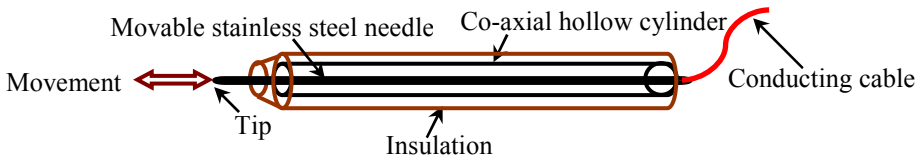

Figure 7.14. Customized coaxial RF thermal probe.

7.4.1.4.2 EM modelling of voxel-based computational RFA models consists of brain and RF probe

Voxel-based computational RFA model is constructed by introducing the RF probe in the Melanix brain model. For simplicity skull bones are discarded. The length of the tip of the RF probe, angle of the probe have been varied to carry out all parametric studies. 3-D geometry of the simulation model used for RFA of brain is shown in Figure 7.15. Finally, this voxel-based RFA computational model is imported in commercially available EM software CST Microwave Studio® which is also capable of EM-thermal simulation.

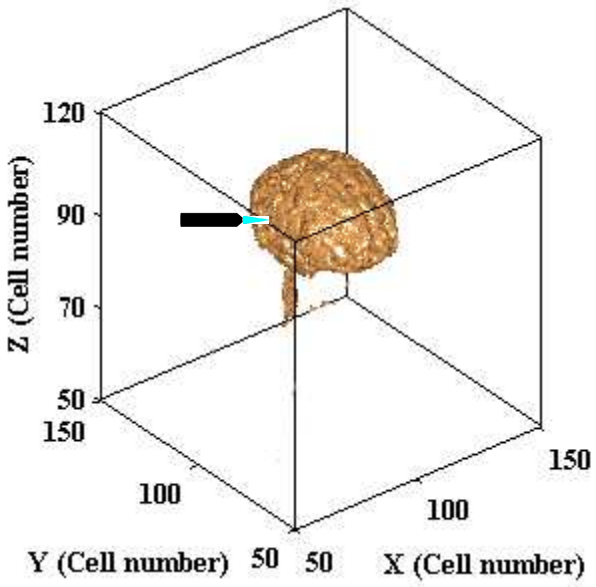

Figure 7.15. Voxel-based computational RFA model consists of brain of the subject Melanix and RF probe.

7.4.1.5 EM-Thermal simulation of RFA model

In this study, EM-thermal simulations have been carried out using commercially available CST Microwave Studio® software. This EM tool is also capable of finding SAR and thermal simulations and can consider BHE for calculating heat generation in biological tissue due to SAR, metabolic processes and heat flow by perfusion of blood [29]. It is related to SAR by the BHE and discussed in section 5.2.1.

7.4.2 Parametric studies for RFA planning

EM-thermal simulations have been carried out using commercially available CST Microwave Studio® software to study the effects of frequency, RF power, depth of probe inside brain tissue and angle of probe with brain surface. All these parameters hold important

role in obtaining optimum thermal rise for ablation treatment. To ablate tumour effectively and avoid carbonization around the tip of the electrode due to excessive heating, the tissue temperature should be maintained in the ideal range of 50^{o}C-100^{o}C to induce necrosis (tissue death) [28]. Therefore, the main objective of RFA therapy is to reach and maintain a temperature range of 50^{o}C – 100^{o}C throughout the entire target volume for at least 4-6 minutes [31]. In this study, during RFA therapy only the steady-state temperature of the brain tissue for different power settings at the coaxial RF thermal probe has been considered.

7.4.2.1 Effect of variation of frequencies

Variations of steady-state temperature with different operating frequencies for 25.0 W input power level are shown in the Figure 7.16 (a-h). For all cases RF probe tip length of 2.0 mm is considered which is inserted into the brain tissue. It is observed that maximum steady-state temperature is found to be in the region of the brain which is closed to the tip of the probe and gradually decreases as the distance from the tip increases. At steady-state, 56.0^{o}C, 64.3^{o}C, 68.5^{o}C, 73.7^{o}C, 80.2^{o}C, 80.6^{o}C, 81.7^{o}C and 82.0^{o}C temperatures are observed for 500 MHz, 1.0 GHz, 1.5 GHz, 2.0 GHz, 2.45 GHz, 2.5 GHz, 2.75GHz and 3.0 GHz, respectively. Thus, maximum steady-state temperature rises with frequency for constant applied power, probe position and probe angle which is possibly due to higher RF current concentration near the probe needle and smaller depth of penetration at higher frequencies. It can also be concluded here that RFA with higher frequencies are more useful for smaller areas.

Variations of maximum value of steady-state temperature with different input power level for 2.45 GHz frequency are shown in Figure 7.17. For all cases RF probe tip length of 2.0 mm is considered which is inserted into the brain tissue. From the figure it is seen that at steady-state temperature of 102.0^{o}C, 100.0^{o}C, 97.3^{o}C, 88.7^{o}C, 80.1^{o}C, 71.4^{o}C, 66.7^{o}C, 56.6^{o}C, 51.6^{o}C, 46.6^{o}C and 41.5^{o}C are observed for 38.0 W, 36.5 W, 35.0 W, 30.0 W, 25.0 W, 20.0 W, 15.0 W, 10.0 W, 7.5W, 5.0 W and 2.5 W input power levels, respectively. It is seen that 7.5 W to 36.5 W input power levels are found suitable for RFA of human brain, in order to keep the temperature within the ideal ablation temperature range of 50^{o}C - 100^{o}C.

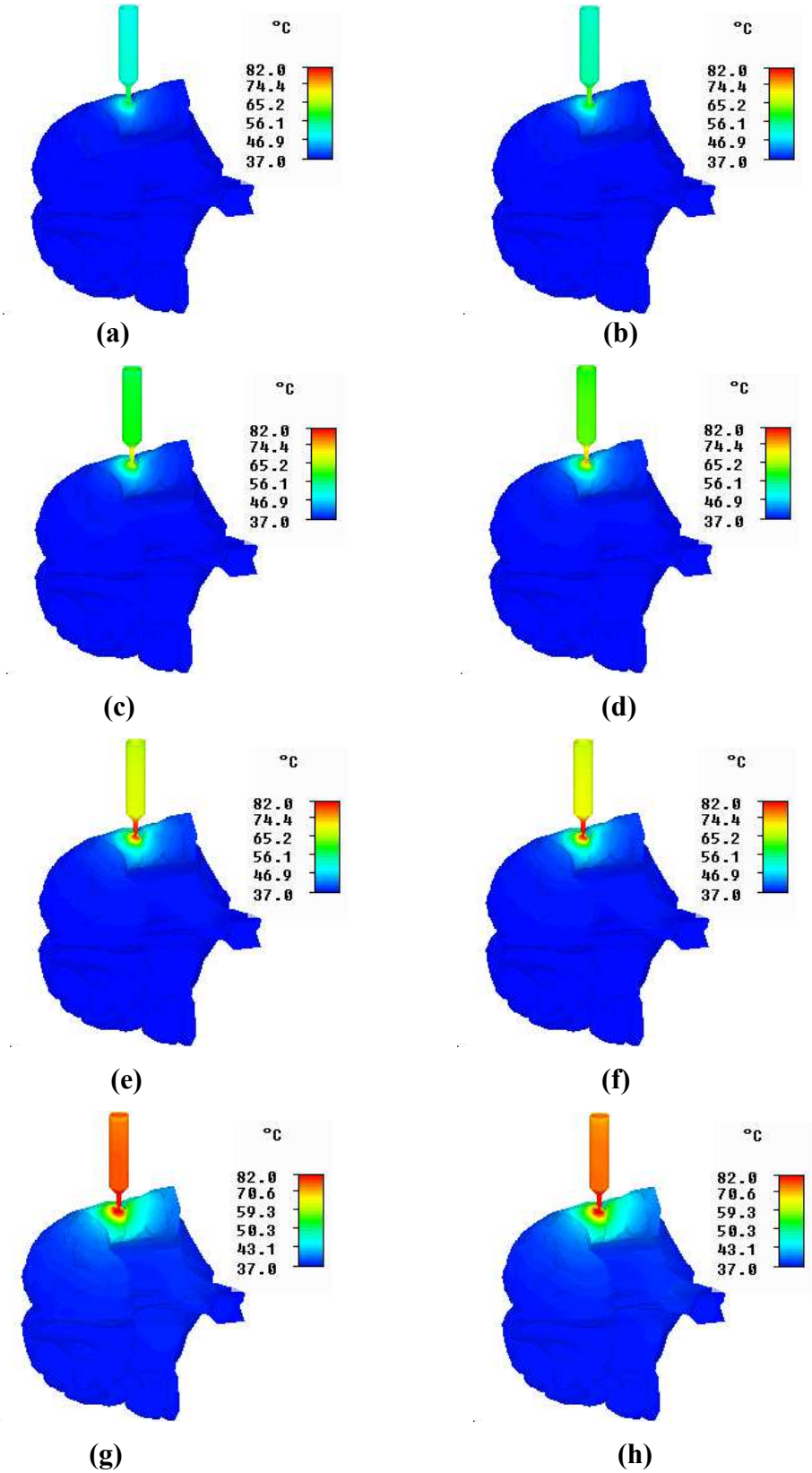

Figure 7.16. Steady-state temperature distribution at (a) 500 MHz, (b) 1.0 GHz, (c) 1.5 GHz, (d) 2.0 GHz, (e) 2.45 GHz, (f) 2.5 GHz, (g) 2.75GHz and (h) 3.0 GHz for 25.0 W input power.

7.4.2.2 Effect of variation of RF power

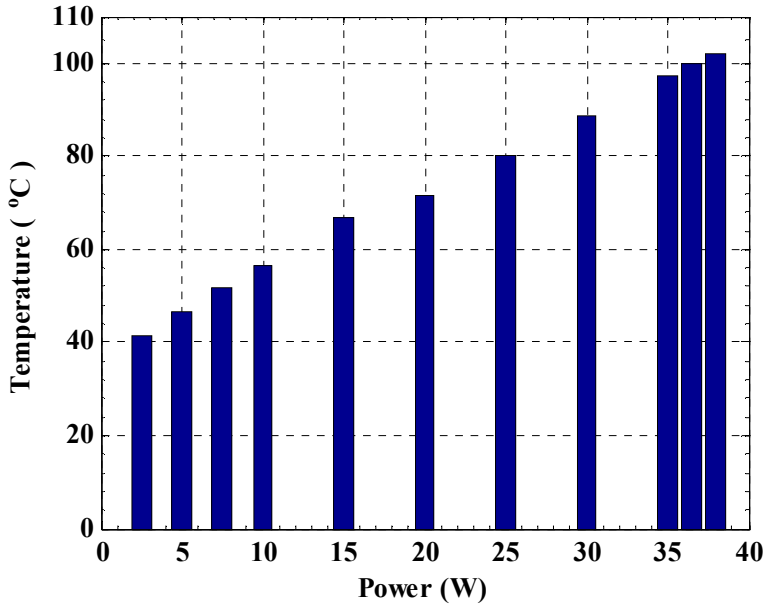

Figure 7.17. Maximum value of steady-state temperature vs. input power at RF probe for 2.0 mm tip length inserted into the brain.

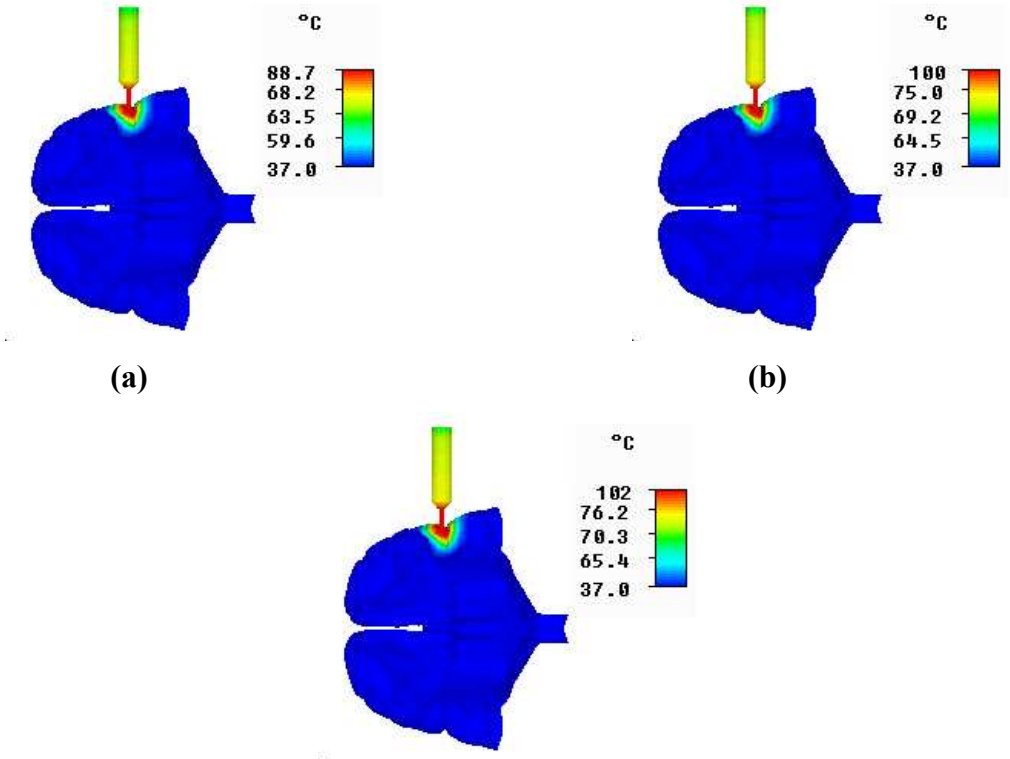

Figure 7.18. Steady-state temperature distribution for 2.0 mm tip length inserted into the brain and input power setting of (a) 30.0 W, (b) 36.5 W and (c) 38.0 W at 2.45 GHz.

Variations of steady-state temperatures inside human brain for 30.0 W, 36.5 W and 38.0 W input power levels are shown in Figure 7.18 (a-c). It is found that with the decrease of input power, peak value of steady-state temperature decreases but the characteristics of the temperature distribution remain almost the same. It can be observed here that for higher input power the RFA takes place over larger area. However, for quick ablation higher input power level is suggested.

7.4.2.3 Effect of variation of probe Angular position

Variations of steady-state temperatures with different probe angular position with respect to brain surface for input power level of 25.0W and 2.45 GHz frequency are shown in Figure 7.19. For all cases RF probe tip length of 2.0 mm is considered which is inserted into the brain tissue. From figure it is seen that at steady-state temperature of 80.2^{o}C, 84.6^{o}C and 88.3^{o}C are observed for 0^{o}, 45^{o} and 90^{o} angular position of the probe. From the Figure 7.19, it is seen that peak value of steady-state temperature is obtained for 90^{o} angular position. It can be concluded that the probe be placed tangentially with respect to the brain surface to achieve higher temperature.

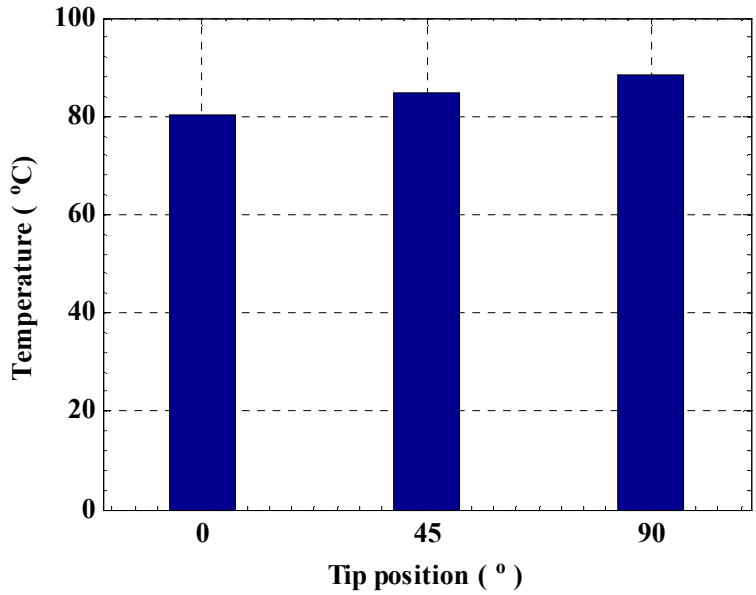

Figure 7.19. Maximum value of steady-state temperature vs. tip position for 25.0 W input power setting at the RF probe.

Variations of steady-state temperatures are shown for 0^{o}, 45^{o} and 90^{o} angular position in Figures 7.20 (a-c). During RFA, depending upon on the situation the angular position is varied to obtain different temperature.

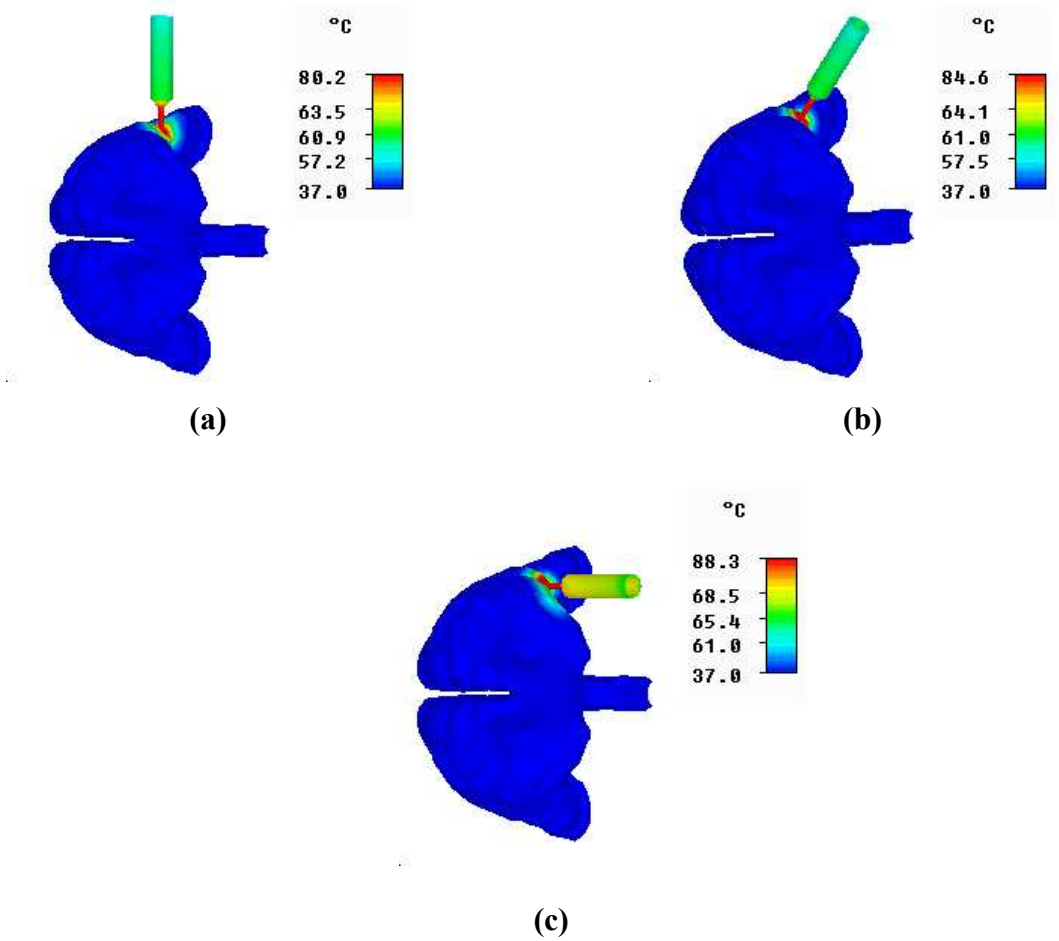

Figure 7.20. Steady-state temperature distribution for 2.0 mm tip length inserted into the brain and 25.0 W input power setting at (a) 0^o, (b) 45^o and (d) 90^o angular position at 2.45 GHz.

7.4.2.4 Effect of variation of probe Length

Variations of steady-state temperatures with different tip lengths inserted into the brain for input power level of 25.0W and 2.45 GHz frequency are shown in Figure 7.21. From Figure 7.21, it is seen that with increase of insertion depth, RF power is distributed over more tissue area resulting in lowering of temperature value. From the Figure 7.21, it is seen that for insertion depth between 6.0 mm to 1.25 mm into the brain is suitable for ideal RFA of human brain, in order to keep the temperature level within the range of 63^oC – 100^oC.

Variations of steady-state temperatures inside human brain for 0.5 mm, 2.0 mm and 3.0 mm tip length inserted into brain are shown in Figures 7.22 (a-c). It is found that with the decrease of tip length inserted into brain, peak value of steady-state temperature increases and the area over which RFA takes place also decreases. Therefore, it is suggested that initially

RFA should be started with minimum insertion depth then according to the requirement tip insertion into the brain be increased.

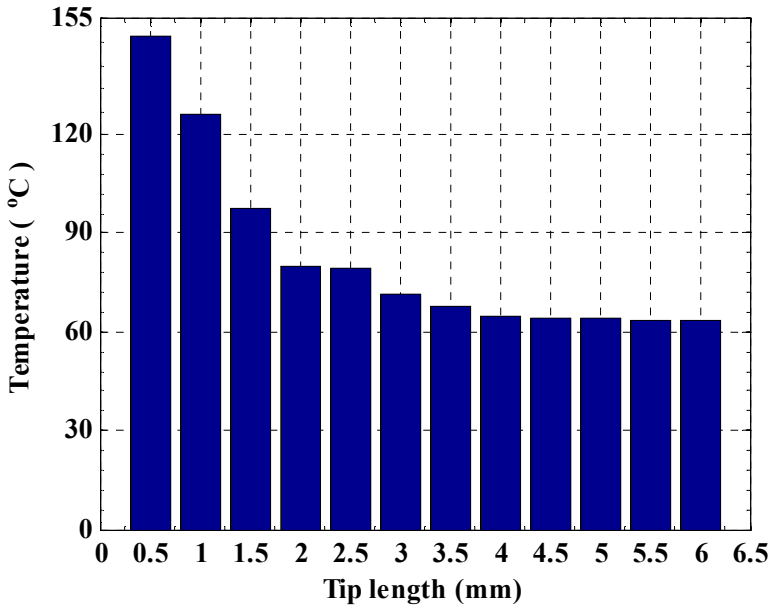

Figure 7.21. Maximum value of steady-state temperature vs. tip length inserted into the brain with 25.0 W input power at the RF probe.

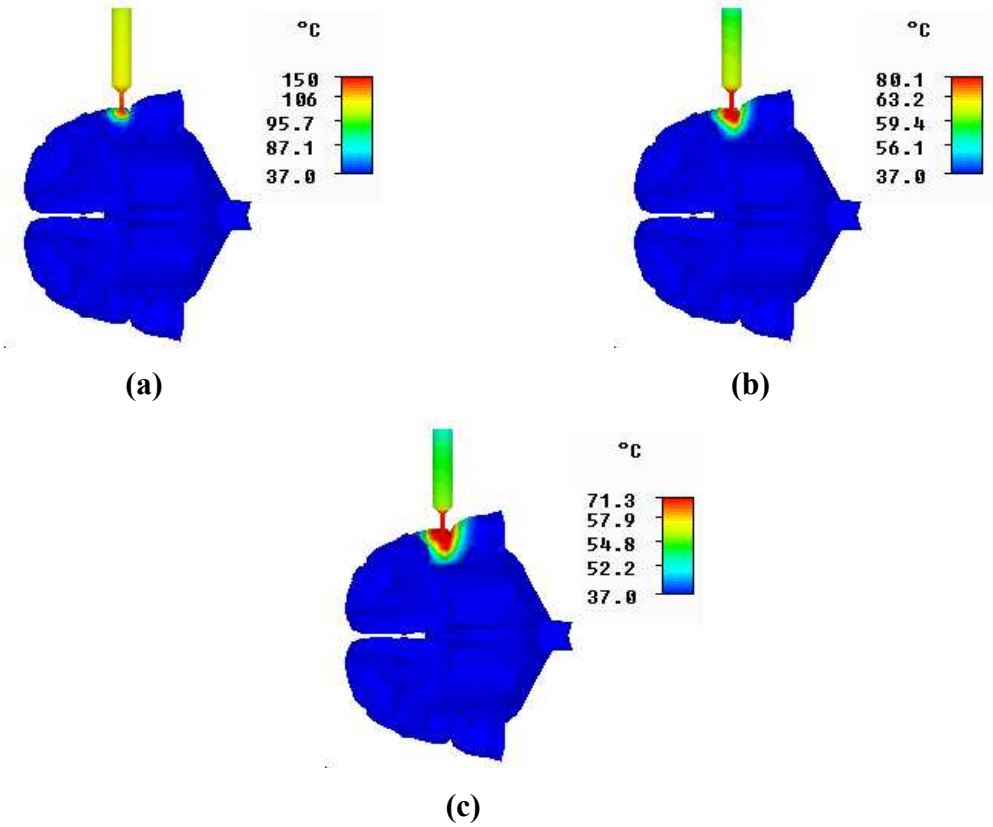

Figure 7.22. Steady-state temperature distribution for 25.0 W input power with the tip length inserted into the brain (a) 0.5 mm, (b) 2.0 mm and (d) 3.0 mm at 2.45 GHz.

7.5 Conclusions

Some typical useful applications of EM waves at microwave frequencies have been carried out in this chapter. FDTD based in-house numerical code has been developed by commercially available MATLAB software to determine the usefulness of EM wave for detection and selective destruction of bacteria colony at THz frequencies. For this purpose, a realistic 3-D electrical model of various type bacteria colony has been developed and placed between a pair of dipole antennas resonating at THz frequency range. EM energy absorption characteristic of different types of bacteria colony has been expressed in terms of variations of S_{21} with frequency. Multiple dips are observed for all types of bacteria cells in the S_{21} plots at electrical resonance frequencies for every individual cell or their numerical and structural combinations in their colony.

FIT based commercially available software CST Microwave Studio® has been used for detection and identification of caries in a human tooth model at GHz frequencies. To carry out the investigation, a realistic 3-D electrical model of human tooth has been developed and placed between a pair of dipole antennas resonating at GHz frequency range. Like bacteria colony, variation of energy absorbing band for normal and affected tooth has been analysed in terms of S_{21} with frequency. It has been found that for the normal tooth peak value of S_{21} is higher compared to the affected tooth and for different carries material peak value of S_{21} is different.

At the end of this chapter, possibility of pre-treatment offline RFA planning has been investigated to reduce accidental destruction of healthy tissues. For this purpose, Voxel-based computational RFA model is constructed by introducing the RF probe in the Melanix brain model. During RFA therapy, steady state temperature variations of the brain tissue for different operating frequency, power input at the coaxial RF thermal probe, tip length inserted into brain and angular position of the probe with respect to the brain surface have been obtained. From steady state temperature distributions inside the brain, it is found that maximum value of steady-state temperature is obtained in the region of the brain which is closed to the tip of the probe and gradually decreases as the distance from the tip increases. It has been found that at 2.45 GHz frequency for tip length of 2.0 mm and 90^{o} angular position 7.5–36.5 W input power levels are suitable for RFA of human brain, in order to keep the temperature within the ideal ablation temperature range of 50–100^{o}C. At the same operating frequency for input power level of 25.0 W, it has also been found that for insertion depth

between 6.0 mm and 1.25 mm into the brain is suitable for ideal RFA of human brain, in order to keep the temperature level within the range of 63–100^{o}C.

References

[1] Matlab 7.8, The MathWorks, Inc. http://www.mathworks.com.

[2] K. Asami, T. Hanai and N. Koizumi, "Dielectric analysis of Escherichia Coli Suspensions in the light of the theory of interfacial polarization," *BIOPHYS*. J. E. Biophysical Society, vol. 31, pp. 215-228, August 1980.

[3] H. Fricke, "A mathematical treatment of the electric conductivity and capacity of disperse systems-I. The electric conductivity of suspension of homogeneous spheroids," *Physic. Rev*., vol. 24, pp. 575-587, 1924.

[4] H. Fricke, "A mathematical treatment of the electric conductivity and capacity of disperse systems-II. The capacity of a suspension of conducting spheroids surrounded by a non-conducting membrane for a current of low frequency," *Physic. Rev*., vol. 26, pp. 678-681, 1925.

[5] T. Hanai, N. Koizumi and A. Irimajiri, "A method for determining the dielectric constant and the conductivity of membrane-bounded particles of biological relevance," *Biophys. Struct. Mech*., vol. 1, pp. 285-294, 1975.

[6] J.C. Maxwell, "A treatise on Electricity and Magnetism," 3rd Edition. vol. 1, Ch. IX. Clarendon Press, pp. 435, Oxford, 1891.

[7] L.M. Prescott, J.P. Harley and D.A. Klein, "Microbiology," 3rd Edition. Wm. C. Brown Publishers, Dubuque, IA, pp. 37-41, 1996.

[8] Functional Anatomy of Prokaryotic and Eukaryotic Cells. http://www.classes.midlandstech.edu/carterp/courses/bio225/chap04/lecture2.htm

[9] Spirillum, From MicrobeWiki, the student-edited microbiology resource. http://microbewiki.kenyon.edu/index.php/Spirillum.

[10] V.S. Santos, M.C. Villac, D.R. Tenenbauml and R. Paranhos, "Auto-and Heterotrophic Nanoplankton and Filamentous Bacteria of Guanabara Bay (RJ, Brazil): Estimates of Cell/Filament Numbers versus Carbon Content," *Brazilian Journal of Oceanography*, vol. 55, No. 2, pp. 133-143, 2007.

[11] C. Bot, C. Prodan, "Quantifying the membrane potential during E. coli growth stages," *Biophysical chemistry*, vol. 146, pp. 133-137, 2010.

[12] W. Bai, K.S. Zhao and K. Asami, "Dielectric properties of E. coli cell as simulated by the threeshell spheroidal model," *Biophysical Chemistry*, vol. 122, pp. 136-142, 2006.

[13] C.M. Mihai, M. Mehedintu and E. Gheorghiu, "The derivation of cellular properties from dielectric spectroscopy data," Bioelectrochemistry and Bioenergetics, vol. 40, pp. 187-192, 1996.

[14] H.S. Langdon and R. Luebbers, "Efficient FDTD calculation of Multi-ports S Parameters for Microstrip and Stripline Circuits," *IEEE Trans. Microwave Theory Tech.*, vol. MTT – 50, No.9, pp. 998-1001, 1997.

[15] CST Microwave Studio Suite 2010, [home] http://www.cst.com.

[16] Tooth Model. Home page http://www.archibase.net.

[17] Dielectric Properties of the Human Body tissue in the Frequency Range of 10 Hz-100GHz. http://niremf.iroe.fi.cnr.it/tissprop.

[18] H.L. Fisher and W.S. Snyder, "Annual progress report for period ending July 31 1966," *Health Physics Division*, Oak Ridge National Laboratory, Oak Ridge TN, USA, 1966.

[19] J.M.L. Hwang, R.L. Shoup and J.W. Poston, "Mathematical description of a one- and five-year-old child for use in dosimetry calculations," Oak Ridge National Laboratory, Oak Ridge TN, USA, 1976.

[20] W.L. Chen, J.W. Poston and G.G. Warner, "An evaluation of the distribution of absorbed dose in child phantoms exposed to diagnostic medical X rays," Oak Ridge National Laboratory, Oak Ridge TN, USA, 1978.

[21] T. Wena, Q. Zhu, W. Qin, L. Li, F. Yang, Y. Xie and J. Gu, "An accurate and effective FMM-based approach for freehand 3D ultrasound reconstruction," *Biomedical Signal Processing and Control-ELSEVIER*, vol. 8, No. 6, pp. 645–656, November 2013.

[22] DICOM files, http:// http://www.osirix-viewer.com/datasets/.

[23] Rumen Rusev, "A Module for Visualisation and Analysis of Digital Images in DICOM File Format," International Conference on Computer Systems and Technologies-CompSysTech'2003.

[24] D.C. Dias Medora and N.E. Prashant, "Morphometric Study of the Ventricular System of Brain by Computerized Tomography," *Journal of the Anatomical Society of India*, vol. 56, No. 1 (2007-01 - 2007-06).

[25] Converting CT Data to Hounsfield Units, Fanning Consulting Services, http://www.idlcoyote.com/fileio_tips/hounsfield.html.

[26] Odelberg W: Godfred N. Hounsfield-Autobiography. The Nobel Prizes, The Noble Foundation, 1979.

[27] F. Terrier, M. Grossholz and C.D. Becker, "Spiral CT of the Abdomen," *Medical Radiology*, *Springer*, 1999.

[28] A. Timothy, Okhai and C.J. Smith, "Principles and Application of RF system for Hyperthermia Therapy," *INTECH*, Chapter: 6, pp. 171-184. [Online] http://www.intechopen.com/download/pdf/44708.

[29] J. Wang and O. Fujiwara, "FDTD computation of temperature rise in the human head for portable telephones," *IEEE Trans. Microwave Theory Tech*., vol. 47, pp. 1528-1534, 1999.

[30] A. Hirata and T. Shiozawa, "Correlation of maximum temperature increase and peak SAR in the human head due to handset antennas," *IEEE Trans. Microwave Theory Tech.*, vol. 51, pp. 1834-1841, 2003.

[31] H. Rhim, S.N. Goldberg, G.D. Dodd, L. Solbiati, K.L. Lim, M. Tonolini and O.N. Cho, "Helping the hepatic surgeon: Essential techniques for successful radio-frequency thermal ablation of malignant hepatic tumours," *Radiographics*, vol. 21, pp. S17-S35, 2001.

Chapter 8

Conclusions and Future Work

8.1 Introduction

This chapter consists summary and brief conclusions of this thesis. Scope for practical use of some observations and further investigations are also suggested.

8.2 Summary

In this thesis, interaction between the EM waves radiated from wireless communication devices and BSAs with human body has been studied to asses EM power absorption in brain and body tissues in terms of different electrical parameters, thermal parameters and SAR. Different types of electrical and thermal changes due to the interaction between the non-ionizing EM waves on human beings and environment have been included considering various tissues models. Theoretical investigations have been carried out using full wave EM simulation techniques to observe different induced energy parameters inside cells or tissue. Numerical methods like MoM, FDTD and FIT based computational tools played important role for all theoretical investigations are also included in this report. For this research work, several in-house computer programs have been developed to carry out many theoretical investigations. To solve the large-scale problems FDTD based SFDTD and hybrid method consisting of Friis transmission equation and FDTD are used. Commercially available EM softwares like Zeland IE3D, Fidelity, MDSpice and CST Microwave Studio® are also used extensively for various studies and for validation of in-house developed tools. For theoretical analysis electrical models of living being also play very crucial roles. CAD models of different handsets consists of suitable antennas are considered in different realistic observations. Homogeneous box type, three layered spherical type, MRI based heterogeneous, and DICOM data based voxel type human head models are used in various simulations.

MLSAR induced in the homogeneous box type human head model has been obtained in the frequency range of 500 MHz to 5 GHz for a set of distances in the range of 1.0 cm to 3.0 cm due to a half-wave dipole antenna having length of 15.5 cm and diameter of 0.5 cm. The results show that when the distance is less than or equal to 1.0 cm then the MLSAR becomes more than the FCC and IEEE's upper safety limit. MLSARs induced inside the three layered inhomogeneous human head model consisting of brain, skull and skin respectively at the frequency range 500 MHz to 3 GHz for a set of distances in the range of 1.0 cm to 3.0 cm are found to be in the range of 1.8 W/kg to 0.15 W/kg.

A half-wave radiating dipole antenna having length of 14.5 cm and width of 0.4 cm has been used to evaluate SAR inside the Zubal head model. The head is assumed to be comprised of twenty two types of tissues. MLSAR vs. distance measured from the end of antenna side shows that when the gap between the head and antenna is equal to 0.4 cm then the value of MLSAR is 1.96 W/kg. Value of MLSAR increases towards the direction of antenna side and decreases significantly away from the antenna side due to smaller penetration of EM waves through the head model. Variation of maximum local electric field, magnetic field, induced current and power density with distance measured from the end of antenna for a gap of 4.0 mm has been calculated. Observed value of maximum local electric field, magnetic field, induced current and power density are 40.64 V/m, 0.121 A/m, 2.674 mA and 2.197 mW/cm^2, respectively. The values of maximum local electric field, magnetic field and absorbed power density obtained by the calculation are found to be below to their corresponding ICNIRP recommended upper safety limits.

Peak 10-g and 1-g SAR induced in the DICOM data based human head model including and excluding hand due to a radiating mobile phone has been simulated for 800 MHz to 1.1 GHz frequency band. The head model is assumed to be consisted of only eleven types of tissues whereas, the hand model is assumed to be consisted of three types of tissues. Variation of peak 10-g and 1-g SAR with frequency for the DICOM data based head model without hand agrees with that obtained from Zubal head model based simulation results. It has been found that for all resolutions, peak SAR value initially increases with increase of frequency and attains to a maximum value near the antenna resonance frequency then decreases with further increase of frequency for both cases. The maximum values of peak 10-g and 1-g SARs induced in the DICOM data based head model excluding hand are found to be 0.30 W/kg and 1.01 W/kg, whereas that for the Zubal head model are found to be 0.37 W/kg and 0.78 W/kg, respectively. The SAR values obtained for DICOM data based model

are close to that obtained using Zubal model but hold different values due to the difference in the size, shape, internal structure and types of tissues considered during construction of these two head models. Maximum value of peak 1-g and 10-g SARs for different type of tissues at 930 MHz has been obtained and it is seen that maximum peak 1-g and 10-g SARs obtained in skin are 1.3238 W/kg and 0.3882 W/kg respectively. The minimum peak 1-g and 10-g SARs obtained in CSF are 0.0084 W/kg and 0.0014 W/kg, respectively. Mouth or sinuses cavities are filled with air and therefore no SAR is induced in it. Variation of peak 10-g, 1-g and 0.1-g SAR with distance measured along saggital plane and coronal plane shows that in saggital plane, peak SAR value attains to maxima near the position of the antenna and decreases rapidly with either increase or decrease of distance. But in coronal plane for all resolutions, peak SAR value attains to maxima in the position close to the antenna and decreases rapidly with increase of distance. The maximum value of peak 10-g, 1-g and 0.1-g SARs obtained in the saggital plane are 0.53 W/kg, 2.26 W/kg and 3.53 W/kg and that obtained in the coronal plane are 0.74 W/kg, 2.11 W/kg and 3.18 W/kg, respectively.

Variations of peak 10-g, 1-g and 0.1-g SARs with frequency in the range of 700 MHz to 1.3 GHz have been observed for Zubal head model and the results show that for all resolutions, peak SAR value initially increases with increase of frequency and attains to maximum near the antenna resonance frequency then decreases with further increase of frequency. At the antenna resonance frequency, maximum power is transmitted from the antenna to head model due to good impedance matching. The maximum value of peak 10-g, 1-g and 0.1-g SARs induced in the head are found to be 1.07 W/kg, 2.45 W/kg and 3.75 W/kg, respectively. These result shows that the absorbed power at the frequency band of study is not uniform throughout the 10-g or 1-g mass of the head tissues. The absorbed power at any frequency within the band of study is concentrated to smaller mass in the form of node or hot spot.

SAR induced inside a three layered spherical human head model exposed to a 100 W mobile BSA at GSM 900 band has been investigated using FDTD method hybridized with Friis transmission equation in order to find out the safety distance of head from the mobile BSA and compared that with SFDTD method. Variation of MLSAR with the distance in the range of 0.5 m to 5.0 m between head and the mobile BSA obtained by hybrid FDTD and SFDTD methods at 925 MHz shows that value of MLSAR is in the range of 4.65 W/kg to 0.05 W/kg for hybrid FDTD method and 4.22 W/kg to 0.05 W/kg for SFDTD method. When the distance is less than 1.0 m then MLSAR is above FCC and IEEE's upper safety limit.

Variation of maximum local 1-g SAR with frequency in the range of 650 MHz to 1.35 GHz has also been obtained by SFDTD and hybrid FDTD methods. For both methods, maximum local 1-g SAR initially increases with increase of frequency and attains to maximum near the antenna resonance frequency of 930 MHz then decreases with further increase of frequency. The peak value of maximum local 1-g SAR induced in the head obtained using SFDTD and hybrid FDTD methods are found to be 1.60 W/kg and 1.59 W/kg, respectively.

SAR_{WB} induced within the full human body model exposed to a BSA at GSM 900 band for a distance in the range of 0.5 m to 5.0 m between the human body and the BSA has been calculated using hybrid FDTD method and compared that with the results obtained by SFDTD method for multiple number of carrier frequencies. It is found that SAR_{WB} obtained by hybrid FDTD method closely agrees with that obtained by the SFDTD method. Either due to increase of the distance or decrease the number of carrier frequencies, SAR_{WB} decreases. For five carriers and distance of 0.5 m, maximum value of SAR_{WB} obtained by both hybrid FDTD and SFDTD methods is found to be 0.69 W/kg which exceeds the occupational exposure safety limit. But for the distance more than 1.5 m, value of SAR_{WB} goes below the general public exposure safety limit. To solve large scale problems, both the hybrid FDTD and SFDTD methods are used in this study to reduce the computational requirements and enhances the practicability of running the simulation on a PC. This study shows that hybrid FDTD method is faster and uses less memory compare to SFDTD method.

Maximum local temperature rise due to EM waves radiated from a mobile phone antenna and hotspots created due to standing wave antinodes inside head cavity have been investigated at the GSM 900 band frequency of 930 MHz. Temperature rise inside head tissues are obtained after calculating the SAR in the human head model using FDTD method and then substituting the SAR values into Pennes' BHE for the antenna input power of 0.6 W. It is found that the rise of temperature inside the head cavity is not uniform in nature and concentrated significantly at some spots with different threshold temperatures. These hotspots are created due to standing wave antinodes formed inside the head cavity. It is also observed that the hotspots with higher threshold value of temperature rise are fewer in number than those with lower threshold values and are concentrated closer to the mobile phone. Hotspots with lower threshold value of temperature rise are many in numbers and are also present in different regions away from the mobile phone. Density of hotspots increases with decrease of threshold values of temperature rise and vice-versa. Short-term maximum local temperature rise at frequency 930 MHz shows that initially maximum local temperature rise inside the

human head increases non-linearly with time and then attains to steady state value. The maximum local temperature rise increases rapidly over the first 15-20 sec, then slows down and the steady state is achieved after approximately 55 sec exposure. At the thermal steady state condition, peak value of maximum local temperature rise is 0.122^{o}C.

Quasi optical effects inside a pregnant woman abdomen due to EM waves with microwave frequencies has been analysed using CST Microwave Studio®. The pregnant woman model has been constructed considering a 25 year old female with 65 kg weight and 5′4″ height. For simplification, other parts of the pregnant woman body except the full abdomen are excluded in the simulation and the pregnant woman abdomen model is assumed to be comprised of only water. From the result of image analysis it is found that the pregnant woman abdomen model behaves like a plano-convex lens at the microwave frequencies.

To examine possibility of induced current through ionic fluid in blood vessels inside human body, some experiments have been carried out using rectenna based sensors. For this purpose different types of rectenna based sensors have been designed where the output DC power of rectenna is connected to a low power LED for visual indication of received EM field for GSM 900 band. Since, significant part of human body is consisting of water; induced current in a conductor loop antenna inside a cup of water is observed. In another case an egg which can in fact represent an animal cell is considered for similar experiment. When a rectenna based sensor is placed inside a cup of water, LED connected with it glows brightly when a phone in operating mode is kept in close proximity. In similar way wnen the rectenna based sensor is placed inside an egg the LED connected with the rectenna based sensor glows brightly when the phone is in operating mode. In these experiments the induced ac current has been converted to dc first for lighting up the LED but in reality when living cells or tissues are exposed to the radiated EM field at RF, some part of it can initiate chemical changes inside body due to the flow of induced ac current. It is true that a copper wire loop antenna can not actually represent an ionic fluid antenna but possibility of conduction through ionic fluids inside blood vessels can not be ignored.

Investigation has been carried out on the interaction between the EM wave radiated from a BSA and green plants. EM wave absorptions inside a Bonsai tree and Money plant have been investigated. The prediction of the EM wave absorption based on evaluating maximum local electric field, magnetic field, 1-g SAR and SE have been calculated for a Bonsai tree by hybridizing Friis transmission equation with FDTD method. Various parameters have been studied inside the realistic 3D CT scan based Bonsai tree model at

GSM 900 band for 5 m distance between BSA and the tree. SAR induced inside a Money plant and SE provided by the Money plant have been calculated as well as measured experimentally by means of a handheld RF power meter. It was observed that green plants can be used as good EM shield.

Investigation has been carried out on the effects of non-ionizing EM radiation on pollen grains. The phase value distributions of electric field and magnetic field at the different planes have been obtained. Two high concentric spots of 180 degree phase difference between these two electric fields are observed inside the pollen grains. These two points represent the electric field image of the source of the dipole antenna. It has also been observed that a single high concentric spot is formed inside the pollen grains due to magnetic field image of the source dipole antenna.

Theoretical investigation has been carried for the detection and selective destruction of bacteria colony at THz frequencies. Simulated results show that significant EM energy absorption occurs in the bacteria cell at THz frequencies near their electrical resonance frequencies for which a number of dips are appeared in the S_{21} plots. It is also observed that the frequency band of EM energy absorption shifts toward lower frequency for bacteria of higher size and vice-versa. The number of dips increases with the increase of bacteria cell density in the colony. This analysis shows that the THz frequencies can be used to detect the presence of bacteria, their type and concentration in the colony.

Numerical investigation has been carried out to determine the usefulness of EM wave for detection and identification of caries in a human tooth model at GHz frequencies. It has been found that due to the absorption of EM energy in the normal and abnormal teeth, different peaks are appeared in the S_{21} plots. It is also observed that for variation of carries material peak value of S_{21} varies. This analysis shows that the GHz frequencies can be used to detect the presence of carries and their composition material but it is unable to give any idea about the position and size of the dental carries.

Possibility of pre-treatment offline RFA planning has also been investigated which may reduce accidental destruction of healthy tissues. Steady state temperature variations in human brain due to different electrical and physical changes have been studied considering different thermal ablation treatment requirements using RF probe. Effect of variations of input power levels, probe length inserted into brain and probe angular position with respect to brain surface on the steady-state temperature have been studied for a fixed operating frequency. It

has been found that maximum value of steady-state temperature inside the brain is obtained in the region of the brain which is closed to the tip of the probe and gradually decreases as the distance from the tip increases. From the study, it has also been found that at 2.45 GHz frequency for tip length of 2.0 mm and 90^{o} angular position, 7.5–36.5 W input power levels are suitable for RFA of human brain, in order to keep the temperature within the ideal ablation temperature range of 50–100^{o}C. At the same operating frequency for input power level of 25.0 W, it is found that for insertion depth between 6.0 mm and 1.25 mm into the brain is suitable for ideal RFA of human brain, in order to keep the temperature level within the range of 63–100^{o}C.

8.3 Scopes for further investigations

Based on the investigations presented in this thesis, further investigations in the areas of effects of non-ionizing EM radiation on the human body and environment can be proposed. Some of these are:

a. Sufficient number of theoretical investigations on the effects of non-ionizing EM radiation radiating from the wireless communication devices and BSAs on human being and environment have been carried out in this study but further experimental studies are required.
b. Theoretical investigations have been carried out for the detection and selective destruction of bacteria colony at THz frequencies and detection and identification of caries in a human tooth model at GHz frequencies in this study but more study is required for pest control, crop and seed identification using microwave.
c. In order to plan the offline RF thermal ablation, steady state temperature variations in human brain due to different electrical and physical changes have been studied considering different thermal ablation treatment requirements using RF probe. But more study is required to analyse the effect of hypertonic saline solution infused into the tissue during RFA. Investigation on the non contact RFA for obtaining deeper lesions is also expected.
d. The effects of inclusion of micro-shield or a mechanism to divert the direction of link through head to reduce the RF hazards need to be analyzed in order to use the mobile device more safely. The effect of variation of composition of the micro-shields should require to be studied.

e. Study of exclusion zone including EM mapping of different urban as well as rural areas nearby the mobile, radio and TV base stations is expected.

8.4 Conclusions

Throughout this research work, the interaction between the EM waves radiated from wireless communication devices with human body and environment has been evaluated for bioelectromagnetic studies to calculate different induced energy parameters. Numerical dosimetry has been conducted extensively using in-house computer-generated programs to assess the induced energy parameters within the exposed human body parts or green plants considering various tissue models. For this purpose, electrical models like homogeneous box type, three layered spherical type, MRI based heterogeneous, and DICOM data based voxel type human head models along with CAD models of different handsets consists of suitable antennas and BSAs have been developed and used. Commercially available EM softwares like Zeland IE3D, Fidelity, MDSpice, CST Microwave Studio® and improved numerical methods based on FDTD have been used for various bioelectromagnetic studies. The accuracy and validation of the in-house developed tools have been verified through a variety of tests and comparisons against some available physical measurements. Apart from the dosimetry calculations, various types of helpful investigations for human beings have also been carried out on RF applications like airborne bacteria treatment process, detection and identification of dental caries and RFA technique. At the end of this thesis a few no. of future investigations have been suggested.

8.5 List of Publications

This thesis is based on the work presented in the following twenty one papers:

8.5.1 Journal Papers

i. **Md.Faruk Ali** and Sudhabindu Ray, “SAR Analysis in a Spherical Inhomogeneous Human Head Model Exposed to Radiating Dipole Antenna for 500 MHz –3 GHz Using FDTD method”, *International Journal of microwave and Optical Technology*, vol. 4. No.1, pp. 35-40, January -2009. ISSN: 1553-0396.

ii. **Md. Faruk Ali** and Sudhabindu Ray, "SAR Analysis for Handheld Mobile Phone Using DICOM Based Voxel Model", *Journal of Microwaves, Optoelectronics and Electromagnetic Applications (JMOe)*, Vol. 12, No. 2, pp. 363-375, December-2013.

iii. **M. F. Ali** and S. Ray, "Quasi Optical Effects of Non-Ionizing Radiation inside Pregnant Woman Abdomen," *Progress In Electromagnetics Research M*, Vol. 35, pp. 31-38, 2014. doi:10.2528/PIERM14010703.

iv. **M. F. Ali** and S. Ray, "Study of EM Wave Absorption and Shielding Characteristics for a Bonsai Tree for GSM-900 Band," *Progress In Electromagnetics Research C*, Vol. 49, pp. 149-157, 2014.

v. **Md. Faruk Ali** and Sudhabindu Ray, "FDTD based SAR analysis in human head using irregular volume averaging techniques of different resolutions at GSM 900 band," *Indian Journal of Radio & Space Physics*, Vol. 43, pp. 235-242, June 2014.

vi. **M. F. Ali** and S. Ray, "Estimation of Whole-body average SAR in Human Body Exposed to a Base Station Antenna," *Progress In Electromagnetics Research* M, Vol. 39, 2014, pp. 19-26, 2014. doi:10.2528/PIERM14080201.

vii. **Md. Faruk Ali** and Sudhabindu Ray, "Offline RF Thermal Ablation Planning Using CT/MRI Scan Data," *Egyptian Journal of Radiology and Nuclear Medicine*, ELSEVIER, Vol. 46, pp. 141-150, 2015.

viii. **Md. Faruk Ali**, S.B.Belamgi and Sudhabindu Ray, "A Study of Specific Absorption Rate and Shielding Effectiveness for Money Plant at 2.4 GHz," *Microwave Review*, Vol. 21, No. 2, pp. 2-6, December 2015..

8.5.2 Conference Papers

ix. **Md.Faruk Ali** and Sudhabindu Ray, "SAR Analysis on Human Head Exposed to Radiating Dipole Antenna for 500 MHz – 5 GHz Frequency Band Using FDTD Method", *National Conference on Communication (NCC),* IIT Bombay*, India,* pp.481-485, 2008.

x. **Md.Faruk Ali** and Sudhabindu Ray, "SAR Distributions in a Spherical Inhomogeneous Human Head Model Exposed to Electromagnetic Field for 500 MHz – 3 GHz Using FDTD method", *National Conference on Communications,* IIT Guwahati, India, pp.64-67, January - 2009.

xi. **Md.Faruk Ali** and Sudhabindu Ray, "SAR Analysis on Child and Adult Head Models for Radiating Dipole Antenna Using FDTD method", *International Symposium on Microwaves and Millimeterwaves : Basics and Technology,* Bose Institute, Kolkata, India, pp.46-48, January - 2009.

xii. **Md.Faruk Ali**, Sujoy Mukherjee and Sudhabindu Ray, "SAR Analysis in Human Head Model Exposed to Mobile Base-Station Antenna for GSM-900 band", *Loughborough Antennas & Propagation Conference,* Loughborough, UK, pp. 289-292, January - 2009, 10.1109/LAPC.2009.5352413.

xiii. **Md.Faruk Ali** and Sudhabindu Ray, "SAR Evaluation in a Tilted Human Head Model in Near-Field of a Half-Wave Dipole Antenna in GSM-900 Band", *International Conference on Control Communication and Computing,* College of Engineering, Thiruvananathapuram, Kerala, India, pp. 316-319, February - 2010.

xiv. **Md.Faruk Ali**, Santanu Mondal and Sudhabindu Ray, "MLSAR Analysis in a Realistic Grounded Human Head Model for a Dipole antenna using FDTD method at 930 MHz", *IEEE CASCOM Post Graduate Student Paper Conference*, Jadavpur University, Kolkata, India, pp. 34-37, November - 2010**.**

xv. **Md. Faruk Ali** and Sudhabindu Ray, "Study of Induced EM Field Parameters Inside a Realistic Human Head Model", *International Conference on Communications Computers and Devices*, IIT Kharagpur, India, Paper ID-82, December - 2010.

xvi. **Md. Faruk Ali** and Sudhabindu Ray, "SAR Analysis in a Realistic Grounded Human Head for Radiating Dipole Antenna", *National Conference on Communications (NCC)*, IISc. Bangalore, India, pp. 211-125, January- 2011. doi: 10.1109/NCC.2011.5734736.

xvii. **Md. Faruk Ali** and Sudhabindu Ray, "SAR Analysis Using DICOM Based Voxel Model", *National Conference on Communications (NCC)*, IIT Kharagpur, India, Paper ID-621, February- 2012. doi: 10.1109/NCC.2012.6176755.

xviii. **Md. Faruk Ali** and Sudhabindu Ray, "Detection and Selective Destruction of Bacteria Colony at THz Frequencies", *National Conference on Communications (NCC)*, IIT Kharagpur, India, Paper ID-417, February-2012. doi: 10.1109/NCC.2012.6176808.

xix. **Md. Faruk Ali** and Sudhabindu Ray, "SAR Analysis Using SFDTD and Hybrid FDTD", *Conference on Computers and Devices for Communication (CODEC)*, Institute of Radio Physics and Electronics, University of Calcutta, India, December-2012.

xx. **Md. Faruk Ali** and Sudhabindu Ray, "Study of Dipole Antenna Characteristic using Different Numerical methods", *International Conference on Communications, Devices and Intelligent Systems (CODIS)*, Department of Electronics and Telecommunication Engineering, Jadavpur University, India, December-2012.

xxi. **Md. Faruk Ali**, Rashmi Ranjan Sahoo and Sudhabindu Ray, "Study of Maximum Local Temperature Rise and Hotspots Distribution in a Human Head for GSM900 Mobile Phone", *International Conference on Eco-friendly Computing and Communication Systems (ICECCS)*, Advances in Energy Aware Computing and Communication System, Tata McGraw Hill, India, pp. 72-78, October-2013, ISBN-13:978-9-35-13432-5.

Chapter 9

Appendices

Appendix 3.A Discretization of Maxwell's equations

In order to implement FDTD code in computer programming, Maxwell's equations in partial differential form (equations 3.5 – 3.10) in Chapter 3 are modified into the corresponding central finite difference equations of space and time derivatives, discretized and solved according to leapfrog manner to obtain the explicit finite difference approximation as [i]-[iii]:

$$E_x^{n+1}\left(i+\frac{1}{2},j,k\right)=\left(1-\frac{\sigma\left(i+\frac{1}{2},j,k\right)\delta t}{\varepsilon\left(i+\frac{1}{2},j,k\right)}\right)\bullet E_x^{n}\left(i+\frac{1}{2},j,k\right)+\frac{\delta t}{\varepsilon\left(i+\frac{1}{2},j,k\right)\delta}$$

$$\left[H_z^{n+\frac{1}{2}}\left(i+\frac{1}{2},j+\frac{1}{2},k\right)-H_z^{n+\frac{1}{2}}\left(i+\frac{1}{2},j-1,k\right)+H_y^{n+\frac{1}{2}}\left(i+\frac{1}{2},j,k-\frac{1}{2}\right)-H_z^{n+\frac{1}{2}}\left(\begin{matrix}i+\frac{1}{2},\\ j,k+\frac{1}{2}\end{matrix}\right)\right]$$

(3A.1)

$$E_y^{n+1}\left(i,j+\frac{1}{2},k\right)=\left(1-\frac{\sigma\left(i,j+\frac{1}{2},k\right)\delta t}{\varepsilon\left(i,j+\frac{1}{2},k\right)}\right)\bullet E_y^{n}\left(i,j+\frac{1}{2},k\right)+\frac{\delta t}{\varepsilon\left(i,j+\frac{1}{2},k\right)\delta}$$

$$\left[H_x^{n+\frac{1}{2}}\left(i,j+\frac{1}{2},k+\frac{1}{2}\right)-H_x^{n+\frac{1}{2}}\left(i,j+\frac{1}{2},k-\frac{1}{2}\right)+H_z^{n+\frac{1}{2}}\left(i-\frac{1}{2},j+\frac{1}{2},k\right)-H_z^{n+\frac{1}{2}}\left(\begin{matrix}i+\frac{1}{2},\\ j+\frac{1}{2},k\end{matrix}\right)\right]$$

(3A.2)

$$E_z^{n+1}\left(i,j,k+\frac{1}{2}\right)=\left(1-\frac{\sigma\left(i,j,k+\frac{1}{2}\right)\delta t}{\varepsilon\left(i,j,k+\frac{1}{2}\right)}\right)\bullet E_z^{n}\left(i,j+\frac{1}{2},k\right)+\frac{\delta t}{\varepsilon\left(i,j,k+\frac{1}{2}\right)\delta}$$

$$\left[\begin{matrix}H_y^{n+\frac{1}{2}}\left(i+\frac{1}{2},j,k+\frac{1}{2}\right)-H_y^{n+\frac{1}{2}}\left(i-\frac{1}{2},j,k+\frac{1}{2}\right)+H_x^{n+\frac{1}{2}}\left(i-\frac{1}{2},j-\frac{1}{2},k+\frac{1}{2}\right)-H_x^{n+\frac{1}{2}}\\ \left(i,j+\frac{1}{2},k+\frac{1}{2}\right)\end{matrix}\right]$$

(3A.3)

$$H_x^{n+1}\left(i,j+\frac{1}{2},k+\frac{1}{2}\right)=H_x^{n-\frac{1}{2}}\left(i,j+\frac{1}{2},k+\frac{1}{2}\right)+\frac{\delta t}{\mu\left(i,j+\frac{1}{2},k+\frac{1}{2}\right)\delta}$$
$$\left[E_y^n\left(i,j+\frac{1}{2},k+1\right)-E_y^n\left(i,j+\frac{1}{2},k\right)+E_z^n\left(i,j,k+\frac{1}{2}\right)-E_z^n\left(i,j+1,k+\frac{1}{2}\right)\right]$$

(3A.4)

$$H_y^{n+1}\left(i+\frac{1}{2},j,k+\frac{1}{2}\right)=H_y^{n-\frac{1}{2}}\left(i+\frac{1}{2},j,k+\frac{1}{2}\right)+\frac{\delta t}{\mu\left(i+\frac{1}{2},j,k+\frac{1}{2}\right)\delta}$$
$$\left[E_z^n\left(i+1,j,k+\frac{1}{2}\right)-E_z^n\left(i,j,k+\frac{1}{2}\right)+E_x^n\left(i+\frac{1}{2},j,k\right)-E_x^n\left(i+\frac{1}{2},j,k+1\right)\right]$$

(3A.5)

$$H_z^{n+1}\left(i+\frac{1}{2},j+1,k\right)=H_z^{n-\frac{1}{2}}\left(i+\frac{1}{2},j+1,k\right)+\frac{\delta t}{\mu\left(i+\frac{1}{2},j+1,k\right)\delta}$$
$$\left[E_x^n\left(i+\frac{1}{2},j+1,k\right)-E_x^n\left(i+\frac{1}{2},j,k\right)+E_y^n\left(i,j+\frac{1}{2},k\right)-E_y^n\left(i+1,j+\frac{1}{2},k\right)\right]$$

(3A.6)

where, δ is the uniform spatial increment i.e., $\Delta x = \Delta y = \Delta z = \delta$ and δt is the time increment.

References

[i] S.I.Y.Al-Mously, Design and performance enhancement of cellular handset antennas and assessment of their EM interaction with a human, [Ph.D. thesis], Department of Electrical and Computer Engineering, School of Applied Sciences and Engineering Academy of Graduate Studies, Janzoor-Tripoli-Libya, August 2009.

[ii] K.S.Yee, "Numerical solution of initial boundary value problems involving Maxwell' s equations," *IEEE Trans. Antenna Propagation*, vol. 14, No. 3, pp. 302-307, May 1966.

[iii] F.Gustrau and D.Manteuffel, "EM Modelling of Antennas and RF Components for Wireless Communication Systems," *Springer*-Verlag Berlin Heidelberg, Germany, pp. 48-54, 2006.

Appendix 5.A Microwave lens

EM waves with microwave frequencies can be refracted, transmitted and reflected when it pass through a dielectric material object [i]-[ii]. Diffraction may occur from edges and corners of dielectric objects where the size of the object is similar to the wavelength. Thus, EM waves at microwave frequencies show many similarities like visible light [iii]. Microwave lens is a dielectric structure which is transparent for microwave and capable of focusing or defocusing the EM energy of the microwave just like an optical lens focuses or defocuses visible light. Homogeneous dielectric materials of refractive index different from the free space have been used for a long time in microwave lens applications [iv].

5A.1 Theory of Microwave lens

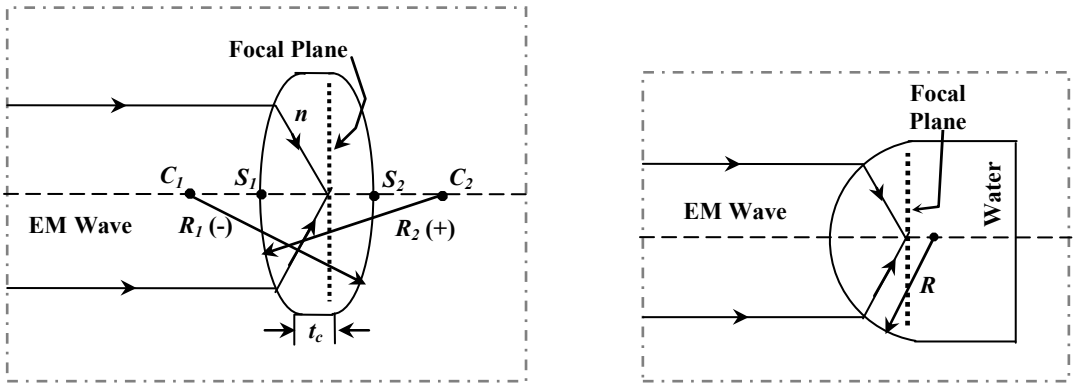

Figure 5A.i. Geometry of (a) thick convex lens and (b) Plano-convex lens.

A thick convex lens is shown in Figure 5A.i (a), where, S_1, S_2 are front and back vertices, C_1, C_2 are front and back centre points, respectively. Focal length f of the lens is given by [v] [vi]:

$$\frac{1}{f} = (n-1)\left[\frac{1}{R_1} - \frac{1}{R_2}\right] + \frac{t_c (n-1)^2}{n R_1 R_2} \qquad (5A.1)$$

where, n is the refractive index of the lens medium, t_c is thickness of the lens and R_1 and R_2 are the radius of curvature of the lens. Placing a microwave source in front of such convex microwave lens at a distance more than focal length, an inverted real image of the source

fields can be obtained [iv] [vii] [viii]. Considering the quasi-optical microwave properties, image position may be obtained using the following rules [ix]:

Rule 1: Image is expected at f when object is located at infinity distance from lens,

Rule 2: Image is expected within f and $2f$ when object is located at more than $2f$ distance from lens and

Rule 3: Image is expected at $2f$ when object is located at $2f$ distance from lens.

If one of the surfaces of the convex lens is made flat, then it is transformed into a plano-convex lens. A thick plano-convex lens is shown in Figure 5A-i (b), where the f can be written as [vi]:

$$f = \frac{R}{(n-1)} \qquad (5A.2)$$

where, n is the refractive index of the lens medium and R is the radius of curvature of the plano-convex lens. Placing a microwave source in front of such plano-convex microwave lens at a distance more than focal length, an inverted image of the source can be obtained inside the lens when its thickness is more than the focal length.

5A.2 Study on Thick Dielectric Plano-Convex Lens

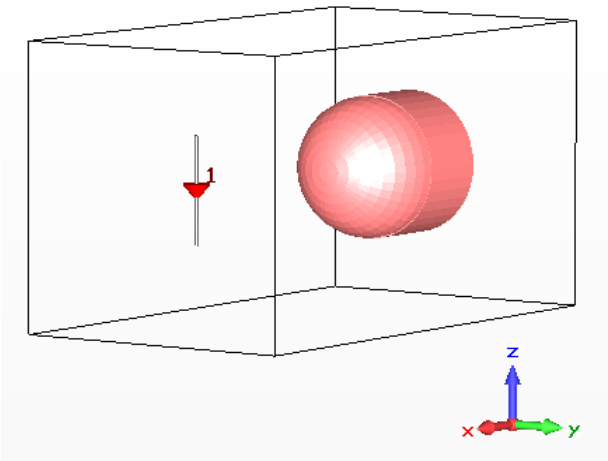

Figure 5A.ii. Geometry of the dielectric Plano-convex lens along with a half-wave dipole antenna.

For simulation, a thick plano-convex lens filled with water along with a half-wave dipole antenna has been developed in CST Microwave Studio® as shown in the Figure 5A.ii. The radius of curvature (R) of the plano-convex lens is 5.0 cm. A half-wave dipole antenna

resonating at 2.0 GHz which acts as imaging object is placed at a distance (*d*) of 15.0 cm from the lens.

Value of the wavelength dependence refractive index (*n*) of water can be obtained from the relation: $n = \sqrt{\varepsilon_r}$, where, ε_r is relative dielectric constant of water [x]. From available literature the value of n is found to be 8.8043 + i 0.4337 at 2.0 GHz [xi]. Thus, using equation (5A.2) focal length of this plano-convex lens is found to be 0.64 cm. The model is then simulated considering 465405 mesh cells. It is found that the *E* and *H* fields are focused at a distance of 0.64 cm, which is equal to the focal length of the lens itself. It is also observed that the image of source *E* and *H* fields is obtained inside the lens.

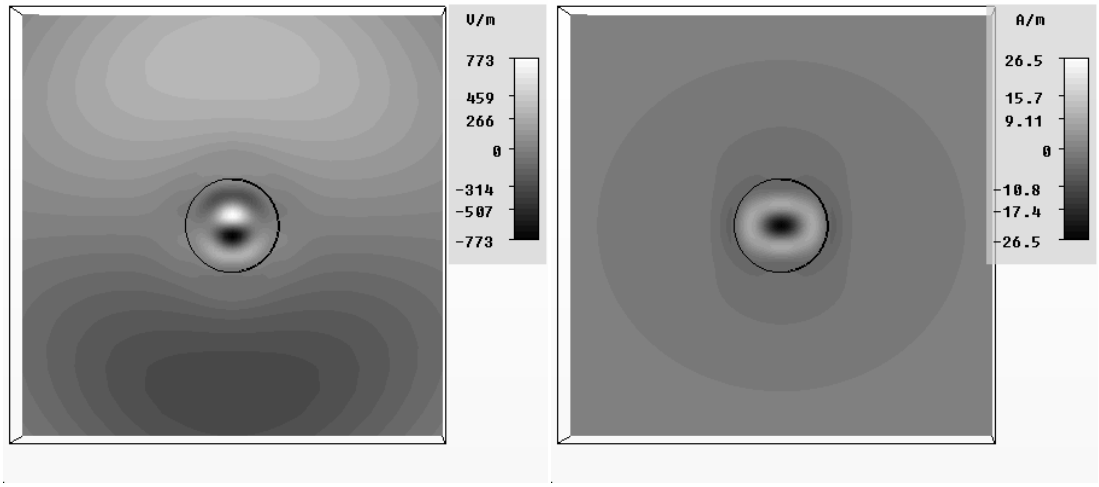

(a) **(b)**

Figure 5A.iii. Distribution of (a) *E* field and (b) *H* field at the focal plane inside the lens.

Distribution of *E* and *H* fields at the focal plane of the plano-convex dielectric lens as obtained from simulation is shown in Figure 5A.iii (a-b), respectively. In Figure 5A.iii (a), two high concentric spots consists of different phase are observed at the focal plane. The phase difference between these two *E* fields, are exactly 180^o, like the phase difference of two poles of the source dipole. These two points represent the electrical field image of the source of the dipole antenna. For a dipole antenna the maximum *E* field exists near the two ends of the dipole. Similarly, from Figure 5A.iii (b), it can be observed that a single high concentric spot is formed at the focal plane. This point represents the high magnetic field formed at the source dipole antenna. For a resonating dipole antenna, the maximum *H* field exists at the centre of the dipole. In the focal plane, maximum *E* and *H* field intensity are 773 V/m and 26.5 A/m, respectively.

Distributions of *E* and *H* fields at 0.5 cm inner plane from the focal plane of the plano-convex dielectric lens are shown in Figure 5A.iv (a-b). From Figure 5A.iv (a), it can be observed that field distribution are almost similar like earlier case, but maximum values of *E* and *H* field intensity at this plane are lower than that obtained at the focal plane due to the defocused fields. In this plane, maximum *E* and *H* field intensity are 667 V/m and 18.6 A/m, respectively.

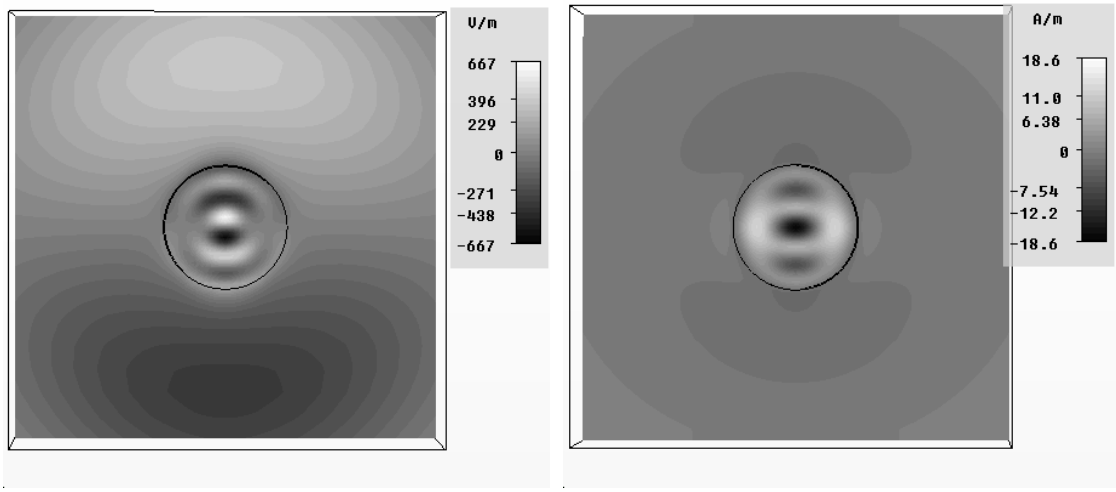

(a) **(b)**

Figure 5A.iv. Distribution of (a) *E* field and (b) *H* field at 0.5 cm from the focal plane inside the lens.

Variation of absolute magnetic field |*H*| with distance (*D*) measured from antenna end for *d* = 15.0 cm using different half-wave dipole antennas resonating at 925 MHz, 1795 MHz and 2.1 GHz respectively, is shown in Figure 5A.v. It is found that maximum magnetic field intensity inside the lens is obtained at the focal plane. Peak value of |*H*| field intensity increases with the increase of frequency which is possibly due to the macroscopic diffraction from the dielectric edges. Diffraction effects are more intensive for dielectric size of similar to wavelength and line of site propagation is more intensive for larger dielectric size with compared to wavelength [xii] [xiii].

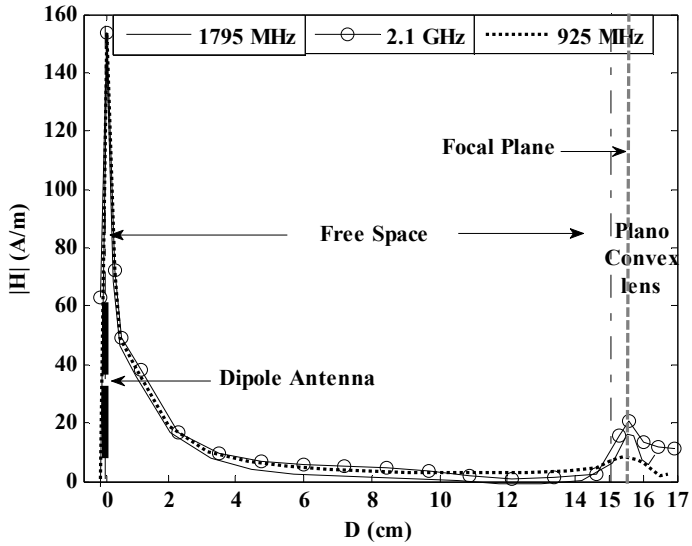

Figure 5A.v. |*H*| vs. *D* for *d* = 15.0 cm at 925 MHz, 1795 MHz and 2.1 GHz.

References

[i] D.W.Preston and E.R.Dietz, The Art of Experimental Physics, Wiley, New York, 1991.

[ii] W.H.Murray, "Microwave Diffraction Techniques from Macroscopic Crystal Models," *American Journal of Physics*, vol. 42, 137, July-1974

[iii] R.Y.Kezerashvili, "Light and electromagnetic waves teaching in engineering education," *International Journal of Electrical Engineering Education*, vol. 46, No. 4, pp. 343-353, November-2007.

[iv] S.Cornbleet, Microwave Optics. New York: Academic Press, 1976.

[v] E.John and Greivenkamp, Field Guide to Geometrical Optics, SPIE Press, pp. 6–9, 2004. ISBN 978-0-8194-5294-8.

[vi] Laser Components Gmbh: Lens Theory, Singlet Lenses, [On Line] Available: www.lasercomponents.com.

[vii] R.Levanda, and A.Leshem, "Image formation in synthetic aperture radio telescopes," pp. 1-13, September-2, 2010. [On Line] Available: http://arxiv.org/pdf/1009.0460.pdf.

[viii] Z.Shi, Y.Nagayama, D.Kuwahara, T.Yoshinaga, M.Sugito and S.Yamaguchi, "Two-dimensional Numerical Simulation of Microwave Imaging Reflectometry," vol. 8, *J. Plasma Fusion Res. Series*, 2009.

[ix] W.B.Dou, H.F.Meng, B.Nie, Z.X.Wang, and F.Yang, "Scanning antenna at THz band based on quasi-optical techniques," *Progress In Electromagnetics Research*, vol. 108, pp. 343-359, 2010. doi:10.2528/PIER10062810.

[x] From Wikipedia: Refractive index, [On Line] Available: http://www.videosec.com/education/Refractive-index.pdf.

[xi] D.Segelstein, "The Complex Refractive Index of Water," M.S. Thesis, University of Missouri-Kansas City, 1981.

[xii] N.S.Kapany, J.J.Burke and K.Frame, "Diffraction by Apertures of Wavelength Dimensions," *Applied Optics*, vol. 4, No. 10, pp. 1229-1238, 1965.

[xiii] T.K.Sarkar , Z.Ji , K.Kim , A.Medour and M.Salazar-Palma, "A survey of various propagation models for mobile communication," *IEEE Antennas Propag. Mag.*, vol. 45, No. 3, pp. 51 -82, 2003.